# Analysis of Polymer Injectivity in Porous Media

## Mohamed Adel Alzaabi

UNIVERSITY OF BERGEN

# Analysis of Polymer Injectivity in Porous Media

Mohamed Adel Alzaabi

Thesis for the degree of Philosophiae Doctor (PhD)
at the University of Bergen

Date of defense: 01.07.2021

Year:      2021

Title:     Analysis of Polymer Injectivity in Porous Media


Name:      Mohamed Adel Alzaabi

Print:     Skipnes Kommunikasjon / University of Bergen

*"Read; and your Lord is the Most Generous.*
*-He- who taught by the pen.*
*-He who- taught human what he never knew."*
*[3 – 5: Al- 'Alaq: Quran]*

# Scientific environment

This dissertation was submitted on April 12th, 2021, as part of the fulfilment for the degree of Philosophiae Doctor (PhD) at the University of Bergen (UiB), department of Chemistry. The thesis is based on simulation studies carried out at the department during the period 2018-2021. The research fellowship was sponsored and funded by Abu Dhabi National Oil Company (ADNOC).

# Acknowledgements

All praise and thanks are due to Allah, the One who by his grace good deeds are completed.

I would like to express my sincere and utmost gratitude to my supervisor, Professor Arne Skauge, for his remarkable guidance and supervision during my PhD journey. He went above and beyond in being an extremely supportive supervisor as well as being a great caring friend.

I extend my appreciation to my co-supervisors, Shehadeh Masalmeh, and Øystein Pettersen for their valuable contributions to the work done in this thesis.

I would also like to offer special thanks to Ken Sorbie, Tormod Skauge, and Iselin Salmo for their valued insights, assistance, and discussions.

I am very grateful as well for the extraordinary support I got from my colleagues Abdul Majid Murad and Jorgen Jacobsen. Thanks for making this journey more exciting and fun.

Appreciation is extended to Hege Ommedal for her support as a PhD-coordinator at the Department of Chemistry.

I am thankful to Abu Dhabi National Oil Company (ADNOC) for their financial support. Special thanks to my ADNOC's academic supervisor Lisa Nichols for her continuous support.

Many thanks to my mother Muna and my father Adel for being such amazing parents. They showered me with their unconditional love and prayers during every moment of my graduate studies abroad and away from home.

Last but not least, the greatest appreciation goes to my beloved wife Noura and my little son Abdullah. They were always there for me with every bit of support, encouragement, patience, and love they could offer.

# Abstract

Polymers are chemical substances that occur both naturally or synthesized and consist of large macromolecules. They are created by the process of polymerization of many smaller molecules also known as monomers. Due to their unique properties, there are tremendous number of daily life applications that involve polymers, from basic food and clothing industries to the manufacturing of advanced machineries. One of the applications of polymers in the oil industry is in the method known as polymer flooding, which is one of the most successful and widely applied chemical enhanced oil recovery techniques.

The recovery of oil from subsurface reservoirs usually involves injection of water to improve oil sweep and maintain pressure. In some cases, however, the mobility ratio between displacing water and displaced oil is unfavorably large which results in significant amount of bypassed oil. Therefore, Polymer is added to injection water to enhance waterflooding sweep efficiency by increasing injected water viscosity and reducing its mobility.

Although polymer flooding is a relatively mature and widely discussed method in the literature, many flow mechanisms and phenomena of polymer flow in porous media are yet to be fully understood. Among these topics is the non-Newtonian shear dependent in-situ rheology of polymer solutions at reservoir conditions, and its impact on polymer injectivity. Another example is the modelling of immiscible viscous fingering observed in the preconditioning waterflooding in heavy oil reservoirs. Accurate modelling of this phenomenon is essential as it provides better understanding of fluids distribution in the reservoir prior to polymer flooding.

In this thesis, numerical simulation studies were conducted to investigate several issues related to polymer injectivity in porous media. The main topics discussed are (1) modelling immiscible viscous fingering of water flooding at adverse mobility conditions, (2) optimizing field polymer injectivity test design by investigating the impact of polymer in-situ rheology on injection bottomhole pressure data, and (3)

analyzing the data of actual field polymer injectivity test conducted in a high temperature high salinity carbonate reservoir in Abu Dhabi, UAE.

Viscous fingering observed in unstable displacement 2D waterflooding experiments were matched using a novel approach that resolves the issue from both physical and engineering perspective. The approach depends mainly on choosing a modified fractional flow function to increase the shock front saturation within established fingers. By combining this concept with a dispersivity-optimized grid sizing and a randomly correlated permeability field representative of micro heterogeneity, four waterflooding experiments at four different heavy oil viscosities were matched adequately for both observed fingering patterns and production data.

Radial lab experiments on HPAM polymer revealed significant deviation in polymer shear dependent viscosity behavior from the one observed in linear experiments. The main difference is seen in the lower magnitude and delayed onset of shear thickening in radial geometry compared to linear. Lab scale simulation studies proved the robustness of utilizing injection pressure data to estimate polymer rheological behavior. Upscaled field simulation models were used to investigate the signature of Newtonian behavior compared to possible non-Newtonian behaviors in near wellbore region. Results have shown that each of shear thickening, shear thinning, and the combined effect rheology behaviors could be distinguished from the injector bottomhole pressure data. For instance, a viscosity profile that increases towards the wellbore (shear thickening) reflects an increasing slope on pressure versus rate plots, and vice versa for shear thinning. Besides, transient pressure behavior exhibits distinctively sharper trends for Newtonian and shear thickening compared to shear thinning.

General guidelines on optimizing polymer injectivity test design were suggested based on observations from several generic simulation studies on homogeneous and vertically heterogenous models. The two main recommendations with regard to the test design are the essential inclusion of rate stepping, besides the importance of injecting for a sufficient time of at least 0.001 pore volumes of the near wellbore region.

Analysis of polymer injectivity test data from a field application in Abu Dhabi have further confirmed the practicality of using bottomhole pressure data to predict polymer in-situ rheology. Sensitivity studies showed a more gradual impact of concentration stepping on the bottomhole pressure response compared to rate stepping. Besides, average weighted residual resistance factor was found equivalent to using permeability dependent RRF correlations. Polymer degradation from pre-shearing prior to injection can be included in the model by inputting modified concentration values that account for degradation percentage. Consequently, by utilizing pressure data and modified concentrations, reliable in-situ rheology curve can be constructed to history match polymer injectivity test data.

# List of papers

**Paper 1:**

Jacobsen, J. G., Alzaabi, M. Skauge, T., Sorbie, K & Skauge, A. (2019): *Analysis and Simulation of Polymer Injectivity*. Presented at the 20th European Symposium on Improved Oil Recovery, Pau, France, 8-11 April.

**Paper 2:**

Alzaabi, M. A., Jacobsen, J. G., Sumaiti, A. A., Masalmeh, S, Pettersen, Ø. & Skauge, A. (2020): *Polymer Injectivity Test Design Using Numerical Simulation*, Polymers, Vol. 12: 1-23.

**Paper 3:**

Alzaabi, M. A., Hinestrosa, J., Skauge, A. & Masalmeh, S. (2021): *Analysis and Simulation of Polymer Injectivity Test in a High Temperature High Salinity Carbonate Reservoir*. Submitted to the journal Polymers, special issue: Polymer Flooding and Rheology.

**Paper 4:**

Salmo, I., Alzaabi, M. A., Sorbie, K., Skauge, A. (2021): *Modelling Immiscible Viscous Fingering: History Match of Water Flood at Adverse Mobility Ratio.*

Draft journal article manuscript. To be submitted.

*All four manuscripts are attached to the last part of this thesis.

# Contents

# List of figures

# List of tables

# Nomenclature

Abbreviations:

| | |
|---|---|
| 2D | two-dimensional |
| 3D | three-dimensional |
| ADNOC | Abu Dhabi National Oil Company |
| $A$ | area/ cross sectional area |
| $ad$ | adsorption |
| AI | artificial Intelligence |
| AMPS | 2-Acrylamido-2-Methyl Propane Sulfonate |
| AP | alkali-polymer |
| AS | alkali-surfactant |
| ASP | alkali-surfactant-polymer |
| $b$ | power law coefficient |
| BHP | bottom-hole pressure |
| bpd | barrels per day |
| C | Celsius |
| $C_p$ | polymer concentration |
| CEOR | chemical enhanced oil recovery |
| cm | centimeter |
| CMG | Computer Modelling Group Ltd. |
| cp | centipoise |
| $D_e$ | Deborah number |
| Da | Daltons |
| DE | differential evolution |
| DECE | designed exploration and controlled evolution |
| $E_D$ | microscopic displacement efficiency |
| $E_R$ | recovery efficiency factor |
| $E_V$ | volumetric efficiency |
| EAGE | European Association of Geoscientists & Engineers |
| EIA | Energy Information Administration |
| EOR | enhanced oil recovery |
| F | force/ Fahrenheit |
| $f_w$ | water fractional flow |
| ft | feet |
| $G'$ | elastic modulus |
| GDP | gross domestic product |
| $h$ | thickness |
| HPAM | partially hydrolyzed polyacrylamide |
| IEO | International Energy Outlook |

| | |
|---|---|
| $II$ | injectivity index |
| IOR | improved oil recovery |
| IPV | inaccessible pore volume |
| $K$ | consistency constant/ constant of proportionality |
| $k$ | permeability |
| $k_r$ | relative permeability |
| $L$ | length |
| $L_f$ | characteristic flow length |
| lb | pound |
| LHPO | Latin hypercube proxy optimization |
| $M$ | mobility ratio |
| mbar | millibar |
| mD | milli-Darcy |
| min | minute |
| mL | milliliter |
| $MW$ | molecular weight |
| $n$ | power index constant |
| $N_{init}$ | total volume of oil originally in place |
| $N_p$ | produced oil volume |
| $P$ | pressure |
| PAM | polyacrylamide |
| PFO | pressure falloff |
| PhD | philosophiae doctor |
| PLT | production logging tool |
| ppm | parts per million |
| psi | pound per square inch |
| PSO | Particle Swarm Optimization |
| PV | pore volume |
| $Q$ | volumetric flow rate |
| $R$ | radius of molecules |
| $r$ | radius |
| $R_k$ | permeability reduction factor |
| RBF | Random Brute Force |
| RCF | random correlation field |
| $Ret$ | viscosity retention |
| RF | resistance factor |
| RRF | residual resistance factor |
| $s$ | skin factor/ seconds |
| $S_{or}$ | residual oil saturation |
| $S_w$ | water saturation |
| SPE | Society of Petroleum Engineers |

| | |
|---|---|
| $t$ | time |
| $T$ | temperature |
| $u$ | velocity |
| $U$ | pore-scale velocity |
| U.S. | United States |
| UAE | United Arab Emirates |
| UiB | University of Bergen |
| $x$ | mass fraction |
| $y$ | distance between moving plates |

Greek Letters:

| | |
|---|---|
| $\alpha$ | relative concentration |
| $\dot{\gamma}$ | shear rate |
| $\gamma$ | strain |
| $\lambda$ | mobility/ relaxation time/ correlation length |
| $\mu$ | viscosity |
| $\pi$ | pi |
| $\tau$ | shear stress |
| $\theta$ | time |

Subscripts:

| | |
|---|---|
| 0 | zero-shear |
| $a$ | after |
| $abs$ | absolute |
| $app$ | apparent |
| $b$ | brine/ before |
| $c$ | critical |
| $e$ | production rim |
| $f$ | flow/ fractional/ front |
| $i$ | pressure port location |
| $L$ | liquid |
| $max$ | maximum |
| $min$ | minimum |
| $NaCl$ | salt |
| $o$ | oil |
| $pm$ | porous media |
| $p$ | polymer |

| | |
|---|---|
| $R$ | polymer relaxation |
| $s$ | solvent |
| $sw$ | polymer-water solution mixture |
| $T$ | total |
| $w$ | water/ well |
| $z$ | Zimm |
| $\infty$ | infinite-shear |

Superscripts

| | |
|---|---|
| $*$ | end-point |
| $0$ | reference condition |

# 1. Introduction

The present-day world is facing an ever-increasing demand for energy, driven by fast global population growth, and accompanied by industrial, technological, and economic advancements on many levels. With a 0.7% global population growth and 3.0% global GDP growth per year, the global energy consumption has been rising steadily seeing projections of nearly 50% increase by 2050 compared to 2010 levels (EIA, 2020). In its International Energy Outlook 2020 (IEO 2020), report, the U.S. Energy Information Administration (EIA) highlighted the emerge and rapid growth of renewable energy sources as the main supplier for power generation purposes by 2050 (Figure 1.1a). Nevertheless, the energy used for power generation accounted for only 40% of total global energy consumption in 2020 with forecasts not exceeding 45% in 2050 (Figure 1.1b).
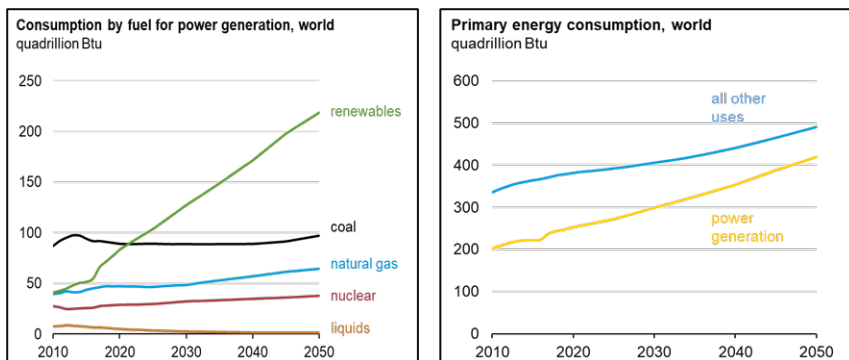


*Figure 1.1: a) World's energy consumption by fuel for power generation purposes. b) World's primary energy consumption (EIA International Energy Outlook, 2020).*

Consequently, even with the substantial share the renewables will hold in global energy sector in the next few decades, EIA's forecasts still predict that hydrocarbons would represent about 48% of the world's total energy basket by 2050 (Figure 1.2). This share, which is divided between natural gas (22%) and petroleum liquids (26%), reflects the important role of hydrocarbons generally and crude oil especially in meeting the world's thriving demand for energy in the mid to long-term outlooks.

The term "peak oil" is used frequently to refer to the time the world achieves its maximum oil production capacity before declining (Hirsch et al., 2005). With the average recovery factor of conventional recovery mechanisms estimated at about 35% (Thomas, 2019), it is believed that in most oil reservoirs, two thirds of oil in place is bypassed and left behind. With conventional oil production reaching its peak in many fields around the world, the industry has been tapping into other solutions to maintain essential oil supply for the energy market. One of these solutions is implementing enhanced oil recovery (EOR) methods which can significantly increase the output of mature reservoirs by increasing recovery factors through various mechanisms.
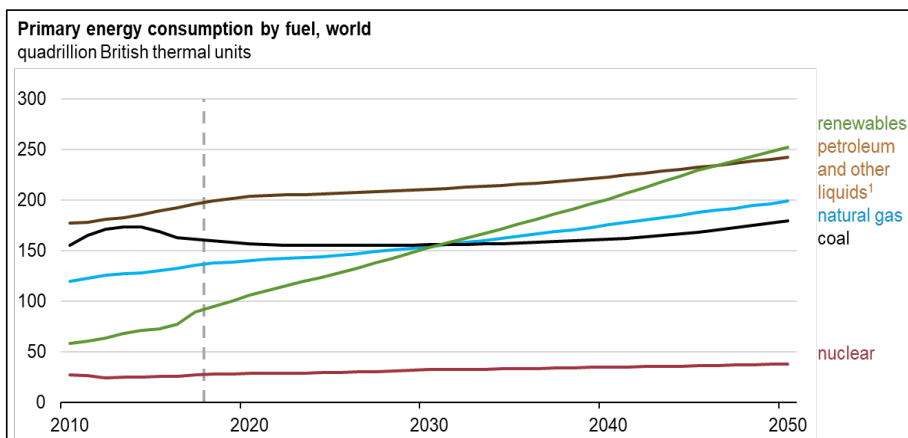


*Figure 1.2: Current levels and forecast of world's primary energy consumption by fuel (EIA International Energy Outlook, 2020).*

Polymer flooding technology is a chemical EOR (CEOR) technique that has been widely and successfully implemented for the past few decades in many projects around the world (Sheng et al., 2015; Manrique et al., 2017). The method mainly involves injecting viscous polymer solutions to improve oil sweep by creating more favorable mobility conditions (Sorbie, 1991). Recent research results have shown that polymer flooding may also reduce residual oil saturation by mobilizing capillary trapped oil (Azad & Trivedi, 2019).

In the next chapters, a comprehensive review is provided on the main mechanisms of conventional, EOR and CEOR recovery mechanisms with emphasis on polymer

flooding technology. The review also includes a discussion of the characteristics and key factors of polymer solution flow in porous media, in addition to topics related to polymer injectivity, modelling, and polymer action in heavy oil reservoirs. This theoretical review should provide an adequate base to discuss the presented results in this thesis.

## 1.1  Research motivation

As research on polymer flooding developed through the years, findings have revealed that polymer solution behavior in porous media is more complex than just a simple viscosified water flood. Firstly, the use of polymer flooding in heavy oil reservoirs has been widely suggested to reduce the impact of unfavorable mobility ratio and improve oil recovery after secondary waterflooding. However, there is a need to understand the phenomenon of viscous fingering associated with flooding at extremely adverse mobility ratio found in extra heavy oil reservoirs. Secondly, the complex non-Newtonian in-situ rheology of polymers in porous media has been a subject of many theories and debates, especially in describing the apparent increase in resistance referred to as shear thickening at high shear rates. Recent findings by Skauge et al. (2016) verified that polymer flow behavior in radial flow differs significantly from linear flow. Since radial geometry is a much closer approximation of the injection conditions around injector's wellbore, these findings imply that uncertainties of considerable extents must be assumed when utilizing polymer in-situ rheology data from linear lab experiments. In addition to lab-scale issues, field-scale applications require solid workflows for injectivity tests design and simulation. Modelling and estimation of polymer injectivity for field applications relies entirely on the accurate prediction of in-situ rheology. Unlike lab data, field data are limited with the only source of data usually being the injection bottom-hole pressure. It is therefore essential to be able to predict in-situ rheology of injected polymers utilizing available data. Moreover, the application of polymer flooding in heavy oil reservoirs adds further factor of complexity in modeling polymer injectivity. This is due to the phenomenon

of viscous fingering caused by the extreme viscosity contrast, referred to as adverse mobility ratio, between the displacing and displaced fluids.

## 1.2  Main objectives

The objectives of this thesis are as follows:

i.   Improve the simulation of viscous fingering observed in waterflooding at adverse mobility conditions in order to accurately measure fluids distribution prior to polymer flooding.

ii.  Propose a methodology to estimate polymer in-situ rheology and injectivity from radial flow pressure data.

iii. Provide guidelines on the optimization of polymer injectivity tests design in order to maximize the information gained from these tests.

iv.  Investigate the viability of using bottom-hole pressure data from field applications to predict polymer in-situ rheology.

## 1.3  Papers contents

**Paper 1 (Jacobsen et al. 2019)** evaluates the influence of different polymer rheological behaviors on bottom hole pressure both at transient and steady state levels in order to distinguish the signatures of each behavior. Additionally, it presents simulation history matching approaches to assess rheology utilizing a radial flow experiment in Bentheimer sandstone.

**Paper 2 (Alzaabi et al. 2020)** investigates the information that can be gained from polymer injectivity tests and proposes recommendations on optimizing the design of the test to maximize gained information. A simulation approach was used to analyze the response of different non-Newtonian rheology on bottom hole pressure with variations of rate and time. Impacts of vertical reservoir heterogeneity, viscosity

mixing, and permeability dependent residual resistance factor have also been discussed.

**Paper 3 (Alzaabi et al. 2021)** analyzes the data from actual field polymer injectivity test conducted in a Middle Eastern carbonate reservoir. The analysis involved utilizing lab and field data to build a representative simulation model that was used to test several generic sensitivities with the purpose of investigating the impacts of rate, concentration, and RRF variations. The results have shown the necessity of using complex in-situ rheology curves at several concentrations to history match polymer injection.

**Paper 4 (Salmo et al .2021)** investigates the application of a new approach proposed to model immiscible viscous fingering seen in waterflooding at adverse mobility ratio unstable displacements. The methodology involved a resolution to the shortcomings of 1D fractional flow function by assigning modified fractional flow that would produce relative permeability curves different than the conventional ones. The paper included history matching of four adverse mobility experiments. Results proved the robustness of the proposed methodology by matching both fingering patterns and production data.

## Thesis structure

The thesis comprises six chapters. Chapter 1 contains an introductory preface to the thesis topics as well as sections on research motivation, main thesis objectives, and papers contents. In chapter 2, methods and mechanisms of different oil recovery techniques are briefly reviewed. Chapter 3 includes a thorough overview of topics related to polymer flooding with emphasis on key factors influencing polymer flow in porous media, polymer injectivity, and flooding at adverse mobility conditions. Chapter 4 briefly discusses the polymer flooding simulation modules in STARS and IMEX simulators from CMG and provides descriptions of the models used in the thesis. In chapter 5, main results and observations are summarized and discussed. Lastly, chapter 6 includes general conclusions and recommendation for further studies.

# 2.    Enhanced oil recovery

This chapter is dedicated to discussing oil recovery mechanisms at different petroleum field development stages and scales. The objective is to demonstrate the importance of applying enhanced oil recovery (EOR) techniques to boost oil production by targeting oil bypassed by primary and secondary recovery techniques.

## 2.1  Primary and secondary oil recovery

Primary recovery is the first stage of production in the lifetime of a petroleum field. In this stage, the reservoir is being produced under its own natural energy mechanisms (Clark, 1969). These mechanisms include water drive, gas drive, and/or gravity drainage. Water drive involves a pressure support from an active aquifer below or at the edge of oil zone. In contrast, gas drive mechanism involves the expansion of dissolved gas or the expansion of a free gas cap above the oil zone. Gravity drainage is a mechanism in which gravity forces drive hydrocarbons to the wellbore. Primary recovery may recover about 10% of the oil in place in average before it slows down and eventually -in theory- stops due to pressure depletion. To remedy this depletion, some artificial lift solutions are usually implemented such as gas-lift, submersible pumps, and rod pumps, which can increase the recovery by an extra 10 to 20% (Stosur et al., 2003). These types of remedies tackle only the problem of differential pressure between wellhead and bottomhole pressure, while the reservoir pressure keeps declining resulting in production loss. Consequently, secondary recovery is typically implemented by injecting external fluids into the reservoir to maintain reservoir pressure. This practice is referred to as "flooding" and it also assists in sweeping the reservoir and displacing oil toward production wells. In most cases, water is used for secondary recovery injection due to its abundance, practicality, and economic feasibility. In some cases, gas injection is used for the same purposes if it proved technically and economically viable.

The efficiency of secondary recovery flooding is governed mainly by the ratio between the mobility of displacing fluid, water for example, and the mobility of displaced fluid which is oil. This ratio is termed mobility ratio ($M$):

$$M = \frac{\lambda_w}{\lambda_o} = \frac{k_{r,w}}{k_{r,o}} \frac{\mu_o}{\mu_w} \qquad \text{Eq. 2.1}$$

where $\lambda_w$ and $\lambda_o$ are water and oil mobilities, respectively, $k_{r,w}$ and $k_{r,o}$ are water and oil relative permeabilities, respectively, $\mu_w$ and $\mu_o$ are water and oil viscosities, respectively. The lower the mobility ratio, the higher is flooding efficiency. This definition implies that heterogeneous reservoirs as well as reservoirs with heavy crudes will exhibit significantly lower recovery efficiency than homogenous and/or light crude reservoirs. High contrasts in permeability and/ or viscosity in the reservoir could cause instability at the front of displacing fluid which results in bypassing significant amount of oil due to channeling or viscous fingering phenomena.

## 2.2 Recovery efficiency

The efficiency of oil exploitation from a petroleum reservoir is measured by recovery efficiency factor, $E_R$. It is defined as the ratio of produced oil volume ($N_p$) to the total volume of oil originally in place ($N_{init}$):

$$E_R = \frac{N_p}{N_{init}} \qquad \text{Eq. 2.2}$$

The overall recovery efficiency can also be divided into two subcategories concerning the type of forces acting on the oil in reservoir at different scales. First is macroscopic sweep or volumetric efficiency ($E_V$) which is related to the viscous forces between displacing fluid and displaced oil. This type of displacement is targeted by the aforementioned flooding techniques. The second type is microscopic displacement efficiency ($E_D$), which reflects capillary forces affecting oil mobilization at the pore scale. The recovery efficiency is thus defined as the product of $E_V$ and $E_D$. According to these definitions, the oil left in the reservoir is either a "bypassed" oil due to

imperfect volumetric sweep efficiency related to viscous forces, or a "residual" oil trapped by capillary forces.

## 2.3  Tertiary oil recovery

As oil reservoirs mature, the recovery efficiency of primary and secondary stages gets to its maximum limit. On average, 65% of the oil is left behind in the reservoir after applying recovery techniques involving only conventional pressure maintenance and volumetric sweeping by injecting water or immiscible gas (Lake et al. 2014). It is thus necessary to apply further enhancement of production by getting into tertiary recovery stage, which is a term used interchangeably with the term "EOR". Despite this common consent, EOR methods are sometimes used simultaneously with secondary or even primary recovery methods.

There are various EOR techniques that have been implemented for decades based on experimental research and field pilots. The selection criteria for EOR depends entirely on each individual reservoir characteristics and fluid properties. The current defined subcategories of EOR are labeled: thermal, chemical, solvent (miscible gas injection) and others (Figure 2.1). Generally, the main objective of EOR is to target bypassed oil after or in conjunction with waterflooding. This goal is achieved by two main mechanisms: increasing viscous force of injected fluid, and/or reducing capillary forces responsible for oil trapping. For instance, thermal EOR methods are typically applied for heavy oil reservoirs, where heat is introduced to the reservoir to reduce oil in-situ viscosity and thus increase its mobility on macroscopic viscous level (Kokal & Al-Kaabi 2010, Lake et al. 2014). On the other hand, solvent injection involves injecting miscible gases, either hydrocarbon or non-hydrocarbon like $CO_2$, to reduce interfacial tension between oil and injected fluids, thus increasing microscopic capillary displacement at pore scale (Stalkup 1983).
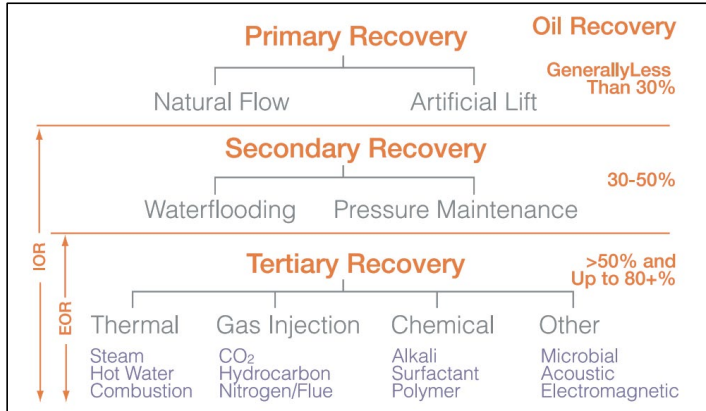
*Figure 2.1: Oil recovery stages and types of EOR methods (Kokal & Al-Kaabi, 2010).*

In chemical EOR (CEOR) techniques, chemical substances are injected in the reservoir to improve waterflooding efficiency via various mechanisms. CEOR gained much popularity during the past few decades due to its relatively higher efficiency and economic feasibility (Gbadamosi et al 2019). Conventionally, three main types of CEOR are recognized: polymers, alkali, and surfactants. Recently, few studies have included also designed brine salinity waterflood and nanofluid flooding as a promising CEOR which involved engineered nanomaterial tailored to tackle specific production impairments. One of the frequently reported advantages of CEOR is their ability to be applied simultaneously, such as the case in alkali-polymer (AP), alkali-surfactant (AS), and alkali-surfactant-polymer (ASP) methods. Alkali and surfactant flooding share similar mechanisms which depend on lowering interfacial tension between injected water and reservoir oil and wettability alteration.

# 3.    Polymer flooding:

Polymer flooding is a CEOR technique that is applied to enhance waterflooding efficiency by augmenting the viscosity of injected water using polymers additives. The main objective is to improve oil sweep efficiency by reducing water mobility and hence remedy production impairment caused by viscous fingering and water channeling, especially in heterogeneous reservoirs (Sheng et al. 2015).

The primary concept of utilizing high viscosity fluids for EOR applications dates back to as early as 1944, when a patent was registered in the U.S. under the name of Kenneth Detling from Shell Development Co. The patent explained the benefits of using high viscosity fluids (aqueous or non-aqueous) to improve waterflooding outcomes in oil sands (Detling 1944). Nevertheless, the significantly high cost of proposed viscosifying agents at that time was a hurdle in the way towards economically justified field application. About twenty years later, the concept was revived once again by the recognition of synthetic partially hydrolyzed polyacrylamide (HPAM) as a potential cost-effective candidate for oil recovery applications due to its low production costs and large commercial availability (Sandiford, 1964; Pye, 1964; Mungan et al, 1966; Gogarty, 1967). Moreover, because of its relatively high molecular weight, researchers have revealed the capability of HPAM to reach targeted water viscosities by adding small amounts only. Consequently, core flooding lab experiments demonstrated promising results of significant increase in oil recovery when using HPAM as a viscosifying agent in injected water (Sorbie 1991).

Recently, polymer flooding has been recognized as one of the most successfully implemented CEOR methods, with growing interest for its application in an increasing number of fields around the world (Skauge et al., 2018). The reasons for this lie behind the increasing understanding of polymers flow mechanisms, besides the continuous advancements in polymers manufacturing allowing enhanced stability that can withstand harsher reservoir conditions. The following sections present an elaborate review of polymers types, properties, and characteristics related to flow in porous media.

## 3.1  Polymer types and properties

Polymers are chain-like molecular compounds consisting of a large number of relatively simple structural repeating units referred to as "monomers" (Hagnauer, 1986). Although there is no minimum number of monomers for a molecule to be regarded as polymeric, polymers molecular weights (MW) are usually larger than 5000 Daltons (Da) for an average of more than 100 monomers per molecule. The monomers are linked by covalent chemical bonds creating linear or branched open-chain or three-dimensional networks. Due to the nature of this type of chemical structures, polydispersity is an inherent characteristic of polymers implying that the molecular weight of a random sample is distributed over a broad spectrum.

Two types of polymers are predominantly used for CEOR applications, biopolymers and synthetic polymers, where xanthan and HPAM being the most frequently used polymers for each type, respectively (Sorbie 1991). Both xanthan and HPAM were available commercially in other industries prior to their link to oil recovery applications which made it easier to adopt them for polymer flooding research.

### 3.1.1 Xanthan biopolymer

Xanthan biopolymer was firstly proposed for EOR applications in late 1970's (Sandvik and Maerker 1977). It is produced industrially from carbon sources by fermentation using a type of bacteria called Xanthomonas campestris (Palaniraj and Jayarman 2011). The molecules of xanthan are usually modeled as rigid helical rod-like molecules. This explains the strong pseudoplastic behavior of xanthan besides its relative insensitivity to temperature, pH, salinity and hardness of solution (Sorbie 1991). Due to the complexity of xanthan production, it lacks the factor of availability and thus lacks practicality compared to HPAM. Moreover, the injection of xanthan is usually mixed with biocides to prevent its degradation. Since biocides can also affect other living organisms, it is considered environmentally harmful. One advantage of using xanthan is its tendency to retain its pseudoplastic bulk behavior when injected into porous media which can assist in injectivity control due to shear thinning behavior at high shear rates.

## 3.1.2 Partially hydrolyzed polyacrylamide (HPAM)

HPAM is by far the most used polymer in field applications with at least 90% of total applications, thanks to its relative high convenience in terms of production and supply. Therefore, and since the data and approaches used in this thesis are based on HPAM exclusively, the focus of the following sections and throughout the rest of the thesis will be on HPAM and its derivates where it applies.

HPAM is a synthetic linear copolymer that consists of straight chains of acrylamide monomers of which some are hydrolyzed. Its molecular conformation is described as flexible which also referred to as random coil in polymer chemistry (Sorbie 1991). Figure 3.1 demonstrates the basic backbone structure of a polyacrylamide molecule (PAM) which has the chemical formula of $C_3H_5NO$. Through the hydrolysis process, some of acrylamide monomers are replaced with acrylic acid due to the substitution of amide groups ($CONH_2$) by carboxyl groups ($COO^-$) (Sun et al. 2012). The degree of hydrolysis reflects the mole fraction of amide groups that are converted by hydrolysis. The typical range of hydrolysis for EOR application is between 25 and 35%.
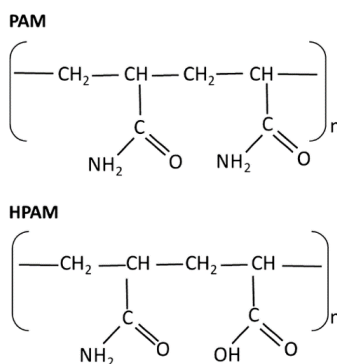


*Figure 3.1: Basic backbone structures of PAM and HPAM (Berdugo-Clavijo et al. 2019).*

Hydrolysis of polyacrylamide converts it from a nonionic compound to an anionic polyelectrolyte with a strong negative charge. This alteration combined with the flexibility of HPAM molecular structure contributes to the strong inverse relationship between HPAM viscosifying power and salinity of the solvent.

## 3.2  Polymer rheology

### 3.2.1 Introduction

Rheology is a term derived from the Greek "rheos", meaning "something flowing", that was proposed by Bingham in 1929 for the science of flow and deformation properties of materials in terms of stress, strain rates, and time (Gooch 2007). By that definition, rheology of fluids is the study of its viscosity behavior at different flow conditions and regimes. From rheological perspective, fluids are classified to Newtonian and non-Newtonian. While Newtonian fluids show strictly constant viscosity at any applied shear, non-Newtonian fluids have shear-dependent viscosities.

Viscosity is a measure for the resistance to shear flow. The physical definition of viscosity can be illustrated by visualizing simple shear flow of a fluid bounded between a moving plate and a stationary surface (Figure 3.2).
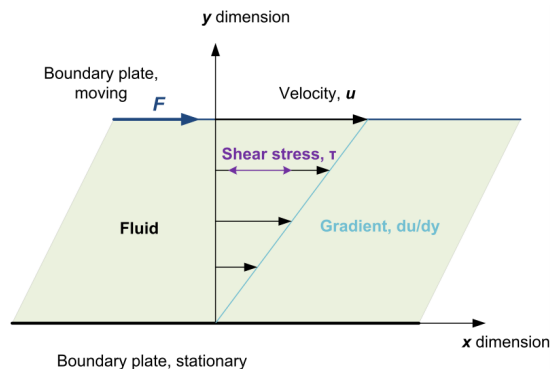


*Figure 3.2: Flow between two parallel plates illustrating shear stress (Mezger, 2011).*

The velocity of fluid particles adjacent to the moving plate will flow at a maximum relative velocity. It decreases away from the moving boundary and reaches its lowest at the stationary boundary. Shear rate is the rate at which velocity ($u$) changes with distance between the two plates ($y$):

$$\dot{\gamma} = \frac{du}{dy} \qquad\qquad \text{Eq. 3.1}$$

The shear stress applied on the fluid ($\tau$) is defined as force applied on the moving plate ($F$) divided by the area the force acts upon ($A$). Viscosity ($\mu$) is defined as the ratio between shear stress and shear rate:

$$\mu = \frac{\tau}{\dot{\gamma}} \qquad\qquad \text{Eq. 3.2}$$

A Newtonian fluid shows strictly linear constant slope on a shear stress versus shear rate plot. Thus, its viscosity is constant regardless of applied shear and steeper slopes representing higher viscosities. In contrast, non-Newtonian fluids exhibit a non-linear relationship between shear stress and shear rate suggesting that their viscosities are shear dependent. A non-Newtonian fluid may either exhibit a pseudoplastic or a dilatant behavior (Figure 3.3). Pseudoplasticity implies that fluid's viscosity decreases with increasing shear rate. In contrast, dilatant behavior is when the fluid exhibits an increasing viscosity with increasing shear.
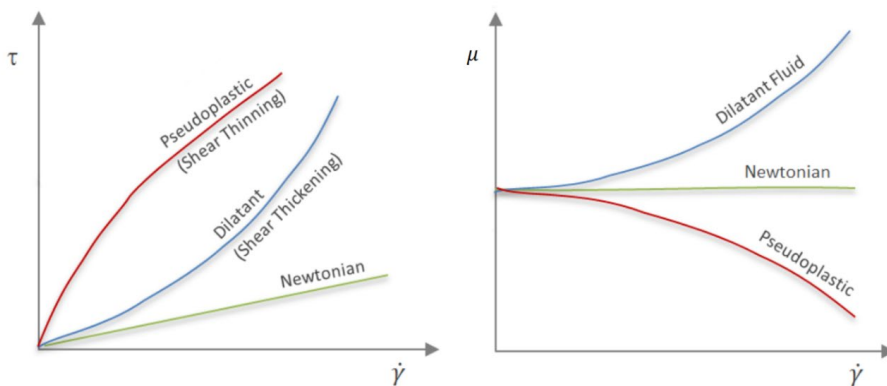


*Figure 3.3: Newtonian, dilatant, and pseudoplastic fluids shear stress and viscosity behaviors at different shear rates (Polymer Data Base, 2021).*

## 3.2.2 Bulk rheology

Polymer solutions used in EOR are essentially non-Newtonian pseudoplastic fluids. In bulk viscosity measurements, the viscosity of polymer solutions is measured using rheometers by putting them through simple shear flow with increasing shear rate in a stepwise scheme. Figure 3.4 illustrates typical bulk viscosity curve of polymer solutions within moderate concentrations range referred to as semi-dilute regime.

Ideally, if bulk measurements were conducted over extensive and sufficient range of shear rates, three regions could be identified over the bulk viscosity curve. The first region is called the upper Newtonian plateau and it referred to as the zero-shear viscosity ($\mu_0$). At this range of low shear rates, polymer solution viscosity is exclusively associated to its concentration and size of polymer molecules. The internal bonds between polymer coils are not altered and thus Newtonian behavior dominates viscosity.
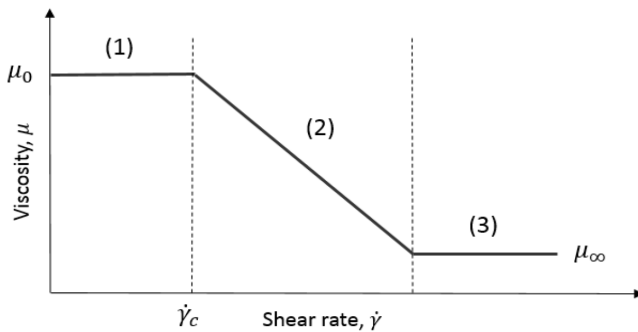


Figure 3.4: Typical bulk viscosity behavior of polymer solutions.

With the continuous increase in shear rates, polymer coils start separating and aligning with flow direction. The alignment of the coils disturbs the Newtonian behavior and leads to reduction in the friction between polymer coils which is reflected as a non-Newtonian shear thinning regime where viscosity decreases with increasing shear. The onset of shear thinning behavior is referred to as the critical shear rate ($\dot{\gamma}_c$). The third region starts when the shear rate is increased to another critical point where the shear is high enough to eliminate all internal bonds between polymer coils leading to the

minimum possible viscosity of the tested polymer solution. Another Newtonian plateau is observed at this range and is referred to as infinite-shear viscosity ($\mu_\infty$).

Many models were proposed to describe the relationship between polymer viscosity and shear rate in simple shear flow. The Ostwald-de Waele relationship, or the power-law fluid, an analytical model which was proposed in 1929, is capable of describing the viscosity behavior in the shear thinning regime (Eq. 3.3),

$$\mu(\dot{\gamma}) = K\,\dot{\gamma}^{\frac{-1+n}{2}} \qquad \text{Eq. 3.3}$$

where $K \geq 0$ and $1 > n > 0$ are given constants called the consistency and the power index, respectively (Saramito 2016). When $n = 1$, the fluid is Newtonian, and its viscosity equals the consistency constant. Although this viscosity model is used widely for its simplicity, it only provides an approximation of the behavior of real non-Newtonian fluids. The shortcoming of power law is its incapability of describing the maximum and minimum effective viscosities (upper and lower Newtonian plateaus), which are related to the physical chemistry at the molecular level (Saramito 2016).

There are various other models that can describe non-Newtonian bulk behavior of polymers over the entire shear flow regimes more adequately, but at the expense of the simplicity of power-law model. One of the broadly applicable models used is Carreau model (1968),

$$\mu(\dot{\gamma}) = \mu_\infty + (\mu_0 - \mu_\infty)[1 + (\lambda\dot{\gamma})^2]^{\frac{-1+n}{2}} \qquad \text{Eq. 3.4}$$

Where $\mu_0$ and $\mu_\infty$ are zero-shear and infinite-shear viscosities, respectively, $\lambda$ is an empirical coefficient related to polymer relaxation time, and $n$ is a power law coefficient.

### 3.2.3 Viscoelasticity

Beside non-Newtonian behavior, polymer solutions are known as viscoelastic substances. Viscoelasticity implies that a material shows both viscous and elastic features when it undergoes deformation. In a perfectly elastic solid, also called

Hookean solid, applied stress results in an immediate corresponding strain response that diminishes instantly when the stress is removed (Figure 3.5). In other words, all the deformation is reverted to the forcing action. An ideal viscous material is represented by Newtonian linear viscosity in the liquid state. Unlike Hookean solid, the strain is preserved in an ideal Newtonian liquid if an applied stress is removed. This implies that the deformation is permanent and if stress is applied again, deformation would resume.
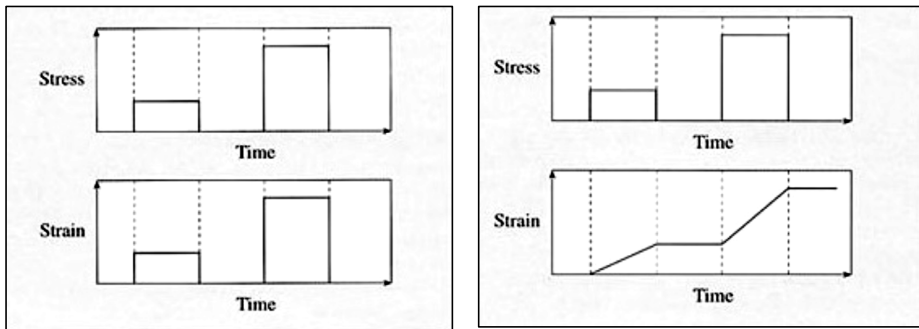


Figure 3.5: Comparison between Hookean solid deformation (left) and ideal Newtonian deformation (right).

For polymer solutions, the viscoelastic behavior combines the elastic tendency to reverse stress effect with the viscous tendency to retain it. This results in a memory effect reflected by the hysteresis observed in the stress-strain curves (Figure 3.6).
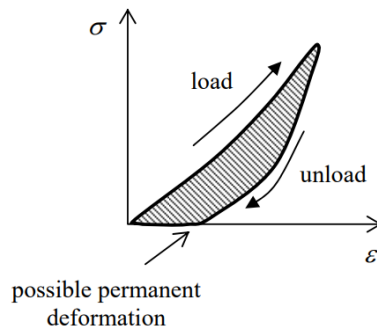


Figure 3.6: Viscoelastic memory-effect hysteresis of polymer solutions on stress-strain curves (Kelly, 2013).

The basic mechanical models of viscoelasticity are the Kelvin and the Maxwell models. Both models describe linear viscoelasticity by considering combinations of a linear elastic spring and a linear viscous dashpot (Kelly 2013). The Kelvin model considers a two-elements model consisting of a spring and a dashpot in parallel, while Maxwell model considers the same configuration in series.

Consequently, the Kelvin model assumes total stress is divided equally between the spring and the dashpot and the strain experienced by the spring is the same as the experienced by the dashpot. Based on these assumptions, the derivation of the shear stress applied on a viscoelastic fluid reduces to the sum of the Newtonian law for viscous fluids presented in Eqn Z.X, and the Hook's law for elastic solids. Hook's law states that the relationship between stress applied on an ideal elastic solid and the yielded strain is linear with a slope equal to a coefficient, $G'$, referred to as the elastic modulus or stiffens of that ideal solid.

$$\tau = \mu\dot{\gamma} + G'\gamma \qquad\qquad \text{Eq. 3.5}$$

Maxwell model, on the other hand, assumes that total strain equals the strain on the spring plus the strain on the dashpot with equal stress on both elements. Therefore, it reduces to,

$$\tau + \theta_R\dot{\tau} = \mu\dot{\gamma}, \qquad\qquad \text{Eq. 3.6}$$

where $\theta_R$ is the relaxation time defined as,

$$\theta_R = \frac{\mu}{G'} \qquad\qquad \text{Eq. 3.7}$$

The relaxation time of a material is a measure of the time it takes for the stress to relax; the shorter the relaxation time, the faster is stress relaxation. For polymers, relaxation time is the time required for polymer solution to revert to equilibrium after deformation. It is an essential parameter in the context of polymers viscoelasticity and in quantifying the memory effect impact on polymer flow. The factors affecting

relaxation time of polymers include molecular weight, degree of hydrolysis, polymer concentration, brine composition, and temperature (Erincik 2018).

Deborah number ($D_e$) is used usually as a measure of polymer's viscoelasticity for flow in porous media utilizing relaxation time. It is defined as the ratio between polymer relaxation time ($\theta_{R,f}$) and the characteristic time of porous media ($\theta_{R,pm}$).

$$D_e = \frac{\theta_{R,f}}{\theta_{R,pm}} \qquad \text{Eq. 3.8}$$

where,

$$\theta_{R,pm} = \frac{L_f}{U} \qquad \text{Eq. 3.9}$$

where, $L_f$ is the characteristic flow length, and $U$ is the pore-scale velocity. By this definition, the Deborah number is zero for Newtonian fluids and infinity for Hookean solids.

It was revealed by many studies on the pore-scale level that the viscoelasticity of polymer solutions can improve microscopic displacement by reducing residual oil saturation ($S_{or}$) (Wang et al., 2000; Xia et al., 2004; Yin et al., 2006; Jiang et al., 2008; Urbissinova et al., 2010; Afsharpoor & Balhoff, 2013; Qi et al., 2017). It is believed that due to elastic behavior of polymer solutions at high shear rates, capillary trapped oil could be mobilized through established normal stress components at pore scale.

### 3.2.4 In-situ rheology

In contrast to simple shear flow in rheometers, polymer flow in porous media is significantly more complex and tortuous. This is attributed to the vast variation in flow geometries encountered by the polymer due to variation in pore sizes and shapes. Hence, flexible polymer molecules (like HPAM) undergo frequent adaptation by contracting and expanding successively when flowing through pore bodies and pore throats. In consequence, the shear rate field observed by the polymer solution is scattered over a wide spectrum, for any particular volumetric unit of the media at each

different volumetric flow rate. The effective viscosity of polymer in porous media is therefore differs drastically than that observed in simple shear flow. An apparent viscosity term ($\mu_{app}$) was introduced to describe the effective viscosity behavior in porous media considering the Darcy law for single-phase, non-Newtonian fluids,

$$\mu_{app} = \frac{kA}{Q} \left( \frac{\Delta P}{L} \right)$$
Eq. 3.10

where $k$ is the absolute permeability of a porous media core sample, $A$ and $L$ are cross sectional area and length of the core, respectively, $Q$ is volumetric flow rate, and $\Delta P$ is the differential pressure across the core. This apparent viscosity is usually measured in lab experiments by injecting polymer through cores and converting differential pressure response to viscosity values.

Due to polymer's inherent viscoelasticity, the apparent viscosity of HPAM estimated by core flooding experiments would ideally observe six distinctive regions, given that tested shear rate range is sufficiently extensive, in the order from low to high shear rates: (1) zero-shear Newtonian plateau, (2) shear-thinning, (3) infinite-shear Newtonian plateau, (4) shear-thickening, (5) maximum viscosity Newtonian plateau and (6) mechanical degradation (Figure 3.7). It is worth to mention that this behavior is strictly associated with flexible coiled synthetic polymers only. Rigid rod-like biopolymers observe pseudoplastic exclusively in both bulk flow and in-situ flow (Al-Shakry et al., 2019).

The aforementioned regions of in-situ flow viscosity are divided into viscous-dominated shear flow and elastic-dominated extensional flow regimes. The following subsections are dedicated for the detailed interpretation of factors affecting both regimes.
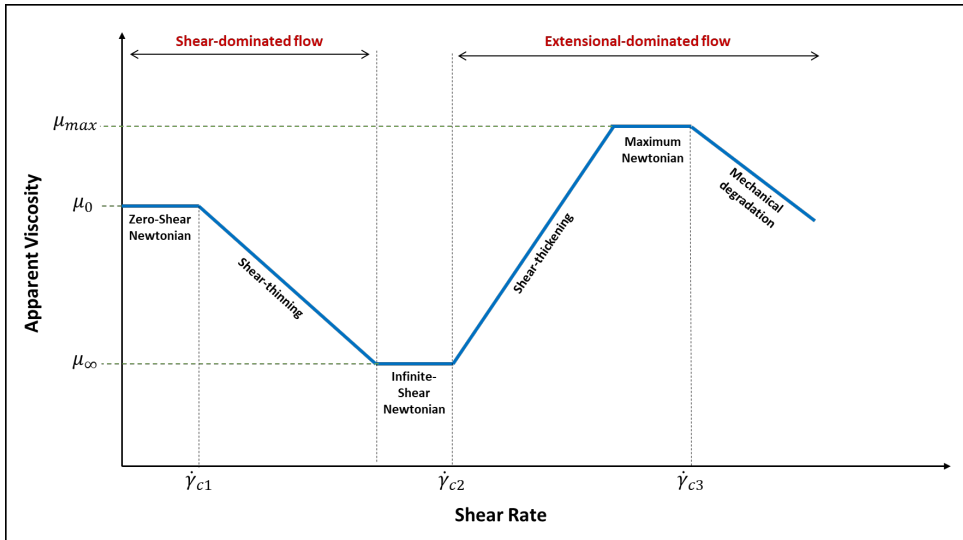
*Figure 3.7: In-situ viscosity behavior of HPAM flow in porous media (modified from Al-Shakry et al., 2019).*

### 3.2.4.1 Shear-dominant flow regime

The first three regions of the polymer apparent in-situ viscosity diagram are in the shear flow dominated regime. Despite the fact that these regions match the behavior of bulk rheology, the magnitude of viscosity in each region and the governing mechanisms may be different in porous media flow conditions. For instance, it was observed in many cases that the zero-shear viscosity in in-situ porous media flow is lower than that of bulk flow (Chauveteau et al., 1984; Zaitoun & Kohler, 1987). This behavior implies that polymer molecules are flowing faster in porous media than in bulk flow at that specific range of shear rates. The pore-scale justification of this behavior relies on two mechanisms, namely inaccessible pore volume (IPV), and depleted layer phenomena. Both mechanisms cause flow acceleration and thus lower zero-shear viscosity. In the first phenomenon of IPV, larger polymer molecules are unable to access portion of the smaller pore throats and thus they deviate toward larger throats in an accelerated manner (Dawson & Lantz, 1972). This phenomenon is more typical in low permeability porous media. The depleted layer effect is a slip effect that occurs when polymer molecules are repulsed by pore walls, depleting the layer adjacent to the walls

and resulting in an accelerated flow (Chauveteau et al., 1984). The depleted layer effect could be observed in all ranges of permeability.

As shear rate increases, a shear-thinning behavior similar to bulk is seen in porous media beyond a critical rate $\dot{\gamma}_{c1}$. The mechanism behind it is also the same as found in bulk, i.e., polymer molecules are forced apart and the bonds between them are weakened causing viscosity reduction. At this stage, the in-situ flow is dominated by viscous flow rather than extensional flow, meaning that the effect of polymer coils stretching is insignificant. Although this kind of behavior is theoretically anticipated, some core flooding experiments in the literature have shown deviating results. Findings of some experiments on linear cores have shown Newtonian or new-Newtonian behavior for polymer flow at low-flux where shear thinning is expected (Seright et al., 2009; Seright et al., 2011; Rodriguez et al., 2014; Skauge et al., 2015; Zhang & Seright, 2015). Other researchers observed either slight shear-thinning (Heemskerk et al., 1984; Masuda et al., 1992) or strong shea-thinning behavior (Dupas et al., 2013; Manichand et al., 2013; Delamaide et al., 2014). Skauge et al. (2016) found that despite HPAM observed Newtonian behavior in low-flux region of linear flow, strong shear-thinning effect was observed in the same flux region in radial flow experiments. This could suggest that flow geometry is a major factor in quantifying shear-thinning behavior of viscoelastic polymers. Since radial geometry is a more representative model to flow around injector's wellbore, radial flow experiments could be considered more accurate in describing in-situ polymer rheology.

By further increasing shear rate, the effects of extensional flow emerge after the polymer coils interactions are mostly eliminated. However, the flow is dominated by neither viscous nor elastic components and thus it observes an apparent infinite-shear Newtonian plateau.

### 3.2.4.2 Extensional-dominant flow regime

At high enough flux and above a critical shear rate $\dot{\gamma}_{c2}$, HPAM would observe a significant increase in the resistance to flow is referred to as shear-thickening. This is referred to as extensional flow or elongational flow. The physical interpretation of this

phenomenon is a subject of scientific debate between two main theories, the coil-stretch model, and the network-transient model.

The coil stretch theory suggests that when shear rate exceeds a critical point ($\dot{\gamma}_{c2}$), molecules of polymer undergo significant deformation of configuration from coiled to stretched states. This abrupt change results in anisotropy of stress tensors between extensions and contractions. Eventually, extensional elastic properties dominate the flow causing apparent viscosity increase. Besides this effect, polymer coils also exhibit an entropic force that resists the forces of increasing flux in an attempt to preserve the original coiled configuration (Degennes 1974).

The transient network theory partially agrees with the coil stretch theory on the impact of coil elongation with increasing shear rate. However, it interprets the apparent shear thickening behavior by the ability of elongated molecules to interact with neighbor molecules with hydrogen bonding in a transient-like effect resulting in apparent shear-thickening (Odell et al. 1988)

The onset and magnitude of extensional viscosity is of a great importance in the study of EOR polymers. Proper estimation of the critical shear rate at which shear thickening commences can have significant impact on the injectivity of polymer and hence on the design of polymer injection plans. Choplin and Sabatie (1986) introduced a method of assessing the critical shear rate at the onset of shear thickening. They suggest that polymer molecules rotate a constant angular velocity ($\omega$) proportional to a constant applied shear rate ($\dot{\gamma}$). The time it takes for each rotation is:

$$t = \frac{\pi}{2} \, K \dot{\gamma} \qquad \qquad \text{Eq. 3.11}$$

where K is a constant of proportionality related to viscosity. This time is then compared to the Zimm relaxation time ($\lambda_z$), which is the time it takes a polymer coil to relax from elongated state to a coiled state, and defined as:

$$\lambda_z = \frac{6}{\pi^2} \frac{M_w}{RT} (\mu_0) \mu_s \qquad \text{Eq. 3.12}$$

where $M_w$ is polymer's molecular weight, $R$ is the radius of molecules, $T$ is the temperature, and $\mu_s$ is the solvent viscosity. Accordingly, the extensional shear thickening does not occur until relaxation time $\lambda_z$ is larger than time $t$.

Skauge et al. (2018) summarized the factors affecting the onset of transition from shear flow to extensional flow, which include: permeability, flow geometry, porous media aspect ratio, polymer concentration, polymer molecular weight, and solvent salinity. In summary, it was found through core flooding lab experiments on HPAM that shear-thickening is delayed to a higher range of shear rates with increasing permeability (Heemskerk et al., 1984; Seright et al., 2011; Al-Shakry et al., 2019), decreasing aspect ratio of porous media (Chauveteau, 1981), and in radial flow geometry compared to linear (Skauge et al., 2016). From polymer and solvent properties perspective, the onset was delayed at lower molecular weights (Heemskerk et al., 1984; Seright et al., 2009; Dupas et al., 2013; Skauge et al., 2015), and at higher solvent salinities (Heemskerk et al., 1984; Chauveteau, 1981). Contradictory results were observed for the impact of polymer concentration suggesting that its impact on shear thickening onset is negligible (Seright et al., 2011; Skauge et al., 2015; Clarke et al., 2016).

As shear rates increases, shear thickening continues until extensional viscosity reaches its maximum and the flow observes an apparent Newtonian behavior. If the shear rate keeps increasing further, the polymer will encounter another critical shear rate ($\dot{\gamma}_{c3}$). Beyond this point, high viscoelastic stress causes mechanical degradation phenomenon, where polymer molecules suffer rupture and chain halving. This degradation is an irreversible process and results in a significant reduction in polymer viscosity. Virtually, the viscosity decreases until it reaches solvent viscosity if enough shear is applied to disintegrate all polymer molecules. Polymer degradation is discussed in further details in the following chapter.

## 3.3  Polymer stability

Stability of polymers depends on their ability to resist degradation. Polymer degradation is defined generally as the alteration of polymer's properties such as shape, tensile strength, color, and molecular weight by the impact of one or more external factors such as applied shear, heat, light, chemicals, or any other applied force (Speight 2020). Sorbie (1991), defined three main types of degradation associated with polymers used in oil recovery applications which are: biological, chemical, and mechanical degradation.

### 3.3.1 Biological degradation

Biological degradation may occur for both synthetic polymers and biopolymers, with its occurrence being far more common for biopolymers. It occurs when polymer molecules go through microbial breakdown if exposed to bacterial micro-organisms. Usually, biocides are injected with the polymer to prevent bacterial impact.

### 3.3.2 Chemical degradation and Thermal Stability

Chemical degradation refers to the disintegration of polymer molecules as a result of alteration in chemical properties. This may occur either through contamination by chemical components such as oxygen and iron, or by extended exposure to hydrolysis. While chemical contamination takes shorter time to affect polymer structure, hydrolysis has a long-term effect that attacks the intrinsic stability of polymer molecules. Since hydrolysis is a product of high temperature conditions, the associated stability impact is referred to as thermal stability. The standard practice that has been followed in improving polymer chemical stability for EOR application relies on eliminating the impact of short-term contamination, and thus delivering the polymer to the reservoir with a minimum degree of degradation (Sorbie 1991).

One of the concerns when considering chemical stability of polymer in reservoir conditions, is its ability to withstand high temperature and high salinity conditions. The classification of polymer stability depends on the measure of its viscosity retention as

a function of time ($Ret(t)$), meaning its ability to preserve its viscosifying power under specific flow conditions with time (Jouenne 2020).

$$Ret(t)\% = \frac{\mu(t) - \mu_s}{\mu(0) - \mu_s} \times 100$$

<div align="right">Eq. 3.13</div>

where $\mu(t)$ is polymer solution viscosity at time $t$, $\mu(0)$ is the initial viscosity at $t = 0$, and $\mu_s$ is solvent viscosity.

The stability of HPAM had been the scope of many studies in the literature (Knight,1973; Akstinat, 1980; Shupe, 1981; Davison and Mentzer, 1982; Martin et al., 1983; Yang and Treiber, 1985; Stahl et al., 1988; Taber et al. 1997; Al-Bahar et al. 2004). Nevertheless, the consensus among many screening criteria for polymer flooding selection with regard to reservoir temperature and salinity, that they do not exceed 100°C and 100,000 ppm, respectively (Sheng et al. 2015). This range is considered to be in the low to moderate typical reservoir temperature and salinity values, which means that polymer flooding option is theoretically omitted for deep reservoirs with harsh conditions of high temperature and high salinity. Until recently, polymer applications were limited to reservoirs with temperatures not exceeding 100°C (Jouenne 2020). The development of polymers tolerating higher temperatures and salinities would open the door to apply the advantages of polymer flooding to new reservoirs unlocking a lot of reserves. The reason behind this slow advancement in this field is in the technical challenges facing developing economically feasible modified polymers that can be produced on a cost-effective commercial level. Recently, studies have shown that stability of HPAM could be improved by introducing 2-Acrylamido-2-Methyl Propane Sulfonate (AMPS) as a copolymer (Dupuis et al. 2017; Alfazazi 2018 et al.; Masalmeh et al. 2019; Seright et al. 2021). Their collective conclusion is that SAV-10, a high-AMPS-content acrylamide polymer manufactured by SNF©, showed excellent thermal stability and salinity tolerance at temperatures up to 140°C and salinities up to 244,000 ppm. This new class of acrylamide-based polymers meets the critical criteria for field applications: thermal stability, cost-effectiveness, and industrial availability (Jouenne 2020).

### 3.3.3 Mechanical degradation

The plausibility of mechanical degradation during flow in porous media increases for flexible coiled polymers such as HPAM. As briefly explained earlier in chapter 3.2.3, at sufficiently high shear rates caused by high-flux flow in porous media, polymer molecules may degrade by breaking down into smaller molecules. The viscosity behavior then sees a decreasing trend due to this degradation. The physical understanding of this phenomena can be explained by Figure 3.8 below. Viscosity reduction occurs as a result of the decrease in hydrodynamic size of polymer molecules and the development of new molecular weight distribution, with a higher peak in the lower range.
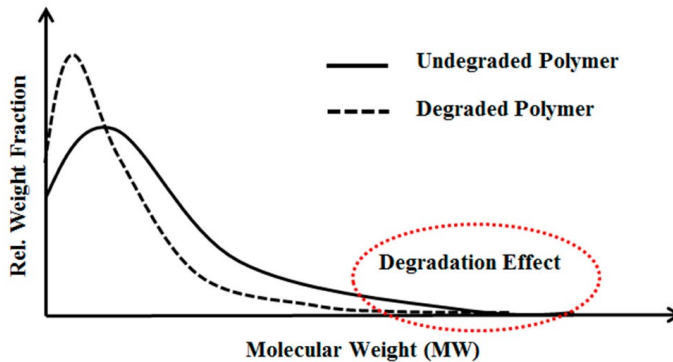


Figure 3.8: Impact of polymer degradation on molecular weight distribution (Al-Shakry et al., 2018).

Findings from studies of Smith (1970), Maerker (1975), and Noik et al. (1995) suggest that the degree of mechanical degradation of polymer solutions in porous media increases with molecular weight, solvent salinity, and in lower permeabilities. Moreover, to quantify the magnitude of mechanical degradation, several correlations were proposed considering factors such as stretch rate, dimensionless length, and maximum polymer rate at the sandface (Maerker, 1975; Morris & Jackson, 1978; Seright, 1983). One major possible drawback to these studies is that they were considering linear flow. The flow in the near-wellbore region in field applications is radial where velocity profile follows a transient-like pattern rather than the constant velocity across linear core floods. Therefore, mechanical degradation correlations

obtained from linear experiments may overestimate the magnitude of degradation occurring in actual field applications.

## 3.4 Polymer retention

As polymer flows through porous media, its molecules go through a complex network of pore throats and pore bodies with varying lengths and sizes. Due to this tortuosity and due to the nature of polymer molecular structure and ionic charges, polymer retention may occur by trapping molecules partially in pores causing flow retardation and permeability reduction.

### 3.4.1 Retention mechanisms

There are three identified main mechanisms of polymer retention: adsorption, hydrodynamic retention, and mechanical entrapment (Sorbie 1991). Figure 3.9 illustrates the three mechanisms in a pore scale visualization. While adsorption may occur both statically and dynamically, mechanical and hydrodynamic mechanisms occurrence is exclusively related to flow through porous media.
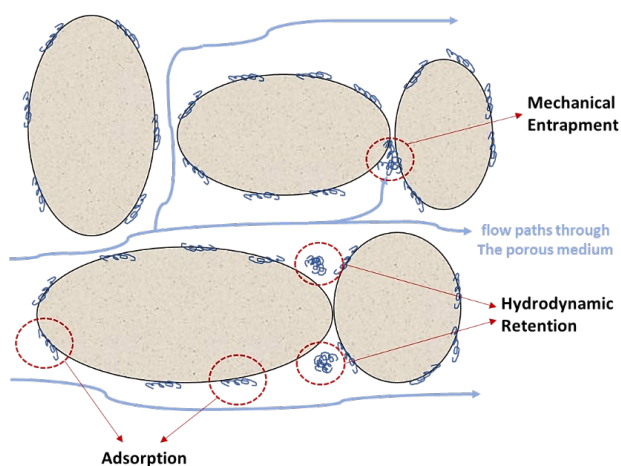


*Figure 3.9: Schematic pore-scale illustration of polymer retention mechanisms (Modified from Sorbie, 1991).*

Adsorption of polymer molecules in porous media may occur due to chemical reactions or physical interactions. Chemical adsorption, or chemisorption, refers to the sorption

of molecules to the walls of pores via substantial sharing of electrons to create a covalent or ionic bond (Kwon et al. 2011). Physical adsorption, or physisorption, refers to sorption caused electrostatic forces between polymer molecules and pore surface. HPAM adsorption is prevalently dominated by physisorption. This mechanism of retention is usually irreversible (Zhang & Seright, 2014), which means that it may cause permanent permeability reduction. The level of polymer adsorption is directly proportional to polymer molecular weight (Wever et al., 2018), polymer concentration (Zhang & Seright, 2015) and solvent salinity (Broseta et al., 1995). It was also found by Smith (1970) that calcium carbonate samples observe significantly higher adsorption rates compared to silica sandstone. He attributed this behavior to the substantial chemical interactions between calcium ions, abundantly existing on calcium carbonate surface, and carboxylate groups in HPAM polymer chains.

Hydrodynamic retention occurs when polymer molecules are dragged by hydrodynamic forces, primarily influenced by the shape of pore throat. Molecules are then held up in stagnant flow regions where the flux forces of the flow are bypassing them (Sorbie 1991). Since this mechanism is only affected by internal pore-scale flow forces without physical contacts to the pore surface, it is considered to be temporary and thus reversible (Chauveteau, 1981; Zhang & Seright, 2015; Chen et al., 2016). The level of hydrodynamic retention is found to be increasing with polymer molecular weight and decreasing with permeability (Chen et al. 2016).

Mechanical entrapment is a retention mechanism which involves physical trapping of larger polymer molecules in narrow pore throats (Dominguez & Willhite, 1977). The effect of this mechanism on polymer flowing through porous media follows a sieve-like pattern, i.e. it is larger at the inlet of the flow where largest molecules are trapped and gradually decreases as the front progresses. This simple physical concept suggests that mechanical entrapment is expected to be directly proportional to polymer molecular size (weight) and inversely proportional to the permeability of porous medium, which aligns with the observation of Mungan et al., 1966; Gogarty, 1967; Szabo, 1975; and Dominguez & Willhite, 1977.

### 3.4.2 Resistance factors

As a result of polymer retention, reduction of permeability is expected when polymer invades porous media. This reduction is usually measured by two parameters: permeability reduction factor ($R_k$) and residual resistance factor ($R_{RF}$). These parameters are both derived from the resistance factor ($R_F$) which is used to measure the flow resistance induced by polymer flow through porous media. $R_F$ is defined as the ratio between the mobility of brine ($\lambda_b$) and the mobility of polymer solution ($\lambda_p$) (Lake et al. 2014). Since $R_F$ incorporates both viscosity-induced flow resistance, and impact of permeability reduction, $R_k$ is defined to isolate the impact of permeability reduction by isolating the ratio between permeability to brine ($k_b$) and permeability to polymer ($k_p$):

$$R_k = \frac{k_b}{k_p} = R_F \frac{\mu_b}{\mu_p} \qquad \text{Eq. 3.14}$$

where $\mu_b$ and $\mu_p$ are brine viscosity and polymer solution viscosity, respectively. Nevertheless, the permeability reduction factor by this definition encompasses both reversible and irreversible retention impacts. Therefore, $R_{RF}$ is used to isolate the irreversible permeability reduction due to retention by comparing brine mobility before ($\lambda_{b,b}$) and after ($\lambda_{b,a}$) polymer injection:

$$R_{RF} = \frac{\lambda_{b,b}}{\lambda_{b,a}} \qquad \text{Eq. 3.15}$$

The residual resistance factor is usually measured and plotted against absolute permeability to define permeability-dependent $R_{RF}$ correlations useful for reservoir simulation purposes.

## 3.5 Lab-scale polymer in-situ rheology measurements

The abovementioned definitions of resistance factors are utilized in lab-scale core flooding experiments to estimate polymers in-situ rheology during flow in porous

media. This section will briefly discuss the lab-scale experimental setups used for this purpose.

The most common method for estimating polymer in-situ rheology in lab is linear core flooding. Cylindrical core plugs are aligned in holders connected to a system of a pump and a piston, so the flow is normal to the faces of the plugs (Figure 3.10). Pressure transducers are attached to the inlet and the outlet of core holders to measure differential pressure. Alternative injection of brine and polymer solution takes place, and the differential pressure across the core plug is measured in a stepwise injection pattern.
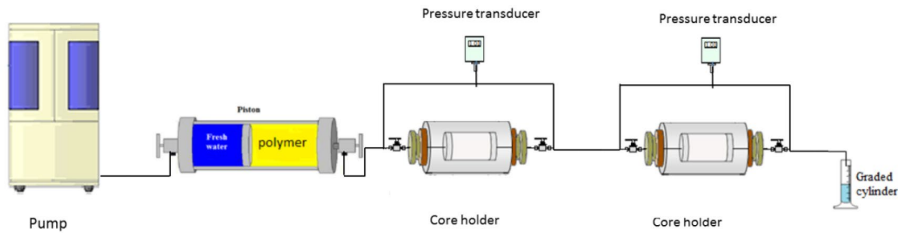


*Figure 3.10: Schematic illustration of rheology linear flow experiment (Skauge et al., 2015).*

The in-situ rheology is then estimated using $R_F$ by comparing differential pressures of polymer solution and brine. As discussed in chapter 3.4.2, $R_F$ encompasses both viscosity-induced flow resistance, and impact of permeability reduction. Therefore, $R_{RF}$ is utilized to decouple the apparent in-situ viscosity from the irreversible permeability reduction, and apparent viscosity is thus represented by $(R_F/R_{RF})$.

Due to the constant velocity conditions in linear core flooding experiments, the degree of mechanical degradation (if occurred) can be underestimated since it may continue far beyond the injection point (Al-Shakry et al., 2018b; Åsen et al., 2019). Therefore, radial flooding experiments were proposed to mimic the more realistic velocity profile around well-bore where velocity decreases as 1/r. In such experiments, brine and polymer solutions are injected alternatingly at the center of a radial core disc and

produced at the rim, while pressure ports distributed along the flow direction towards the rim measure the internal pressure drops at specified injection rates (Figure 3.11).
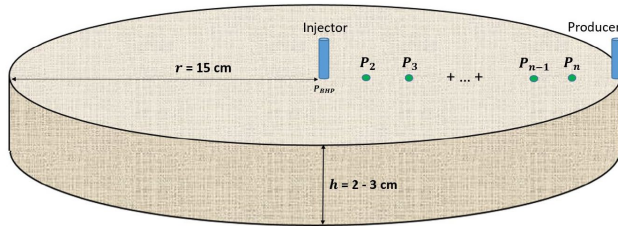


*Figure 3.11: Illustration of radial flow in-situ rheology experiments (Jacobsen et al., 2019).*

Considering Darcy's law for radial flow in porous media, the apparent in-situ viscosity $\mu_{app}$ at each flow rate ($Q$) is:

$$\mu_{app} = \frac{(2\pi h k_b)\Delta P}{Q} \ln \frac{r_e}{r_i}$$

Eq. 3.16

Where $h$ is disc thickness, $k_b$ is permeability to brine, and $\Delta P$ is the pressure drop between a pressure port at radius $r_i$ and the disc rim $r_e$.

The in-situ behavior measured in radial experiments is presented as continuous rheology curves for each injection rate, in opposition to the single viscosity values obtained from linear experiments. Therefore, numerical simulation tools could be utilized to predict polymer in-situ viscosity in radial flow using pressure data exclusively (Jacobsen et al. 2019).

## 3.6  Polymer injectivity

In any EOR flooding application, accurate estimation of fluid injectivity into the reservoir is one of the key factors towards project's success. Injectivity is defined through an index, $II$, which is defined as the ratio of volumetric injection rate ($Q$) to the corresponding injection pressure ($\Delta P$) (Civan 2007). For polymer flooding applications in particular, injectivity is an extremely essential factor in assessing the

economic feasibility of the project. For instance, Seright (2010) found that poor polymer injectivity had significant impact on the economics of heavy oil projects that surpassed the impact of polymer cost. Since pressure drop seen by the injector, $\Delta P$, is directly proportional to the viscosity of the injected fluid according to Darcy's law, injectivity decline is highly anticipated during viscous polymer injection. Moreover, due to the non-Newtonian behavior of polymers, accurate injectivity estimation is essential to avoid operating the well neat or under formation fracturing conditions.

### 3.6.1 Factors affecting polymer injectivity

The rheological behavior of polymer in porous media is the main contributing factor that influences HPAM polymer injectivity (Dupas et al., 2013; Li & Delshad, 2014). This includes non-Newtonian characteristics like shear thinning and shear thickening, besides the phenomenon of mechanical degradation at extremely high shear rates (De Simoni et al., 2018).

Due to the high velocity domain in the near-well bore region of the injection well, HPAM typically shows strong shear-thickening behavior driven by high shear rate proportional to velocity. This suggests that the viscosity of HPAM could be at its maximum just at the sandface of wellbore, which may cause severe injectivity impairment. Dupas et al., 2013 and Al-Shakry et al., 2019 found that pre-shearing HPAM solution prior to injection may reduce the viscoelastic behavior and hence reduce shear-thickening level. Pre-shearing refers to a controlled mechanical degradation of polymer solution through shearing device prior to injection into reservoir. This, however, may come at the expense of reducing both microscopic and volumetric sweep efficiencies as a result of reducing viscoelasticity and apparent viscosity, respectively.

In contrast to shear-thickening effect, mechanical degradation of HPAM molecules may occur at the near-well bore region, also due to high shear rate and velocity (Åsen et al., 2019). This phenomenon can positively influence injectivity by reducing viscosity and thus pressure drop. Nevertheless, the improvement of injectivity as a result of mechanical degradation comes also at the expense of risking sweep efficiency.

Beside the pre-shearing remedy to control the degree of mechanical degradation, it was found that operating under fracturing conditions may reduce the effect of mechanical degradation (Wang et al. 2008). The basic explanation is that the presence of fractures may suppress the expected shear rate field in the near well-bore region and thus reduce the possibility of mechanical degradation occurrence. It is worth to mention, however, that in many cases, the presence of fracture (induced or natural) is seen as an unfavorable factor that can negatively affect reservoir sweep.

Aside from rheological impacts, the presence of insoluble debris particles in injected polymer solution is another main factor affecting polymer injectivity (Sorbie 1991). These particles may accumulate at the wellbore's sandface, causing pore plugging and creating a growing external filter cake around the wellbore which in turn will reduce injectivity by inducing additional pressure drop. Although polymer solutions undergo filter tests to assess pores plugging possibility, significant uncertainties are expected from these tests due to complex nature of reservoir media compared to lab filters. To prevent formation plugging, practices of pre-shearing and pre-filtering are performed on the polymer solution before injection. Pre-shearing, as explained earlier, would mechanically degrade the polymer in a controlled manner, resulting in shifting the peak of molecular weight distribution towards low molecular weight values. Findings demonstrated that pre-shearing could improve injectivity without risking target in-situ viscosity at low flux conditions (Dupas et al. 2013; Al-Shakry et al. 2019). Pre-filtering on the other hand, is a less invasive method that would remove insoluble debris from polymer solution without influencing its beneficial viscolastic properties (Glasbergen et al. 2015).

### 3.6.2 Polymer injectivity modelling

Modelling and prediction of polymer injectivity is an ongoing field of research that yet to be conclusive. The main reason behind the complexity of polymer injectivity modeling is the diversity of factors influencing polymer behavior as well as the extremely wide range or encountered reservoir porous media in field applications. Additionally, most of the data used in the attempts to construct representative models

are depending on estimation of in-situ rheology from linear core flooding experiments. As discussed earlier, it was found that polymer in-situ behavior in radial flow deviates significantly from the one seen in linear flow. Therefore, better modelling of polymer injectivity is believed to be achieved by utilizing radial flow geometry (Lotfollahi et al. 2016) coupled with in-situ rheology description obtained from radial disc flooding experiments (Skauge et al 2016).

In the following, a brief review of few polymer injectivity modelling attempts is presented. One of the early models was proposed by Zeito (1968). He created a 3D numerical model to predict polymer injection performance in any type of reservoirs. The model, however, was lacking the inclusion of non-Newtonian rheology of polymers, which was found to be fundamental for polymer flow in porous media. Bondor et al. (1972), included the non-Newtonian behavior in their model using modified Blake-Kozeny power law for fluids, as well as the impacts of permeability reduction and mixing of polymer and water. Seright (1983) proposed an analytical model for injectivity in radial geometry, that included mechanical degradation and resistance factor correlations, to calculate total injection pressure drop. Yerramilli et al. (2013) developed a numerical model for estimating polymer injectivity during single phase flow in porous media. Their model, however, was not valid in the shear thinning rheology cases. Li and Delshad (2014) had a predictive analytical modeling tool for field injectivity applications, that incorporated both shear thinning and shear thickening behaviors. Their findings included prediction of injectivity reduction with concentration, as well as a description of grid sensitivity of simulation models. One of the recent recognized models was proposed by Lotfollahi et al. (2016), to simulate injectivity decline on both lab and field scales. Their findings included an analysis of factors causing poor injectivity. The main factors identified were oil bank formation in near-wellbore region, shear-thickening behavior, and polymer plugging.

## 3.7 Polymer flooding in heavy oil reservoirs

The classification of crude oils in terms of viscosity puts them in two main categories: 1) light oils, with viscosities between 10 and 200 cp, and 2) heavy oils, with viscosities above 200 cp (Briggs et al 2013). Until recently, the consensus in most literature describing screening criteria for polymer flooding applications, was leaning to set a maximum limit on the reservoir oil viscosity to not exceed 200 cp (Taber et al. 1997). This means that the majority of polymer flooding pilots and applications were limited to light oil reservoirs. The main reason was the common belief that heavy oil reservoirs with high viscosities, would require higher polymer viscosities which in turn would impact polymer injectivity significantly. Nevertheless, the introduction of horizontal and multilateral drilling technologies has revived the idea of using polymer in heavy oil recovery due to their potential ability to eliminate or reduce the risk of associated injectivity loss (Delamaide et al., 2014). Consequently, recent literature has documented many successful implementations of polymer flooding in heavy oil reservoirs with the most famous and largest of them being the Pelican Lake field application (Delemaide et al. 2014). Other successful projects include East Bodo (Wassmuth et al., 2009), Marmul (Alsaadi et al. 2012), Seal, Mooney and Suffield Caen (Delamaide et al. 2014). The success of these projects is reflected by increasing the recovery factors from an average of 7% to an average of 25%.

### 3.7.1 Viscous fingering and crossflow

With the injectivity loss issue being suppressed by the remedy of horizontal drilling, the main challenge that faces water flooding and polymer flooding in heavy oil reservoirs is the phenomenon of viscous fingering, also referred to as unstable displacement. This occurs due to the unfavorable high contrast between the viscosity of the displacing fluid and the displaced heavy oil, which induces adverse mobility ratio conditions. As a result, even with high viscosity polymer solutions, the mobility ratio is usually still large. For example, using a polymer solution with effective viscosity of 20 cp in a reservoir with 2000 cp oil would yield M = 100. During unstable displacement, the injection fluid tends to channel through the heavy oil creating a

finger-like pattern that gets more pronounced with larger viscosity contrast (Figure 3.12). The phenomena of viscous fingering had been studied extensively on the lab-scale with experimental work on this topic dates back to as early as 1950's (Engelberts & Klinkenberg, 1951; Hill, 1952; Saffman and Taylor, 1958). Most recent experimental work on immiscible viscous fingering can be found in the work of Skauge and co-workers (Skauge et al. 2009, 2011, 2012, 2014), where they presented the results of flooding experiments in 2D rock slabs, including adverse mobility ratios up to M = 7000.
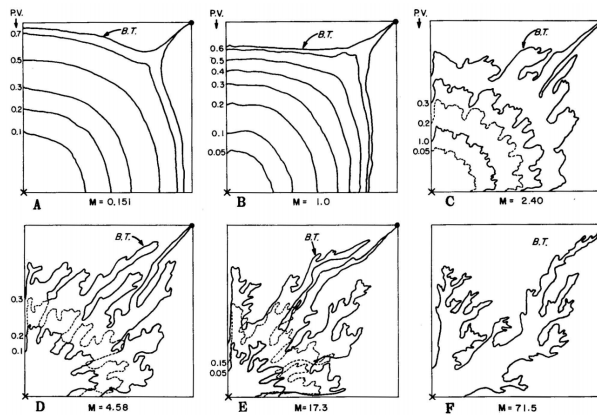


*Figure 3.12:Schematic illustration of viscous fingering in unstable displacement at different mobility ratios (Habermann,1960).*

The results from field applications and lab experiments shows a significant increase in oil recovery when using polymer flooding as a tertiary recovery method following waterflooding. Skauge et al (2012) have attributed this increase to the phenomena of viscous crossflow. The main concept is that injected polymer follows the path of least resistance and immiscibly displaces oil that again displaces water in the water channels established by prior waterflooding. This phenomenon results in an almost instantaneous response to polymer flooding and a rapid increase in oil production. Figure 3.13 shows the 2D visualization obtained by Skauge et al. (2012) of the waterflooding fingering patterns. Figure 3.14 illustrates the impact of tertiary polymer flooding on the same slab showing changes in oil and water saturations due to viscous crossflow.
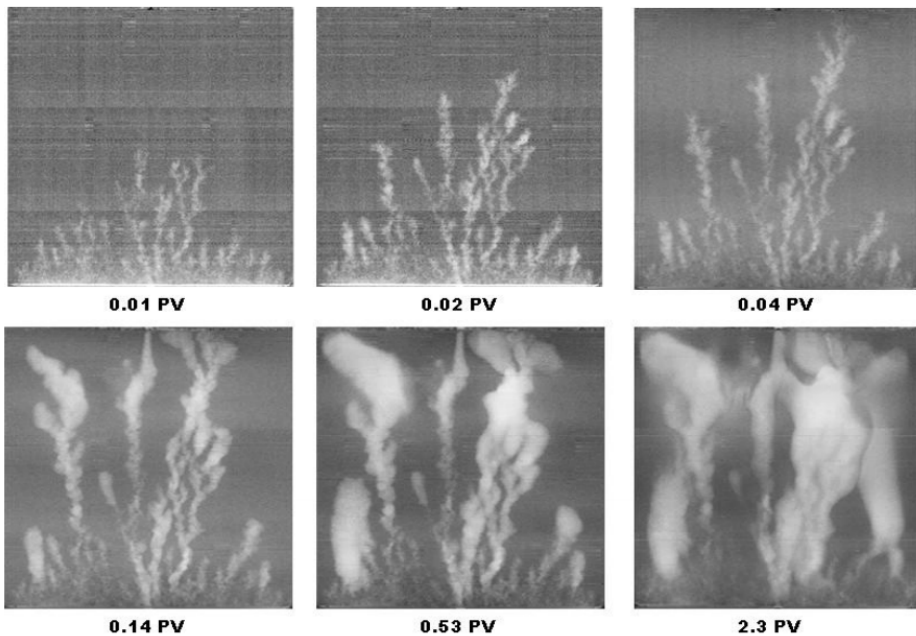
Figure 3.13: X-ray images showing 2D visualizations of viscous fingers at several injected pore-volumes (Skauge et al. 2012).
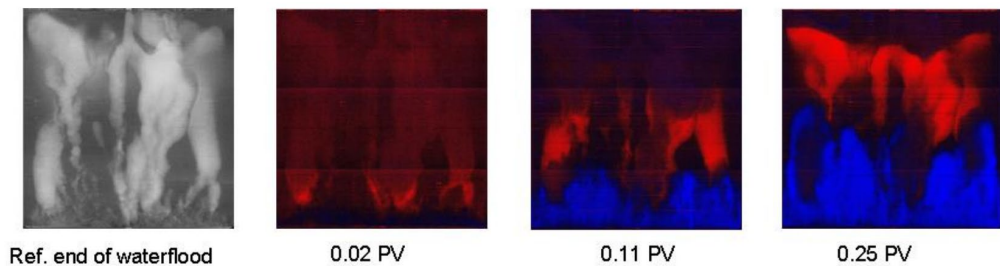


Figure 3.14: Visualization of polymer flood into Bentheimer sandstone slab at 1/2000 mobility ratio. Red and blue colors represent changes in oil and water saturations, respectively (Skauge et al. 2012).

## 3.7.2 Modelling immiscible viscous fingering

The numerical simulation of immiscible viscous fingering is regarded as a challenging issue which requires incorporation of complex features. Studies by Saffman and Taylor (1958), Chuoke et al. (1959) Peters and Flock (1981), Homsy (1987), Peters et al. (1984), Christie and Bond (1987) Tan and Homsy (1988), and Zimmerman and Homsy (1992), have suggested that besides mobility ratio, immiscible unstable displacement

depends on physical dispersion, flow geometry, heterogeneity, interfacial tension, capillary number, and rock wettability. Nonetheless, most of the literature on the subject of modelling viscous fingering is identifying the problem as being numerical rather than physical. Sorbie et al. (2020) have in contrary identified the problem as being behind the physics and related mathematical formulation. They proposed a methodology to the modelling of actual two-phase immiscible viscous fingering that can match lab-scale experiments of water displacing heavy oil. Their methodology consists of four main steps:

i)  Identify and choose a water factional flow value, $f_w^*$, from direct observations of experimental data. This value corresponds to, $S_{wf}^*$, a shock front water saturation higher than what found in conventional relative permeability curves, to account for high saturations in the fingers. From $f_w^*$, the ratio of relative permeabilities $(k_{ro}^*/k_{rw}^*)$ can be calculated as:

$$\frac{k_{ro}^*}{k_{rw}^*} = \left(\frac{\mu_o}{\mu_w}\right)\left(\frac{1}{f_w^*(S_w)} - 1\right) \qquad \text{Eq. 3.17}$$

ii)  Using selected $f_w^*$, one can generate infinite number of corresponding relative permeability sets. The optimum set for the purpose would be the set that yields maximum total mobility, $\lambda_T$, which is the sum of water and oil mobilities. The maximum $\lambda_T$ corresponds to the minimum pressure drop across the fingering system.

iii)  Generate a randomly correlated permeability field with a given average permeability. The field have to encompass heterogeneity and structure quantifiably, thus its permeability variance range can be described by the ratio of maximum to minimum permeability in a correlation structure. The structure is characterized by a dimensionless correlation length defined as the ratio between correlation length of the permeability field and the total system length.

iv) Lastly, an adequately fine spatial gridding scheme is selected in a 2D system, where the ratio of both $\Delta x$ and $\Delta y$ to the total system length is sufficiently smaller than the selected correlation length from the previous step.

Figure 3.15 shows results of viscous fingering simulations performed using the proposed workflow. More details on the selection and optimization of inputs can be found in Sorbie et al. (2020).
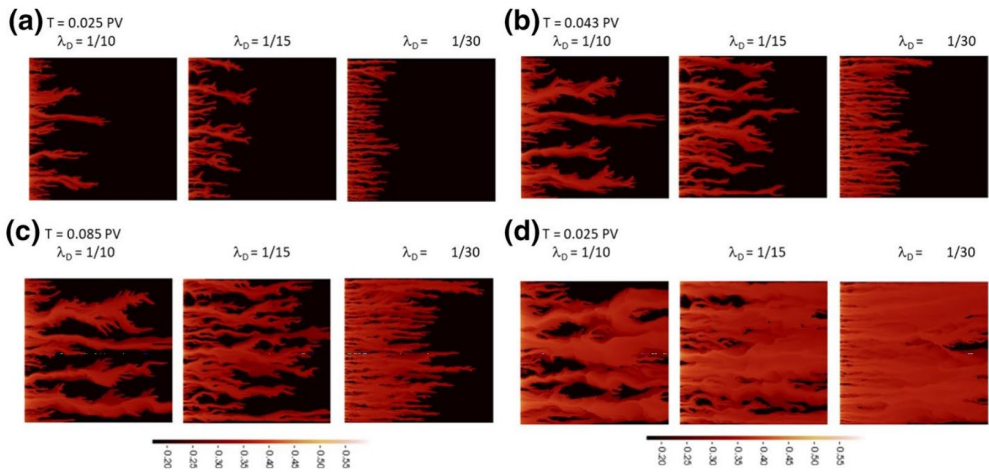


*Figure 3.15: Viscous fingering simulations at $(\mu_o/\mu_w)=1600$, at several injected pore volumes, showcasing the impact of correlation length, $\lambda_D$ (Sorbie et al. 2020).*

# 4. Simulation modules and models

Reservoir simulation is a fundamental reservoir engineering tool used to numerically model the physical processes associated with the flow of fluids in porous media. It is used for multiple purposes, such as predicting field performance under certain conditions and testing field development scenarios utilizing data inputs from core samples, well logs, production and pressure data etc. It is also used to simulate lab-scale studies as well as field-scale single-well applications, to improve the scientific understanding of a certain flow phenomena. The latter uses are the ones of interest for the objectives of this thesis as it concerns evaluation of polymer injectivity both on lab-scale adverse mobility ratio conditions, and field-scale single well applications.

It is essential for the studies of polymer in-situ behavior and polymer injectivity, to have a reservoir simulator with the capabilities of accurately modelling polymer-related physics and phenomena. There are quite few commercial and open-source simulators that can handle advanced processes associated with polymer flow mechanisms. Goudarzi et al. (2013) mentioned three widely used commercial software that include polymer flooding modules: REVEAL of Petroleum Experts, ECLIPSE 100 of Schlumberger, and STARS of Computer Modelling Group Ltd. (CMG). They also evaluated the open-source benchmarking UTCHEM simulator of University of Texas at Austin. Furthermore, Bekbauov et al. (2017) presented a numerical validation study that included ECLIPSE 300/500 of Schlumberger, IMEX of CMG, and the open-source PennSim simulator by The Pennsylvania State University.

The simulation studies performed to achieve the objectives of this thesis were conducted using the simulators STARS and IMEX of CMG. The justification of selection is attributed to many aspects including their relatively extensive polymer options, availability for use, high computational performance, and prior experience of the author.

STARS is a three-phase multi-component advanced modelling software that is developed as a thermal and chemical processes reservoir simulator (CMG website

2021). Its capabilities include simulating thermal recovery process such as steam flooding and in-situ combustion, besides modelling the physics of in-situ recovery processes such as chemical EOR, microbial EOR, and low salinity water flooding. For polymer flooding simulation, STARS includes options for shear-dependent viscosity, adsorption, inaccessible pore volume, and resistance factors. However, these options in STARS are not defined in a dedicated polymer option, but rather depends on defining polymer solution as an aqueous and adsorbed component and then use provided related modelling tools.

IMEX is a multi-phase black-oil and unconventional reservoir simulator. It differs than STARS that it is isothermal and includes extra options for unconventional reservoirs modelling. With regard to polymer flow modelling, unlike STARS, IMEX has a dedicated polymer option that is able to model several polymer flow properties such as adsorption, permeability reduction, viscosity mixing, shear dependent viscosity, degradation, and salinity effect.

Since the objectives are strictly related to evaluating polymer injectivity and in-situ behavior, the thesis does not include a comparison between the simulators as they were both utilized for the purposes of numerical interpretation and prediction only. The following sections are dedicated for detailed description of the polymer modules included in STARS and IMEX simulators. The references for this review are IMEX User Guide (CMG 2020a) and STARS User Guide (CMG 2020b).

## 4.1  Polymer modules

### 4.1.1 Fluid component model

This section describes how polymer is incorporated in the fluid model of each simulator.

- *STARS:*

The fluid model in STARS is based on defining components by their type. The types allowed are water, oil, gas, adsorbed or trapped, and solid components. For polymer

solution, it is defined in STARS as both aqueous and adsorbed. A set of required properties has to be defined for the solution at predefined reference conditions including molecular weight, critical pressure and temperature, density, and liquid viscosity. The liquid viscosity refers to the reference viscosity of a specific component in liquid phase, and it can be temperature-dependent or a function of both pressure and temperature. The keywords *AVISC and *BVISC are used to define temperature dependence coefficients, $avisc$ and $bvisc$ for liquid viscosity ($\mu_L$) correlation:

$$\mu_L = avisc * e^{bvisc/T_{abs}} \hspace{3cm} \text{Eq. 4.1}$$

where $T_{abs}$ is the absolute temperature. The temperature dependence of viscosity can be also defined using a tabular form that includes list of temperatures and corresponding viscosities using the keyword *VISCTABLE. The same keyword can be extended by defining multiple temperature-viscosity tables at different pressures using the keyword *ATPRES.

- *IMEX:*

In IMEX, the polymer is defined in the fluid model section via dedicated preset models through the keywords *POLY, which is used for the case with gas flow, and *POLYOW, which uses a polymer model with no gas flow or variation in solution gas. There are also two extra polymer models that incorporates seawater co-injection model the keywords *POLY_SEAWATER and *POLYOW_SEAWATER. For the latter keywords, the salinity effect of polymer viscosity could be specified by *PVISCSALT which is used to define the coefficients required for the following correlation of polymer viscosity in saline solution ($\mu_s$):

$$\mu_s = \mu_s^0 \left(\frac{x_{salt}}{x_{min}}\right)^{sp} \text{ for } x_{salt} > x_{min} \hspace{2cm} \text{Eq. 4.2}$$

Where, $\mu_s^0$ is the polymer viscosity at a reference polymer concentration, $x_{salt}$ is the salinity mass fraction defined as the ratio between salt concentration and the sum of pure water density and salt concentration, $x_{min}$ is the salinity mass fraction below

which the polymer viscosity is considered independent of salinity, and $sp$ is the slope on a log-log plot of polymer viscosity versus ratio of salinity over $x_{min}$.

## 4.1.2 Non-Newtonian rheology

Shear-dependent non-Newtonian behavior is the most significant element in modelling polymer flow in porous media. This section describes how polymer in-situ rheology option is incorporated in each simulator. Both simulators have the option of using either shear rate or velocity as the governing variable for shear-dependent viscosity measurements. In addition, both simulators use viscosity mixing as the basis of toggling the shear-dependent viscosity option.

- *STARS:*

In STARS, shear-dependent viscosity for any defined component in the fluid model, has to be initiated by defining liquid viscosity mixing function whether it is linear or non-linear. In the case of polymer, the mixing function could be defined using the keyword *VSMIXCOMP, to designate the pre-defined polymer component as the component used for viscosity mixing. Then keywords *VSMIXENDP and *VSMIXFUNC are used to define the viscosity mixing function using eleven table entries representing the shape of natural log of viscosity over a range of weighting coefficients representing the polymer mass fraction in solvent. Linear mixing is defaulted in STARS if no non-linear mixing function is defined. After defining viscosity mixing rule, shear effects can be incorporated either by built-in power law relations or by a tabular input form. For the first option, keywords *SHEARTHIN, *SHEARTHICK, and *SHEARTHCKT can be used to define power law shear thinning for the first one, and power law shear thickening for the other two keywords. A combined shear effect can be applied by using *SHEARTHIN and *SHEARTHICK (or *SHEARTHCKT) together. The other option of incorporating shear-dependent viscosity in STARS is by using the keyword *SHEARTAB. This option involves a straightforward two-column tabular data entry using range of velocities/shear rates in one column and the corresponding viscosity in the other column. Therefore, this option

can be utilized to include any polymer rheology model by directly substituting corresponding data.

- *IMEX:*

For in-situ rheology definition in IMEX, the main governing keyword is *PMIX, which defines the viscosity mixing model for the polymer solution. Using this keyword, one can choose between six viscosity mixing rules: linear (*LINEAR), non-linear (*NONLINEAR), power-law (*POWERLAW), concentration dependent (*TABLE), salinity dependent (*SALTABLE), and velocity dependent (*VELTABLE).

The first three options use built-in mixing equation to calculate mixture viscosity ($\mu_{sw}$) within a predefined range of concentrations between zero and a maximum reference concentration value defined by *PREFCONC. The general equation used is:

$$\mu_{sw} = [\alpha \mu_s^{-b} + (1 - \alpha) \, \mu_w^{-b}]^{-1/b} \qquad \text{Eq. 4.3}$$

Where $\alpha$ is the relative concentration, $\mu_s$ is reference polymer solution viscosity defined by *PVISC, $\mu_w$ is base water phase viscosity, and $b$ is a power law coefficient. Figure 4.1 below illustrates the relation between different mixing rules assuming $\mu_w$= 0.3 cp and $\mu_s$= 20 cp.

The other three options allow entering tabular data manually for correlations between concentration and viscosity. While *TABLE involves only concentration effect, *SALTABLE allows entering multiple tabular data specifying the viscosity dependence on both salinity and concentration. The keyword *VELTABLE is the one of interest for incorporating shear effect. It allows entering multiple velocity tables where each table represents a specific viscosity and within it the impact of concentration can be incorporated using relative concentration values. This option allows flexibility of using any rheology model including the complex combined rheology where shear thickening takes place at higher velocities.
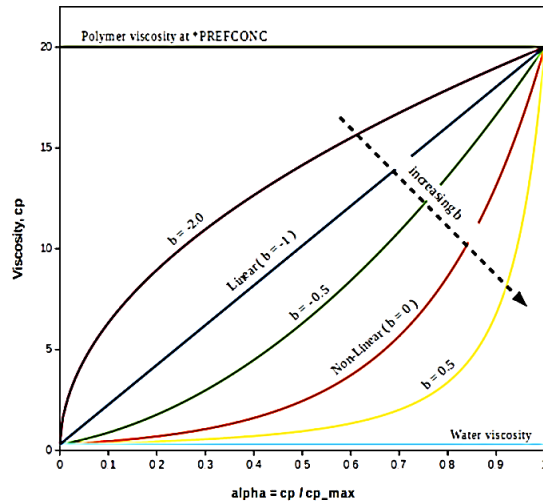
Figure 4.1: Plots of viscosity mixing models versus relative concentration for different power law coefficients.

IMEX has also dedicated keywords for built-in models of shear thinning (*SHEARTHIN) and shear thickening (*SHEARTHICK). However, unlike STARS, IMEX does not have the option of including combined effect by using both keywords. Therefore, the only way of encompassing combined rheology in IMEX is by using *VELTABLE.

### 4.1.3 Adsorption and resistance factors

The permeability reduction effect caused by polymer adsorption can be modelled by both simulators. The resultant residual resistance factors can also be incorporated as well. This section describes the options available for adsorption and related permeability reduction modeling.

- *STARS:*

Polymer adsorption is included by defining adsorbing component functions. The keyword *ADSCOMP is used to define the adsorbing component and the phase from which its composition dependence will be taken. The amount of adsorption is specified by the Langmuir isotherm which gives the adsorbed moles of polymer per unit pore volume as:

$$ad = \frac{(tad1 + tad2 * x_{NaCl}) * C_p}{1 + tad3 * C_p} \qquad \text{Eq. 4.4}$$

Where $ad$ is the adsorption, $tad1$ and $tad3$ are constants controlling the amount of adsorption, $tad2$ is a constant describing salinity effect, and $C_p$ is the polymer concentration. Another way of defining adsorption dependence on concentration and/or temperature is through a tabular data input option using the keyword *ADSTABLE.

After defining adsorbed component (polymer this case) and the correlations governing adsorption amount, STARS has an option to assign permeability dependence data for polymer through a set of keywords. Maximum adsorption capacity can be set using the keyword *ADMAXT. The reversibility of adsorption could be controlled by the keyword *ADRT which reflects residual adsorption level. A value of zero would denote a completely reversible adsorption, while a value equal to maximum capacity would imply that its completely irreversible. Inaccessible pore volume and residual resistance factor can be assigned for the rock type in which adsorption takes place by using the keywords *PORFT and *RRFT, respectively. Several permeability-dependent adsorption models could be incorporated using the keyword *ADSROCK, if several rock types were defined in the model.

- *IMEX:*

The adsorption of polymer has a dedicated keyword in IMEX namely *PADSORP. It defines adsorption function as a tabular input that consists of polymer concentrations and corresponding polymer adsorption levels. The lab data for adsorption is usually provided in the form of µg/g which stands for unit mass of polymer per unit mass of rock. IMEX requires the adsorption input to be per unit volume of rock, thus the lab data have to be converted my multiplying by rock density. Moreover, the rock-volume based adsorption could be converted to pore-volume based using the keyword *PADSPOR_REF which defines the reference porosity used for the conversion.

The abovementioned adsorption keywords do not take an effect if the permeability table keyword *PPREM is not encountered. The permeability table is used to define

the absolute permeability dependent polymer properties and contains five columns. The first column is for absolute permeability values, and the other four columns are for the corresponding maximum adsorption capacity, residual sorption level, polymer accessible pore volume, and residual resistance factor. Using *PPERM in IMEX, one can specify permeability-dependent RRF correlations and assign wide range of adsorption data inputs without the need to create specific rock-types like in STARS.

## 4.2  History matching

In reservoir simulation terminology, history matching refers to the process of matching production and/or injection data from lab experiments or field applications. Examples of some key data are injection pressure, oil production, and water cut. It is an essential preliminary step toward tuning simulation model parameters to obtain the closest approximation of the real characteristics of the reservoir. A general rule is that the more accurate and robust is the history matching, the more representative is the forecast of future reservoir performance. History matching was typically done manually by adjusting input data relying on available data and their associated uncertainty levels. Recently, automatic history matching has gained much interest where machine learning and artificial intelligence algorithms are utilized to perform assisted history matching with minimal human interference, excluding potential errors that might result from biased tuning. Besides, it helps in boosting the process efficiency by reducing the time required to solve the problem.

CMG simulation packages include a dedicated automatic history matching tool, CMOST, which is used specifically in the part of modelling immiscible viscous fingering in this thesis. CMOST works as a platform with a fully integrated interface that includes extensive options for assisted history matching of any of CMG's simulators data files (IMEX, GEM and STARS). The simulator data file is modified through pre-defined dedicated scripts to assign tuning parameters that CMOST would focus on to reach optimal solution. The optimization success is typically measured

through a global error objective function that measures the relative difference between the generated solution and the history file.

CMOST allows selecting one of many included "engines" which are basically algorithms with different solving approaches. The engines included in CMOST are: Particle Swarm Optimization (PSO), CMG Designed Exploration and Controlled Evolution (DECE), CMG Bayesian engine, Latin Hypercube Proxy Optimization (LHPO), Differential Evolution (DE), and Random Brute Force (RBF). The selection of an engine depends mainly on choosing the most efficient one with regard to computing time and solution optimization, and it depends on the type and nature of each individual problem. More information on the details for each algorithm can be found in the CMOST manual (CMOST User Guide) (CMG 2020c). The engine selected and used for the work in this thesis is the PSO, which works by initializing the run with a population of random solutions, navigating through parameterized search space, and converging towards the optimal matching solution.

## 4.3  Description of simulation models

This section presents a brief description of the properties and objectives of each of the models used in this thesis. The four primary models used were: a STARS quadratic Cartesian model, two STARS radial models, and an IMEX radial model.

### 4.3.1 STARS quadratic cartesian model

A 2D quadratic model was used to simulate the adverse mobility ratio flooding experiments performed by Skauge et al. (2012). The model dimensions are 30 cm x 30 cm x 2 cm. The injection side is represented by a horizontal injection well with perforation along the edge. On the other side, a horizontal production well is placed to simulate effluent production. This configuration ensures uniform pressure across the model by activating both edges. Gravity effects are neglected through equaling densities for both oil and water. Capillary forces are also neglected so they do not overshadow the dominating viscous forces as suggested by Skauge et al. (2009 and 2011). Previous numerical dispersion sensitivity studies performed by Iselin et al.

(2020), have shown that a total of 2500 grid cells (50 x 50 x 1) was an optimal selection for history matching both oil production and water cut (Figure 4.2)
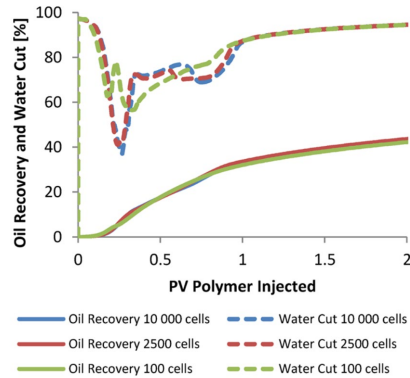


*Figure 4.2:Grid size sensitivity impact on oil recovery and water cut for quadratic model (Iselin et al., 2020).*

Nonetheless, the objective of the work in this thesis is to simulate immiscible viscous fingering behavior and reproduce the fingering pattern as seen from lab experiments. According to Sorbie et al. (2020), it is a requirement for this objective is that grid sizes are sufficiently refined to capture the physical distribution of injected fluid as it channels through heavy oil in a micro level. Therefore, the base case used for tuning the model parameters is a 100 x 100 x 1 gridding case (10,000 cells). The results from the base case are then used in a refined gridding scheme towards achieving an adequate grid size that would successfully reproduce immiscible viscous fingering.

As discussed earlier in chapter 3.7, Sorbie et al. (2020) proposed an adequate methodology to simulate immiscible viscous fingering, which is followed in the work of this thesis. One of the requirements was to input permeability as a randomly correlated field to capture microscale heterogeneity. A gaussian distribution function was used to generate random permeability fields which was implemented in the model (Figure 4.3).
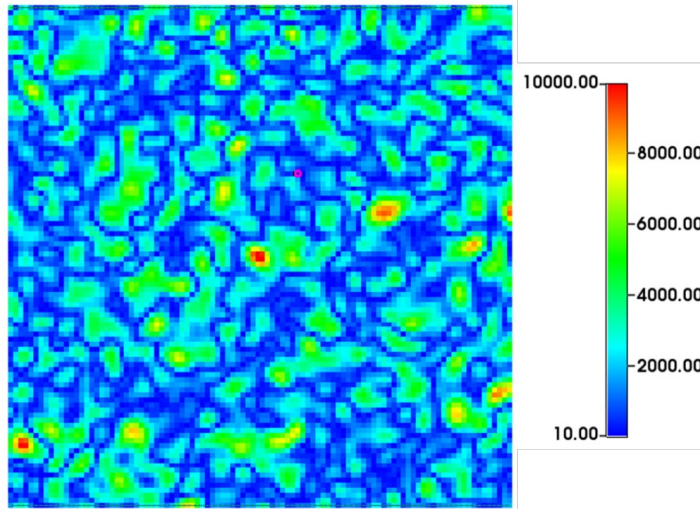
*Figure 4.3: Randomly correlated permeability field presenting gaussian distribution function with average permeability of 2000 mD.*

## 4.3.2 STARS radial models

Two STARS field-scale radial models were used in this thesis. Both models were utilized for the objectives of assessing polymer in-situ rheology impact on injectivity and optimizing the design of polymer injectivity tests. The major tuning parameter for both models were the non-Newtonian shear-dependent viscosity which was controlled via the keyword (*SHEARTAB). The inputs for the tabular format were generated using a modified version of an extended Carreau model (Delshad et al, 2008), where shear rate terms are substituted by Darcy velocity ($u$) as follows:

$$\mu_{app} = \mu_{\infty} + \frac{\mu_0 - \mu_{\infty}}{(1 + (\lambda_1 u)^2)^{\frac{1-n_1}{2}}} + \mu_{max} \left[1 - \exp(-(\lambda_2 u)^{n_2 - 1})\right] \qquad \text{Eq. 4.5}$$

Details of used viscosity curves and associated parameters are presented in Chapter 5.

The first STARS model is a 2D radial single-well model used to investigate the impact of in-situ rheology in the near-well bore region, on the response of injection bottom-hole pressure. This model is a field-scale version of a model used by Jacobsen et al. (2019) to history match radial disc experiments on HPAM in-situ rheology performed by Skauge et al (2016). The purpose was to utilize the same input parameters on an up

scaled version using the same simulator to find the effect of inherent non-Newtonian behavior of HPAM. Therefore, the same fluid and rock data were used in the upscaled version and are shown in Table 4.1. Besides, relative permeability curves from lab data were used in the model and are shown in Figure 4.4.

Table 4.1: Fluid and rock data parameters used in the STARS 2D radial model.

| Property | Value | Unit |
|---|---|---|
| Density (equal for all fluids) | 62.4 | lb/ft$^3$ |
| Water viscosity | 0.96 | cp |
| Oil viscosity | 250 | cp |
| Water saturation | 80 | % |
| Oil saturation | 20 | % |

The model consists of a single layer and 124 radial grids spanning 360° (124 x 1 x 1). The gridding scheme followed an exponentially increasing pattern from an innermost grid radius of 0.25 ft up to 100 ft radius, and then further extended via uniform gridding up to a 1083 ft radius (Figure 4.5). The purpose for this gridding choice is to capture high velocities anticipated in the near-well bore region more accurately and avoid velocity smearing and averaging caused by larger grid sizes. Moreover, the purpose of the extended radius was to isolate the impact of in-situ rheology and allow pressure stabilization in a steady-state manner associated with an expanding drainage radius or infinite-boundary conditions.

The second STARS model is a 3D model with a base gridding configuration of (58 x 1 x 5), which represents 58 grids in the radial direction with five layers and no divisions in the angular direction (360°). This generic model was utilized for the purpose of optimizing polymer injectivity test design to predict in-situ polymer rheology. The definition of layering allows the inclusion of gravity effects and the ability to test vertical heterogeneity. The gridding starts with a 0.41 ft innermost grid and exponentially increasing in size toward an outermost radial size of 5.58 ft and a total radius of 100 ft. This type of gridding is automatically generated by the CMG pre-

processor simulation model building tool, BUILDER, by predefining the sizes of inner and outer radii, and the number of radial grids.
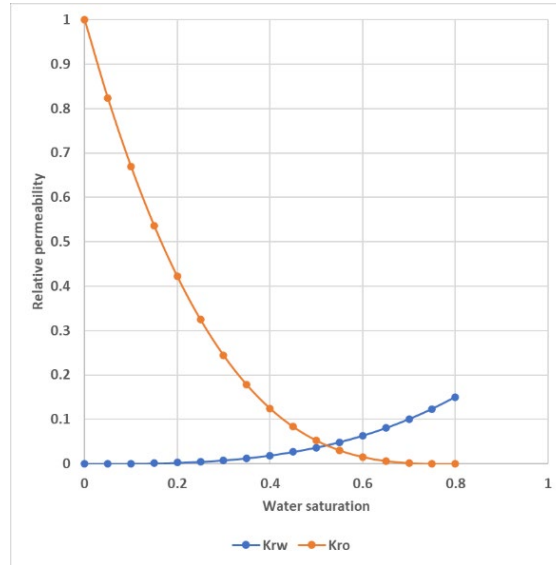


*Figure 4.4: Relative permeability curves used in 2D STARS radial model.*

The choice of this gridding pattern and sizing was arbitrary with the objective of achieving sufficient fine gridding around the wellbore which would reflect on a more definitive velocity profile, without compromising numerical stability. The same convention applies on the selection of total radius, as the near-wellbore region varies drastically for different reservoir based on reservoirs and fluids characteristics. Overall, the main issue is that the selection of grid sizes and total radius allows the system to capture the whole spectrum of predefined generic viscosity-velocity curves.
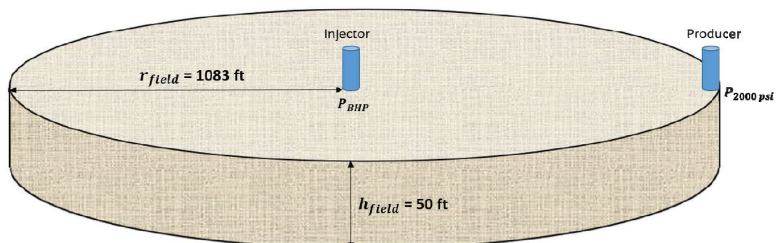


*Figure 4.5: Schematic illustration of the 2D radial model setup.*

Additionally, it is a common practice when modelling single-well injection to place a producer on the outer grid for material balance and model stabilization purposes. It was noticed however, that a no-boundary effect may significantly impact the pressure response as injection exceeds one pore-volume and create an artificial higher injection pressure response. The solution to this problem is to place several producers on the outer grid of the model instead of one. A sensitivity test was performed to optimize the number of additional producers that would result in a stable pressure build up without increasing computing time. The production patterns tested included one producer, two producers, four producers (five-spot), eight producers (nine-spot), and twelve producers. It was evident that a nine-spot pattern was an optimal selection for the required purpose (Figure 4.6).

Another issue that was addressed is the viscosity mixing between polymer and water in the reservoir at the polymer front. The predefined viscosity-velocity curves take effect only behind the polymer front where maximum polymer concentration is satisfied (Figure 4.7). However, at the front of polymer slug, the viscosity is determined by the mixing rule input in the model. The default in STARS is a linear mixing rule which was implemented in the model. Ideally, the true impact of defined non-Newtonian behavior is reflected only after a minimum of one pore volume is injected (Figure 4.8).
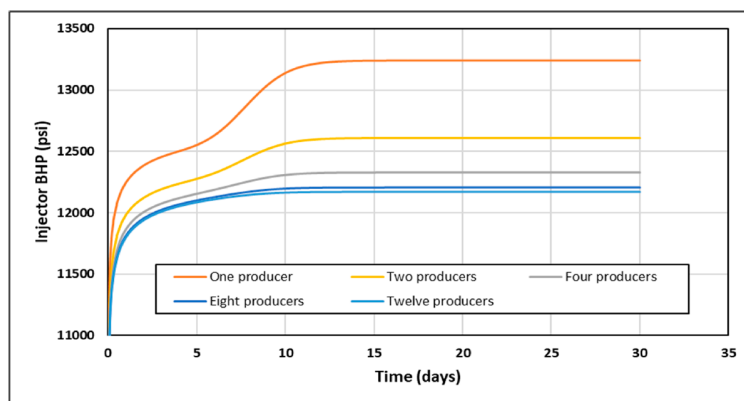


Figure 4.6: Bottomhole pressure sensitivity to number of producers on the production rim of 3D radial model.
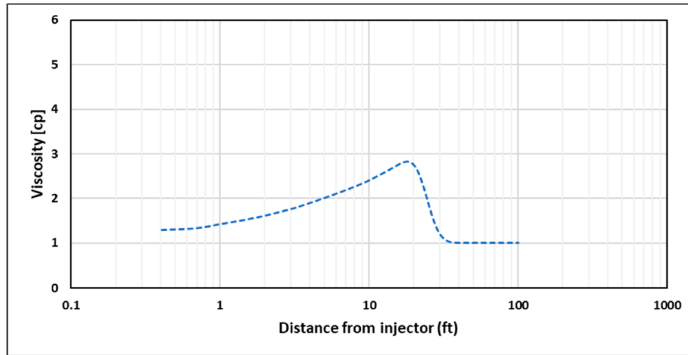
Figure 4.7: Viscosity profile after injecting 0.06 PV at 5000 bpd for shear thinning rheology.
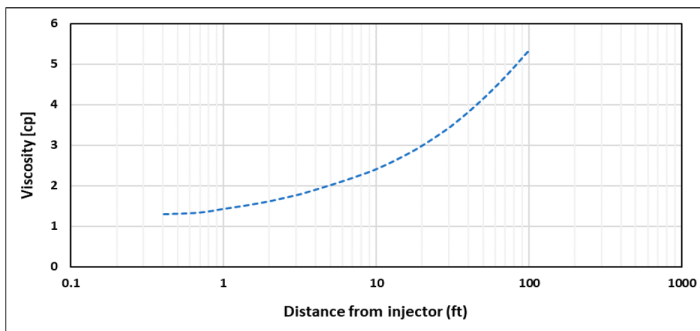


Figure 4.8: Viscosity profile after injecting one PV at 5000 bpd for shear thinning rheology.

## 4.3.3 IMEX radial model

A 3D IMEX single-well model was built for the purpose of history matching and interpreting actual field data from an injectivity test performed in Abu Dhabi, UAE. The main objective of the model is to utilize the test dynamic data generally and pressure specifically to predict in-situ rheology of polymer. The reason for selecting IMEX for this task is to use its more extensive updated polymer options (compared to STARS), that allows more flexibility and control of input data, especially the ability to use multiple in-situ rheology tables. The versatility of IMEX allows better representation of complex data from injectivity test including concentration variation, variable injection rates, variable pre-shearing rates, and skin build-up.

The grid system of the model consists of 20 grids in the radial direction spanning 360º, with grid sizes increasing exponentially from an innermost grid size of 0.25 ft up to a total radius of 3000 ft. The vertical distribution of permeability was obtained from petrophysical log interpretation and core data from offset wells. Provided initial geological model defines 460 layers with 0.5 ft resolution which reflects extreme cyclicity and vertical heterogeneity of the reservoir. Since this resolution is unnecessarily refined and may cause significant simulation performance issues, the distribution was upscaled to a resolution averaging 5 ft, with a refined average resolution of 2 ft in the perforated section (Figure 4.9). The total number of layers after upscaling is 89 totaling a 295 ft thickness, with the perforated section being between layers 23 and 55.
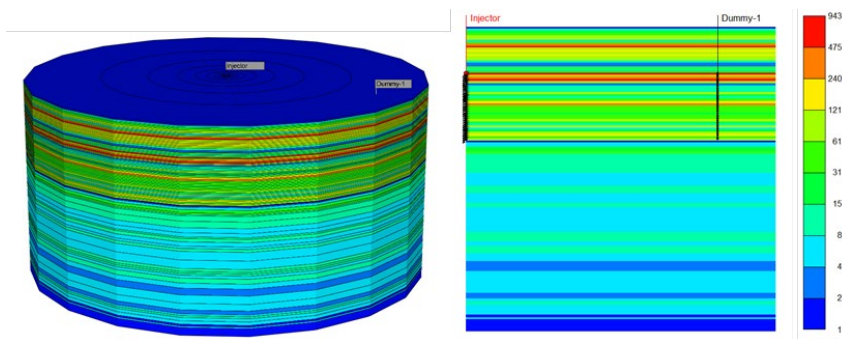


Figure 4.9: 3D visualization of IMEX model (left), and vertical permeability distribution (right).

The fluid model input is based on PVT data of reservoir fluid sample and water analysis data of injected water. Table 4.2 summarizes fluid model parameters. Two main rock types were defined in the model with different sets of relative permeability curves and capillary pressure curves for permeabilities below and above 100 mD, based on the work of Masalmeh et al. (2012) (Figure 4.10). Nevertheless, the impact of relative permeability curves is almost negligible due to oil saturation being at residual level in the near wellbore region according to saturation logs conducted prior to polymer

injection. However, the rock typing is useful for defining residual resistance factors correlations based on permeability as shown later in chapter 6.

Table 4.2: PVT data used in IMEX 3D model.

| Parameter | Value |
|---|---|
| Reservoir temperature | 248 °F |
| Bubble point pressure | 2140 psi |
| Oil density | 50.89 lb/ft$^3$ |
| Oil viscosity | 0.32 cp |
| Water density | 73.34 lb/ft$^3$ |
| Water viscosity | 0.43 cp |
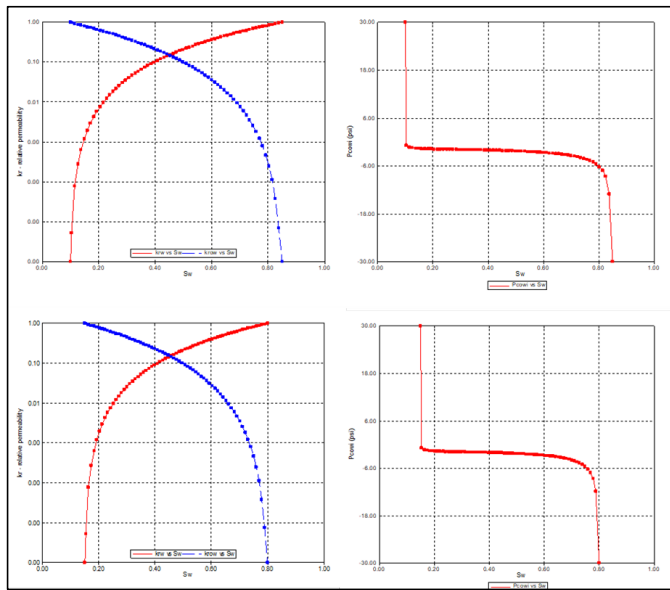


Figure 4.10: Relative permeability and capillary pressure curves of the two rock types used in IMEX 3D model.

# 5. Results and discussion

This Chapter comprises three sections that include discussion of the main results and findings obtained in this thesis.

Section 5.1 summarizes the findings presented in **Paper 4** that are related to modelling immiscible viscous fingering in unstable displacement. Moreover, the section also includes background of experimental data used as the basis for matching.

Section 5.2 discusses results of generic simulations that were conducted to investigate the impact of polymer in-situ rheology on injectivity. In addition, the section includes a discussion of the findings toward forming general guidelines to optimize the design of field polymer injectivity tests. Results and findings discussed in this section are presented in **Paper 1** and **Paper 2**.

Section 5.3 presents the findings of **Paper 3** which involves history matching a field polymer injectivity test that was performed in a UAE carbonate reservoir. Background data are briefly discussed, followed by the history matching procedure and results.

## 5.1 Flooding at adverse mobility ratio

This section presents the results and findings of simulating immiscible viscous fingering phenomena that are seen in unstable adverse mobility ratio waterfloods. The objective of the simulations was to history match lab experiments from literature (Skauge et al. 2012 and 2014) and reproduce the obtained patterns by adopting a novel approach suggested by Sorbie et al. (2020).

### 5.1.1 Experimental data and background

The experimental data utilized in this thesis were obtained from a set of experiments performed by Skauge et al. (2012) and (2014) as part of a study to describe and analyze oil mobilization at adverse mobility displacement by injection of brine and polymer. The experiments involved 2D flooding of sandstone outcrop slabs. Previous work on immiscible displacement presented in Skauge et al. (2009) and (2011) have shown that

capillarity overrides instability at adverse mobility ratio for flooding at water wet conditions. Therefore, subject experiments were performed on slabs that were aged to a non-water wet state in order to reduce the impact of capillary forces and pronounce viscous fingering effect. The rock material used is Bentheimer sandstone collected from outcrop quarry in Germany. Bentheimer is a fairly homogenous sandstone with almost no clay content which signifies its compatibility for mechanistic flow behavior studies. Its typical porosity averages between 23 and 25% with absolute permeability averaging 2500 mD. Four square slab samples were coated with epoxy gel after attaching injection and production lets on the sides to create a confined sample (Figure 5.1). The inlet and outlet sides were perforated with grooved cuts to mimic a horizontal injector and producer on each edge.
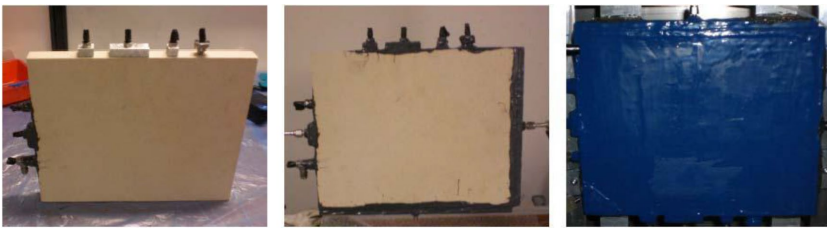


Figure 5.1: Setup of 2D slab adverse mobility ratio experiments.

Each slab sample was dried at 80°C and vacuum saturated with brine. Next, oil drainage was performed with reservoir heavy oil diluted with Iododecane to target viscosities of 400, 600, 2000 and 7000 cp, respectively, till reaching irreducible water saturation, $S_{wi}$. All slabs were then aged at 50°C for three to four weeks. Table 5.1 shows a summary of petrophysical data of the slabs after aging.

Table 5.1: Petrophysical data of 2D adverse mobility experiments.

| Experiment # | 1 | 2 | 3 | 4 |
|---|---|---|---|---|
| Slab dimensions | 14.8 x 14.9 x 2.10 | 30 x 30 x 2.91 | 30 x 29.8 x 2.55 | 29.7 x 29.9 x 2.05 |
| Porosity (Fraction) | 0.22 | 0.24 | 0.248 | 0.24 |
| Pore Volume (cm³) | 102 | 633 | 546 | 440 |
| $S_{wi}$ (Fraction) | 0.102 | 0.146 | 0.13 | 0.07 |
| $k_w$ (mD) | 1920 | 1760 | 2300 | 2800 |
| Oil viscosity (cp) | 412 | 616 | 2000 | 7000 |

Next, brine was injected at 0.025 ml/min for Experiment #1 with the smaller dimensions, and at 0.05 ml/min for other experiments. To visualize immiscible viscous fingering and capture local water saturation changes, an x-ray imaging system was utilized where the slabs were mounted vertically in a 2D x-ray scanning rig (Figure 5.2).
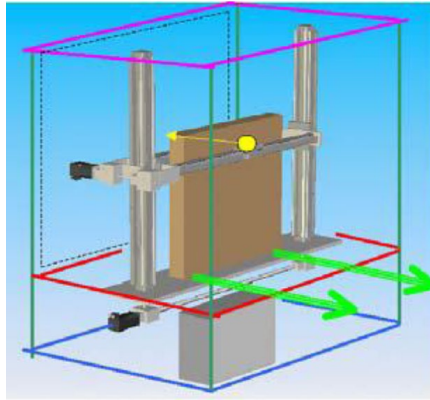


Figure 5.2: Schematic illustration of the x-ray imaging setup.

The imaging system consists of an x-ray and a gamma source which emits an electromagnetic radiation beam. The intensity of attenuated beam, which mirrors the rock and fluids composition, is measured by a photon counting detector and an x-ray camera. Results of attenuation intensity during injection are then converted to saturation maps by comparing them to a reference sample of 100% brine saturated slab. Further information on the mechanisms and details of x-ray image filtering and processing can be found in the work of Skauge et al. (2009) and (2012). Results of processed x-ray images for the four experiments are shown in Figure 5.3. The experiments have shown the direct correlation between oil recovery efficiency for water flooding at adverse mobility conditions, and the ratio between oil and water viscosities. Figure 5.4 shows oil recovery profiles of the experiments until the end of water injection, which was suspended at one injected PV for experiments #1 and #2, at 2.3 PV for experiment #3, and at 5.1 PV for experiment #4. The recovery decreases as oil-to-brine viscosity ratio increases. The recovery efficiency at the end of water injection is relatively low for all the experiments ranging between 25 and 33%.

Nonetheless, all water floods showed a steady increase in oil recovery up to the end of the flood, indicating their potential to produce more oil if water injection continued.
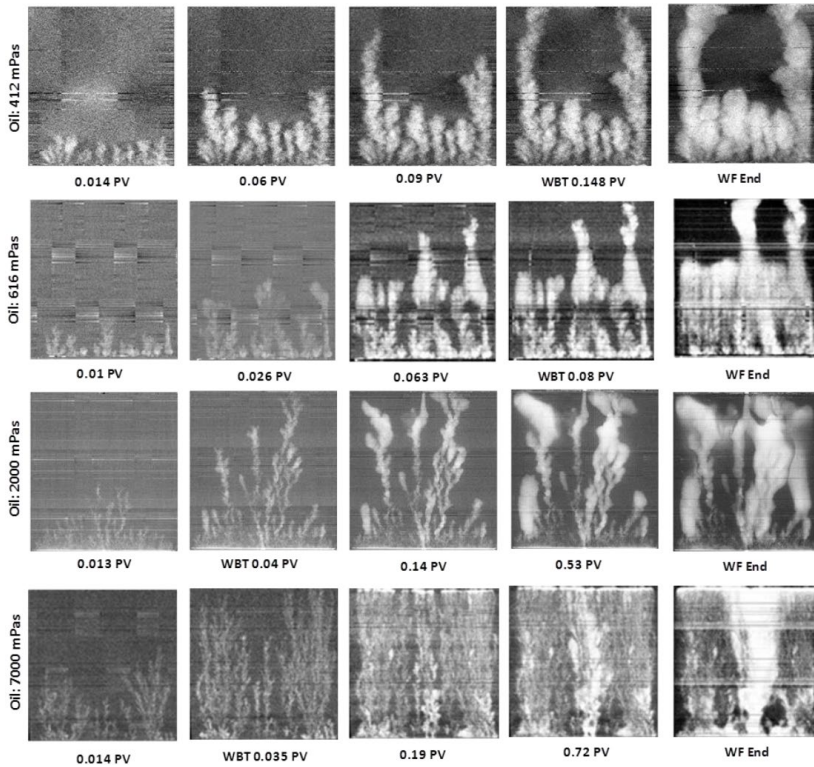


*Figure 5.3: 2D x-ray images of water flooding of all subject experiments at different PV of injected water.*
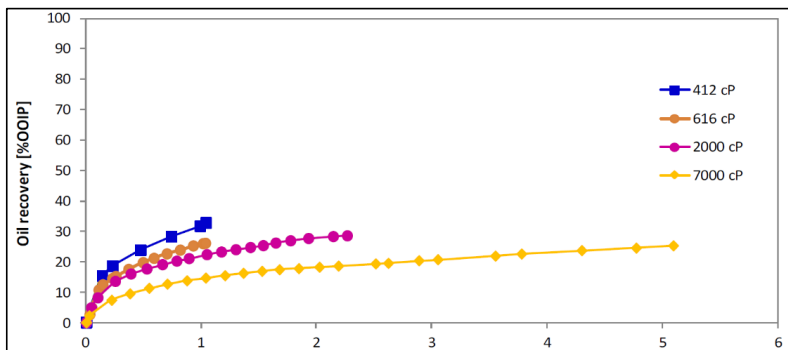


*Figure 5.4: Oil recovery profiles of 2D adverse mobility experiments.*

From the visual analysis of x-ray images, it is evident that water breakthrough occurs earlier at higher oil viscosity. This can be generally explained through the established pattern of fingers for different viscosity conditions. For the extra heavy 2000 cp and 7000 cp oils, images showed the development of thin fractal-shaped fingers that worm through rapidly resulting in very early water breakthrough at 0.043 and 0.035 PV, respectively. While the 7000 cp case exhibits larger number of fingers, in both cases the fingers keep branching and coalescing to form wider channels. In comparison, the lighter viscosity cases of 412 cp and 616 cp shows a bit delayed breakthrough at 0.148 and 0.08 PV, respectively. In the latter cases, thin fingers develop initially and propagate parallelly through the slab until a specific distance half-way where couple of fingers take the lead creating a front at that distance. Consequently, the pattern becomes dominated by widening of initially developed fingers at the established front. Table 5.2 shows a summary of the results of all four experiments.

Table 5.2: Summary of adverse mobility 2D slab experiments.

| Experiment # | 1 | 2 | 3 | 4 |
|---|---|---|---|---|
| Oil viscosity (cp) | 412 | 616 | 2000 | 7000 |
| Oil: brine viscosity ratio | 474 | 700 | 2060 | 7220 |
| Injected PV at breakthrough | 0.148 | 0.080 | 0.043 | 0.035 |
| Total oil recovery (%OOIP) | 32.8 | 25.5 | 28.5 | 25.3 |
| Oil recovery at 1 PV injected (%) | 32.8 | 25.5 | 22.3 | 14.7 |
| Water cut at end of water flood (%) | 86 | 94 | 98 | 98 |
| Injection flow rate (ml/min) | 0.025 | 0.05 | 0.05 | 0.05 |

## 5.1.2 Modelling immiscible viscous fingering

As discussed earlier in section 3.7.2, Sorbie et al. (2020) argued that the observed failure in simulating viscous fingering in some literature, is caused by overlooking essential physics and related mathematical formulation, rather than being related to numerical issues. The main rationale behind this argument is that conventional relative permeability curves are usually describing the solution to 1D fractional flow theory which fails to describe viscous fingering, where the driving mechanisms are essentially 2D or 3D. The work conducted in this thesis follows generally the approach suggested

by Sorbie et al. (2020) to resolve what they refer to as the "M-paradox" as discussed in detail earlier. From reservoir engineering perspective, the selection of suitable fine grid size to simulate the fingers has to be optimized by considering the impact of dispersivity on the actual scale of the experiment. Considering an experiment with dimensions 30 x 30 x 2.5 cm$^3$, Figure 5.5 shows that the grid size must be at least in the order of 0.5 mm as it represents dispersivity length. Consequently, it was decided that a gridding system of 600 x 600 x 1 is sufficiently fine spatial gridding for the purpose of this study.
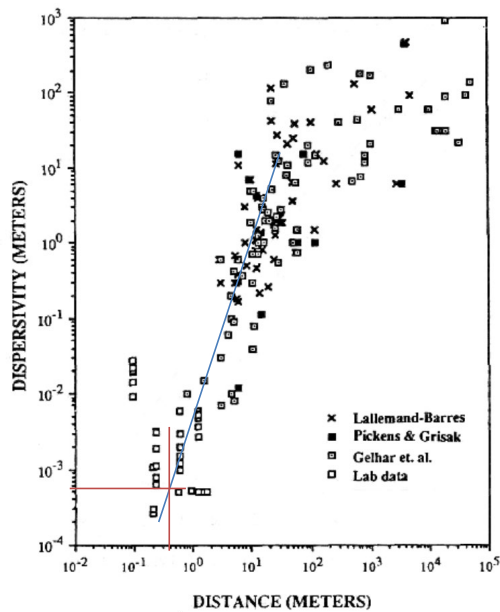


Figure 5.5: Field and lab data of dispersivity as a function of length scale (Modified from Arya 1986).

Next, the random correlated permeability field is described for different correlation lengths. Even though the experimental rock material is homogenous, heterogeneity exists inherently as the scale goes down to pore size. To account for this type of heterogeneity, Gaussian random permeability fields were adopted where the distribution function is controlled by four parameters: average (mean) permeability, minimum permeability, maximum permeability, and the correlation length. The correlation length represents the number of gird blocks at which the distribution

function locally defined. The dimensionless correlation length, $\lambda_D$, is used to describe the ratio of correlation length to the total number of grids. According to Sorbie et al. (2020), $\lambda_D$ has a significant impact on the number of total induced fingers as well as the number of dominating lead fingers as shown in Figure 3.15. On the other hand, they found that the ratio between maximum and minimum permeability did not affect the results in terms of both fingering pattern and production data matching. Table 5.3 below summarizes the selected gridding size and the parameters of random correlated permeability fields used to match the experiments. Figure 5.6 shows an example of stochastic random correlated permeability map measuring 600 x 600 grids with a correlated length of 18 gird blocks.

*Table 5.3: Summery of gridding size and the parameters of random correlated permeability fields.*

| Experiment # | 1 | 2 | 3 | 4 |
|---|---|---|---|---|
| **Grid dimensions** | 300x300x1 | 600x600x1 | 600x600x1 | 600x600x1 |
| $k_{avg}$ **(mD)** | 1985 | 1944 | 2024 | 2024 |
| $k_{min}$ **(mD)** | 10 | 10 | 10 | 10 |
| $k_{max}$ **(mD)** | 8200 | 8000 | 10000 | 10000 |
| **Correlation length (# grids)** | 9 | 36 | 18 | 18 |
| $\lambda_D$ | 0.03 | 0.06 | 0.03 | 0.03 |
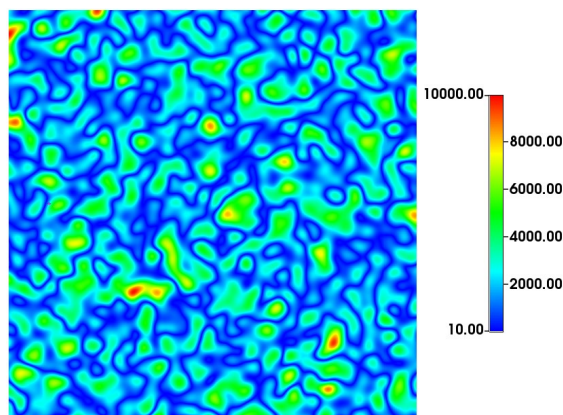


*Figure 5.6: Permeability map of 600x600 grid with $\lambda_D$=0.03.*

After defining gridding requirements in terms of spatial size and permeability distribution, the next step is to consider the selection of a fractional flow function, $f_w^*$, with a higher shock front saturation, $S_{wf}^*$. The modified $f_w^*$ is chosen to match the water saturation in the fingers as observed in experimental data. The tangent of the new fractional flow function should intercept at a higher water saturation that is close enough to the established saturation within the fingers. Figure 5.7 illustrates the impact of the shape of fractional flow function on the frontal advance behavior and breakthrough time.
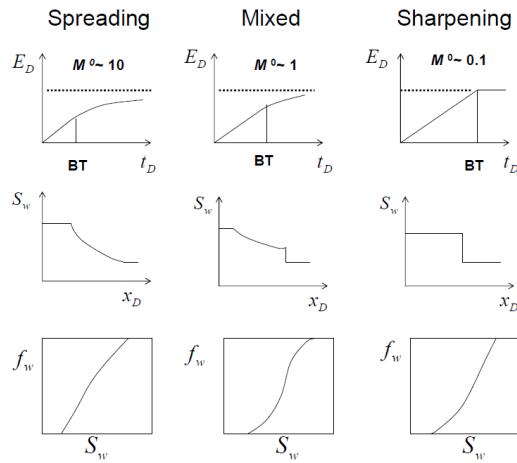


Figure 5.7: Graphical illustration of the impact of fractional flow function on frontal advance.

The ratio of modified relative permeabilities ($k_{ro}^*/k_{rw}^*$) is then calculated using Equation 3.17, however, this corresponds to an infinite number of relative permeability pairs. The resolution relies on selecting the pair that would maximize total mobility, $\lambda_T$, which approximately equals water relative permeability for extra heavy oil conditions ($\lambda_T \approx k_{rw}$).

The selection of relative permeability curves to match subject experiments was done through anchoring on history matching production data. CMG CMOST automatic history matching was used along with manual history matching to match cumulative oil production and water cut data of the experiments, by adjusting water relative

permeability. The LET versatile relative permeability correlation (Lomeland et al., 2005) was used to tune relative permeability curves in the history matching process. The LET correlation describes relative permeability curves as follows:

$$k_{rw} = k_{rw}^0 \frac{S_{wn}{}^{Lw}}{S_{wn}{}^{Lw} + E_w\,(1 - S_{wn})^{Tw}}$$

Eq. 5.1

where $k_{rw}^0$ is the endpoint of water relative permeability curve, and $S_{wn}$ is the normalized water saturation defined as:

$$S_{wn} = \frac{S_w - S_{wi}}{1 - S_{wi} - S_{or}}$$

Eq. 5.2

where $S_{wi}$ is the irreducible water saturation, and $S_{or}$ is the residual oil saturation. $L$, $E$, and $T$ terms are non-physical empirical tuning parameters.

Figures 5.8 and 5.9 show the best matches obtained from history matching production data and fingering pattern of the four experiments, for fractional flow functions and corresponding optimized total mobility, respectively. Total mobility is essentially identical to relative water permeability as discussed earlier.
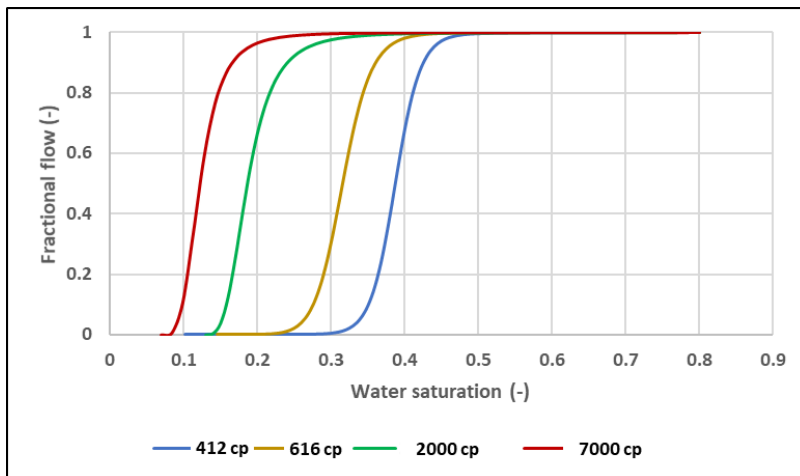


Figure 5.8: Fractional flow functions chosen to history match viscous fingering of the adverse mobility experiments.
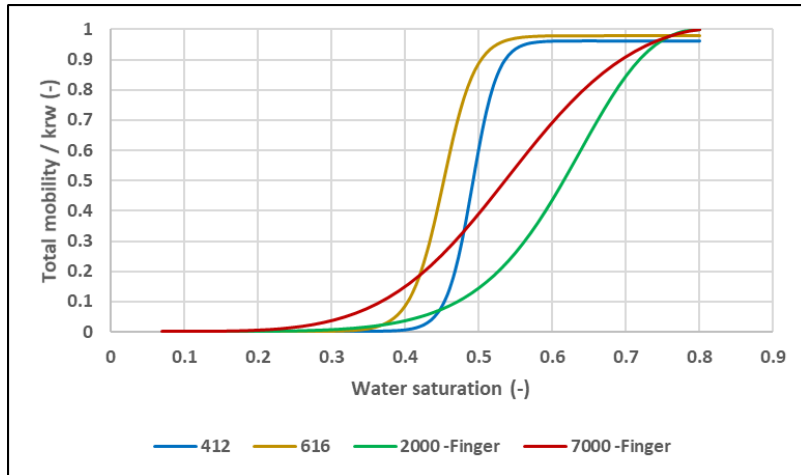
*Figure 5.9: Total mobility/ water relative permeability curves corresponding to chosen $f_w^*$ functions and used to match adverse mobility ratio fingering.*

For the cases with lighter oil in experiments #1 and #2, the matching was successfully obtained for both fingering pattern and production data with fair accuracy. However, experiments #3 and #4 with heavier oil showed some deviation in the match of production data especially at early stage. This deviation is attributed to the formation of thinner and weaker fingers as mobility ratio increases causing lower water saturation in the fingers and early breakthrough. Hence, production data could be numerically matched only at more lower shock front saturation which in turn induces pale fast propagating fingers or what is referred to as "ghost fingers". The same reasoning applies to the parallel shift observed for fractional flow functions that fit the fingering pattern. As oil viscosity increases, a lower shock front saturation is required to mimic observed fingers, reducing $\Delta S_w$ between saturation at the front, $S_{wf}$, and the irreducible water saturation, $S_{wi}$.

The results obtained from matching the experiments are as follows:

- ***Experiment #1 – 412 cp***:

Figure 5.10 shows a visual comparison between experimental x-ray images of experiment #1 and corresponding simulation results at the same injected PV. The obtained simulation results are showing qualitatively adequate matching. The number

of initiated fingers is approximately the same, however, the leading fingers are fewer in the simulation results. The simulation pattern has also observed a pair of dominating fingers that reached production edge much faster than the other fingers, creating a front-like phenomena similar to the one observed in the experiment. Nonetheless, the production in the experiment continued exclusively through the established dominating channels until the end of the waterflood, while the simulation observed production from almost all established fingers. Both oil recovery and water cut were adequately matched as well with marginal errors (Figure 5.11).
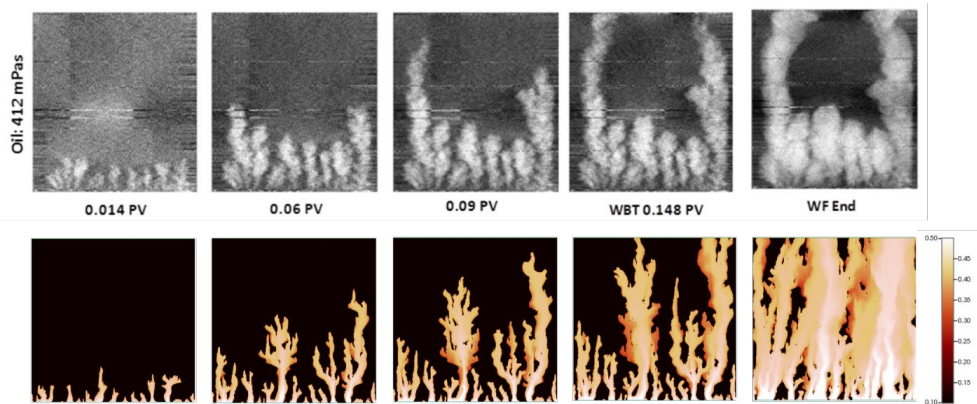


Figure 5.10: Comparison between experimental x-ray images of experiment #1 and corresponding simulation results at the same injected PV.
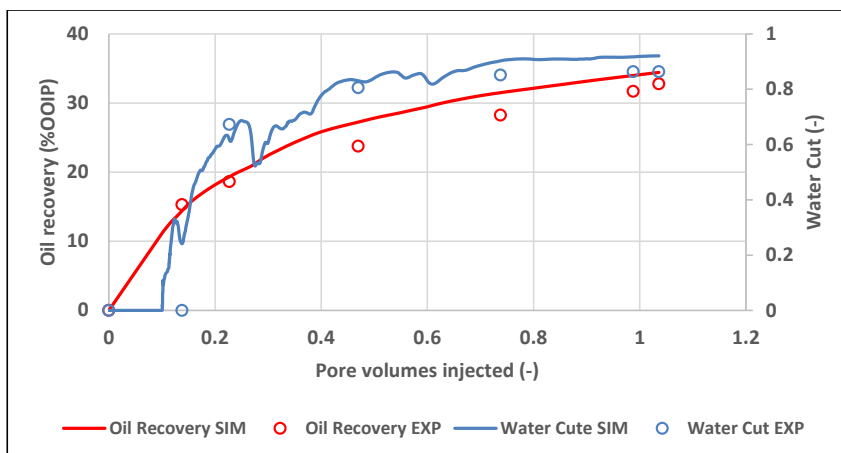


Figure 5.11: History matching of production data for experiment #1.

- *Experiment #2 – 616 cp:*

Figure 5.12 shows the comparison between experimental images and simulation visualization at different injected pore volumes for experiment #2 at 616 cp.
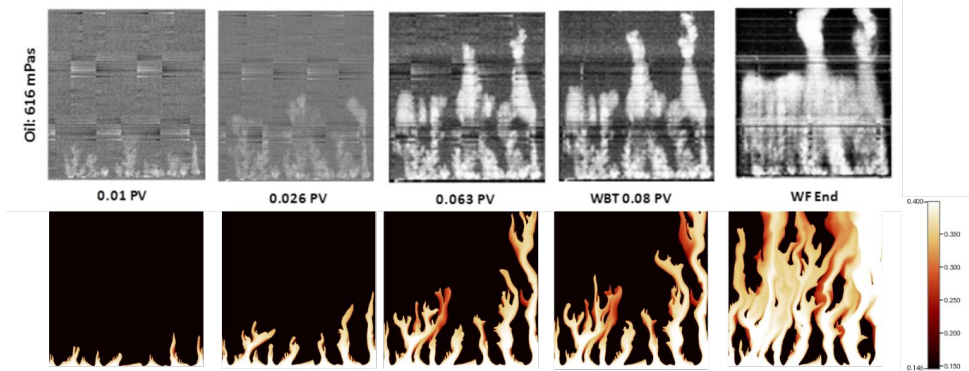


*Figure 5.12: Comparison between experimental x-ray images of experiment #2 and corresponding simulation results at the same injected PV.*

The fingering pattern observed in experimental data is analogous to the one seen in experiment #1 with 412 cp. The similar distinctive feature is the development of numerous fingers at the beginning from which two become more dominating and form faster channels. Sequentially, the rest of the fingers slow down and form a front-like advancing pattern. The simulation results captured number of originating fingers with fair accuracy and exhibited two dominating lead fingers (far right) as well. Moreover, simulation results had successfully replicated the areas of bypassed oil between the fingers, indicating decent capture of actual physics observed in experimental data. Figure 5.13 shows matching results for production data of experiment #2.

- *Experiment #3 – 2000 cp:*

Figure 5.14 shows the results of best matching case for the fingering pattern in experiment #3 at 2000 cp. Although simulation results observed a smaller number of original fingers at the beginning, the propagation and branching matched the behavior seen in the experimental data.
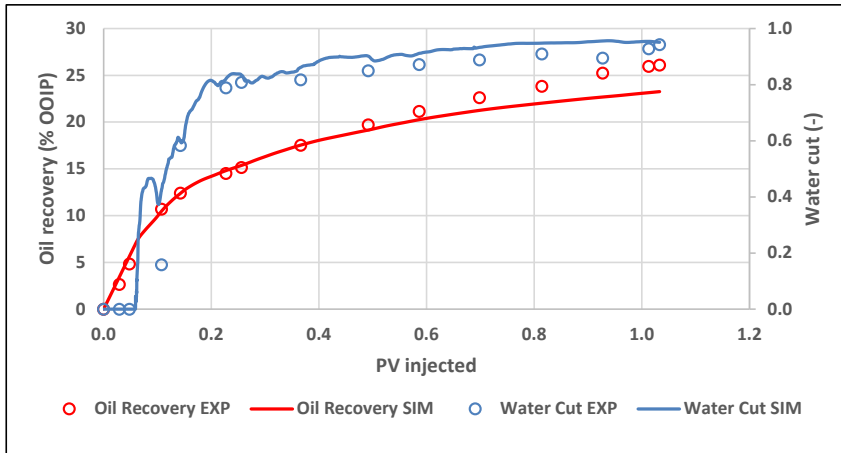
Figure 5.13: History matching of production data for experiment #2.
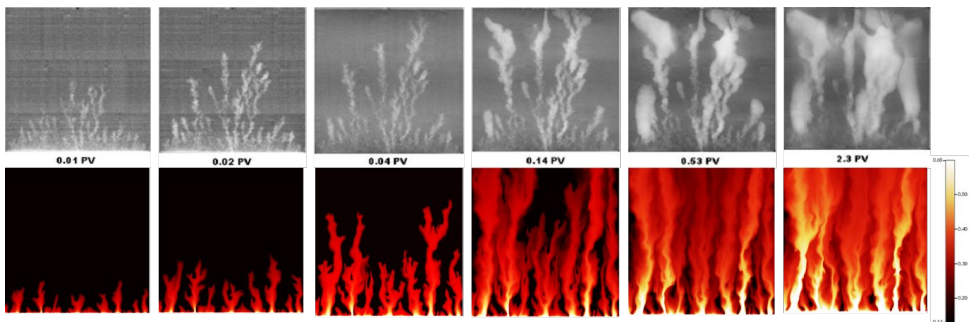


Figure 5.14: Comparison between experimental x-ray images of experiment #3 and corresponding simulation results at the same injected PV.

Nonetheless, the frontal advancement in the simulation was slower which caused a slightly delayed breakthrough. After water breakthrough, experimental data showed significant widening of established fingers. These leading fingers dominated the flow in later stages with water channeling exclusively through them. This behavior is partially recognized in simulation results as the flow is higher through three main channels, judging from water saturation levels. Figure 5.15 shows the matching results for production data of experiment #3.
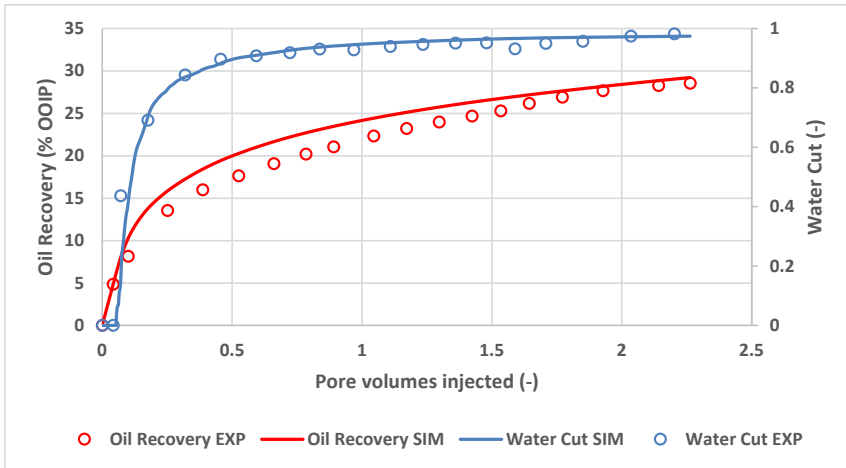
Figure 5.15: History matching of production data for experiment #3.

- *Experiment #4 – 7000 cp:*

Figure 5.16 shows the comparison between experimental images and simulation visualization at different injected pore volumes for experiment #4.
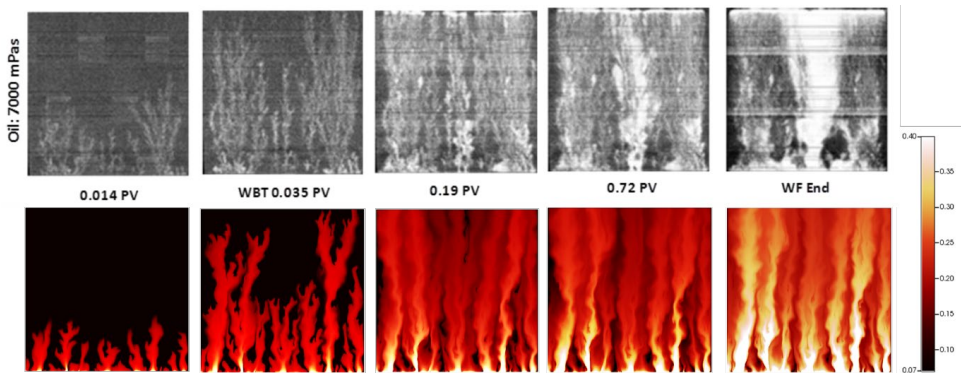


Figure 5.16: Comparison between experimental x-ray images of experiment #4 and corresponding simulation results at the same injected PV.

The simulation yielded very good replication of the fingering seen in the experimental scans, especially for the period prior to water breakthrough. Similar number of induced fingers is observed as well as similar branching pattern. The lead fingers in the simulation even followed similar paths as the actual lead fingers, however, this is just a coincidence since the permeability field in the simulation is randomly generated and

the water would follow the least resistance path, which happens to occur at approximately similar spots in both experimental slab and simulation gird. As injection continues, experimental data observes the formation of wide high saturation channel in the middle at which most of the injected water flows through. The same phenomenon is not observed in simulation results as the water keeps flowing through established channels that widens accordingly with increasing saturation. Figure 5.17 shows the oil recovery and water cut profiles obtained for this case.
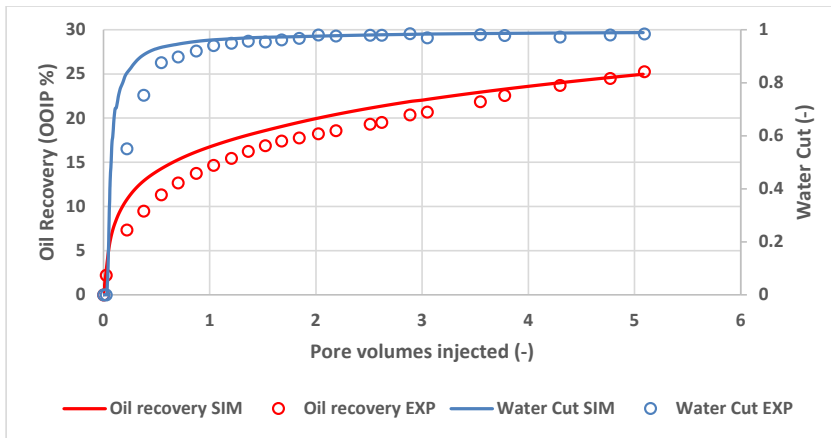


*Figure 5.17: History matching of production data for experiment #4.*

## 5.2 Polymer injectivity

This section discusses the findings of **Paper 2** and **Paper 3,** focusing on simulating the impact of polymer in-situ rheology on injection bottom-hole pressure, and on the design of field polymer injectivity tests. The overall objective of this part of the thesis is to evaluate the effect of different non-Newtonian behaviors of HPAM that might be encountered in the reservoir. Additionally, the obtained information and findings are used to establish preliminary robust guidelines for polymer injectivity tests that can improve gains from these tests in terms of interpreting in-situ polymer behavior.

## 5.2.1 Impact of in-situ rheology on bottom-hole pressure

Data from field injection applications are usually limited, and typically does not provide more than the injection bottom-hole pressure against time. Therefore, it is important to exploit the maximum benefit from this type of data for the assessment of applicability and effectiveness of the project, and gain utmost understanding of the physics and kinetics of flow behavior. For polymer injection, bottom-hole pressure can be a valuable tool in assessing in-situ non-Newtonian behavior. This can be explained simply through the radial Darcy's law for flow in porous media:

$$\Delta P = \frac{Q \, \mu}{2 \, \pi \, k \, h} \ln\left(\frac{r}{r_w}\right) + s \qquad \text{Eq. 5.3}$$

where $\Delta P$ is the pressure drop between an injector with radius of $r_w$ and a point at $r$ distance in a reservoir with $h$ thickness, $Q$ is injection rate, $\mu$ is injected fluid viscosity, and $s$ is the skin factor. Considering this relation, the pressure drop, $\Delta P$, for a non-Newtonian fluid can be seen as a function of injection rate, $Q$, and viscosity. Therefore, the bottom-hole pressure response at the injector should reflect the shear-dependent viscosity behavior seen at the near well bore region.

History matching of lab-scale radial experiments presented in **Paper 2** has shown that polymer rheology curves obtained from history matching bottom-hole pressure are identical to those obtained from history matching pressure readings from internal transducers. Injection bottom hole pressure was matched against volumetric rate (Figure 5.18), while internal pressures were matched as a function of radial distance (Figure 5.19). The rheology curves obtained from both matching procedures are shown in Figure 5.20. A vertical parallel shift was observed in the rheology curve obtained from matching bottom hole pressure. This shift is attributed to the use of initial permeability prior to polymer injection in the history matching process, while pressure measurements were conducted after polymer injection and thus after the effect of polymer retention. Hence, the impact of permeability reduction due to polymer adsorption and mechanical entrapment is reflected as an increase in the pressure

response for injection bottom hole pressure which essentially shifts up apparent viscosity.
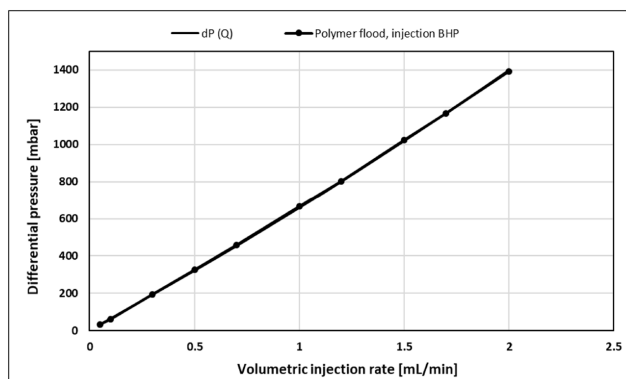


*Figure 5.18: History match of injection BHP as a function of volumetric injection rate for polymer flood.*
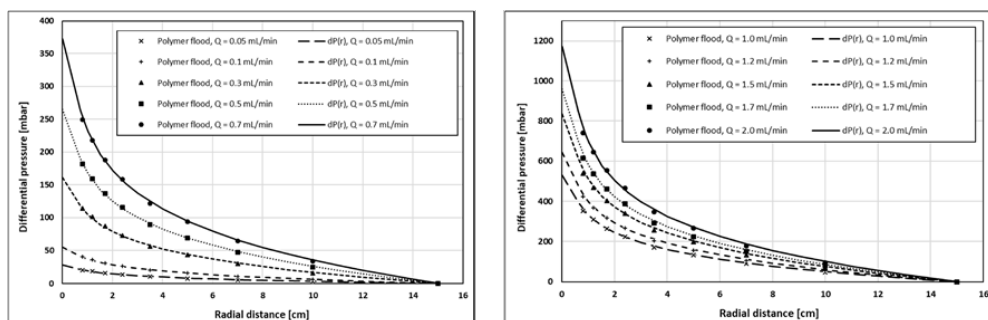


*Figure 5.19: History match of internal pressures as a function of radial distance.*

The above work on history matching bottom-hole pressure from lab-scale radial experiments have validated the robustness of using such data for predicting polymer in-situ rheology in porous media. Consequently, an upscaled field-scale generic model was used alongside selected generic rheology curves to examine the response of bottom-hole pressure to different possible behaviors around wellbore in field applications. Using extended Carreau model as a base to generate rheology curves, four different in-situ rheology curves were tested based on typical expected HPAM behaviors while encountering various levels of shear rates or velocities. The observations of HPAM behavior in flow in porous media were discussed earlier in

section 3.2. The investigated behaviors are shear-thinning, shear-thickening, shear-thinning followed by shear-thickening (combined effect), and Newtonian followed by shear-thickening. Figure 5.21 below illustrates the four rheology curves.
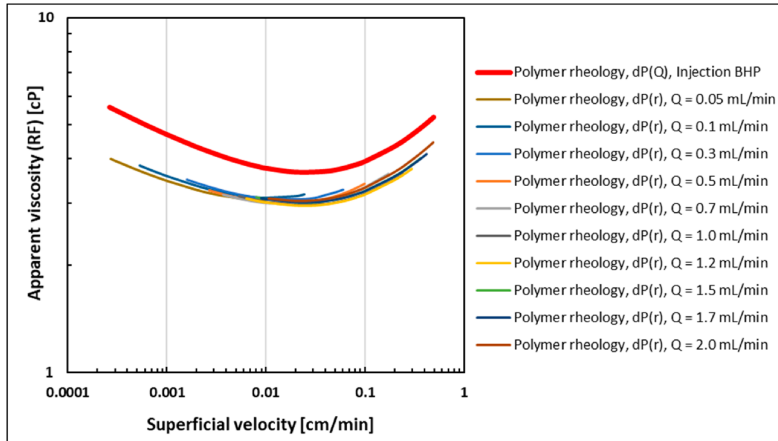


Figure 5.20:Polymer rheology curves obtained from history matching BHP as a function of injection rate and internal differential pressures.

The velocity range which bounds the generated curves are selected to represent the range of tested injection rates in order to ensure that the injection well observes the intended rheology. STARS simulations were conducted for twelve different injection rates ranging between 5 and 1600 bpd. This range of injection rates may represent the lower range of field application typical rates; however, the purpose of this specific study was to isolate the impact of in-situ rheology on bottom-hole pressure. Each injection rate was tested separately in a constant manner for a total of 1270 days, giving the pressure enough time to stabilize. Besides non-Newtonian behavior, two Newtonian cases were tested at 1 cp, representing typical water viscosity, and at 4 cp, representing high viscosity Newtonian fluid. The obtained stabilized bottom-hole pressures were plotted against respective injection rates for each rheology case (Figure 5.22).

The Newtonian cases showed expected linear behavior according to radial Darcy's law, indicating the constant viscosity that the well sees as the injected fluid propagates in the reservoir. It is evident that increasing the viscosity of Newtonian injection would

be reflected by an increase in the slope of the line proportional to the respective increase in viscosity.
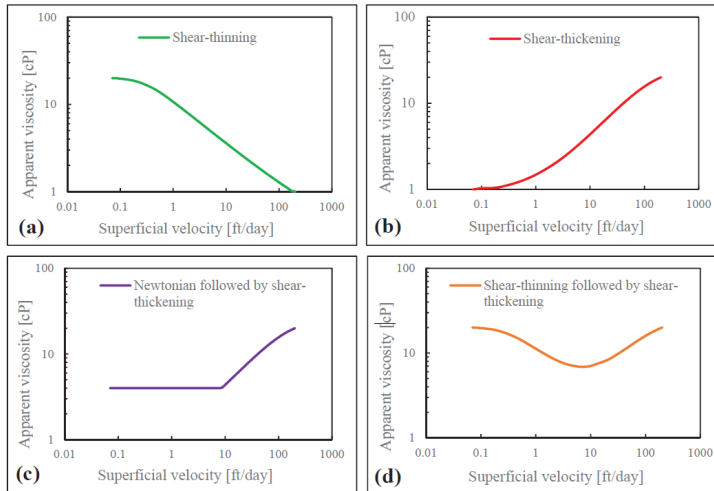


Figure 5.21: Carreau generic rheology curves used in 2D radial model.
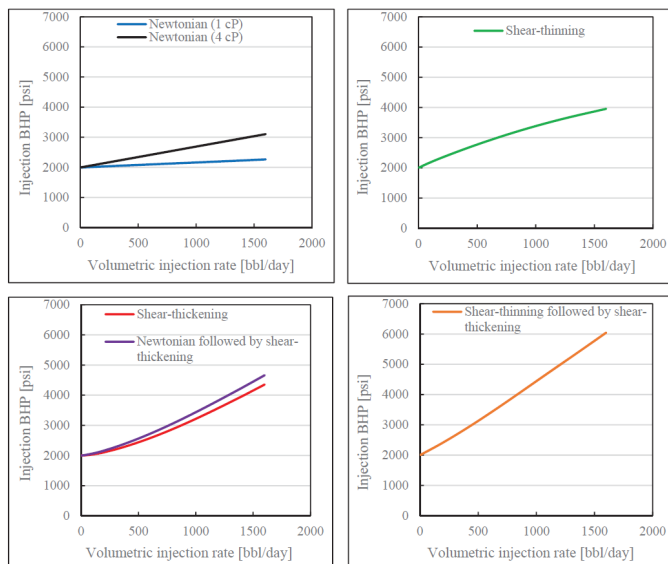


Figure 5.22: BHP response for different non-Newtonian and Newtonian behaviors.

For non-Newtonian cases, the plots of bottom-hole pressure versus injection rate shows a non-linear behavior. Shear-thinning rheology shows a decreasing slope trend as the

injection rates increases due to the exhibited low viscosity in the near well bore region. In contrast, both cases where shear-thickening is dominant at high velocities show distinctive increasing slopes. It is noted though that the pressure response is higher for the case with Newtonian behavior at lower velocities, and that is attributed to the higher viscosity the injector observes according to input rheology curves. This observation confirms that both rheology behaviors would show identical pressure response if the Newtonian part of the curve was set at a lower viscosity. Nonetheless, it can be confirmed that an increasing slope on the pressure versus rate plot is an exclusive signal for shear-thickening behavior in the near wellbore region. The combined theology case is less distinctive overall and shows a nearly linear trend. This is attributed to the consecutive slope changes as it decreases in the shear-thinning region, almost flattens at the transition near-Newtonian region, and increases in the shear-thickening region of the theology curve. It can also be observed that combined rheology induced the largest pressure response over the entire injection rate range. This is due to the higher average viscosity of the tested rheology curve compared to other cases. Indeed, it can be verified that at certain constant viscosity model parameters, the combined rheology can be distinguished with the significant difference in pressure response as the well observes high viscosities at both endpoints of the curve.

Another potential pressure signature of polymer in-situ rheology is the pressure transient trend with time. Lab radial experiments have demonstrated the difference between pressure falloffs for Newtonian brine and non-Newtonian polymer solutions as injection rate is decreased in a stepped manner. Figure 5.23 and 5.24 show the injection bottom hole pressure versus time for brine flooding and polymer flooding, respectively. It is evident that both brine floods before and after polymer injection demonstrate minimal pressure falloff time compared to distinctive transient behavior seen in polymer flood. Additionally, the observed transient time toward stabilization is increasing as injection rate decreases. This suggests that polymer rheology is different at low injection rates compared to higher rates.
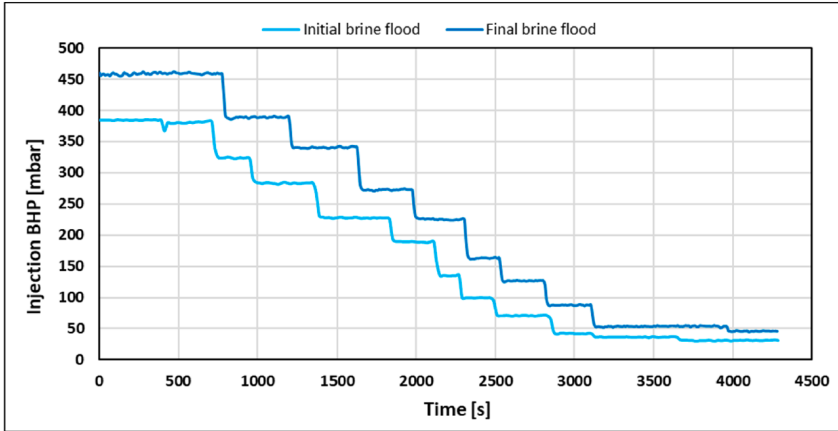
*Figure 5.23: Injection BHP versus time brine floods before and after polymer flood.*
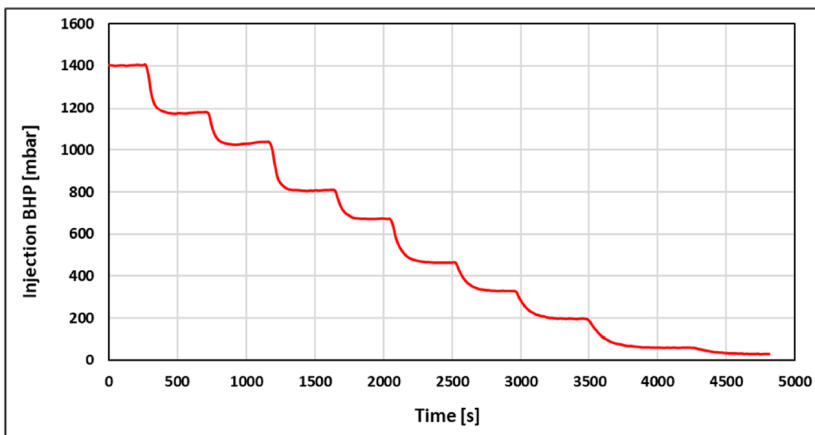


*Figure 5.24: BHP falloff for the polymer flood rate steps.*

Consequently, the response of bottom hole pressure buildup with time was analyzed for the field scale model. Figure 5.25 below shows the pressure response against time for all tested rheology cases at an injection rate of 200 bpd. The pressure build for Newtonian fluid is almost instantaneous with near zero transient time. On the other hand, non-Newtonian rheology cases observe a transient time that differs for different rheology and/or injection rate. For the specific injection rate of 200 bpd, the case with only shear-thickening showed the least stabilized pressure. However, the buildup took approximately one day. For the case with Newtonian plateau at lower velocities

followed by shear-thickening, pressure response observed a much longer transient time of 100 days. This is explained by the increase in viscosity of polymer front as it propagated in the reservoir for the latter case compared to pure shear-thickening rheology. The concept is also supported by the responses of the cases with shear-thinning included which showed much longer buildup times. Moreover, the combined effect showed the highest stabilized pressure level as expected due to the higher average effective viscosity across the injection region. From these observations, one can identify distinctive qualitative and quantitative signals for different rheology behaviors which can be used ultimately in improving understanding of polymer in-situ rheology and optimizing injectivity tests and polymer injection plans.
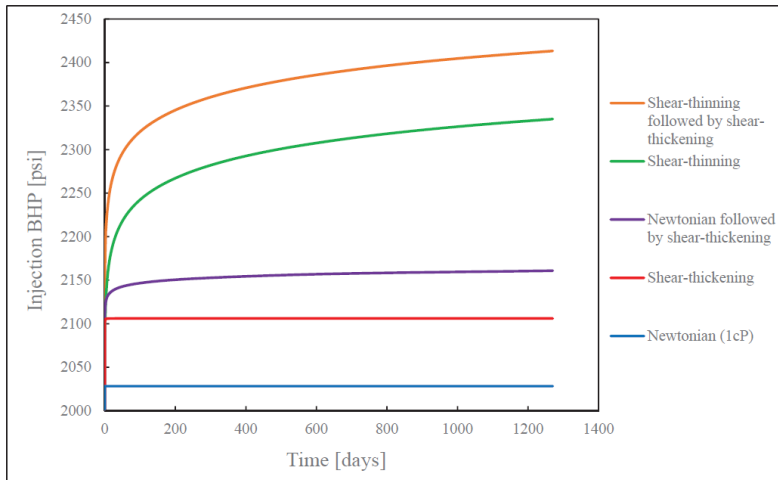


*Figure 5.25: BHP buildup versus time for different rheology cases at 200 bpd.*

## 5.2.2 Optimizing polymer injectivity test design

Given the recognition of the robustness of using bottom-hole pressure in predicting polymer in-rheology via numerical simulation, a generic 3D field scale STARS radial model was used to investigate realistic field injection rates and the impact of vertical heterogeneity on the bottom hole pressure response. The objective was to validate the previous findings from both lab-scale simulations and upscaled 2D generic field simulations in order to set general guidelines to improve the workflow of designing polymer injectivity tests.

The approach taken was to test three different in-situ rheology cases that are most representative of HPAM behavior in near wellbore region. The three cases are shear-thinning only, shear-thickening only, and a combined effect of both. HPAM can observe only shear-thinning in the near wellbore region when shear flow dominates the in-situ behavior due to low molecular weight and/or low concentrations (Skauge et al. 2016). Comparably, it may observe shear-thickening only at high enough molecular weights or concentrations, where extensional flow dominates the in-situ behavior shadowing the impact of shear flow even at low range of shear rates/velocities. The third case is the most seen in lab rheology experiments for HPAM where shear thinning rakes place at low velocities and apparent shear thickening kicks in at high velocities.

Using the modified version of extended Carreau curve where Darcy velocity replaces shear rate terms, three main rheology curves were generated using constant parameters to ensure consistency of the curves. The infinite viscosity term, $\mu_\infty$, which represent pure solvent viscosity was set at 1 cp. $\mu_{max}$ and $\mu_0$ which represent maximum viscosity and zero-shear viscosity, respectively, were assigned equal values of 10 cp. These values can be obtained from lab measurements with fair accuracy. The terms of $\lambda$ and $n$ were adjusted so that the generated curves are smooth and consistent for all rheology cases. Table 5.4 below shows a summary of Carreau parameters for the curves used in the study. Figure 5.26 shows the generated rheology curves. The range of velocities was decided based on the expected encountered velocities at all tested injection rates. The injection rates for this study were selected to be between 1000 and 10,000 bpd, representing typical injection rates in field applications.

Table 5.4: Carreau parameters of rheology curves used in injectivity test design analysis.

| $\mu_\infty$ | $\mu_0$ | $\mu_{max}$ | $\lambda_1$ | $n_1$ | $\lambda_2$ | $n_2$ |
|---|---|---|---|---|---|---|
| 1 | 10 | 10 | $10^6$ | 0.46 | $10^4$ | 1.4 |
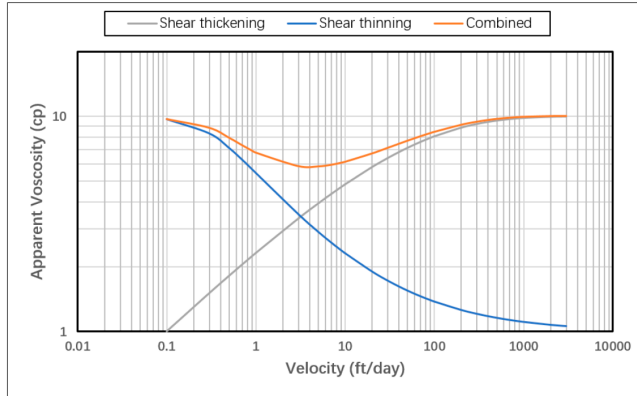
*Figure 5.26: Generic In-situ rheology curves used in injectivity test design analysis.*

The simulations were conducted for a homogeneous case with uniform permeability, and a simple vertically heterogenous case representing typical layered reservoirs. Vertical heterogeneity is highly expected in reservoirs and it adds to the complexity of interpreting pressure data from injectivity tests. For instance, the existence of high permeability layers or open fractures may result in the occurrence of several in-situ rheology behaviors at the same time in the near-well bore region. Similarly, permeability reduction due to polymer retention may affect the velocity at which polymer flows through the porous media, which alternates the expected in-situ rheology. The tested heterogeneous case comprises a layered system with alternating high and low permeability layers at 1000 mD and 100 mD, respectively (Figure 5.27).
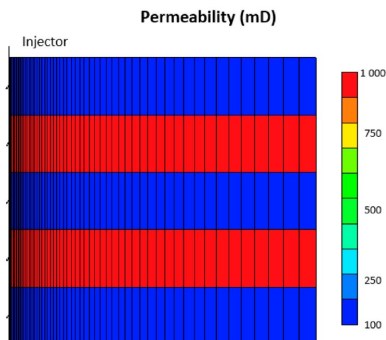


*Figure 5.27: Cross sectional illustration of vertical heterogeneity layered case.*

Figure 5.28 shows stabilized bottomhole pressure plotted against corresponding injection rate for each rheology case after injecting one pore-volume. As discussed earlier in section 4.3, the injection of one-pore volume is essential for eliminating the impact of viscosity mixing at the front and isolate the impact of in-situ rheology. Expectedly, the plots show increasing slope for shear-thickening, decreasing slope for shear-thinning, and a combined slope change for the combined effect. To detect the slope changes, the pressure was fitted with a second order polynomial, and hence the coefficients of the second order term could be used to detect the direction of slope changes where positive coefficients indicate increasing slope and negative coefficients indicate decreasing slope.

Considering the vast variations in determining near-well bore region for each specific reservoir, and the difficulty of achieving one pore-volume injection especially at low injection rates, the viability of using smaller pore-volumes to detect the rheology impact on pressure was investigated. Bottomhole pressure versus rate was plotted at 0.001 PV, 0.01 PV, and 0.1 PV, to confirm that the same rheology signature could be detected during pressure transient prior to stabilization, and with the presence of viscosity mixing effect at the front (Figures 5.29, 5.30, and 5.31).

Although the slopes are getting less distinctive with shorter injection times, the coefficients of second order polynomial fitting curves are used to detect the changes associated with the pressure response to each in-situ rheology. To analyze the data in a systematic approach, the range of injection rates is divided into three main subranges low, medium, and high. The low range of rates is between 1000 and 3000 bpd, medium is between 4000 and 7000 bpd, and high is between 8000 and 10000 bpd. Table 5.5 below presents the coefficients of second order polynomial trendline functions for each rheology case at different injected pore-volumes.
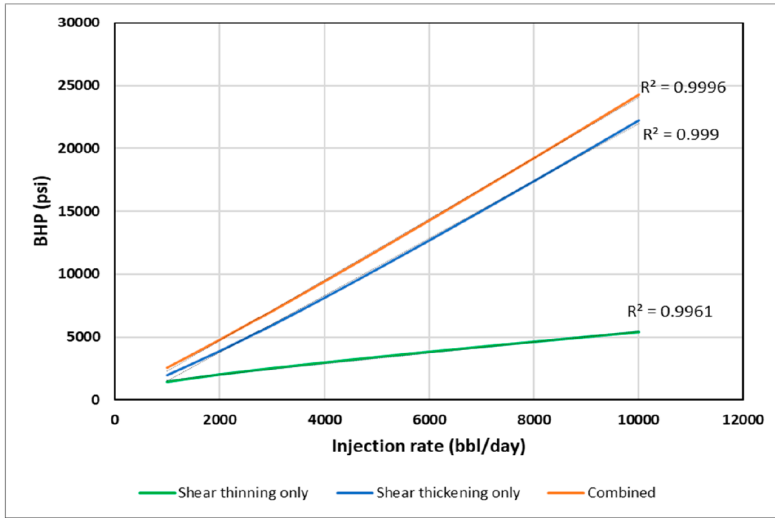
Figure 5.28: Stabilized BHP versus injection rate for different in-situ rheology in the homogenous case.
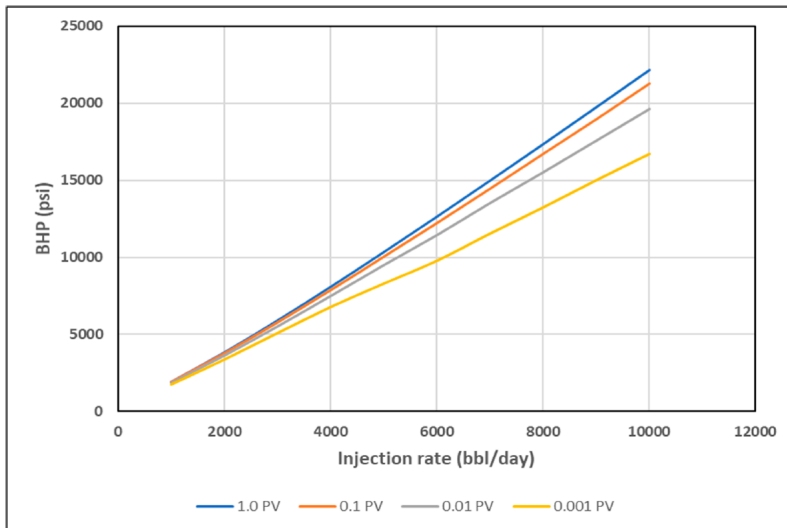


Figure 5.29: BHP versus injection rate for shear thickening homogenous case at different PVs.
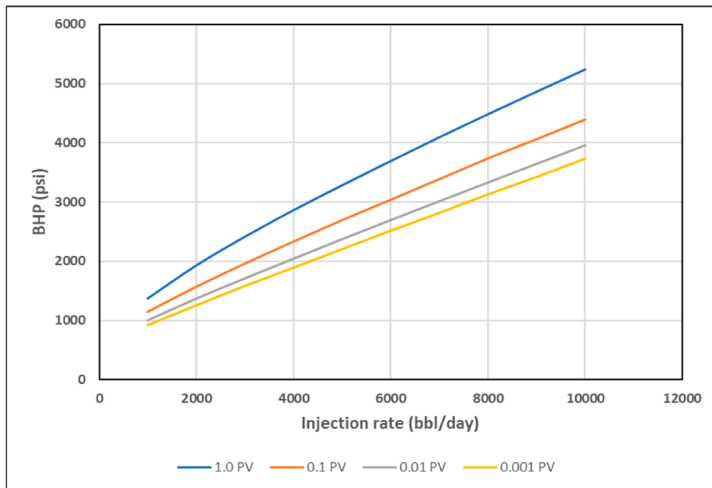
Figure 5.30: BHP versus injection rate for shear thinning homogenous case at different PVs.
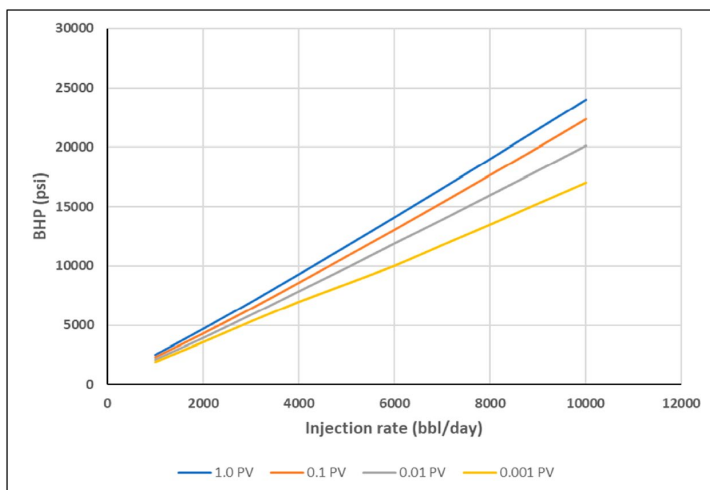


Figure 5.31: BHP versus injection rate for combined rheology homogenous case at different PVs.

Table 5.5: Coefficients of 2<sup>nd</sup> order polynomial trendline functions of BHP versus injection rate at different injected PVs.

*Table 5.5: Coefficients of $2^{nd}$ order polynomial trendline functions of BHP versus injection rate at different injected PVs.*

| | Coefficient of 2nd Order Polynomial Trendline Function ($\times 10^{-5}$) | | | | | | | | | | | |
| --- | --- | --- | --- | --- | --- | --- | --- | --- | --- | --- | --- | --- |
| | 0.001 PV | | | 0.01 PV | | | 0.1 PV | | | 1.0 PV | | |
| Rheology | High | Med | Low | High | Med | Low | High | Med | Low | High | Med | Low |
| Shear thinning | 0.8 | −0.4 | −0.2 | −0.03 | −0.3 | −1.0 | 0.3 | −0.4 | −2.0 | −0.2 | −0.5 | -4.0 |
| Shear thickening | −3.0 | 6.0 | 5.0 | −2.0 | 2.0 | 6.0 | 3.0 | 2.0 | 7.0 | 6.0 | 2.0 | 8.0 |
| Combined rheology | −1.0 | 6.0 | 3.0 | 0.9 | 0.5 | 6.0 | 4.0 | 1.0 | 5.0 | −0.05 | 1.0 | 4.0 |

The obtained coefficients demonstrate that the signature of each rheology can be detected even at shorter injection times. The shear-thinning case shows predominantly negative values indicating that the slope of pressure versus rate is decreasing, while positive coefficients are obtained for shear-thickening only case. In both cases there are instants of outlying points occurring specifically at high range of injection rates especially at smaller pore-volumes, such as the positive value for shear-thinning and the negative value for shear-thickening at 0.001 PV. These outliers are explained by the effect of viscosity mixing at the polymer front which would have its most significant impact during early injection. The reason why such deviation is not captured at low and med range is that the viscosity seen by the injector is dominated by in-situ rheology behavior rather than viscosity mixing. Combined rheology was also dominated by the impact of shear-thickening as it is the viscosity behavior that is first seen by the injector in the near wellbore region. Adding vertical heterogeneity to the model did not result in any changes in the qualitative signatures seen in homogeneous case. Figure 5.32 below shows the plot of bottomhole pressure versus injection rate for the layered case where the slope behavior is identical the homogonous case. This suggests that the same methodology can be used to detect in-situ viscosity behavior even at the presence of vertical permeability variations.

As discussed earlier, another tool of analyzing in-situ rheology signature is the transient time it takes the pressure to build up toward stabilization. Plots of pressure build up for both homogenous and heterogenous cases at 5000 bpd injection rates are shown in Figures 5.33 and 5.34, respectively.
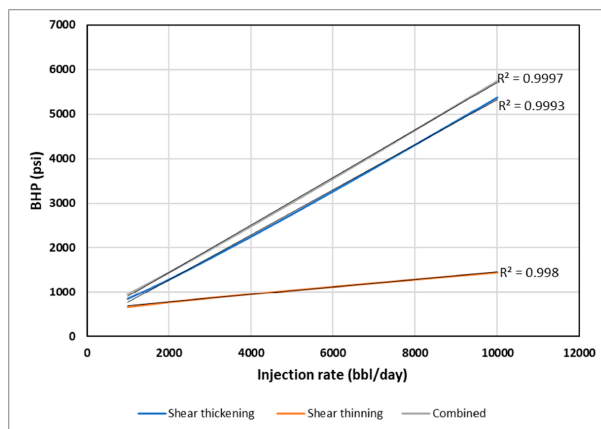
*Figure 5.32: BHP versus injection rate for different in-situ rheology in the layered case.*

Due to the model size, gridding scheme, and producers' pattern; injection bottomhole pressure stabilization was assured after injecting at least one pore-volume. Therefore, the pressure response was plotted against log time represented by log PV, which allows better visualization of the pressure transient behavior at early stages of injection. It is evident from the plots that each in-situ rheology produces a distinctive transient behavior. Shear-thinning results in a gradual pressure build up that takes much longer time to stabilize compared to shear-thickening. In contrast, the other two cases where shear-thickening is encountered firstly at the injection point, show a sharp increase in pressure toward a near-stabilization level in much shorter times. The combined rheology case has interestingly shown a combination of both shear-thinning and shear-thickening signatures, as the pressure behavior shows a sharp increasing the near wellbore region and a more gradual build up at distances away toward the boundary. These observations suggest that the impact of thinning or thickening immediately at the injection point, could be detected after injecting as low as 0.0001 pore-volume. However, the more complex combined rheology would require longer periods of at least one pore-volume to be detectable from pressure versus time measurements. Moreover, considering the data on Figure 5.34, vertical heterogeneity does not affect the observations of in-situ rheology signature qualitatively, however, the existence of

high permeability layers increases the formation capacity (product of permeability and thickness) and hence reduces the pressure significantly. Consequently, the heterogenous case which has a formation capacity of about 8800 mD · ft have observed pressure levels at a quarter of the magnitude of pressures seen in the homogeneous case with a formation capacity of 1000 mD · ft.
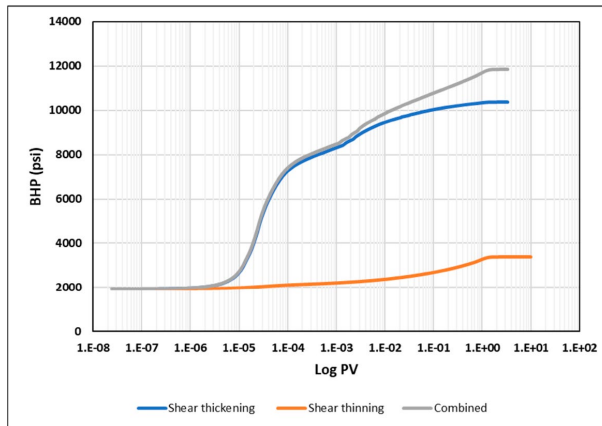


*Figure 5.33: BHP versus log PV for different rheology cases at 5000 bpd in the homogenous case.*
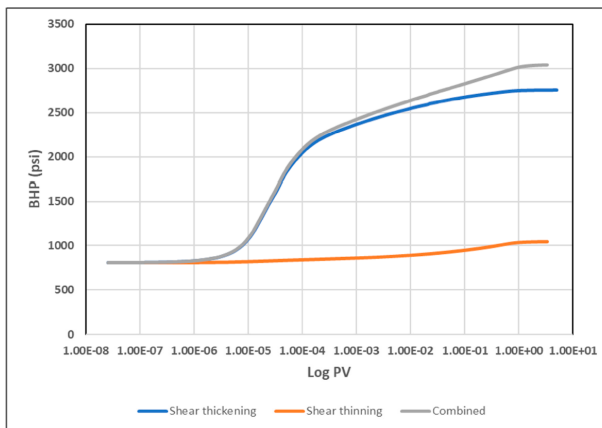


*Figure 5.34: BHP versus log PV for different rheology cases at 5000 bpd in the layered case.*

From the above findings, it can be concluded that a rate-stepping scheme is of a great benefit for polymer injectivity tests since it will result in significant understanding of

the in-situ rheology behavior. A minimum of three rate steps has to be included in the design of injectivity tests with the selection of rates varying between low and high rates in order to cover wider velocity range. Besides, pressure buildup (or falloff) could be used as a qualitative measurement for rheology behavior even at times as short as 0.0001 pore-volume, with the accuracy getting better with longer times. The pressure readings generally can also be used to quantitatively to measure the impact of permeability variation and decide effective formation capacity.

## 5.3  Field polymer injectivity test analysis

In this section, the results of data analysis from a field polymer injectivity test conducted in Abu Dhabi is presented. The application is the first of its kind ever worldwide, in a high-salinity high-temperature carbonate reservoir. The information and experience gained from generic studies performed in near-ideal conditions were utilized to improve the understanding of polymer in-situ behavior at actual conditions, characterized by harsh environment, significant heterogeneity, and high uncertainties. Findings related to this section is presented in **Paper 4**.

### 5.3.1 Background and available field data

The data analyzed in this work is from a single-well polymer injectivity test that was performed as part of a de-risking program aiming to verify the potential of a full-field implementation of polymer flooding in an Abu Dhabi carbonate reservoir. The subject reservoir is a highly heterogeneous Lower Cretaceous limestone reservoir with a cyclic stratigraphy that observes severe layering in the scale of few feet (Masalameh et al. 2014). Besides its inherent heterogeneity, the reservoir is characterized by high salinity and temperature levels with formation water salinities exceeding 250,000 ppm and in-situ temperatures exceeding 120°C. The average thickness of the reservoir is between 150 ft and 300 ft.  The reason behind considering polymer flooding as a potential EOR method is that the reservoir is divided into two main zones from permeability perspective. The upper zone has alternating high permeability and low permeability layers with an average permeability 10 to 100 times higher than the lower zone, which

lacks the high permeability streaks and instead consists of uniformly distributed low permeability layering. This permeability contrast, coupled with the lack of flow barrier between the two zones, creates an unfavorable sweeping pattern where injected water ends up overriding and advancing in the upper zone mostly, even for injectors completed only in the lower zone (Figure 5.35). Consequently, much of the oil in place of the lower zone equaling 60% of the reservoir's total is being bypassed, resulting in poor recovery efficiency. Polymer flooding can thusly improve the vertical sweep efficiency by enhancing mobility ratio conditions and reducing crossflow between the two zones.

Due to the harsh nature of the reservoir from salinity and temperature perspectives, extensive laboratory work was conducted to qualify candidate polymer that can maintain adequate degree of stability. SAV-10, a high-AMPS-content acrylamide polymer manufactured by SNF©, was selected based on detailed experimental work conducted by Masalameh et al. (2019).
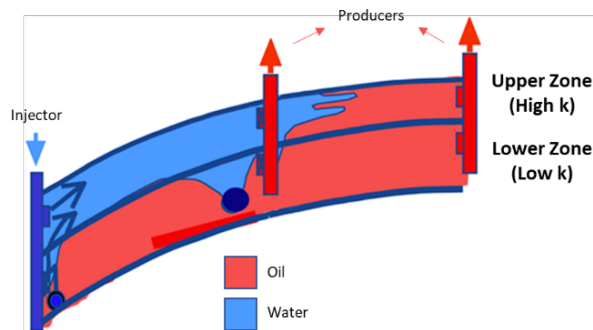


*Figure 5.35: Schematic cross sectional illustration of the two main permeability zones of the subject reservoir.*

The lab data provided for analysis in the work of this thesis include bulk and in-situ measurements that demonstrates the response of SAV-10's viscosity for different shear levels both in bulk flow and flow in porous media (Figures 5.36a and 5.36b). Experimental results confirmed the inherent viscoelastic behavior of SAV-10 as an HPAM derivative, showing exclusive shear thinning in bulk flow and combined effect in porous media where apparent shear-thickening kicks in at high shear. Besides, data

on the impact of pre-shearing and presence of oil on the onset and magnitude of shear-thickening are presented in Figures 5.37a and 5.37b. From these results one can observe that the shear-thickening behavior of SAV-10 is significantly affected by pre-shearing and the presence of oil, where both factors result in delaying the apparent thickening onset to higher velocities and reducing the magnitude of viscosity increase.
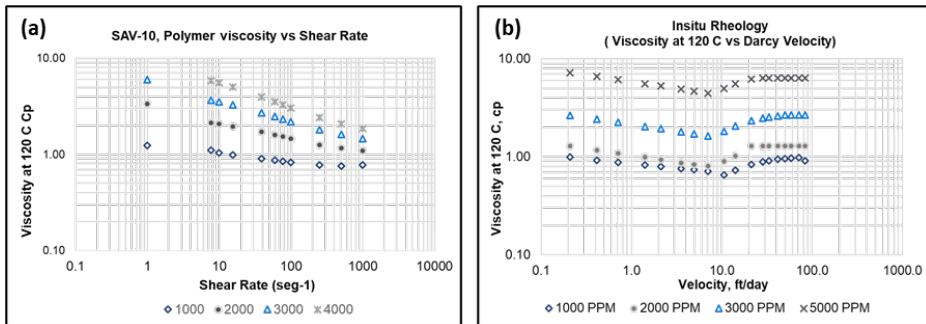


Figure 5.36: a) Bulk viscosity measurements of SAV-10 at different concentrations and b) In-situ viscosity measurements of SAV-10 at different concentration at 120ºC.
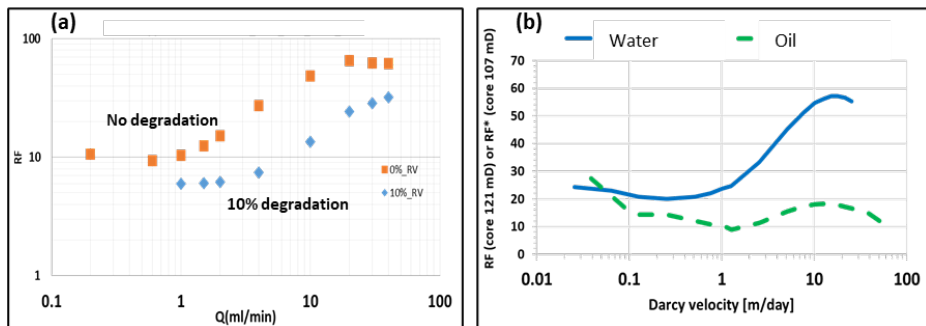


Figure 5.37: a) Impact of degradation from pre-shearing and b) Impact of Oil presence, on the onset of SAV-10 apparent shear thickening in porous media.

The field injectivity test program was carried out upon the completion of a single water injector in the targeted high permeability zone with a perforation interval of 65 ft. The test took place over three main phases, starting with establishing water injection baseline for about 13 months where water was injected at rates ranging between 500 and 8000 bpd. The second phase was the actual polymer injectivity test where polymer

injection with variable rates, concentrations and pre-shearing levels, was performed over a 4.5-month period. The final phase was the chase water injection, which started immediately after polymer injection completion, and continued for about nine months. Figure 5.38 below presents a summary of the injectivity test phases. During water injection baseline, several multi-rate production logging tool (PLT) logs were conducted to evaluate vertical distribution of injection. Additionally, two acid stimulation jobs were performed to enhance injectivity. Moreover, two pressure fall off (PFO) tests were conducted during the polymer injection phase. Results from PFOs interpretation via a two-layer radial composite models have shown a growing skin impairment with time along with the polymer injection. Besides, in-situ effective viscosity of polymer was estimated at 3 cp from PFO analysis.
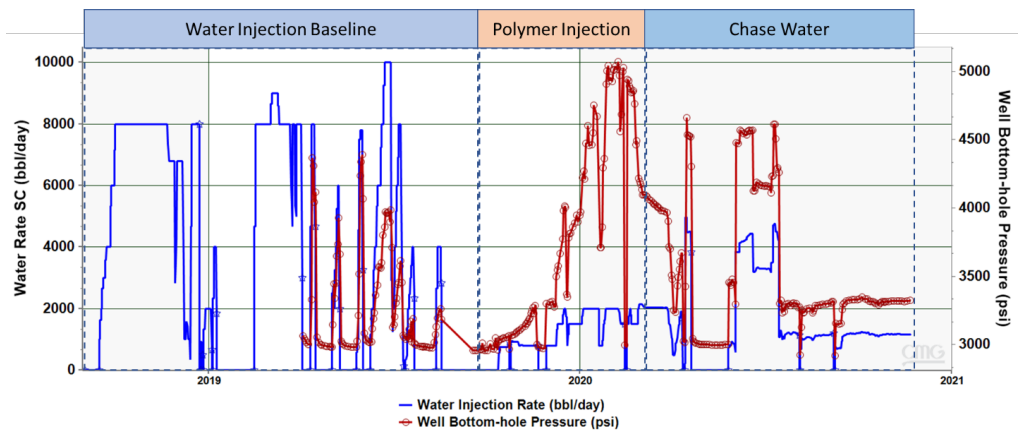


*Figure 5.38: Summary of injection rates and BHP data of the injectivity test.*

## 5.3.2 Results and findings

The main objective of the analysis was to confirm the concept of predicting polymer in-situ rheology using injection bottom-hole pressure data. The approach taken towards this objective was thus depending on isolating bottomhole pressure as the main matching parameter and setting up a workflow to serve this purpose. Hence, the suggested workflow is as follows:

i.   History match water injection baseline to establish reliable model inputs.

ii.  Evaluate bottomhole pressure response to rate and concentration stepping.

iii. Test the sensitivity to RRF dependence on permeability and different RRF correlations.

iv. Analyze field bottomhole pressure data to obtain in-situ rheology signatures.

v. History match polymer injection using in-situ rheology and RRF as the main tuning parameters.

vi. Obtain representative polymer in-situ viscosity behavior and compare it to lab data.

Considering water injection baseline history matching, the major uncertainty in available data was the permeability distribution. As explained earlier, the target reservoir has a high degree of variation in vertical permeability distribution. Available permeability data was obtained from a static geological model that relied on petrophysical and well logs data from offset wells in the reservoir. Therefore, an approach depending on PLT logs data was selected, where the vertical profile of injected water is used to modify permeability in the model by applying certain multipliers. Six PLT logs were made available for analysis, of which four were conducted during water injection baseline and two during polymer injection (Figure 5.39).

As mentioned previously, acid stimulation jobs were conducted during water injection baseline phase to improve injectivity. The results of a PLT log after acid stimulation revealed an alteration in the upper most section of vertical injection profile, that has continued through polymer injection. This has been interpreted as a permeability alteration that can be due to fracture initiation or a wormhole activation as a consequence of carbonate reaction to acid. Hence, a dynamic permeability technique was adopted where the upper sector permeability multiplier was altered after acid stimulation. This can be done through the simulation restart functionality in IMEX. The interpretation of PLT logs has yielded a division of the perforated section into four main sectors. Moreover, a set of multipliers averaging about 2.4 across the whole perforation were applied. It is a common practice to modify the permeability input when modelling highly heterogeneous to account for the amount of uncertainty even at the presence of substantial data. Figure 5.40 below illustrates the applied multipliers

pre and post acid stimulation jobs alongside with the original permeability input from static geological model. Besides permeability alteration, extra tuning of skin factor was required to complement the matching process and best matches were obtained with a +3.5 skin before the first acid stimulation, +2.0 after first acid stimulation, and -0.45 after second acid stimulation. The obtained pressure history match for water injection baseline is shown in Figure 5.41.
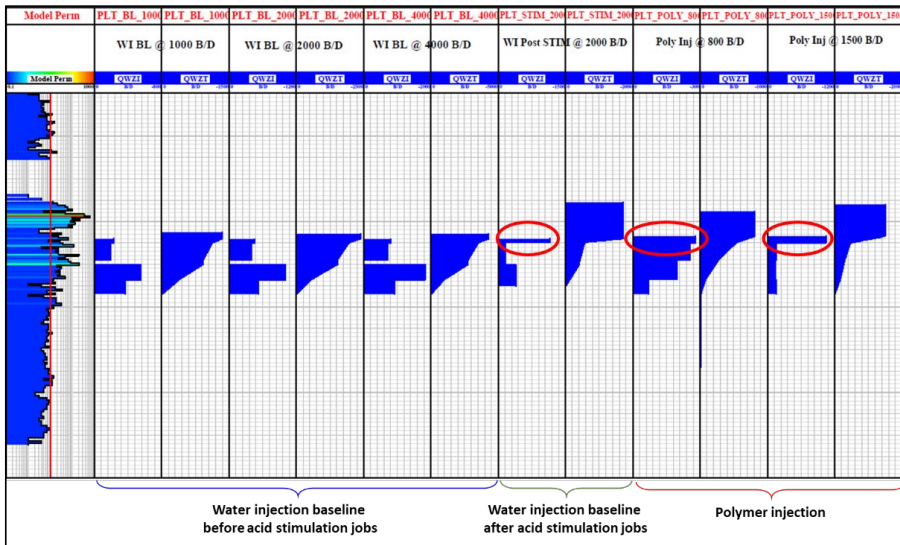


Figure 5.39: Production logging tool logs conducted during injectivity test.
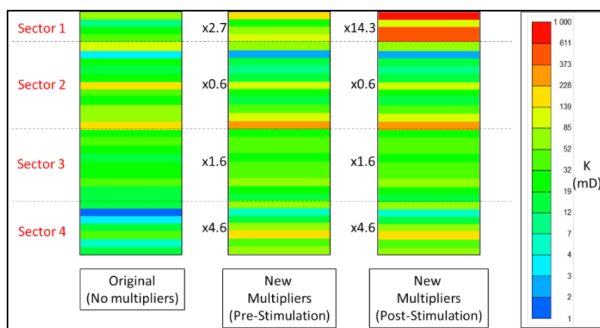


Figure 5.40: Permeability multipliers applied to match PLT logs before and after acid stimulation jobs.

After essentially establishing reliable permeability inputs, the model was used to evaluate several rate and concentration stepping cases over the same actual period in which polymer injection took place. The purpose of this sensitivity analysis is to evaluate the impact of rate and concentration stepping on pressure response in the simulator at Newtonian and non-Newtonian conditions. The cases considered for the analysis include constant rate and concentration, concentration steps, and rate steps.
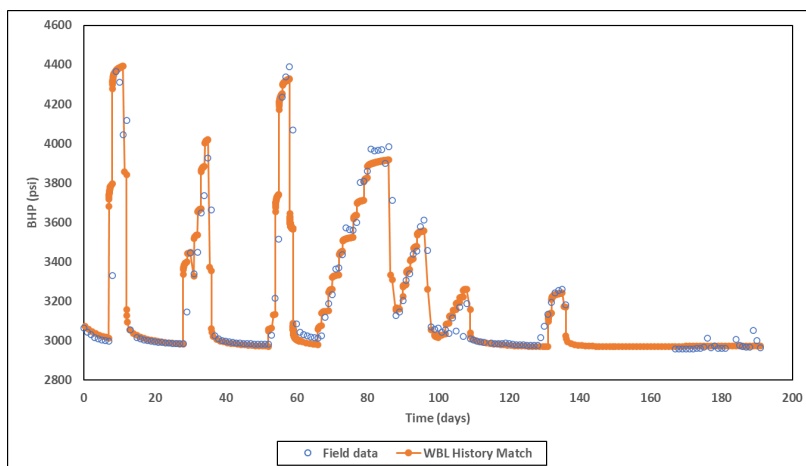


*Figure 5.41: History match of water injection baseline BHP.*

For Newtonian rheology cases, water viscosity was set at 0.43 cp, which is the viscosity of the water used in the actual test. For non-Newtonian rheology cases, three generic rheology curves were created using extended Carreau model. A combined rheology was adopted for the viscosity behavior with distinctive shear-thinning and shear-thickening over a range of velocities representing expected velocity field around wellbore. The curves were set to mimic the impact of concentration at three different levels: 600, 1600, and 2700 ppm (Figure 5.42). Table 5.6 below summarize Carreau parameters of generated rheology curves.

Figures 5.43 and 5.44 show the results of the pressure sensitivity to rate and concentration stepping. It is evident from the findings that non-Newtonian rheology exhibits a significantly longer transient time during pressure build up toward stabilization, compared to the much shorter stabilization seen for Newtonian rheology.
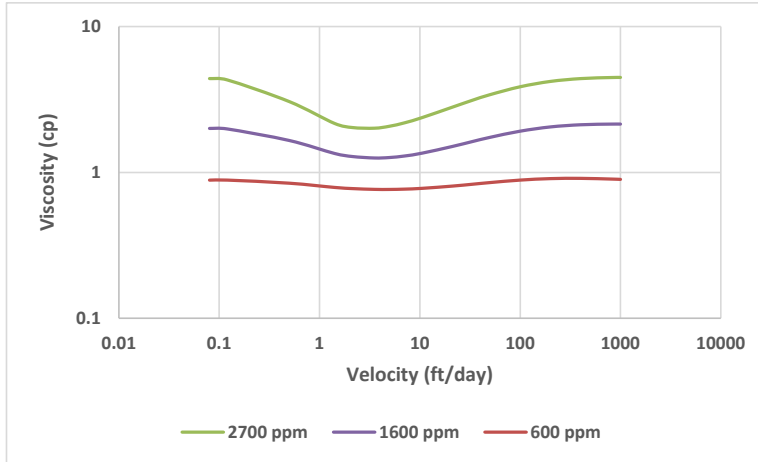
Figure 5.42: In-situ rheology curves used in the sensitivity of rate and concentration stepping.

Table 5.6: Parameters used to generate in-situ rheology curves for sensitivity tests.

| | 2700 ppm | 1600 ppm | 600 ppm |
|---|---|---|---|
| $u$ | 0.1 to 1000 ft/day | | |
| $\mu_{max}$ | 10 | 4.5 | 1.35 |
| $n_2$ | 1.5 | | |
| $\lambda_2$ | $10^4$ | | |
| $\mu_\infty$ | 0.43 | | |
| $\mu_0$ | 10 | 4.5 | 2 |
| $n_1$ | 0.2 | 0.5 | 0.8 |
| $\lambda_1$ | $10^6$ | | |

This transient behavior is seen in both constant rate and rate stepping cases, with the latter having more pronounced non-Newtonian effect. The other major difference is that Newtonian rate steps exhibit proportional linear increase in stabilized pressure, while the pressure increase is non-linear for non-Newtonian rheology. The impact of shear-thickening, as the nearest rheology behavior to the wellbore, can be detected through the non-linear increase of bottomhole pressure with increasing rate. Besides, for the smallest rate step, the pressure stabilization trend appears closer to the

Newtonian behavior which reflects the near-Newtonian part of the rheology curve at med velocity range. Concentration stepping cases were conducted at constant rate, increasing rate steps, and decreasing rate steps. Given the impact of concentration reduction on rheology curves seen in Figure 5.44, concentration stepping yielded a more pronounced gradual increase in pressure compared to rate stepping. The impact of increasing and decreasing the rate was deemed with no influence as both cases exhibit similar pressure transient and similar level of stabilization. Overall, the results of pressure transient sensitivity to rate and concentration stepping have confirmed the ability to detect different rheological signatures of polymer in-situ viscosity behavior, which can be beneficial to the analysis of actual field data with fluctuating rate and concentration conditions.
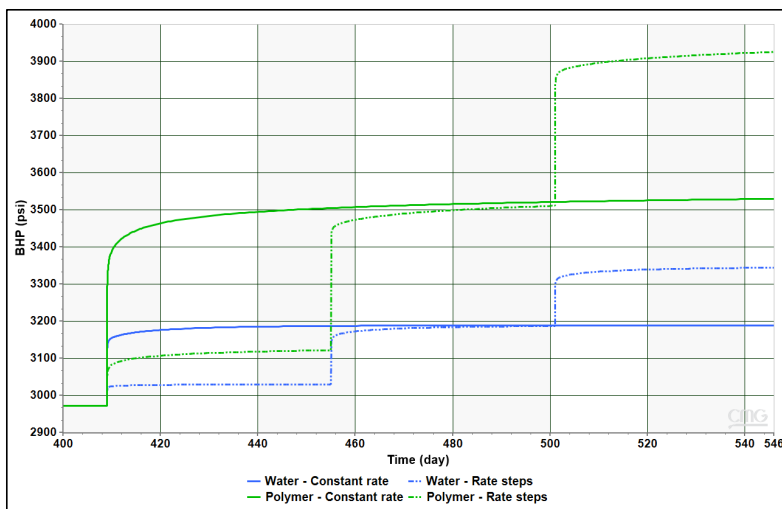


*Figure 5.43: Impact of rate stepping on Newtonian and non-Newtonian injection.*

In addition to the impact of rheology, rate and concentration stepping sensitivity was tested against the impact of residual resistance factor (RRF). As discussed earlier in section 3.4, irreversible reduction of permeability due to polymer retention is typically measured by RRF. Generally, the magnitude of RRF is inversely proportional to permeability, i.e., low permeability porous media exhibits higher RRF values due to higher polymer retention caused by tighter pore bodies and throats and larger

inaccessible pore volume. Therefore, RRF is a major tuning parameter in history matching polymer injectivity as it has a great impact on the injection bottomhole pressure as a permeability-related factor. Figure 5.45 below shows RRF-permeability correlations of obtained from lab core flooding experiments of SAV-10 polymer flow in cores from subject reservoir.
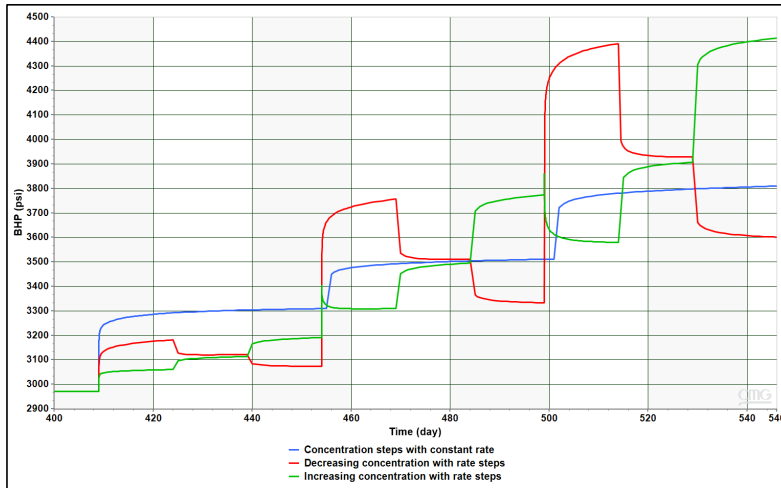


Figure 5.44: Impact of concentration stepping with different patterns on polymer injection.

The proposed correlations depend on measured RRF data points at several saturation conditions combined with an assumed lower endpoint of permeability for each correlation, representing the lower boundary of permeability impact on RRF. The correlations were denoted low, mid and high. Each correlation was included in rate and concentration stepping sensitivity to investigate its impact on pressure response. Moreover, weighted average RRF values of the correlations based on the established permeability distribution of the model were also tested to investigate the impact of average values compared to correlations. Table 5.7 below provides a summary of the RRF correlations and average values.

Results of bottomhole pressure sensitivity to RRF correlations and average RRF values along with rate and concentration stepping are a shown in Figure 5.46 and 5.47.
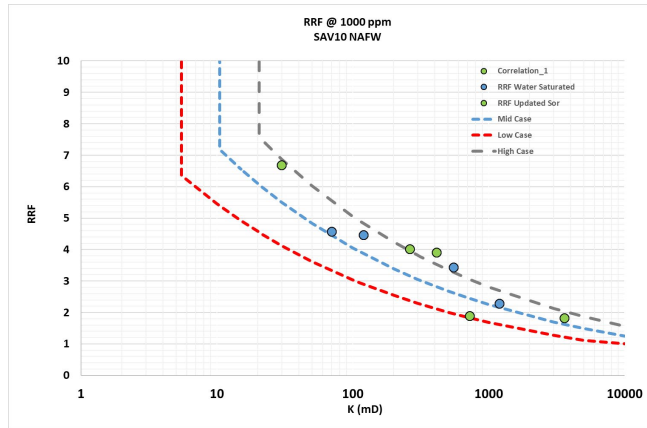
Figure 5.45: RRF lab data at different conditions and proposed correlations.

Table 5.7: Summary of RRF correlation scenarios and respective weighted average value.

| Scenario | RRF correlation | $k_{min}$ | Weighted Average RRF |
|---|---|---|---|
| Low | $RRF = 9.6 \times (k)^{-0.251}$ | 5 | 4.171 |
| Mid | $RRF = 13.0 \times (k)^{-0.255}$ | 10 | 3.322 |
| High | $RRF = 16.4 \times (k)^{-0.255}$ | 20 | 2.506 |
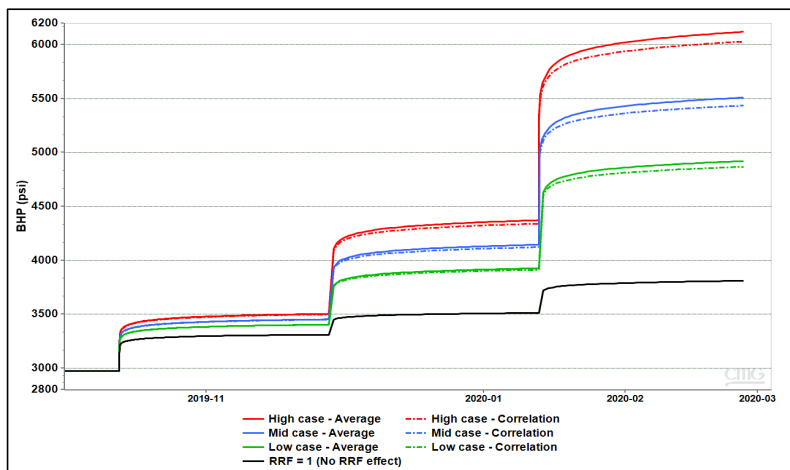


Figure 5.46: Impact of RRF scenarios on concentration stepping.
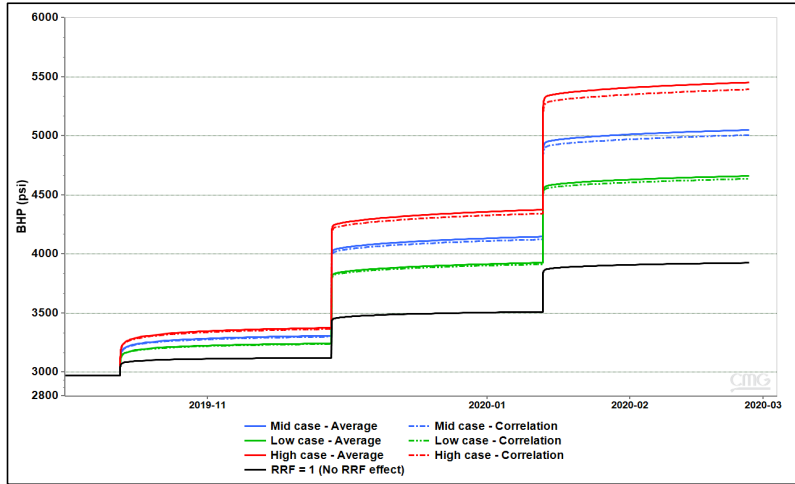
*Figure 5.47: Impact of RRF scenarios on rate stepping.*

It is evident from the simulations that both correlations and average values yield almost identical responses. This suggests that average RRF values can be used to replace correlations in the model to increase efficiency and simplify data input. Moreover, applied RRF does not affect the impact of rate and concentration stepping, where the impact of stepping up concentration shows significantly more pronounced transient effect that can be explained by the time it takes for the concentration to reach required levels.

The information gained from rate steps and concentration steps sensitivity at different rheological and RRF conditions were utilized alongside lab and field data in history matching actual polymer injection phase. Available field data of the polymer injection included daily records of injection rates, injected concentrations, and bottomhole pressure. In addition, as polymer solution was injected through a shearing device before entering wellbore, daily data of polymer degradation % from shearing and viscosity measurements before and after the choke of the device were also available. The polymer injection phase encompasses four main rate steps: 800, 1500, 2000 and 1500 bpd, as illustrated in Figure 5.48 below. The procedure included concentration stepping as well, which was implemented only in the first rate step of 800 bpd. Constant concentration was maintained for the second and third rate steps, while the last rate

step witnessed a gradual concentration tapering towards the end of polymer injection phase.
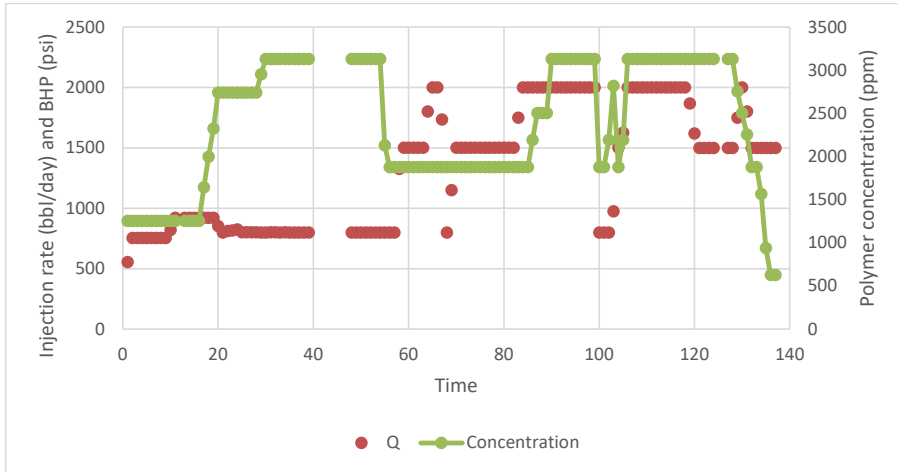


Figure 5.48: Summary of polymer concentrations used in the injectivity test with respective injection rates.

For polymer pre-shearing, the program procedure included a variety of polymer degradation levels ranging between 10% and 50% as shown in Figure 5.49. This practice is usually performed to improve polymer injectivity, however, it adds to the complexity of data analysis as it creates a variety of apparent concentration or rheology behaviors that have to be incorporated in the matching process. Beside pre-shearing data, viscosity measurements were conducted upstream the choke of shearing device for all injection rates. Downstream measurements were conducted as well but only for when the wellhead pressure was zero and the well is operating at vacuum. Downstream viscosities were estimated from a shearing device correlation for the periods at which wellhead pressure is not zero and measurements are thus not possible. Figure 5.50 shows viscosity data including upstream measurements and downstream measurements and estimations.

To account for the impact of degradation from pre-shearing, the model's inputs for injected polymer concentrations were adjusted using the daily data of degradation percentage at each injection rate. This practice allows flexible control of the rheological

behavior at apparent concentration levels and the incorporation of the impact of pre-shearing which was proven to have significant effect on shear-thickening onset and magnitude. Therefore, by adopting concentration adjustment using degradation, several in-situ rheology curves could be defined in the model to describe the impact of both pre-shearing and concentration stepping.
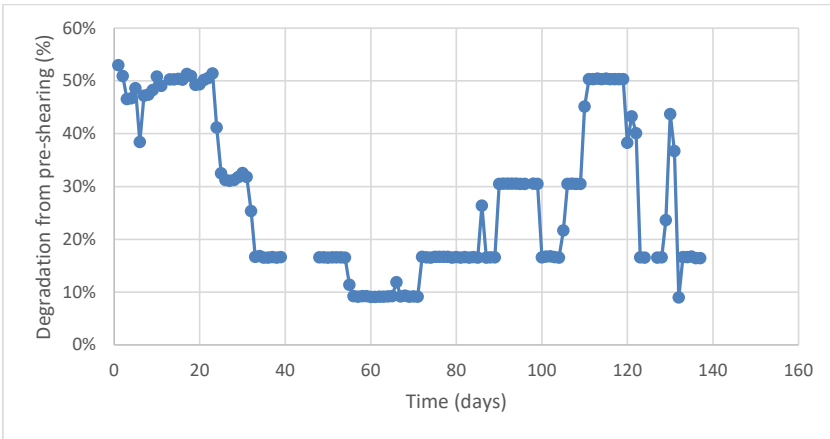


Figure 5.49: Percentage of degradation from pre-shearing applied on polymer solution prior to injection.
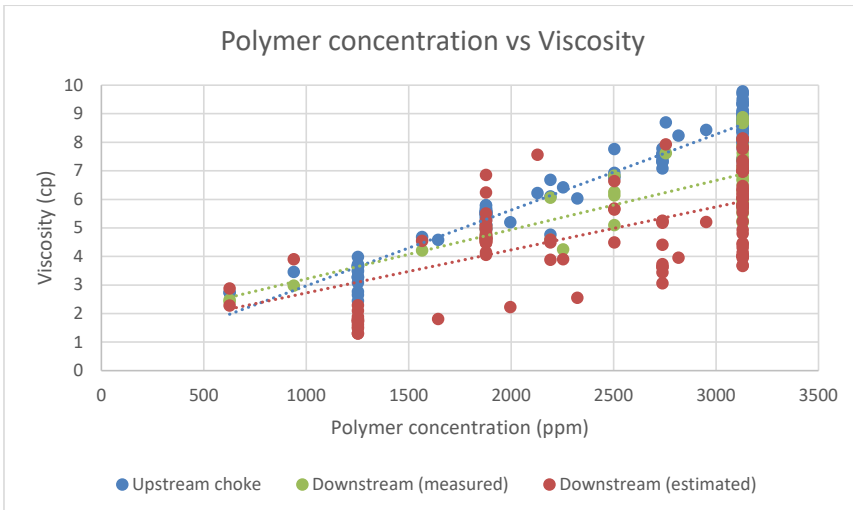


Figure 5.50: Polymer viscosity measurements across the shearing device choke and estimated downstream viscosities.

The next step in the analysis workflow employs earlier findings on the signatures that distinguish Newtonian rheological behavior from non-Newtonian. It is evident that non-Newtonian rheology results in a non-linear trend in the plots of bottomhole pressure versus injection rate, where the slope of the curve defines the viscosity behavior of the fluid. On the other hand, Newtonian flow reflects linear trend in such plots indicating constant viscosity across all injection rates. Besides, the transient time of pressure buildup observes longer periods in non-Newtonian compared to Newtonian.

Field bottomhole pressure data during water injection baseline and polymer injection phases were plotted against respective injection rates to compare pressure signatures of Newtonian and non-Newtonian flow, respectively. Injection rates during water injection baseline were highly fluctuating and pressure data is available for about half of the 13 months period (Figure 5.51).
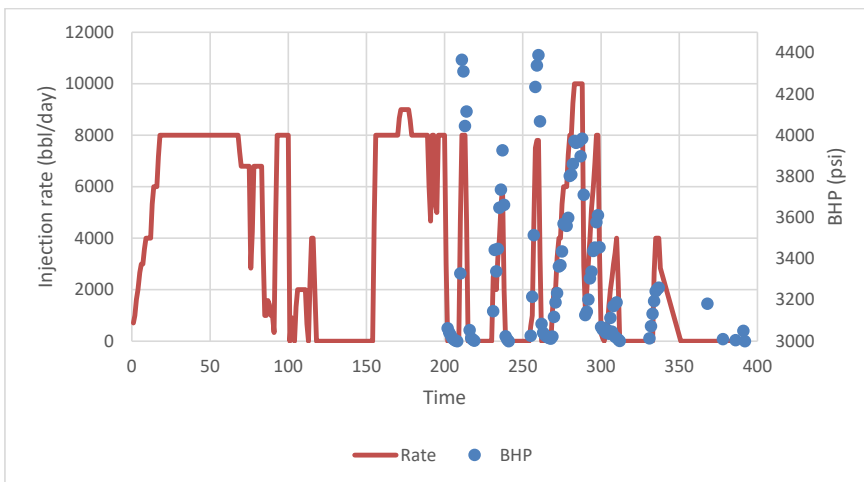


*Figure 5.51: Field data of injection rates and BHP during water injection baseline.*

Hence, a period of 20 days was selected for pressure analysis as it observed a steady rate stepping scheme of five rates steps between 2000 and 10000 bpd with clear pressure records (Figure 5.52). It is evident from pressure response to rate stepping that pressure stabilization occurs in short times of about one day only for each rate step, as

expected from Newtonian flow. Stabilized pressure data demonstrate a distinctive linear response when plotted against injection rate as shown in Figure 5.53.
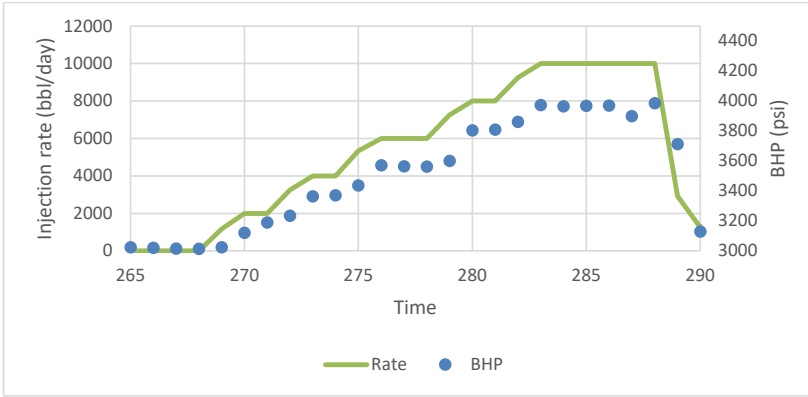


Figure 5.52: Segment of water injection baseline used for BHP analysis with rate steps.
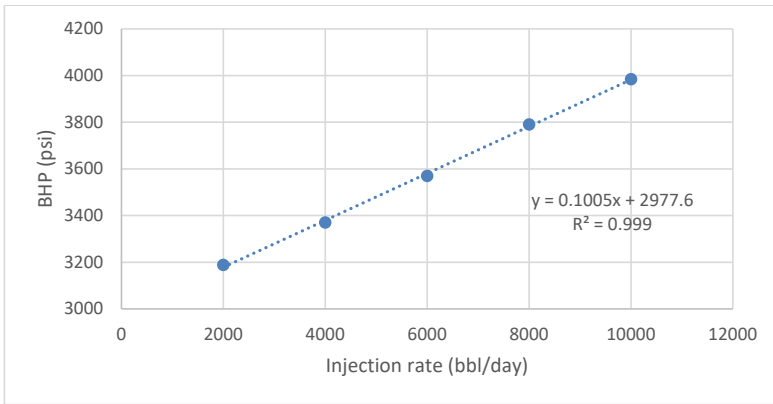


Figure 5.53: Plot of BHP versus injection rate for part of water injection baseline.

Similarly, bottomhole pressure data of the polymer injection phase rate steps were analyzed. Plots of bottomhole pressure versus injection rate at several different injected pore-volumes between 0.003 and 0.025 are presented in Figure 5.54. A distinctively clear shear-thickening signature of increasing slope is observed over all injected pore-volumes. This type of pressure response suggest that the polymer behavior exhibit higher viscosity at higher injection rates which is an indication of apparent shear-

thickening in the high velocity range. Moreover, bottomhole pressure buildup time for each injection rate is illustrated in Figure 5.55. The pressure buildup for 1500 and 2000 bpd rates shows a sharp increase as a signal of shear-thickening behavior. The pressure response at 800 bpd showed multiple behaviors where it has a moderate increase in the beginning followed by a sharper surge at later times. This is explained by the impact of low concentrations at the beginning where the rheology is likely observing near-Newtonian or even shear-thinning behavior. As concentration was stepped up, polymer behavior started exhibiting shear-thickening towards the end of the 800-bpd rate step.
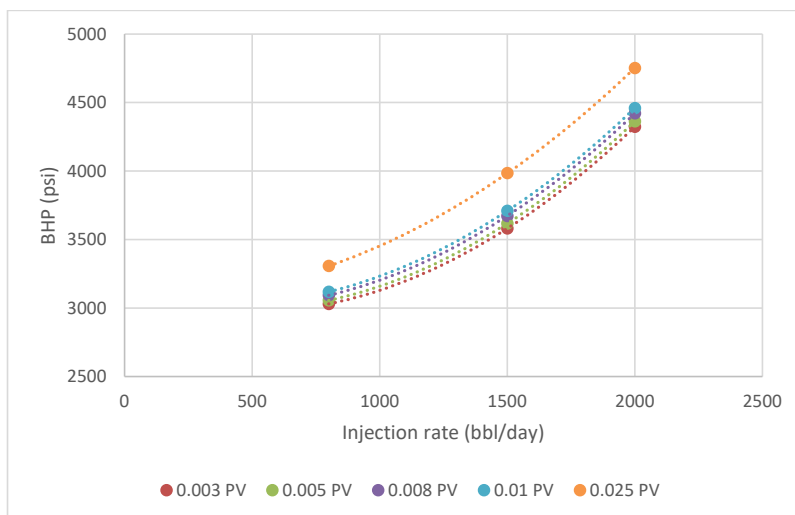


Figure 5.54: BHP versus injection rate for polymer injection at several pore-volumes.

By establishing shear-thickening behavior as the rheology most likely to have been encountered in the near-wellbore region during polymer injection, the consequent step was to investigate possible scenarios of shear-thickening. Three generic cases of shear-thickening were considered to encompass all possible scenarios. The cases assume that polymer behavior over encountered range of velocities in the near-wellbore region could see either shear-thickening only, shear-thickening at high velocities followed by Newtonian at low velocities, or a typical combined rheology behavior. Each case was represented by a rheology curve generated using extended Carreau model (Figure 5.56).
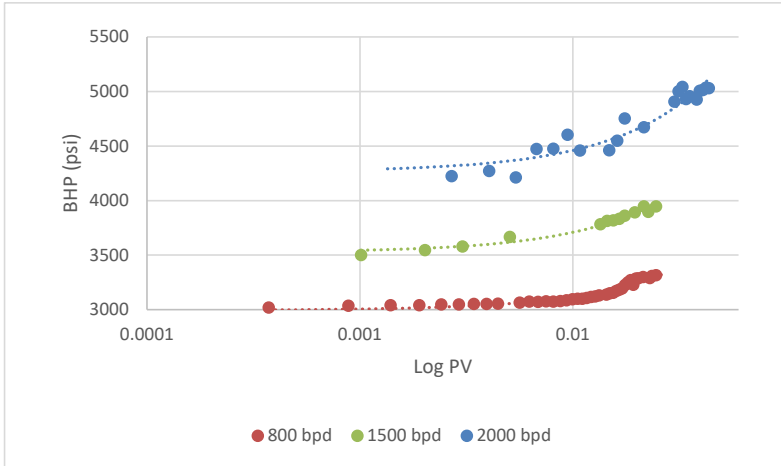
Figure 5.55: BHP versus log pore-volume at different injection rates.
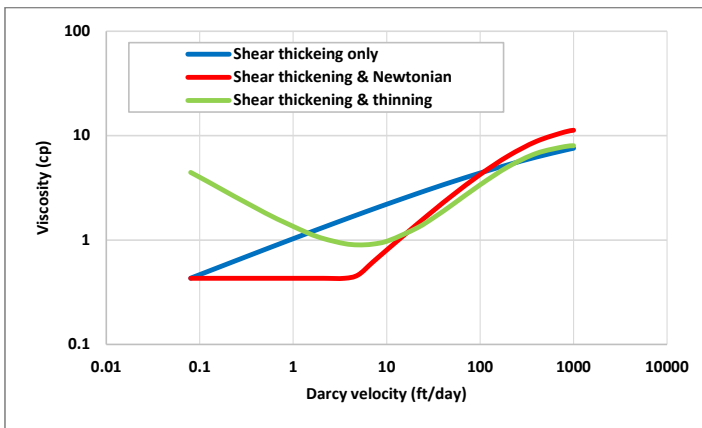


Figure 5.56: Shear thickening rheology scenarios tested for polymer injection history matching.

In each case, the rheology curve corresponds to a specific single concentration value which is set at the maximum concentration encountered in field application. For other concentration levels, IMEX simulator calculates water-polymer mixture velocity for each grid block and performs a two-dimensional interpolation to calculate relative polymer viscosity based on relative concentration. This essentially results in apparent parallel shifted rheology curves with the same slope for concentrations lower than maximum concentration.

The three cases were tested over the actual field injection rates and injected concentrations. Figure 5.57 below presents the results of bottomhole pressure simulation for each case. Although all cases have equal average viscosity over the velocity range, the highest pressure response is seen in the shear-thickening only case, followed by the combined rheology case, and the least pressure is seen in the case with Newtonian rheology. This could suggest that the main acting velocity range is actually between 1 to 100 ft/day, where the viscosity is higher for the shear thickening only case. The bottomhole pressure response over the entire period is overall following the polymer concentration level which is represented by injected polymer mass rate in Figure 5.57. Nonetheless, the pressure transient behavior for each case shows different behavior at different injection rates and concentrations. For example, each rheology case shows different trend for the gradual pressure increase towards the end of 800 bpd rate step. This behavior can be seen as well with different levels of clarity at several points where injection rate or concentration is changing.
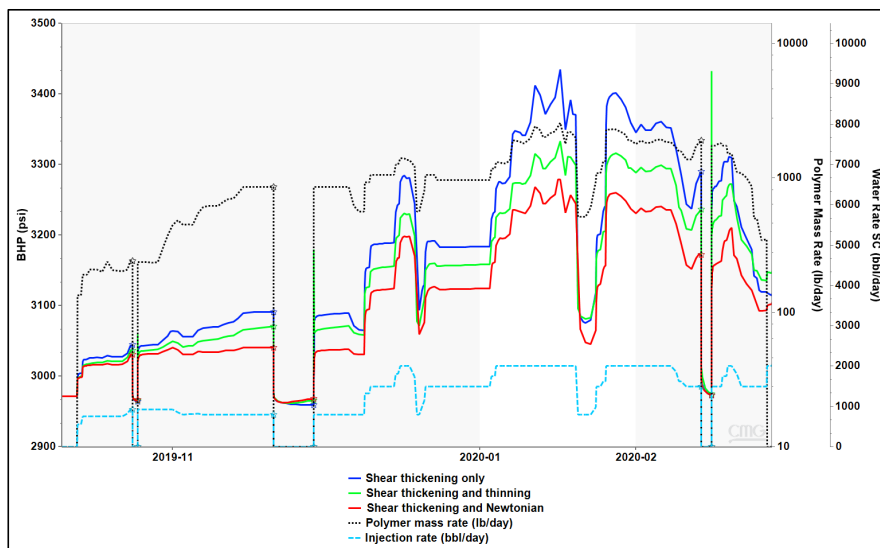


*Figure 5.57: BHP response of the shear thickening cases using actual field rates and concentrations.*

Outcomes of the generic sensitivity study demonstrate the ability of controlling pressure response by tuning in-situ rheology inputs to account for viscosity behavior at

different concentration levels. Consequently, and by considering above findings, manual history matching of pressure data resulted in obtaining satisfactory matching of the field bottomhole pressure data of polymer injection and chase water phases (Figure 5.58). The matching procedure took into consideration three main tuning parameters which are in-situ rheology, average RRF, and skin factor. For in-situ rheology, the pressure behavior was matched using a combination of five rheology curves representing five concentrations. The dominant rheological behavior is combined rheology where polymer exhibits shear-thickening at high velocities and thinning at low velocities. The impact of concentration is incorporated as a delay in the onset of shear thickening for lower concentration as well as lower viscosity values (Figure 5.59). Input rheology curves were constructed using extended Carreau model with the parameters shown in Table 5.8.
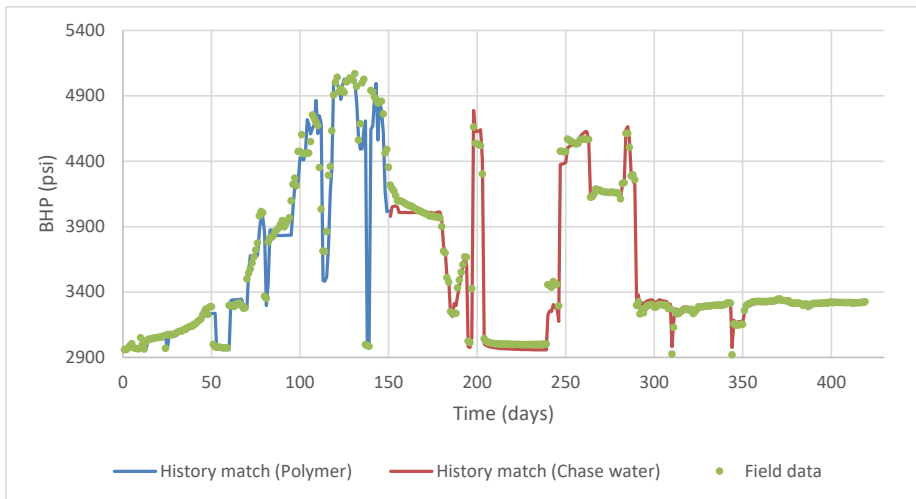
Figure 5.58: History matching BHP of polymer injection and chase water.

For RRF tuning, best matches for both polymer injection and chase water were obtained with an average RRF value of 4.1. This value corresponds to the weighted average RRF of the high case correlation proposed earlier depending on lab measurements. Moreover, skin factor tuning was found essential to simulate skin growth associated with polymer injection. This increasing skin impairment effect was detected through PFO analysis as mentioned earlier and is probably caused by filter

cake-like phenomenon caused by polymer invasion and is exclusive to the region immediately at and beyond sandface.
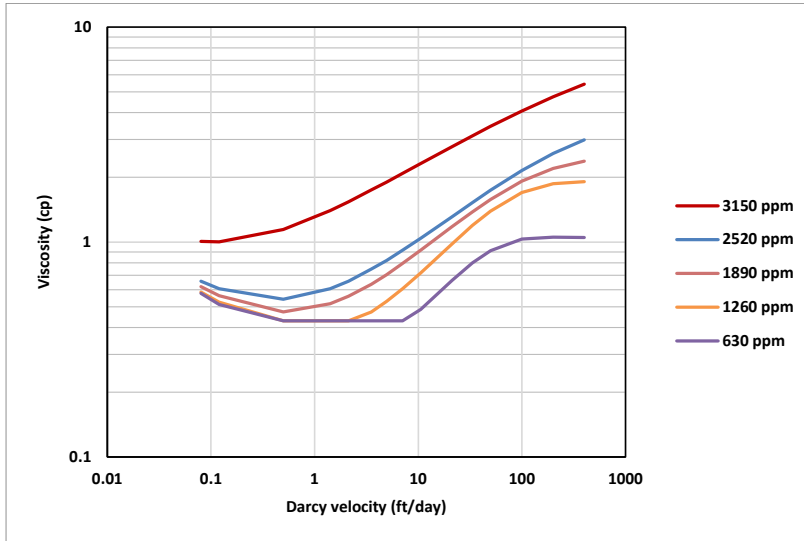


*Figure 5.59: Rheology curves used in history matching polymer injection.*

*Table 5.8: Extended Carreau equation parameters used to create matching rheology curves.*

|  | 3150 ppm | 2520 ppm | 1890 | 1260 ppm | 630 ppm |
|---|---|---|---|---|---|
| u | 0.1 to 400 ft/day | | | | |
| $\mu\_max$ | 17 | 8 | 5.5 | 4 | 2 |
| n2 | 1.36 | 1.52 | 1.6 | 1.75 | 2.2 |
| $\lambda 2$ | 1.2E+03 | 2.0E+03 | 4.0E+03 | 6.0E+03 | 1.0E+04 |
| $\mu\infty$ | 0.43 | | | | |
| $\mu 0$ | 2 | | | | |
| n1 | 0.5 | | | | |
| $\lambda 1$ | 1.00E+07 | | | | |

Dynamic skin was applied to the wellbore starting from -0.45 before polymer injection, up to +7.5 by the end of polymer injection. Upon the start of chase water injection, the skin impairment had to be reduced gradually to match pressure response. This confirms

the assumption that observed skin impairment is a temporary effect of polymer invasion which is washed away by chase water. Therefore, skin was gradually reduced during chase water to a value of 1.5 (Figure 5.60).
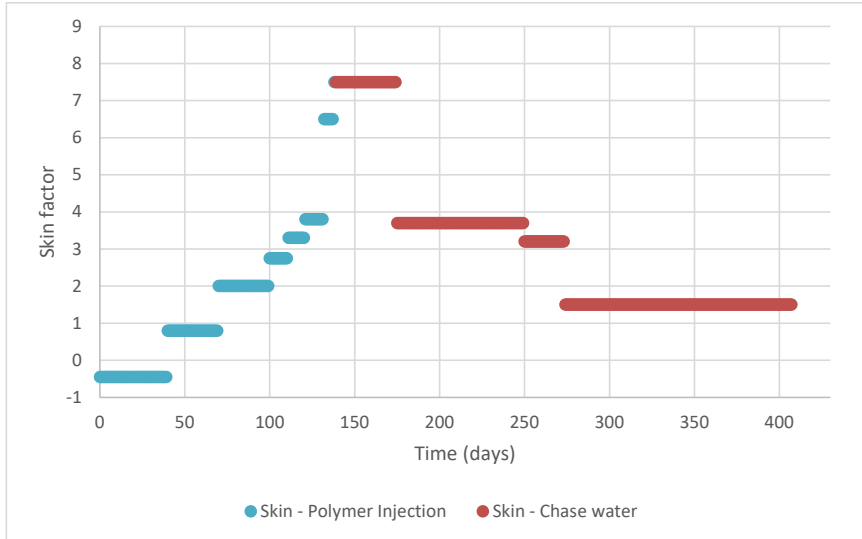


*Figure 5.60: Skin factor applied along polymer injection and chase water in history match.*

# 6. Conclusions and recommendations

The work performed to meet the objectives of this thesis comprised several numerical simulation studies on polymer flooding issues focusing mainly on flow behavior at adverse mobility conditions, and the impact of in-situ rheology on polymer injectivity. In this chapter, the conclusions of each of the main topics presented in chapter 5 are summarized. Besides, recommendations on way forward research suggestions and extensions are presented.

## 6.1 Conclusions

### 6.1.1 Modelling immiscible viscous fingering

Four 2D slab experiments of waterflooding at adverse mobility ratios were history matched using a conventional simulator, but a new approach relying mainly on modifying Buckley Leverett fractional flow function to assign higher shock front saturation. The main conclusion of this study was verifying the validity of this proposed methodology as a robust procedure to reproduce immiscible viscous fingering of unstable displacement using simple numerical scheme. The fingering patterns observed in the experiments were matched to a qualitatively adequate level from start of waterflood until water breakthrough. Besides, the proposed models had successfully matched production data of oil recovery and water cut within acceptable error margins.

Besides modifying fractional flow function, the selection of proper gridding size and proper permeability field deemed essential for adequate matching. The grid size is selected so it is lower than the dispersivity length for the corresponding slab dimensions. Moreover, permeability has to be defined through a randomly correlated field using a minimum and maximum permeability for the distribution and apply a correlation length for the local permeability. The correlation length of the distribution function is tuned for the required amount and width of observed fingers.

It was evident from the results that there is a relationship between oil viscosity and the shock front saturation required to mimic the fingers. As oil viscosity increases, the

difference between the saturation inside and outside the fingers is reducing, which means lower front saturation. The suggested explanation is the fact that injected water forms thinner, weaker, and faster fingers for higher oil viscosity cases which decreases the saturation buildup within fingers and causes earlier water breakthrough.

## 6.1.2 Impact of in-situ rheology on injectivity

Numerical history matching studies on lab scale models have established the ability of estimating polymer in-situ rheology from bottomhole pressure data at different injection rates. The results of lab scale history matching also included a proof of the robustness of utilizing differential pressure data from internal ports to obtain rheological behavior. Nevertheless, data available in field applications are usually limited and the most common type of obtainable data is usually bottom-hole pressure exclusively. Thus, an up-scaled field model was tested over several generic HPAM rheological behaviors, that are anticipated to occur in the near wellbore region. It was evident that the pressure response for each rheology reflects a unique signature in terms of both build up time, and the slope of stabilized pressures versus corresponding injection rates. Besides, non-Newtonian behavior of polymer can be clearly distinguished from that of Newtonian behavior. This is important for the analysis of field data to detect the type of viscosity behavior the polymer exhibits in the near wellbore region in order to calibrate injectivity estimations accordingly. Signature of rheology impact on bottomhole pressure is seen as an increasing slope on the pressure versus rate graph for shear thickening, and a decreasing slope for the shear thinning behavior. The signature of a combined rheology is dominated by shear thickening closer to the injection point compared to shear thinning which occurs at further distance from the well. The pressure buildup time signature can be utilized to distinguish combined rheology which exhibits a buildup trend that shows both characteristics of thickening and thinning. Build up time for a polymer showing only shear thickening is much shorter and sharper when compared to a shear thinning polymer.

The above findings were further assessed to come up with particular general guidelines to optimize the design of polymer injectivity tests. It was concluded that systematic

rate variation is an extremely essential element that have to be included in the injectivity test procedure. By applying controlled rate variations over sufficient amount of time, bottomhole pressure data would turn to a highly valuable source of information to understand polymer viscosity behavior.

A minimum of three rate steps must be considered in the test procedure with the rates carefully selected to cover the entire expected range of Darcy velocities in the reservoir. Moreover, the duration of each rate step has to be sufficient in terms of having equal injected pore volumes for each rate step. Optimal results can be obtained at the injection of at least one pore volume for each rate step, however, shorter periods for as low as 0.0001 PV were found to produce the same distinctive rheology signatures that can still be utilized for analysis, given that equal pore volumes are injected for each rate step.

Furthermore, although the above findings were obtained for homogenous models, the same signatures were found to be applicable for vertically heterogenous models, but with less pronounced signals. This concludes that the above guidelines can be considered for heterogenous reservoirs as well.

### 6.1.3 Field polymer injectivity test analysis

The conclusions presented here are related to the analysis of a field polymer injectivity test that was conducted in an Abu Dhabi carbonate reservoir. The analysis was partially based on the preliminary conclusions presented in 6.1.2 which were found from generic simulation studies on the impact of in-situ rheology on polymer injectivity. The main objective was to confirm the applicability of utilizing injectivity test pressure data to predict polymer in-situ rheology and thus improve quality of history matching by fine tuning viscosity inputs in the model.

Firstly, the uncertainty in near-well vertical permeability distribution can be vitally reduced by tuning permeability multipliers to match available production logging tool (PLT) data. This practice proved to be essential to establish reliable permeability inputs in the model during water injection baseline phase and prior to polymer injection. Secondly, although the model observed extreme cyclic layering and heterogeneity, the

distinctive signature of non-Newtonian viscosity behavior could be clearly distinguished from an alternative Newtonian behavior through pressure build up duration. The pressure transient time to establish steady state for non-Newtonian injection is significantly longer compared to Newtonian injection. This confirms the preliminary conclusions of the practicality of using bottomhole pressure in predicting in-situ polymer rheology. Moreover, the sensitivity to rate stepping and concentration stepping showed different impact on the pressure response. Concentration stepping found to have gradual pressure response in the simulator compared to the sharper increase observed with rate steps. Furthermore, using a permeability dependent RRF (residual resistance factor) correlation did not have significant impact on pressure response compare to using average RRF value. It was concluded that including RRF as an average value corrected to weighted average formation capacity can reduce model input complexity without risking outcome quality.

Following above conclusions, systematic analysis of bottomhole pressure data was carried out to predict polymer in-situ rheology in the near wellbore region and validate it by history matching data. Plotting stabilized rate-stepped bottomhole pressure data have confirmed the impact on non-Newtonian non-linear pressure trend compared to the Newtonian linear behavior. The analysis of bottomhole pressure data in the polymer injection phase led to detecting shear-thickening behavior in the near-well bore region. Consequently, a sensitivity analysis to investigate several different scenarios of shear-thickening was performed, and it was concluded that the history match should involve a combined rheology input at different concentration levels. The bottomhole pressure of polymer injection phase was then conclusively matched with a set of five rheology curve at five different concentration levels. It was found that degradation from polymer pre-shearing prior to injection can be represented by assigning different concentration levels corresponding to the degree of degradation (percentage).

The main outcome of this study was the proof of the capability of utilizing actual polymer injectivity field pressure data to improve the interpretation of injectivity test results by enhancing the prediction of polymer in-situ rheology at reservoir conditions.

## 6.2 Recommendations for future research

The mechanisms that govern polymer flow in porous media have been studied for decades with several breakthroughs in the past few years. Nonetheless, there yet to be many topics that need more attention and research to build a better understanding of polymer behavior and thus optimize polymer flooding practices and maximize their benefits. The following suggestions are related to the topics discussed in this thesis.

Modelling of immiscible viscous fingering observed in flooding in heavy oil reservoirs, could be improved by adopting lab experiments that consider various extra conditions. Designing experiments with different geometries, rock types, or petrophysical features could provide much more insights and data to improve the overall understanding of the phenomena.

With regard to polymer in-situ rheology, radial injectivity experimental data have shown significant deviation from typical linear-core data. Hence, the implementation of radial geometry in injectivity experiments at varying conditions and rock types, may reveal valuable data that can be utilized to enhance the prediction of polymer viscosity behavior in porous media.

The analysis of polymer injectivity field data could be significantly improved if field practices were modified to strictly follow a stable and well-defined procedure. The information gained from field applications are highly affected by noise resulting from large variations. Hence, it is essential to identify the key reliable information in the large noise of information from the field observations.

# References

Afsharpoor, A. & Balhoff, M. (2013): *Static and Dynamic CFD Modeling of Viscoelastic Polymer: Trapped Oil Displacement and Deformation at the Pore-Level*. Presented at the SPE Annual Technical Conference and Exhibition, New Orleans, Louisiana, USA, 30 September - 2 October 2013. https://doi.org/10.2118/166114-MS.

Akstinat, M. H. (1980): *Polymers for Enhanced Oil Recovery In Reservoirs Of Extremely High Salinities And High Temperatures*. Paper presented at the SPE Oilfield and Geothermal Chemistry Symposium, Stanford, California, May 1980. doi: https://doi.org/10.2118/8979-MS

Al-Bahar, M. A., Merrill, R., Peake, W., Jumaa, M., & Oskui, R. (2004): *Evaluation of IOR Potential within Kuwait*. Paper presented at the Abu Dhabi International Conference and Exhibition, Abu Dhabi, United Arab Emirates. doi: https://doi.org/10.2118/88716-MS

Alfazazi, U., AlAmeri, W., & Hashmet, M.R. (2018): *Screening of New HPAM Base Polymers for Applications in High Temperature and High Salinity Carbonate Reservoirs*. Paper presented at the Abu Dhabi International Petroleum Exhibition & Conference, Abu Dhabi, UAE. doi: https://doi.org/10.2118/192805-MS

Al-Saadi, F.S., Amri, B.A., Nofli, S., Van Wunnik, J., Jaspers, H.F., Harthi, S., Shuaili, K., Cherukupalli, P.K., & Chakravarthi, R. (2012): *Polymer Flooding in a Large Field in South Oman - Initial Results and Future Plans*. Paper presented at the SPE EOR Conference at Oil and Gas West Asia, Muscat, Oman, April 2012. doi: https://doi.org/10.2118/154665-MS.

Al-Shakry, B., Skauge, T., Shiran, B. S. & Skauge, A. (2018): *Impact of Mechanical Degradation on Polymer Injectivity in Porous Media*, Polymers, Vol. 10: 1-23. https://doi.org/10.3390/polym10070742.

Al-Shakry, B., Skauge, T., Shiran, B. S. & Skauge, A. (2019): *Polymer Injectivity: Investigation of Mechanical Degradation of Enhanced Oil Recovery Polymers*

*Using In-Situ Rheology*, Energies, Vol. 12: 1-25.
https://doi.org/10.3390/en12010049.

Arya, A. (1986): *Dispersion and reservoir heterogeneity.* PhD dissertation, Univ. of
Texas, Austin.

Azad, M. S. & Trivedi, J. J. (2017): *Injectivity Behavior of Copolymer and
Associative Polymer Decoded Using Extensional Viscosity Characterization:
Effect of Hydrophobic Association*. Presented at the SPE Western Regional
Meeting, Bakersfield, California, 21-23 April 2017.
https://doi.org/10.2118/185668-MS.

Bekbauov, B., Berdyshev, A., Baishemirov, Z. & Bau, D. (2017): *Numerical
Validation of Chemical Compositional Model for Wettability Alteration
Processes*. Open Engineering, vol. 7, no. 1, 2017, pp. 416-427.
https://doi.org/10.1515/eng-2017-0049.

Berdugo-Clavijo, C., Sen, A., Seyyedi, M., Quintero, H., O'Neil, B., & Gieg, L.M.
(2019): *High temperature utilization of PAM and HPAM by microbial
communities enriched from oilfield produced water and activated sludge*.
AMB Expr 9, 46. https://doi.org/10.1186/s13568-019-0766-9.

Bondor, P.L., Hirasaki, G.J., & Tham, M.J. (1972): *Mathematical Simulation of
Polymer Flooding in Complex Reservoirs*. SPE J. 12 (1972): 369–382. doi:
https://doi.org/10.2118/3524-PA.

Briggs, P., Baron, P.R., Fulleylove, R. & Wright,. (2013): *Development of Heavy-Oil
Reservoirs.* Journal of Petroleum Technology. 40. 206-214.
https://doi.org/10.2118/15748-PA.

Broseta, D., Medjahed, F., Lecourtier, J. & Robin, M. (1995): *Polymer
Adsorption/Retention in Porous Media: Effects of Core Wettability and
Residual Oil*. Society of Petroleum Engineers Advanced Technology Series.
Vol. 3: 103-112. https://doi.org/10.2118/24149-PA.

Carreau, P.J., MacDonald, I.F., & Bird, R.B. (1968): *A nonlinear viscoelastic model
for polymer solutions and melts—II*, Chemical Engineering Science, Volume

23, Issue 8, Pages 901-911, ISSN 0009-2509, https://doi.org/10.1016/0009-2509(68)80024-7.

Chauveteau, G. (1981): *Molecular Interpretation of Several Different Properties of Flow of Coiled Polymer Solutions Through Porous Media in Oil Recovery Conditions*. Presented at the SPE Annual Technical Conference and Exhibition, San Antonio, Texas, USA, 4-7 October 1981. https://doi.org/10.2118/10060-MS.

Chauveteau, G., Tirrell, M. & Omari, A. (1984): *Concentration Dependence of the Effective Viscosity of Polymer Solutions in Small Pores with Repulsive or Attractive Walls*, Journal of Colloid and Interface Science, Vol. 100: 41-54. https://doi.org/10.1016/0021-9797(84)90410-7.

Chen, Z., Du, C., Kurnia, I., Lou, J., Zhang, G., Yu, J. & Lee, R. L. (2016): *A Study of Factors Influencing Polymer Hydrodynamic Retention in Porous Media*. Presented at the SPE Improved Oil Recovery Conference, Tulsa, Oklahoma, USA, 11-13 April 2016. https://doi.org/10.2118/179607-MS.

Choplin, L., & Sabatie, J. (1986): *Threshold-Type Shear-Thickening in Polymeric Solutions*. Rheol. Acta 1986, 25, 570–579.

Christie, M.A., & D.J. Bond. (1987): *Detailed Simulation of Unstable Processes in Miscible Flooding*. SPE Reservoir Engineering 2: 514–522. https://doi.org/10.2118/14896-PA.

Chuoke, R.L., Van Meurs, P., & Van Der Poel, C. (1959): *The Instability of Slow, Immiscible, Viscous Liquid-Liquid Displacements in Permeable Media*. In: Transactions of the American Institute of Mining, Metallurgical, and Petroleum Engineers: Petroleum Development and Technology 1959, ed.Vol.216, SPE-1141-G, 188–194. Dallas, Texas: Society of Petroleum Engineers.

Civan, F. (2007): *Reservoir Formation Damage (Fundamentals, Modeling, Assessment, and Mitigation)*, 2nd edition. Gulf Professional Publishing, Oxford

Clark, N. J. (1969): *Elements of Petroleum Reservoirs*, Monograph (SPE of AIME): Henry L. Doherty series.

Clarke, A., Howe, A. M., Mitchell, J., Staniland, J. & Hawkes, L. A. (2016): *How Viscoelastic-Polymer Flooding Enhances Displacement Efficiency*. Society of Petroleum Engineers Journal, Vol. 21: 675-687. https://doi.org/10.2118/174654-PA.

Computer Modelling Group (2020a): *IMEX User Guide: Black Oil Reservoir Simulator*, Calgary, Alberta, Canada.

Computer Modelling Group (2020b): *STARS User Guide: Advanced Processes & Thermal Reservoir Simulator*, Calgary, Alberta, Canada.

Computer Modelling Group (2020c): *CMOST-AI User Guide: Intelligent Optimization & Analysis Tool*, Calgary, Alberta, Canada.

Computer Modelling Group Ltd. (CMG). (2021): *https://www.cmgl.ca/* (Accessed Feb 2021).

Davison, P., & Mentzer, E. (1982): *Polymer Flooding in North Sea Reservoirs*. SPE J. 22 353–362. doi: https://doi.org/10.2118/9300-PA

Dawson, R. & Lantz, R. B. (1972): *Inaccessible Pore Volume in Polymer Flooding*, Society of Petroleum Engineers Journal, Vol. 12: 448-452. https://doi.org/10.2118/3522-PA.

De Simoni, M., Boccuni, F., Sambiase, M., Spagnuolo, M., Albertini, M., Tiani, A. & Masserano, F. (2018): *Polymer Injectivity Analysis and Subsurface Polymer Behavior Evaluation*. Presented at the SPE EOR Conference at Oil and Gas West Asia, Muscat, Oman, 26-28 March 2018. https://doi.org/10.2118/190383-MS.

Degennes, P.G. (1974): *Coil-Stretch Transition of Dilute Flexible Polymers under Ultrahigh Velocity Gradients*. J. Chem.Phys. 60, 5030–5042.

Delamaide, E., Tabary, R., Renard, G. & Dwyer, P. (2014): *Field Scale Polymer Flooding of Heavy Oil: the Pelikan Lake Story*. Presented at the 21st World Petroleum Congress, Moscow, Russia, 15-19 June 2014.

Delshad, M., Kim, D. H., Magbagbeola, O. A., Huh, C., Pope, G. A. & Tarahhom, F. (2008): *Mechanistic Interpretation and Utilization of Viscoelastic Behavior of Polymer Solutions for Improved Polymer-Flood Efficiency*. Presented at the SPE Symposium on Improved Oil Recovery, Tulsa, Oklahoma, USA, 20-23 April 2008. https://doi.org/10.2118/113620-MS.

Detling, K.D., Shell Development Co. (1944): *Process of recovering oil from oil sands*. U.S. Patent 2,341,500.

Dominguez, J. G. & Willhite, G. P. (1977): *Retention and Flow Characteristics of Polymer Solutions in Porous Media*. Society of Petroleum Engineers Journal, Vol. 17: 111-121. https://doi.org/10.2118/5835-PA.

Dupas, A., Henaut, I., Rousseau, D., Poulain, P., Tabary, R., Argillier, J. F. & Aubry, T. (2013): *Impact of Polymer Mechanical Degradation on Shear and Extensional Viscosities: Towards Better Injectivity Forecasts in Polymer Flooding Operations*. Presented at the SPE International Symposium on Oilfield Chemistry, The Woodlands, Texas, USA, 8-10 April 2013. https://doi.org/10.2118/164083-MS.

Dupuis, G., Antignard, S., Giovannetti, B., Gaillard, N., Jouenne, S., Bourdarot, G., Morel, D., & Zaitoun, A. (2017): *A New Thermally Stable Synthetic Polymer for Harsh Conditions of Middle East Reservoirs. Part I. Thermal Stability and Injection in Carbonate Cores*. Paper presented at the Abu Dhabi International Petroleum Exhibition & Conference, Abu Dhabi, UAE. doi: https://doi.org/10.2118/188479-MS

Engelberts, W.F., & Klinkenberg L.J. (1951): *Laboratory Experiments on the Displacement of Oil by Water from Packs of Granular Material*. Paper presented at the 3rd World Petroleum Congress, The Hague, the Netherlands, May 1951.

Erincik, M. Z., Qi, P. , Balhoff, M. T., & Pope, G.A. (2018): *New Method To Reduce Residual Oil Saturation by Polymer Flooding*. SPE Journal 23: 1944–1956. doi: https://doi.org/10.2118/187230-PA.

Gbadamosi, A.O., Junin, R., Manan, M.A., Agi, A., & Yusuff, A.S. (2019): *An overview of chemical enhanced oil recovery: recent advances and prospects*. Int Nano Lett 9, 171–202. https://doi.org/10.1007/s40089-019-0272-8

Glasbergen, G., Wever, D., Keijzer, E. & Farajzadeh, R. (2015): *Injectivity Loss in Polymer Floods: Causes, Preventions and Mitigations*. Presented at the SPE Kuwait Oil and Gas Show and Conference, Mishref, Kuwait, 11-14 October 2015. https://doi.org/10.2118/175383-MS.

Gogarty, W. B. (1967): *Mobility Control with Polymer Solutions*. Society of Petroleum Engineers Journal, Vol. 7: 161-173. https://doi.org/10.2118/1566-B.

Gooch, J.W. (Ed.), (2007): *Encyclopedic Dictionary of Polymers*. Springer, New York, NY, 781-781. https://doi.org/10.1002/app.13403.

Goudarzi, A., Delshad, M., & Sepehrnoori, K. (2013): *A Critical Assessment of Several Reservoir Simulators for Modeling Chemical Enhanced Oil Recovery Processes*. Paper presented at the SPE Reservoir Simulation Symposium, The Woodlands, Texas, USA, February 2013. doi: https://doi.org/10.2118/163578-MS.

Heemskerk, J., Rosmalen, R., Janssen-van, R., Holtslag, R. J. & Teeuw, D. (1984): *Quantification of Viscoelastic Effects of Polyacrylamide Solutions*. Presented at the SPE Enhanced Oil Recovery Symposium, Tulsa, Oklahoma, USA, 15-18 April 1984. https://doi.org/10.2118/12652-MS.

Hill, S. (1952). *Channeling in packed columns*. Chemical Engineering Science, 1(6), 247-253.

Hirsch, R. L., Bezdek, R., & Wendling, R. (2005): *Peaking of World Oil Production: Impacts, Mitigation, and Risk Management*. United States: N. p. Web. https://doi.org/10.2172/939271.

Homsy, G.M. (1987): *Viscous Fingering in Porous Media*. Annual Review of Fluid Mechanics Vol.19:271-311. https://doi.org/10.1146/annurev.fl.19.010187.001415.

Jacobsen, J. G., Alzaabi, M., Skauge, T., Sorbie, K. & Skauge, A. (2019): *Analysis and Simulation of Polymer Injectivity*. Presented at the 20th European Symposium on Improved Oil Recovery, Pau, France, 8-11 April.

Jiang, H., Wu, W., Wang, D., Zeng, Y., Zhao, S. & Nie, J. (2008): *The Effect of Elasticity on Displacement Efficiency in the Lab and Results of High Concentration Polymer Flooding in the Field*. Presented at the 2008 SPE Annual Technical Conference and Exhibition, Denver, Colorado, USA, 21-24 September 2008. https://doi.org/10.2118/115315-MS.

Jouenne, S. (2020): *Polymer Flooding in High Temperature, High Salinity Conditions: Selection of Polymer Type and Polymer Chemistry, Thermal Stability*. Journal of Petroleum Science and Engineering, 195, https://doi.org/10.1016/j.petrol.2020.107545.

Kelly, P. (2013): *Solid mechanics part I: An introduction to solid mechanics*. Solid mechanics lecture notes, University of Auckland.

Knight, G.J. & Wright, W.W. (1973): *Thermal stability studies on vinylidene fluoride/hexafluoropropene copolymers*. Brit. Poly. J., 5: 395-411. https://doi.org/10.1002/pi.4980050507

Kokal, S. & Al-Kaabi, A. (2010): *Enhanced oil recovery: challenges & opportunities*. World Petroleum Council: Official Publication 2010. 64 – 69.

Kwon, S., Fan, M., Dacosta, H., Armistead, R., Berchtold, K. & Manvendra, D. (2011): *Chapter 10 - CO2 Sorption*. In book: Coal Gasification and Its Applications (pp.293-339) Publisher: William Andrew Publishing https://doi.org/10.1016/B978-0-8155-2049-8.10010-5.

Lake, L. W., Johns, R., Rossen, B. & Pope, G. (2014): *Fundamentals of Enhanced Oil Recovery*. New Jersey, USA: Society of Petroleum Engineers.

Li, Z. & Delshad, M. (2014): *Development of an Analytical Injectivity Model for Non-Newtonian Polymer Solutions*. Society of Petroleum Engineers Journal, Vol. 19: 381-389. https://doi.org/10.2118/163672-PA.

Lotfollahi, H., Farajzadeh, R., Delshad, M., Al-Abri, A., Wassing, B. M., Al-Mjeni, R., Awan, K. & Bedrikovetsky, P. (2016): *Mechanistic Simulation of Polymer*

*Injectivity in Field Tests*. Society of Petroleum Engineers Journal, Vol. 21: 1178-1191. https://doi.org/10.2118/174665-PA.

Maerker, J. M. (1975): *Shear Degradation of Partially Hydrolyzed Polyacrylamide Solutions*. Society of Petroleum Engineers Journal, Vol. 15: 311-322. https://doi.org/10.2118/5101-PA.

Manichand, R. N., Let, K. P. M. S., Gil, L., Quillien, B. & Seright, R. S. (2013): *Effective Propagation of HPAM Solutions Through the Tambaredjo Reservoir During a Polymer Flood*. Society of Petroleum Engineers Production & Operations, Vol. 28: 358-368. https://doi.org/10.2118/164121-PA.

Manrique, E., Ahmadi, M. & Samani, S. (2017): *Historical and Recent Observations in Polymer Floods: An Update Review*. CT&F- Ciencia, Tecnología y Futuro, 6(5). 17-48.

Martin, F.D., Hatch, M.J., Shepitka, J.S., & Ward, J.S. (1983): *Improved Water-Soluble Polymers for Enhanced Recovery of Oil*. Paper presented at the SPE Oilfield and Geothermal Chemistry Symposium, Denver, Colorado. doi: https://doi.org/10.2118/11786-MS

Masalmeh, S. K., Wei, L., Hillgartner, H., Al-Mjeni, R., & Blom, C. (2012): *Developing High Resolution Static and Dynamic Models for Waterflood History Matching and EOR Evaluation of a Middle Eastern Carbonate Reservoir*. Paper presented at the Abu Dhabi International Petroleum Conference and Exhibition, Abu Dhabi, UAE, November 2012. https://doi.org/10.2118/161485-MS.

Masalmeh, S., AlSumaiti, A., Gaillard, N., Daguerre, F., Skauge, T., & Skuage, A. (2019): *Extending Polymer Flooding Towards High-Temperature and High-Salinity Carbonate Reservoirs*. Paper presented at the Abu Dhabi International Petroleum Exhibition & Conference, Abu Dhabi, UAE. doi: https://doi.org/10.2118/197647-MS

Masuda, Y., Tang, K., Miyazawa, M. & Tanaka, S. (1992): *1D Simulation of Polymer Flooding Including the Viscoelastic Effect of Polymer Solution*. Society of Petroleum Engineers Reservoir Engineering, Vol. 7: 247-252. https://doi.org/10.2118/19499-PA.

Mezger, T. G. (2011): *The Rheology Handbook*. European Coatings Tech Files, 3rd revised edition.

Morris, C. W. & Jackson, K. M. (1978): *Mechanical Degradation of Polyacrylamide Solutions in Porous Media*. Presented at the SPE Symposium on Improved Methods of Oil Recovery, Tulsa, Oklahoma, USA, 16-17 April 1978. https://doi.org/10.2118/7064-MS.

Mungan, N., Smith, F. W. & Thompson, J. L. (1966): *Some Aspects of Polymer Floods*. Journal of Petroleum Technology, Vol. 18: 1143-1150. https://doi.org/10.2118/1628-PA.

Noïk, C., Delaplace, P. & Muller, G. (1995): *Physico-Chemical Characteristics of Polyacrylamide Solutions after Mechanical Degradation through a Porous Medium*. Presented at the SPE International Symposium on Oilfield Chemistry, San Antonio, Texas, USA, 14-17 February 1995. https://doi.org/10.2118/28954-MS.

Odell, J. A., Müller, A. J. & Keller, A. (1988): *Non-Newtonian behavior of hydrolysed polyacrylamide in strong elongational flows: a transient network approach*. Polymer, Vol. 29: 1179-1190. https://doi.org/10.1016/0032-3861(88)90042-0.

Palaniraj, Aa., & Jayaraman, V. (2011): *Production, Recovery and Applications of Xanthan gum by Xanthomonas campestris*. Journal of Food Engineering. 106. 1-12. https://doi.org/10.1016/j.jfoodeng.2011.03.035.

Peters, E., Broman W. Jr., Broman, J., et al. (1984): In SPE Annual Technical Conference and Exhibition. Society of Petroleum Engineers.

Peters, E.J., & Flock, D.L. (1981): *The Onset of Instability During Two-Phase Immiscible Displacement in Porous Media*. SPE J. 21 (1981): 249–258. https://doi.org/10.2118/8371-PA.

Polymer Data Base (2021): *https://polymerdatabase.com/* (Accessed Feb 2021).

Pye, D. J. (1964): *Improved Secondary Recovery by Control of Water Mobility*. Journal of Petroleum Technology, Vol. 16: 911-916. https://doi.org/10.2118/845-PA.

Qi, P., Ehrenfriend, D. H., Koh, H. & Balhoff, M. T. (2017): *Reduction of Residual Oil Saturation in Sandstone Cores by Use of Viscoelastic Polymers*, Society of Petroleum Engineers Journal, Vol. 22: 447-458. https://doi.org/10.2118/179689-PA.

Rodriguez, F., Rousseau, D., Bekri, S., Djabourov, M. & Bejarano, C. (2014): *Polymer Flooding for Extra-Heavy Oil: New Insights on the Key Polymer Transport Properties in Porous Media*. Presented at the SPE International Heavy Oil Conference and Exhibition, Mangaf, Kuwait, 8-10 December 2014. https://doi.org/10.2118/172850-MS.

Saffman, P.G., & Taylor, G.I. (1958): *The penetration of a fluid into a porous medium or Hele-Shaw cell containing a more viscous liquid*. Proc. R. Soc. Lond. A245312–329 http://doi.org/10.1098/rspa.1958.0085

Sandiford, B. B. (1964): *Laboratory and Field Studies of Water Floods Using Polymer Solutions to Increase Oil Reservoirs*. Journal of Petroleum Technology, Vol. 16: 917-922. https://doi.org/10.2118/844-PA.

Sandvik, E. I., & Maerker, J. M. (1977): *Extracellular Microbial Polysaccharides*. 242-264 https://doi.org/10.1021/bk-1977-0045. ch019

Saramito, P. (2016): *Quasi-Newtonian Fluids*. In: Complex fluids. Mathématiques et Applications, vol 79. Springer, Cham. https://doi.org/10.1007/978-3-319-44362-1_2

Seright, R. S. (1983): *The Effects of Mechanical Degradation and Viscoelastic Behavior on Injectivity of Polyacrylamide Solutions*. Society of Petroleum Engineers Journal, Vol. 23: 475-485. https://doi.org/10.2118/9297-PA.

Seright, R. S. (2010): *Potential for Polymer Flooding Reservoirs with Viscous Oils*. Society of Petroleum Engineers Reservoir Evaluation & Engineering, Vol. 13: 730-740. https://doi.org/10.2118/129899-PA.

Seright, R. S., Fan, T., Wavrik, K. & Balaban, R. d. C. (2011): *New Insights into Polymer Rheology in Porous Media*. Society of Petroleum Engineers Journal, Vol. 16: 35-42. https://doi.org/10.2118/129200-PA.

Seright, R. S., Seheult, J. M. & Talashek, T. (2009): *Injectivity Characteristics of EOR Polymers*. Society of Petroleum Engineers Reservoir Evaluation & Engineering, Vol. 12: 783-792. https://doi.org/10.2118/115142-PA.

Seright, R. S., Wavrik, K. E., Zhang, G., & AlSofi, A. M. (2021): *Stability and Behavior in Carbonate Cores for New Enhanced-Oil-Recovery Polymers at Elevated Temperatures in Hard Saline Brines*. SPE Res Eval & Eng 24: 1–18. doi: https://doi.org/10.2118/200324-PA

Sheng, J. J., Leonhardt, B. & Azri, N. (2015): *Status of Polymer-Flooding Technology*, Journal of Canadian Petroleum Technology, Vol. 54: 116-126. https://doi.org/10.2118/174541-PA.

Shupe, R. D. (1981): *Chemical Stability of Polyacrylamide Polymers*. J Pet Technol 33: 1513–1529. doi: https://doi.org/10.2118/9299-PA

Skauge, A., Horgen, T., Noremark, B., & Vik, B. (2011): *Experimental Studies of Unstable Displacement in Carbonate and Sandstone Material*. EAGE IOR Symposium 12th – 14th April 2011 in Cambridge, UK.

Skauge, A., Ormehaug, P. A., Vik, B. F., Fabbri, C., Bondino, I., & Hamon, G. (2013): *Polymer Flood Design for Displacement of Heavy Oil analysed by 2D-imaging*. EAGE 17th European Symposium on Improved Oil Recovery, St. Petersburg, Russia, 16 - 18 April.

Skauge, A., Sorbie, K. S., Ormehaug, P. A., & Skauge, T. (2009): *Experimental and Numerical Modeling Studies of Viscous Unstable Displacement*. Proceedings of the Improved Oil Recovery Symposium, Paris, France, April 27-29.

Skauge, A., Zamani, N., Jacobsen, J. G., Shiran, B. S., Al-Shakry, B. & Skauge, T. (2018): *Polymer Flow in Porous Media: Relevance to Enhanced Oil Recovery*. Colloids and Interfaces, Vol. 2: 1-27. https://doi.org/10.3390/colloids2030027.

Skauge, T., Kvilhaug, O. A., & Skauge, A. (2015): *Influence of Polymer Structural Conformation and Phase Behavior on In-situ Viscosity*. Presented at the 18th European Symposium on Improved Oil Recovery, Dresden, Germany, 14-16 April 2015. https://doi.org/10.3997/2214-4609.201412154.

Skauge, T., Skauge, A., Salmo, I. C., Ormehaug, P. A., Al-Azri, N., Wassing, L. M., Glasbergen, G., van Wunnik, J. N. & Masalmeh, S. K. (2016): *Radial and Linear Polymer Flow – Influence on Injectivity*. Presented at the SPE Improved Oil Recovery Conference, Tulsa, Oklahoma, USA, 11-13 April 2016. https://doi.org/10.2118/179694-MS.

Skauge, T., Vik, B. F., Ormehaug, P. A., Jatten, B. K., Kippe, V., Skjevrak, I., & Skauge, A. (2014): *Polymer flood at adverse mobility ratio in 2D flow by X-ray visualization*. Presented at SPE EOR Conference at Oil and Gas West Asia, 31 March-2 April, Muscat, Oman, SPE-169740-MS.

Smith, F. W. (1970): *The Behavior of Partially Hydrolyzed Polyacrylamide Solutions in Porous Media*. Journal of Petroleum Technology, Vol. 22: 148-156. https://doi.org/10.2118/2422-PA.

Sorbie, K. S. (1991): *Polymer-Improved Oil Recovery*, Glasgow: Blackie & Son Ltd.

Sorbie, K. S., Al Ghafri, A. Y., Skauge, A., & Mackay, E. J. (2020): *On the Modelling of Immiscible Viscous Fingering in Two-Phase Flow in Porous Media*. Transport in Porous Media, 135(2), 331-359. https://doi.org/10.1007/s11242-020-01479-w.

Speight, J.G. (2020): *Polymer Degradation*. Handbook of Industrial Hydrocarbon Processes (Second Edition), Chapter 3 - Hydrocarbons from crude oil. Gulf Professional Publishing. Pages 95-142, ISBN 9780128099230, https://doi.org/10.1016/B978-0-12-809923-0.00003-5.

Stahl, G. A., Moradi-Araghi, A., & Doe, P. H. (1988): *High temperature and hardness stable copolymers of vinylpyrrolidone and acrylamide*. In: Water soluble polymers for petroleum recovery, 121–130. New York, Plenum Press.

Stalkup, Jr, F I. (1983): *Status of miscible displacement*. United States: N. p. Web. https://doi.org/10.2118/9992-PA.

Stosur, G.J., Hite, J.R., Carnahan, N.F., & Miller, K. (2003): *The Alphabet Soup of IOR, EOR and AOR: Effective Communication Requires a Definition of Terms*. Paper presented at the SPE International Improved Oil Recovery

Conference in Asia Pacific, Kuala Lumpur, Malaysia, October 2003.
https://doi.org/10.2118/84908-MS.

Sun, Y., Saleh, L., & Bai, B. (2012): *Measurement and Impact Factors of Polymer Rheology in Porous Media*. Rheology. Ch.8. 187-202
https://doi.org/10.5772/35715.

Szabo, M. T. (1975): *Some Aspects of Polymer Retention in Porous Media Using a C14-Tagged Hydrolyzed Polyacrylamide*. Society of Petroleum Engineers Journal, Vol. 15: 323-337. https://doi.org/10.2118/4668-PA.

Taber, J.J., Martin, F.D., & Seright, R.S. (1997): *EOR Screening Criteria Revisited— Part 1—Introduction to Screening Criteria and Enhanced Recovery Field Projects*. SPE Res Eng12 (3): 189–198.
https://doi.org/http://dx.doi.org/10.2118/35385-PA.

Tan, C., & Homsy, G. (1988): *Simulation of Nonlinear Viscous Fingering in Miscible Displacement*. Phys. Fluids 31(6), 1330. https://doi.org/10.1063/1.866726.

Thomas, A. (2019): *Essentials of Polymer Flooding Technique*, New Jersey, USA: John Wiley & Sons Ltd.

U.S. Energy Information Administration (EIA). (2020): *International Energy Outlook 2020*. Available at: https://www.eia.gov/outlooks/ieo/pdf/ieo2020.pdf.

Urbissinova, T. S., Trivedi, J. & Kuru, E. (2010): *Effect of Elasticity During Viscoelastic Polymer Flooding: A Possible Mechanism of Increasing the Sweep Efficiency*, Journal of Canadian Petroleum Technology, Vol. 49: 49-56.
https://doi.org/10.2118/133471-PA.

Wang, D., Cheng, J., Yang, Q., Gong, W., Li, Q. & Chen, F. (2000): *Viscous-Elastic Polymer Can Increase Microscale Displacement Efficiency in Cores*. Presented at the 2000 SPE Annual Technical Conference and Exhibition, Dallas, Texas, 1-4 October 2000. https://doi.org/10.2118/63227-MS.

Wang, D., Han, P., Shao, Z., Hou, W. & Seright, R. S. (2008): *Sweep-Improvement Options for the Daqing Oil Field*. Society of Petroleum Engineers Reservoir Evaluation & Engineering, Vol. 11: 18-26. https://doi.org/10.2118/99441-PA.

Wassmuth, F.R., Green, K., Arnold, W., & Cameron, N. (2009): *Polymer Flood Application to Improve Heavy Oil Recovery at East Bodo*. J Can Pet Technol 48 : 55–61. doi: https://doi.org/10.2118/09-02-55

Wever, D. A. Z., Bartlema, H., Ten Berge, A. B. G. M., Al-Mjeni, R. & Glasbergen, G. (2018): *The Effect of the Presence of Oil on Polymer Retention in Porous Media from Clastic Reservoirs in the Sultanate of Oman*. Presented at the SPE EOR Conference at Oil and Gas West Asia, Muscat, Oman, 26-28 March 2018. https://doi.org/10.2118/190430-MS.

Xia, H., Ju, Y., Kong, F. & Wu, J. (2004*): Effect of Elastic Behavior of HPAM Solutions on Displacement Efficiency Under Mixed Wettability Conditions*. Presented at the 2004 SPE International Petroleum Conference, Puebla, Mexico, 8-9 November 2004. https://doi.org/10.2118/90234-MS.

Yang, S.H., & Treiber, L.E. (1985): *Chemical Stability of Polyacrylamide Under Simulated Field Conditions*. Paper presented at the SPE Annual Technical Conference and Exhibition, Las Vegas, Nevada. doi: https://doi.org/10.2118/14232-MS

Yerramilli, S. S., Zitha, P. L. J. & Yerramilli, R. C. (2013): *Novel Insight into Polymer Injectivity for Polymer Flooding*. Presented at the SPE European Formation Damage Conference & Exhibition, Noordwijk, The Netherlands, 5-7 June 2013. https://doi.org/10.2118/165195-MS.

Yin, H., Wang, D. & Zhong, H. (2006): *Study on Flow Behaviors of Viscoelastic Polymer Solution in Micropore With Dead End*. Presented at the 2006 SPE Annual Technical Conference and Exhibition, San Antonio, Texas, USA, 24-27 September 2006. https://doi.org/10.2118/101950-MS.

Zaitoun, A. & Kohler, N. (1987): *The Role of Adsorption in Polymer Propagation Through Reservoir Rocks*. Presented at the SPE International Symposium on Oilfield Chemistry, San Antonio, Texas, USA, 4-6 February 1987. https://doi.org/10.2118/16274-MS.

Zeito,G.A. (1968): *Three Dimensional Numerical Simulation of Polymer Flooding in Homogeneous and Heterogeneous Systems* .In Proceedings of the Fall Meeting of the Society of Petroleum Engineers of AIME, Houston, TX, USA.

Zhang, G. & Seright, R. S. (2015): *Hydrodynamic Retention and Rheology of EOR Polymers in Porous Media*. Presented at the SPE International Symposium on Oilfield Chemistry, The Woodlands, Texas, USA, 13-15 April 2015. https://doi.org/10.2118/173728-MS.

Zimmerman, W., & Homsy, G. (1992): *Viscous fingering in miscible displacements: unification of effects of viscosity contrast, anisotropic dispersion, and velocity dependence of dispersion on nonlinear finger propagation*. Phys. Fluids A Fluid Dyn. 4(11), 2348. https://doi.org/10.1063/1.858476.

Åsen, S. M., Stavland, A., Strand, D. & Hiorth, A. (2019): *An Experimental Investigation of Polymer Mechanical Degradation at the Centimeter and Meter Scale*. Society of Petroleum Engineers Journal, Vol. 24: 1700-1713. https://doi.org/10.2118/190225-PA.

# Appendix A: Simulation data files

## STARS Quadratic Model:

```
RESULTS SIMULATOR STARS 2018

INUNIT LAB

WSRF WELL 1
WSRF GRID TIME
WSRF SECTOR TIME

WRST TNEXT

OUTSRF GRID PRES SG SO SW TEMP VISW
OUTSRF WELL LAYER NONE

WPRN GRID 0

OUTPRN GRID NONE
OUTPRN RES NONE

GRID VARI 100 100 1
KDIR DOWN
DI IVAR
100*0.3
DJ JVAR
100*0.3
DK ALL
10000*2.05
DTOP

10000*1
PERMI
INCLUDE '100_100_3.inc' ** Include file for randomly correlated      permeability
                                  field
PERMJ EQUALSI
PERMK EQUALSI
NULL CON           1
POR CON        0.24
PINCHOUTARRAY CON           1
END-GRID

MODEL 2 2 2 1
COMPNAME 'Water'  'Dead_Oil'
CMM      0.018   0.456
PCRIT    0             0
TCRIT    0             0
MASSDEN  0.001         0.001
CP       0         0
PRSR 101
PSURF 101

AVISC      1        7000

ROCKFLUID
```

```
RPT 1 WATWET

INCLUDE 'E7000_RP.txt' **Include file for relative permeability
INITIAL
VERTICAL OFF

INITREGION 1
PRES CON            101
MFRAC_WAT 'Water' CON            1
MFRAC_OIL 'Dead_Oil' CON             1

NUMERICAL
**DTMIN 1.44e-015

TFORM ZT
ISOTHERMAL

NEWTONCYC 30
SDEGREE 2
ITERMAX 300
NCUTS 15
NORTH 100

RUN
DATE 1901 1 1
DTWELL 0.005
**$
WELL  'inj'
INJECTOR MOBWEIGHT EXPLICIT 'inj'
INCOMP  WATER  1.  0.
OPERATE  MAX  STW  0.05  CONT REPEAT
GEOMETRY  I  0.05  0.249  1.0  0.0
PERF  GEOA  'inj'
** UBA         ff   Status  Connection
INCLUDE 'INJ_100.txt'  **Include file for injector perforations

WELL  'prod'
PRODUCER 'prod'
OPERATE  MIN  BHP  101.  CONT REPEAT
GEOMETRY  I  0.05  0.249  1.0  0.0
PERF  GEOA  'prod'
** UBA        ff   Status  Connection
INCLUDE 'PROD_100.txt' **Include file for producer perforations

DATE 1901 1  1.00694

.

.

.

DATE 1901 1 31.90310
DATE 1901 2  1.25032

STOP
```

## STARS 2D Radial Model

```
RESULTS SIMULATOR STARS 201410

TITLE1 'RADIAL WELL MODEL-5000 ft'
TITLE2 'SHEARTHIN'

INUNIT        FIELD
OUTUNIT FIELD
SHEAREFFEC SHV     **Specifies viscosity dependence option (SHV or SHR)
**Indicates how often to write results for grid blocks
WPRN GRID 1
** Specifies what particular results are reported for grid blocks
OUTPRN GRID KRW PRES RFW SO SW VISW W X Z
OUTPRN WELL ALL
WPRN ITER TIME
OUTPRN ITER NEWTON
WSRF WELL 1
WSRF GRID TIME
**WSRF         SECTOR 1
**Limits what well data, grid data and reservoir data are printed
OUTSRF WELL MOLE COMPONENT ALL
OUTSRF GRID KRW PRES RFW SHEARSTRSW SHEARW SO SW VISCVELW VISW W X Z
GRID RADIAL 124 1 1 *RW         0.25
KDIR DOWN
DI IVAR      0.0318261      0.0358777      0.0404451      0.0455939
       0.0513982      0.0579415      0.0653177      0.0736329      0.0830067
       0.0935738      0.105486      0.118915      0.134053      0.151119
       0.170357      0.192044      0.216492      0.244053      0.275122
       0.310146      0.349629      0.394138      0.444314      0.500877
       0.564641      0.636522      0.717554      0.808902      0.911879
       1.02796      1.15883      1.30635      1.47266      1.66013
       1.87148      2.10972      2.3783      2.68107      3.02238
       3.40714      3.84089      4.32985      4.88106      5.50244
       6.20292      6.99258      7.88277      8.88628      10.0175
       11.2928  12.0      12.0      12.0      12.0
   12.0      12.0      12.0      12.0      12.0
   12.0      12.0      12.0      12.0      12.0
   12.0      12.0      12.0      12.0      12.0
   12.0      12.0      12.0      12.0      12.0
   12.0      12.0      12.0      12.0      12.0
   12.0      12.0      12.0      12.0      12.0
   12.0      12.0      12.0      12.0      12.0
   12.0      12.0      12.0      12.0      12.0
   12.0      12.0      12.0      12.0      12.0
   12.0      12.0      12.0      12.0      12.0
   12.0      12.0      12.0      12.0      12.0
   15.0      15.0      15.0      15.0      15.0
   15.0      15.0      15.0      15.0      15.0
   25.0      25.0      25.0      25.0      25.0
DJ JVAR          360
DK ALL
 124*50
DTOP
 124*1000
PVCUTOFF 0
PERMI CON         2000
```

```
**  0 = null block, 1 = active block
NULL CON            1
POR CON         0.15
PERMK EQUALSI
**  0 = pinched block, 1 = active block
PINCHOUTARRAY CON             1
PERMJ EQUALSI
END-GRID
** Model and number of components
** Model and number of components
MODEL 3 3 3 2
COMPNAME 'Polymer' 'H2O' 'Oil'
CMM
8 0.018 0.456
PCRIT
0 0 0
TCRIT
0 0 0
PRSR 14.7
PSURF 14.7
MASSDEN
62.4 62.4 62.4
CP
0 0 0


VISCTABLE
200 20.00 0.96 250

VSMIXCOMP 'Polymer'
VSMIXENDP 0 1.8e-006



SHEARTAB

** ROCK-FLUID (REL-PERM)
ROCKFLUID
RPT 1 WATWET
**       Sw           krw           krow
SWT
           0             0             1
        0.05  3.66211e-005      0.823975
         0.1   0.000292969      0.669922
        0.15    0.00098877      0.536377
         0.2    0.00234375      0.421875
        0.25    0.00457764      0.324951
         0.3    0.00791016      0.244141
        0.35      0.012561      0.177979
         0.4       0.01875         0.125
        0.45     0.0266968      0.0837402
         0.5     0.0366211      0.0527344
        0.55     0.0487427      0.0305176
         0.6     0.0632813      0.015625
        0.65     0.0804565      0.0065918
         0.7      0.100488      0.00195313
        0.75      0.123596      0.000244141
         0.8          0.15             0
**        Sl           krg           krog
SLT
```

```
       0.2         0.5              0
    0.246875    0.411987    0.000244141
     0.29375    0.334961    0.00195313
    0.340625    0.268188     0.0065918
      0.3875    0.210938      0.015625
    0.434375    0.162476     0.0305176
     0.48125     0.12207     0.0527344
    0.528125   0.0889893     0.0837402
       0.575      0.0625         0.125
    0.621875   0.0418701      0.177979
     0.66875   0.0263672      0.244141
    0.715625   0.0152588      0.324951
      0.7625   0.0078125      0.421875
    0.809375   0.0032959      0.536377
     0.85625 0.000976562      0.669922
    0.903125  0.00012207      0.823975
        0.95           0             1
**ADSCOMP 'Polymer' WATER     **ADSCOMP = Adsorbing component
**ADSPHBLK W
**ADSTABLE
**     Mole Fraction  Adsorbed moles per unit pore volume
**          0                         0
**      1.8e-006             1.656273168e-008
**ADMAXT 1.656273168e-008     ** Maximum adsorption
**ADRT 1.656273168e-008      **Equal to ADMAXT if the adsorption is irreversibel
as it is assumed to be in our case
**PORFT 1      **PORFT = Accsessible pore volume
**RRFT 1      **RRFT = Residual resistance factor for the adsorbing component
**INITIALIZATION
INITIAL
VERTICAL OFF

INITREGION 1
PRES CON         2000
TEMP CON          200
SW CON          0.8
SO CON          0.2
MFRAC_WAT 'H2O' CON            1

NUMERICAL
MAXSTEPS 100000
TFORM ZT
ISOTHERMAL

**RECURRENT DATA
RUN
DATE 2018 1 1
DTWELL 0.0001
**
**
WELL  'Well-1'
INJECTOR MOBWEIGHT EXPLICIT 'Well-1'
INCOMP  WATER  0.0  1.0  0.0
TINJW  200.0
OPERATE  MAX  STW  10.0  CONT
** UBA              ff          Status  Connection
**          rad  geofac  wfrac  skin
GEOMETRY  K  0.05  0.5  1.0  0.0
```

```
     PERF      GEOA  'Well-1'
** UBA            ff          Status Connection
   1 1 1         1.0  OPEN    FLOW-FROM  'SURFACE'  REFLAYER
**
**
WELL  'Well-2'
PRODUCER 'Well-2'
OPERATE  MIN  BHP  500.0  CONT
OPERATE      MAX  STW  10.0  CONT
** UBA            ff           Status  Connection
**         rad  geofac  wfrac  skin
GEOMETRY  K  0.05  0.235  1.0  0.0
     PERF      GEOA  'Well-2'
** UBA            ff          Status  Connection
   124 1 1        1.0  OPEN    FLOW-TO  'SURFACE'  REFLAYER


DATE 2018 1  2.00000
.


.

STOP
```

## STARS 3D Radial Model

```
RESULTS SIMULATOR STARS 201710

INUNIT      FIELD
OUTUNIT FIELD

SHEAREFFEC SHV     **Specifies viscosity dependence option (SHV or SHR)

WPRN GRID 1        **Indicates how often to write results for grid blocks

OUTPRN GRID KRW PRES RFW SO SW VISW W X Z ** Specifies what particular results
are reported for grid blocks
OUTPRN WELL ALL
WPRN ITER TIME
OUTPRN ITER NEWTON
WSRF WELL 1
WSRF GRID TIME
OUTSRF WELL MOLE COMPONENT ALL
OUTSRF GRID KRW PRES RFW SHEARSTRSW SHEARW SO SW VISCVELW VISW W X
          Z

GRID RADIAL 58 8 5 *RW        0.136

KDIR DOWN
DI IVAR
       0.272 0.287 0.302 0.319
0.336 0.355 0.374 0.394 0.416
0.438 0.462 0.487 0.514 0.542
0.571 0.602 0.635 0.670 0.706
0.744 0.785 0.828 0.873 0.920
0.970 1.023 1.079 1.137 1.199
1.265 1.333 1.406 1.483 1.563
1.648 1.738 1.832 1.932 2.037
2.148 2.265 2.388 2.518 2.655
2.800 2.952 3.113 3.282 3.461
3.649 3.848 4.057 4.278 4.510
4.756 5.015 5.287 5.575

DJ JVAR
    45 45 45 45 45 45 45 45
DK ALL
 2320*10
DTOP
 464*1000
PVCUTOFF 0
NULL CON           1    **  0 = null block, 1 = active block

POR CON         0.15

PERMI CON         100    ** k = 100 mD (isotropic)
PERMK  EQUALSI
PERMJ  EQUALSI

END-GRID

** Model and number of components
```

```
MODEL 3 3 3 2
COMPNAME 'Polymer' 'H2O' 'Oil'
CMM
8 0.018 0.456
PCRIT
0 0 0
TCRIT
0 0 0
PRSR 14.7
PSURF 14.7
MASSDEN
62.4 62.4 62.4
CP
0 0 0
VISCTABLE
200 9.71 1.0 250


** ROCK-FLUID (REL-PERM)
ROCKFLUID
RPT 1 WATWET

**          Sw          krw          krow
SWT
            0            0            1
            1            1            0



**INITIALIZATION
INITIAL
VERTICAL OFF

INITREGION 1
PRES CON          2000
TEMP CON           200
SW CON         1.0
SO CON         0.0
MFRAC_WAT 'H2O' CON              1

NUMERICAL


TFORM ZT
ISOTHERMAL
DTMAX 0.05


**RECURRENT DATA

RUN
DATE 2018 1 1
DTWELL 0.00000001
**
**

WELL   'INJ'
INJECTOR MOBWEIGHT EXPLICIT 'INJ'
```

```
INCOMP  WATER  0.0  1.0 0.0
TINJW  200.0
OPERATE  STW  5000.0 CONT
**          rad geofac wfrac  skin
GEOMETRY  K  0.005  0.5  1.0  0.0
      PERF      GEOA  'INJ'
** UBA            ff         Status  Connection
    1 1 1         1.0  OPEN    FLOW-FROM  'SURFACE'  REFLAYER
    1 1 2         1.0  OPEN    FLOW-FROM  1
    1 1 3         1.0  OPEN    FLOW-FROM  2
    1 1 4         1.0  OPEN    FLOW-FROM  3
    1 1 5         1.0  OPEN    FLOW-FROM  4
**
**


WELL  'PROD-1'
PRODUCER 'PROD-1'
OPERATE  BHP  500 CONT

**          rad geofac wfrac  skin
GEOMETRY  K  0.5  0.235  1.0  0.0
      PERF      GEOA  'PROD-1'
** UBA             ff         Status  Connection
    58 1 1        1.0  OPEN    FLOW-TO  'SURFACE'  REFLAYER
    58 1 2        1.0  OPEN    FLOW-TO  1
    58 1 3        1.0  OPEN    FLOW-TO  2
    58 1 4        1.0  OPEN    FLOW-TO  3
    58 1 5        1.0  OPEN    FLOW-TO  4


WELL  'PROD-2'
PRODUCER 'PROD-2'
OPERATE  BHP  500 CONT

**          rad geofac wfrac  skin
GEOMETRY  K  0.5  0.235  1.0  0.0
      PERF      GEOA  'PROD-2'
** UBA             ff         Status  Connection
    58 2 1        1.0  OPEN    FLOW-TO  'SURFACE'  REFLAYER
    58 2 2        1.0  OPEN    FLOW-TO  1
    58 2 3        1.0  OPEN    FLOW-TO  2
    58 2 4        1.0  OPEN    FLOW-TO  3
    58 2 5        1.0  OPEN    FLOW-TO  4


WELL  'PROD-3'
PRODUCER 'PROD-3'
OPERATE  BHP  500 CONT

**          rad geofac wfrac  skin
GEOMETRY  K  0.5  0.235  1.0  0.0
      PERF      GEOA  'PROD-3'
** UBA             ff         Status  Connection
    58 3 1        1.0  OPEN    FLOW-TO  'SURFACE'  REFLAYER
    58 3 2        1.0  OPEN    FLOW-TO  1
    58 3 3        1.0  OPEN    FLOW-TO  2
    58 3 4        1.0  OPEN    FLOW-TO  3
    58 3 5        1.0  OPEN    FLOW-TO  4
```

```
WELL  'PROD-4'
PRODUCER 'PROD-4'
OPERATE  BHP  500 CONT

**          rad  geofac  wfrac  skin
GEOMETRY  K  0.5  0.235  1.0  0.0
      PERF      GEOA  'PROD-4'
** UBA            ff        Status Connection
    58 4 1        1.0  OPEN  FLOW-TO  'SURFACE'  REFLAYER
    58 4 2        1.0  OPEN  FLOW-TO  1
    58 4 3        1.0  OPEN  FLOW-TO  2
    58 4 4        1.0  OPEN  FLOW-TO  3
    58 4 5        1.0  OPEN  FLOW-TO  4

WELL  'PROD-5'
PRODUCER 'PROD-5'
OPERATE  BHP  500 CONT

**          rad  geofac  wfrac  skin
GEOMETRY  K  0.5  0.235  1.0  0.0
      PERF      GEOA  'PROD-5'
** UBA            ff        Status Connection
    58 5 1        1.0  OPEN  FLOW-TO  'SURFACE'  REFLAYER
    58 5 2        1.0  OPEN  FLOW-TO  1
    58 5 3        1.0  OPEN  FLOW-TO  2
    58 5 4        1.0  OPEN  FLOW-TO  3
    58 5 5        1.0  OPEN  FLOW-TO  4

WELL  'PROD-6'
PRODUCER 'PROD-6'
OPERATE  BHP  500 CONT

**          rad  geofac  wfrac  skin
GEOMETRY  K  0.5  0.235  1.0  0.0
      PERF      GEOA  'PROD-6'
** UBA            ff        Status Connection
    58 6 1        1.0  OPEN  FLOW-TO  'SURFACE'  REFLAYER
    58 6 2        1.0  OPEN  FLOW-TO  1
    58 6 3        1.0  OPEN  FLOW-TO  2
    58 6 4        1.0  OPEN  FLOW-TO  3
    58 6 5        1.0  OPEN  FLOW-TO  4

WELL  'PROD-7'
PRODUCER 'PROD-7'
OPERATE  BHP  500 CONT

**          rad  geofac  wfrac  skin
GEOMETRY  K  0.5  0.235  1.0  0.0
      PERF      GEOA  'PROD-7'
** UBA            ff        Status Connection
    58 7 1        1.0  OPEN  FLOW-TO  'SURFACE'  REFLAYER
    58 7 2        1.0  OPEN  FLOW-TO  1
    58 7 3        1.0  OPEN  FLOW-TO  2
    58 7 4        1.0  OPEN  FLOW-TO  3
    58 7 5        1.0  OPEN  FLOW-TO  4

WELL  'PROD-8'
```

```
PRODUCER 'PROD-8'
OPERATE  BHP  500 CONT

**          rad  geofac  wfrac  skin
GEOMETRY  K  0.5  0.235  1.0  0.0
      PERF      GEOA  'PROD-8'
** UBA              ff        Status  Connection
    58 8 1          1.0  OPEN  FLOW-TO  'SURFACE'  REFLAYER
    58 8 2          1.0  OPEN  FLOW-TO  1
    58 8 3          1.0  OPEN  FLOW-TO  2
    58 8 4          1.0  OPEN  FLOW-TO  3
    58 8 5          1.0  OPEN  FLOW-TO  4

DATE 2018 1  1.1
.
.

DATE 2018 1 10.00000

STOP
```

## IMEX Radial Model

```
RESULTS SIMULATOR IMEX 202010
FILENAMES SR3-IN 'BM-008.rstr.sr3'
SRFORMAT SR3
RESTART 12772
INUNIT FIELD
RESTART_SR2 SEPARATE
**OUTSRF identifies what information is written to the Simulation Results File.
OUTSRF WELL ALL
OUTSRF RES ALL
OUTSRF GRID BPP BSOIRW EFFPVIS KRO KRW OILPOT PADSORP PCONC PCOW PRES RFW SHEARW
SO BSOIRW SORH BSORW SW BSWCON BSWCRIT VELOCRC VELOCSC VISO VISW WINFLUX
OUTSRF WELL LAYER ALL DOWNHOLE

**WSRF Control the frequency of dumping information flagged by *OUTSRF to the
simulation result output files
WSRF GRID 0 **
WSRF WELL 1
**WSRF WELL-TEST 1
WSRF SECTOR 1

**OUTPRN identifies what information is written to the output file.
OUTPRN GRID ALL
OUTPRN RES ALL

**WPRN controls the frequency of writing data to the output file.
WPRN GRID 0


**  Distance units: ft
RESULTS XOFFSET          0.0000
RESULTS YOFFSET          0.0000
RESULTS ROTATION          0.0000  **  (DEGREES)
RESULTS AXES-DIRECTIONS 1.0 -1.0 1.0
** ***************************************************************************
** Definition of fundamental cylindrical grid
** ***************************************************************************
GRID RADIAL 20 1 89 *RW        0.25
KDIR DOWN
DI IVAR
0.3 0.4 0.5 0.7 1 1.5684 2.50851 4.01213 6.41704 10.2635 16.4154 26.255 41.9924
67.163 107.421 171.81 274.794 439.507 702.951 1124.31

DJ JVAR
360
DK ALL
2       2       2       2       2       2       2       2       2       2       2       2       2
        2       2       2       2       2       2       2
.
.
.
2.75    2.75    2.75    2.75    2.75    2.75    2.75    2.75    2.75    2.75    2.75    2.75    2.75
        2.75    2.75    2.75    2.75    2.75    2.75    2.75
2       2       2       2       2       2       2       2       2       2       2       2       2
        2       2       2       2       2       2       2
```

```
11.5   11.5   11.5   11.5   11.5   11.5   11.5   11.5   11.5   11.5   11.5   11.5   11.5
       11.5   11.5   11.5   11.5   11.5   11.5   11.5


DTOP 20*7975
PERMI KVAR
1 13 21 48 61 99 5 48 346 644 95 222 85 132 65 101 15 2*3 31 11 24
66 8 27 38 2*115 4 24 18 24 196 48 2*24 64 82 207 20 32 28 18 28 22
47 14 13 17 1 4 17 34 7 17 1 2*5 18 33 10 14 8 4.555555 7.736842 12
8 7.285714 6 9 4.5 6.162162 8.454545 10 14 5 12 5.3125 2.461539 7.615385
4.545455 3.6875 7 10 7 5 1 4 1
*MOD
**Permeability multiplier applied to PERMI for each layer (zone), this is to take
into account the expected underestimation of permeability due to heterogneity of
reservoir
** ZONE 1
1:20 1 23:26 * 14.29
** ZONE 2
1:20 1 27:37 * 0.6
** ZONE 3
1:20 1 38:47 * 1.56
** ZONE 4
1:20 1 49:55 * 4.61
PERMJ  EQUALSI
PERMK  EQUALSI * 0.856
**  0 = null block, 1 = active block
NULL CON            1
POR KVAR
0.035575 0.035275 0.0361 0.03735 0.03182 0.033025 0.07645001 0.08335
0.06605 0.065625 0.10835 0.266825 0.29865 0.290025 0.274575 0.219325
0.232875 0.2773333 0.2966 0.301675 0.3255 0.323475 0.32925 0.328275
0.324 0.3234 0.3258 0.3238 0.325575 0.33595 0.330875 0.32322 0.33945
0.344425 0.3473 0.346 0.33024 0.32315 0.35074 0.347725 0.34385 0.3478
0.338325 0.3642 0.350175 0.32456 0.346125 0.36805 0.35465 0.352425
0.354925 0.3466 0.344125 0.34688 0.352325 0.328275 0.3004 0.2953 0.301975
0.3219 0.337875 0.3405 0.3431333 0.3409667 0.3006211 0.2294 0.31498
0.3522357 0.34484 0.340325 0.3258667 0.3305459 0.3343273 0.32156 0.3326833
0.33874 0.3349583 0.3288687 0.3181077 0.2922577 0.2901045 0.2833312
0.2941 0.28198 0.2578333 0.2400154 0.2297286 0.1944 0.166425
VOLMOD CON              1
*MOD
20 1 1:89 = 5
**  0 = pinched block, 1 = active block
PINCHOUTARRAY CON              1
**Defining Sectors (Zones/Layers)
SECTORARRAY 'Zone4' KVAR
48*0 7*1 34*0
SECTORARRAY 'Zone3' KVAR
37*0 10*1 42*0
SECTORARRAY 'Zone2' KVAR
26*0 11*1 52*0
SECTORARRAY 'Zone1' KVAR
22*0 4*1 63*0


CPOR 4e-6
PRPOR 4000


MODEL POLYOW_SEAWATER
```

```
TRES 248
**         p        Rs         Bo        Eg        viso       visg
PVT EG 1
14.696   6.35537     1.09182    4.19304  0.975579  0.0121702
156.383  39.1953     1.10898    45.5528  0.848958  0.0123343
298.07   78.4651     1.12999    88.6605  0.746666  0.0125742
439.757  121.539      1.1536    133.584  0.667755  0.0128716
581.444  167.427     1.17934    180.367  0.605876  0.0132238
723.131  215.581     1.20695     229.02  0.556212  0.0136318
864.818  265.649     1.23625    279.502  0.515474  0.0140981
1006.5   317.382     1.26711    331.707  0.481421  0.0146258
1148.19  370.595     1.29943    385.449  0.452492  0.0152176
1289.88  425.143     1.33314    440.451  0.427577  0.0158758
1431.57   480.91     1.36815    496.347  0.405864  0.0166012
1573.25  537.801     1.40442    552.694  0.386749  0.0173928
1714.94  595.735     1.44188    609.004  0.369771  0.0182477
1856.63  654.644      1.4805    664.778  0.354576  0.0191612
1998.31  714.469     1.52023    719.546  0.340882  0.0201269
2140     775.159     1.56103    772.905  0.328466  0.0211374
2772     1055.32     1.75529    987.237  0.284598  0.0259877
3404     1348.84     1.96791    1159.03  0.253214  0.0309792
4036     1653.72     2.19714    1294.32   0.22945  0.0357771
4668     1968.51  2.421617113   1402.26  0.210714  0.0402647
5300     2292.13  2.638741495   1490.41  0.195489  0.0444344


BOT 1
**         p        Bo
2175.7   1.5699
3014.7   1.5373
6014.7   1.4663
9014.7   1.4344


VOT 1
**         p        viso
2175.7   0.2863
3014.7    0.31
6014.7    0.388
9014.7    0.465
BWI 1.04642
CVW 0
CW 3.1e-06
DENSITY OIL 50.8910662824207
REFPW 4000
VWI 0.43
GRAVITY GAS 0.750001

DENSEAWAT **Seawater stock tank density as a function of salt concentration (In
our case: density is
**cs      denssw
0.0   73.3403681
20.0  73.3403682


PADPOR_REF 0                    ** Reference porosity for the following
** adsorption rock-to-pore volume conversion

PADSORP   **Polymer Adsorption Table: cp: polymer concentration (lb/stb)
ads_level: polymer adsorption level
```

```
**cp      ads_level
0             0
1.3       1.25E-05

PPERM
2     2.50E-05    2.50E-05    0.75  4.1
500   2.50E-05    2.50E-05    0.75  4.1

PVISC 20 **Relative viscostity at 120 c, 5000 ppm. 19.717 at 100C.
SVISC 0.43
PREFCONC 1.3
PTYPE CON            1

SHEAREFFEC SHV

**PMIX  LINEAR

PMIX VELTABLE

VWT         0.08
0.000       1.00
0.200       1.34
0.400       1.36
0.600       1.44
0.800       1.53
1.000       2.34

VWT         0.12
0.000       1.00
0.200       1.19
0.400       1.22
0.600       1.31
0.800       1.41
1.000       2.33

VWT         0.50
0.000       1.00
0.200       0.84
0.400       0.92
0.600       1.10
0.800       1.26
1.000       2.66

VWT         1.41
0.000       1.00
0.200       0.75
0.400       0.92
0.600       1.20
0.800       1.41
1.000       3.26

VWT         2.12
0.000       1.00
0.200       0.76
0.400       0.97
0.600       1.30
0.800       1.53
1.000       3.58
```

```
VWT          3.53
0.000        1.00
0.200        0.80
0.400        1.10
0.600        1.48
0.800        1.74
1.000        4.06

VWT          4.94
0.000        1.00
0.200        0.87
0.400        1.23
0.600        1.64
0.800        1.91
1.000        4.42

VWT          7.06
0.000        1.00
0.200        0.97
0.400        1.41
0.600        1.85
0.800        2.13
1.000        4.85

VWT          10.58
0.000        1.00
0.200        1.13
0.400        1.67
0.600        2.13
0.800        2.42
1.000        5.39

VWT          21.16
0.000        1.00
0.200        1.54
0.400        2.28
0.600        2.74
0.800        3.05
1.000        6.46

VWT          33.33
0.000        1.00
0.200        1.86
0.400        2.78
0.600        3.21
0.800        3.55
1.000        7.26

VWT          49.99
0.000        1.00
0.200        2.12
0.400        3.24
0.600        3.67
0.800        4.05
1.000        8.03

VWT          100.00
```

```
0.000        1.00
0.200        2.40
0.400        3.95
0.600        4.46
0.800        5.00
1.000        9.47

VWT          200.00
0.000        1.00
0.200        2.45
0.400        4.34
0.600        5.12
0.800        6.01
1.000        11.02

VWT          400.00
0.000        1.00
0.200        2.44
0.400        4.44
0.600        5.53
0.800        6.95
1.000        12.62

VWT          800.00
0.000        1.00
0.200        2.44
0.400        4.44
0.600        5.70
0.800        7.70
1.000        14.17

VWT          1000.00
0.000        1.00
0.200        2.44
0.400        4.44
0.600        5.72
0.800        7.88
1.000        14.64


ROCKFLUID
RPT 1
**        Sw          krw          krow        Pcow        Pcowi
SWT
0.1515                0               1      39.867       39.867
0.155002051    5.248875e-06    0.9771428571          0  -0.83657
.
.
.

0.7748650866           0.753   0.001249757143          0   -4.6644
0.7853712397       0.7850375   0.0007988142857          0   -5.0453
0.7958773929       0.8178625   0.0004724428571          0   -5.5314
0.806383546        0.8515125   0.0002503857143          0   -6.1814
0.8168896992        0.885975   0.0001123928571          0   -7.1136
0.8273958523       0.9212625   3.822285714e-05          0   -8.6187
0.8379020055        0.957375   7.620571429e-06          0   -11.729
0.85                      1               0          0  -30.702
```

```
RPT 2
**        Sw         krw        krow       Pcow      Pcowi
SWT
0.151500    0.000000    1.000000    39.867 39.867
0.154751    0.000005    0.977143    0.000000    -0.836570
0.164505    0.000078    0.933500    0.000000    -1.312400
0.174260    0.000276    0.891171    0.000000    -1.462700
.
.
.

0.749752    0.817863    0.000472    0.000000    -5.531400
0.759506    0.851513    0.000250    0.000000    -6.181400
0.769260    0.885975    0.000112    0.000000    -7.113600
0.779014    0.921263    0.000038    0.000000    -8.618700
0.788768    0.957375    0.000008    0.000000    -11.729000
0.800000    1.000000    0.000000    0.000000    -30.702000
RTYPE KVAR
8*2 2*1 2 1 2 1 2 1 10*2 2*1 4*2 1 5*2 1 50*2
BSWCON CON         0.05

INITIAL
VERTICAL DEPTH_AVE WATER_OIL EQUIL

REFDEPTH 8020
REFPRES 2944
DWOC 8300

DATUMDEPTH 8020 INITIAL
PB CON         2140
SWINIT KVAR
2*1 0.985525 0.93085 0.98098 0.88755 0.38605 0.34135 0.43425 0.4397
0.3389 0.190375 0.2846 0.346375 0.328775 0.429175 0.442625 0.4602333
0.4241 0.484275 0.709975 0.704475 0.65315 0.64215 0.651025 0.63385
0.5795 0.5755 0.582225 0.583775 0.602125 0.64066 0.689525 0.69745
0.6794667 0.6834 0.58564 0.371375 0.34468 0.358625 0.353 0.2705 0.202025
0.13308 0.1103 0.1006 0.08285 0.0712 0.068625 0.064875 0.06135 0.06045
0.059375 0.05818 0.05655 0.060075 0.0649 0.0655 0.06160833 0.05548
0.0529 0.053225 0.05969259 0.06094445 0.06208947 0.083125 0.06464
0.06287857 0.06675 0.06747501 0.07029167 0.07048649 0.07347272 0.0766
0.07303333 0.0702 0.0678 0.06538125 0.06865384 0.08515769 0.1071636
0.1321438 0.1238167 0.13128 0.15015 0.1782769 0.2032286 0.2497 0.32065


NUMERICAL
MAXSTEPS 10000000
DTMIN 0.000001
DTMAX 1.0
**NORM PRESS 100
**NORM SATUR 0.03
**PRECC 1.e-6
CONVERGE MAXRES POLYMER 1e-05
CONVERGE POLY 0.0001
NORTH 100
ITERMAX 100
NEWTONCYC 20
```

```
RUN
DATE 2018 8 30

**
WELL  'SB492101H'
INJECTOR MOBWEIGHT 'SB492101H'
INCOMP  WATER
OPERATE  MAX  STW  0.0  CONT
**          rad  geofac  wfrac  skin
GEOMETRY  K  0.25  0.37  1.0  3.5
PERF     GEOA  'SB492101H'
** UBA            ff         Status  Connection
1 1 23        1.0  OPEN    FLOW-FROM  'SURFACE'  REFLAYER
1 1 24        1.0  OPEN    FLOW-FROM  1
1 1 25        1.0  OPEN    FLOW-FROM  2
.
.

1 1 54        1.0  OPEN    FLOW-FROM  31
1 1 55        1.0  OPEN    FLOW-FROM  32
SHUTIN 'SB492101H'

**
WELL  'Dummy-1'
PRODUCER 'Dummy-1'
OPERATE  MIN  BHP  2985.0  CONT
**          rad  geofac  wfrac  skin
GEOMETRY  K  0.25  0.37  1.0  0.0
PERF     GEOA  'Dummy-1'
** UBA            ff         Status  Connection
20 1 23        1.0  OPEN    FLOW-TO  'SURFACE'  REFLAYER
20 1 24        1.0  OPEN    FLOW-TO  1
20 1 25        1.0  OPEN    FLOW-TO  2
.
.

20 1 54        1.0  OPEN    FLOW-TO  31
20 1 55        1.0  OPEN    FLOW-TO  32
DATE 2018 9  1.00000
INJECTOR MOBWEIGHT 'SB492101H'
INCOMP  WATER
OPERATE  MAX  STW  0.0  CONT
ALTER 'SB492101H'
0
DATE 2018 9 15.00000
ALTER 'SB492101H'
1000.0
PRODUCER 'Dummy-1'
OPERATE  MIN  BHP  2976.0  CONT
OPEN 'Dummy-1'
DATE 2018 9 16.00000
ALTER 'SB492101H'
1625.0
DATE 2018 9 17.00000
.
.
.
STOP
```

# Appendix B: Papers (1-4)

# Paper 2:

# Polymer Injectivity Test Design Using Numerical Simulation

# Polymer Injectivity Test Design Using Numerical Simulation

Mohamed Adel Alzaabi [1,*], Jørgen Gausdal Jacobsen [1,2], Shehadeh Masalmeh [3], Ali Al Sumaiti [3], Øystein Pettersen [2] and Arne Skauge [1,4]

[1] Department of Chemistry, University of Bergen, 5007 Bergen, Norway; joja@norceresearch.no (J.G.J.); arne.skauge@energyresearch.no (A.S.)

[2] Norwegian Research Center, 5008 Bergen, Norway; oype@norceresearch.no

[3] Abu Dhabi National Oil Company, P.O. Box 898 Abu Dhabi, UAE; smasalmeh@adnoc.ae (S.M.); aalsumaiti@adnoc.ae (A.A.S.)

[4] Energy Research Norway, 5007 Bergen, Norway

[*] Correspondence: mal075@uib.no

**Abstract:** Polymer flooding is an enhanced oil recovery (EOR) process, which has received increasing interest in the industry. In this process, water-soluble polymers are used to increase injected water viscosity in order to improve mobility ratio and hence improve reservoir sweep. Polymer solutions are non-Newtonian fluids, i.e., their viscosities are shear dependent. Polymers may exhibit an increase in viscosity at high shear rates in porous media, which can cause injectivity loss. In contrast, at low shear rates they may observe viscosity loss and hence enhance the injectivity. Therefore, due to the complex non-Newtonian rheology of polymers, it is necessary to optimize the design of polymer injectivity tests in order to improve our understanding of the rheology behavior and enhance the design of polymer flood projects. This study has been addressing what information that can be gained from polymer injectivity tests, and how to design the test for maximizing information. The main source of information in the field is from the injection bottom-hole pressure (BHP). Simulation studies have analyzed the response of different non-Newtonian rheology on BHP with variations of rate and time. The results have shown that BHP from injectivity tests can be used to detect in-situ polymer rheology.

**Keywords:** chemical EOR; polymer flooding; in situ rheology; polymer injectivity; polymer modeling

## 1. Introduction

Polymer flooding is a well-established chemical enhanced oil recovery (CEOR) method that has been widely used for more than half a century. It was initially introduced to alleviate the issues related to unfavorable mobility ratio, induced by reservoir heterogeneity and/or high oil viscosity. These issues were remediated by adding polymers to the injected water to improve overall aerial and volumetric sweep efficiency [1]. The main mechanisms of polymer flooding are sweep improvement that consists of mitigating viscous fingering and improving crossflow between vertical heterogeneous layers [2,3]. In addition, numerous studies indicate that non-Newtonian polymer solutions can improve microscopic displacement efficiency and may reduce water-flood residual oil saturation [3,4].

The most commonly used polymer for CEOR applications is synthetic polymer partially hydrolyzed polyacrylamide (HPAM), with a typical hydrolysis degree range of 15%–33%. In bulk flow, viscosity measurements from rheometers show that HPAM exhibit shear thinning behavior, which can be explained by the disentanglement and realignment of polymer coils as velocity increases in the laminar flow regime. In addition, numerous polymer flow experiments in porous media have shown that HPAM exhibits an apparent shear thickening behavior beyond a critical shear rate [5]. Consequently,

apparent viscosity attains a maximum value in the immediate near-wellbore region. This viscosity increment is often referred to as extensional or elongational viscosity as it is attributed to the extensional flow regime of the polymer. Both the coil-stretch theory and transient network theory has been suggested to account for the extensional flow phenomenon. According to the coil-stretch theory, which is adhered to by the authors of this paper, the flexible coiled molecules of HPAM experience stretching, entanglement and collisions at high shear, which results in a larger flow resistance, i.e., apparent shear thickening behavior. This behavior is a special property of elastic polymers in flow through porous media and is not observed for biopolymers such as xanthan [6].

Injectivity is one of the most important parameters in the design of any reservoir flooding application. Failure in estimating injectivity within acceptable error margins can have a significant impact on the expected recovery increment and thus on the economic feasibility of the project. For polymer flooding applications, accurate estimation of injectivity is more significant due to the polymer high viscosity and its non-Newtonian behavior. This behavior may result in the well operating near (or under) formation fracturing conditions, which can significantly affect in-situ polymer rheology.

Several important observations have been made in recent years that may explain the deviation between field injectivity results compared to initial expectations. Skauge et al. demonstrated that onset of shear thickening occurs at significantly higher velocities in radial compared to linear flow [7]. In addition, the extent of shear thinning was more pronounced in radial flow, while the extent of shear thickening was reduced compared to linear flow. The presence of residual oil is another factor that may have a significant impact on polymer in-situ rheology. Authors of [5] observed a significant reduction of polymer in-situ viscosity in the presence versus absence of residual oil. Furthermore, it was demonstrated through experimental work that the preshearing polymer before injection helps in improving injectivity by reducing elastic properties of the polymer while maintaining viscous properties, i.e., reducing or eliminating the extensional shear thickening behavior at high shear rates near the well-bore [8].

### 1.1. Modeling and Simulation of Polymer Injectivity

Numerical simulation is an essential tool for the assessment of polymer flooding lab results and fundamental theory. It is also important for designing polymer field projects as well as predicting the performance and outcomes of the project.

One of the early attempts to model polymer flooding was by Zeito (1968) [9]. He created a 3D numerical simulation to predict the performance of polymer flooding in any type of reservoir. His model, however, was missing the component of in-situ non-Newtonian behavior of polymer, which was later found to be fundamental in polymer flooding mechanisms. Bondor et al. (1972) added the polymer in-situ rheology impact through using modified Blake-Kozeny power law for fluids [10]. They also included the impact of other factors such as permeability reduction and non-linear mixing of polymer and water. Seright (1983) developed an analytical model for injectivity in radial coordinates [11]. His model combined a mechanical degradation correlation, linear core flood results of resistance factor and Darcy equation in radial flow, to calculate total injection pressure drop. Recently, Lotfollahi et al. (2016) have proposed an injectivity model to simulate polymer injectivity decline in both laboratory and field tests [12]. Their model coupled the effects of deep-bed filtration and external filter-cake formation caused by polymer adsorption/retention, to the viscoelastic polymer rheology. They also emphasized the advantage of using radial coordinates with a fine gridding scheme to reduce the error of velocity calculation in the near-wellbore area and hence capture polymer rheology more accurately. Some commercial reservoir simulation software have also included modules to model polymer flooding such as STARS of Computer Modeling Group Ltd. (CMG), ECLIPSE 100 of Schlumberger, and REVEAL of Petroleum Experts [13]. The simulator used in this study is STARS of CMG, which includes polymer modules that accounts for polymer rheology dependence on the shear rate or velocity, polymer adsorption, permeability reduction and impact of polymer concentration and salinity on viscosity.

This study aims to utilize numerical simulation of polymer flooding on both lab and field scales in order to optimize the design of field polymer injectivity tests. The main objective is to analyze the relationship between the injector bottom-hole pressure (BHP) and polymer in-situ rheology. Beside rheology, the impact of simple heterogeneity is also investigated along with the impact of permeability reduction because of polymer adsorption in low-permeability layers. This is to simplify the process of interpreting field tests data, since the sole source of data in the field is usually BHP variations with time and BHP as a function of different injection rates.

## 2. Materials and Methods (Lab Scale)

The radial flow experiment history matched in this paper was performed on a circular Bentheimer disc (radius = 15 cm, thickness = 2 cm, injection well radius = 0.325 cm and porosity = 0.25). Before oil was introduced, absolute permeability was measured and was equal to 2200 mD. The sample was prepared according to the method described in the literature for circular Bentheimer discs with internal pressure taps [6,7]; including ageing with heavy crude oil, followed by brine flooding to residual oil saturation of 0.34. Pressure ports were mounted both internally and in an injection well and producer, as depicted in Figure 1.
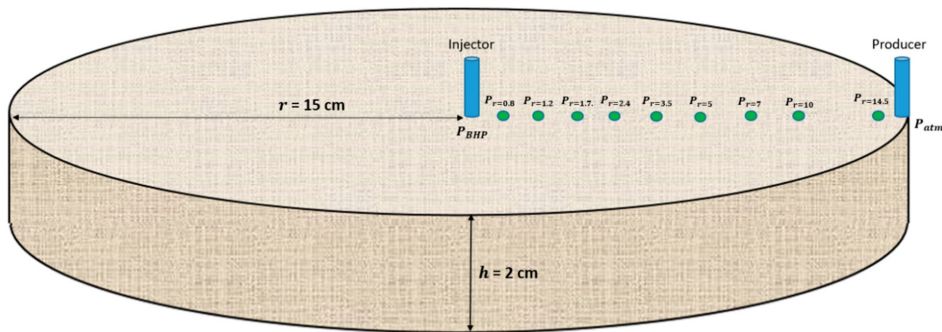


**Figure 1.** Illustration of the circular Bentheimer disc with pressure ports.

A relatively low salinity brine (7000 ppm TDS) was used in this study, with a viscosity of 1.02 cP at 22 °C. A 1000 ppm HPAM polymer solution was used (Flopaam 3330S, 8 MDa, 30% hydrolysis, SNF Floerger) and prepared according to the API method (RP 63, 1990, American Petroleum Institute). Shear viscosity of the polymer solution was measured to be 11.5 cP at $10\,\text{s}^{-1}$, with zero shear viscosity extrapolated to 13.9 cP. It was concluded that negligible mechanical degradation occurred based on injected versus effluent viscosity measurements.

Initially, the brine solution was injected at ten different flow rates (0.05–2 mL/min) and effective permeability to brine ($k_{b,init}$) was calculated from Darcy's law for radial flow:

$$k_{b,init} = -\frac{\mu Q}{2\pi h \Delta} \quad \frac{r_i}{r}$$

where $\mu$ is brine viscosity, $Q$ is volumetric injection rate, $h$ is disc thickness, $\Delta P$ is the pressure drop between a specified port at radius $r_i$ and the producer at $r$.

Following the initial brine flood, a 1000-ppm HPAM solution was injected at similar injection rates (0.05–2.0 mL/min). Before measurements began, the polymer solution was injected at 0.1 mL/min for at least two pore volumes to ensure that retention was satisfied. Tapering was also performed and the final step of the radial polymer flood experiment consisted of a final brine flood to determine the permeability after the polymer flood and to calculate the residual resistance factor (RRF), which was

equal to 1.2 for this experiment. Since permeability values obtained from initial brine flood was used in simulations, apparent viscosity is equal to resistance factor (RF) in this paper, where RF is defined as:

$$RF = \frac{\Delta P_p}{\Delta P_{b,init}}$$

where $\Delta P_p$ is the pressure drop during polymer flow and $\Delta P_{b,init}$ is the pressure drop during brine flow before polymer was introduced to the porous media.

*Simulation of Radial Flow Experiments*

A radial grid with 360 sectors constituted the simulation model. Each of these sectors consist of 150 grid blocks, where the grid block cell size was 1 mm. Sensitivity analysis showed a negligible accuracy improvement when reducing the grid block size below 1 mm. Residual oil saturation after the brine flood resulted in a non-uniform oil saturation profile between the injector and producer. The history match of the brine differential pressure between internal pressure ports and the producer enabled determination of local permeabilities. Since Bentheimer sandstone is assumed to be homogeneous, the average effective permeability was used together with local permeabilities to calculate correction factors accounting for the non-uniform oil saturation.

## 3. Results and Discussion (Lab Scale)

Average effective permeability was 33.8 and 28 mD using the differential pressure response from the initial and final brine flood, respectively. Injection BHP build-up was also recorded for each individual injection rate during both brine floods as shown in Figure 2.
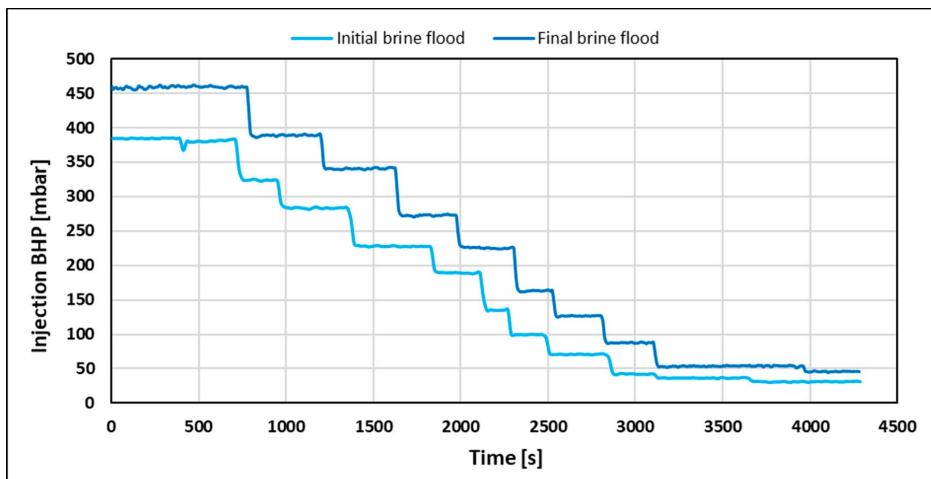


**Figure 2.** Injection bottom-hole pressure (BHP) versus time for initial (prior to polymer flood) and final brine flood (after polymer tapering).

Injection BHP stabilization time was independent of volumetric injection rate and equal to 40 s for both brine floods. However, pressure stabilization was expected to occur instantaneously when injecting a Newtonian fluid. Thus, it was concluded that the system had a delay of 40 s. The delay was attributed to incomplete pressure communication due to low values of counter pressure from the production line (2–4 mbar). To investigate if stabilization time is dependent on polymer rheology, the injection BHP build-up for the polymer (Figure 3) was also recorded.
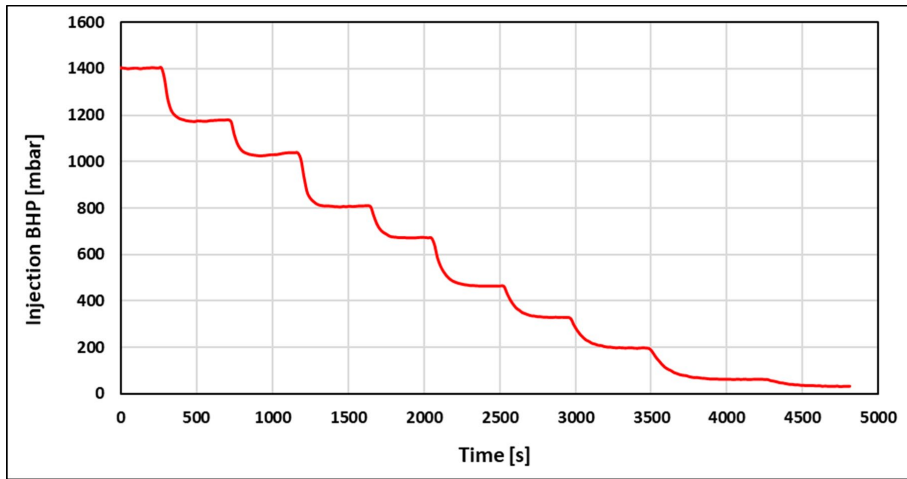
**Figure 3.** Pressure build up for the 1000-ppm polymer flood.

Injection BHP build-up from the polymer flood was clearly distinguishable from the Newtonian pressure response obtained from brine floods. Firstly, pressure stabilization time during the polymer flood was significantly higher (3–9 times) than for brine floods. In addition, stabilization time increased monotonically with decreasing volumetric injection rate (from 140 at 2 mL/min to 360 s at 0.05 mL/min). This suggests that the polymer rheology behavior is different at low compared to high injection rates.

To quantitatively analyze the polymer rheology of the 1000-ppm HPAM solution in the presence of residual oil, stabilized polymer pressure response was history matched as a function of both the volumetric injection rate, dP(Q), and radial distance, dP(r):

- dP(Q): Analogue to conventional polymer rheology estimation from field data, pressure drop across the entire disc (injection BHP) is history matched as a function of the volumetric injection rate, yielding a single rheology curve. Since injection BHP is influenced by near-well effects such as skin and mechanical degradation, the robustness and accuracy of this method may be debatable.
- dP(r): Using only internal pressure ports, the pressure drop between individual ports and the producer is history matched as a function of the radial distance, yielding an individual rheology curve for each volumetric injection rate. This method excludes the near-well effects mentioned above and will provide local rheology curves for each injection rate, spanning different velocity intervals of the complete rheology curve.

History match of injection BHP as a function of the volumetric injection rate (Figure 4) shows excellent agreement with the polymer pressure response. The history match error, defined in accordance with Gogarty, W.B. 1967, was 2.38% [14]. The history match of internal pressures as a function of radial distance (Figures 5 and 6) also showed very good agreement with the polymer pressure response. Here, the average of history match errors was equal to 2.94%.
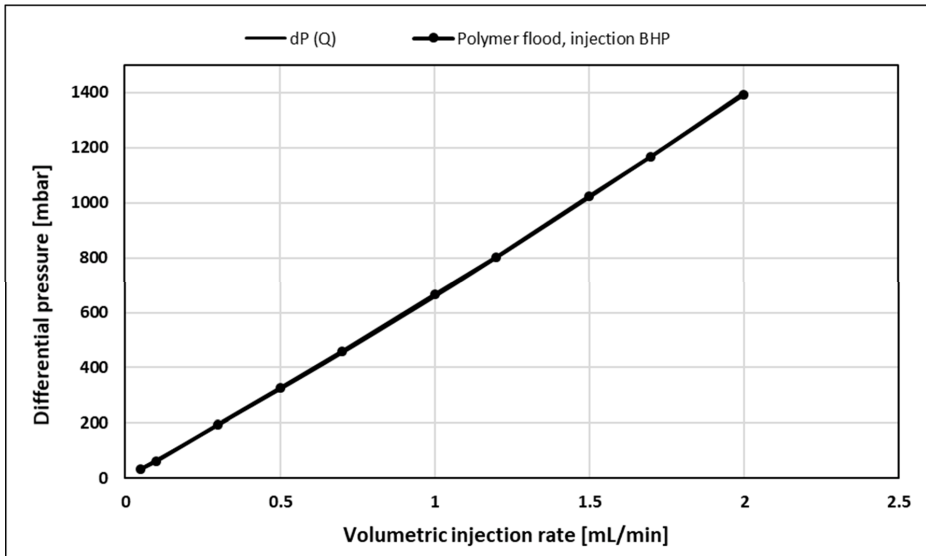
**Figure 4.** History match of injection BHP as a function of volumetric injection rate, dP(Q), for polymer flood.
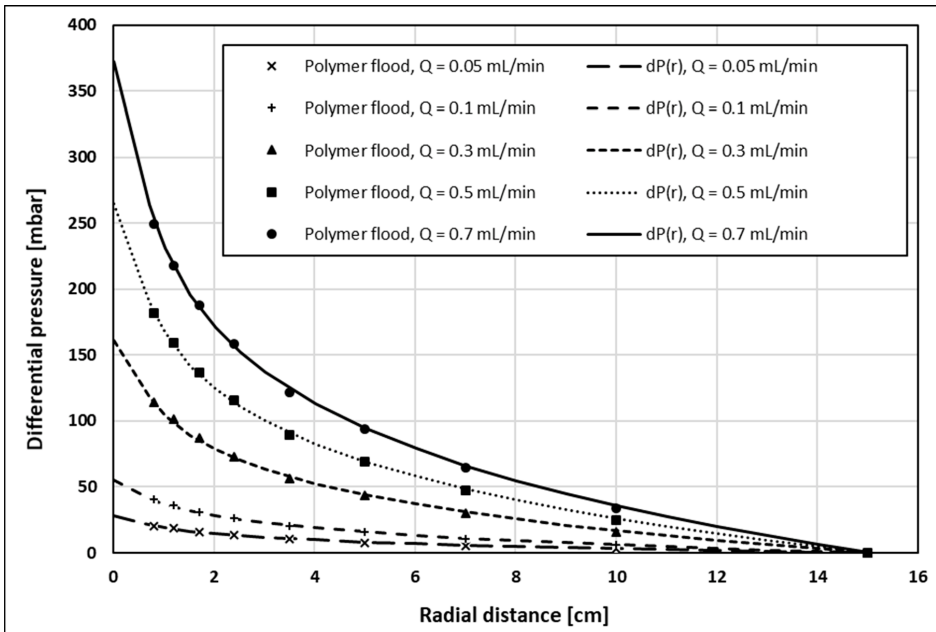


**Figure 5.** History match of internal pressures as a function of radial distance, dP(r), for volumetric injection rates of 0.05–0.7 mL/min.
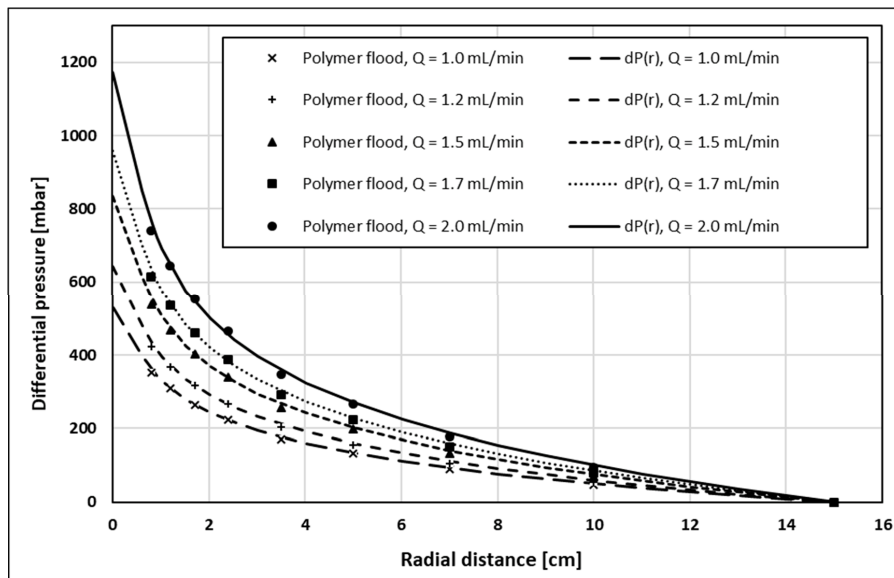
**Figure 6.** History match of internal pressures as function of radial distance, dP(r), for volumetric injection rates of 1.0–2.0 mL/min.

Polymer rheology curves obtained from both history match methods are shown in Figure 7. Since permeability obtained from the initial brine flood (before polymer flood) was used, apparent viscosity is represented by RF. Here, polymer rheology curves obtained by history matching differential pressure as a function of radial distance from the injection well are denoted dP(r). Using this history match method, individual rheology curves are obtained for each volumetric injection rate. However, since each curve was obtained at different injection rates, their maximum velocities at the injection point and their minimum velocity at the production rim were different. Rheology curves obtained at the lowest injection rates spanned the lower velocity interval, and were representing the shear-thinning rheology regime. In contrast, the highest injection rates spanned the higher velocity interval where the polymer behavior was increasingly shear-thickening. Even though they represent different injection rates and resulting velocity ranges of the polymer rheology, overlapping rheology curves were obtained, thus excluding the occurrence of rate effects. In addition, differential pressure was history matched as a function of the volumetric injection rate using injection BHP. This curve is denoted dP(Q) and shows the same shape as the remaining rheology curves.

Therefore, all polymer rheology curves show approximately the same functional relationship (shape) and two distinct flow regimes: Shear dominant flow is occurring at low to intermediate rates while extensional dominant flow is predominant in the high velocity regime. This rheology behavior is in accordance with the injection BHP build-up response where stabilization time was decreasing with injection rate, thus representing the transition from shear thinning behavior at a low rate to shear thickening behavior at higher injection rates.
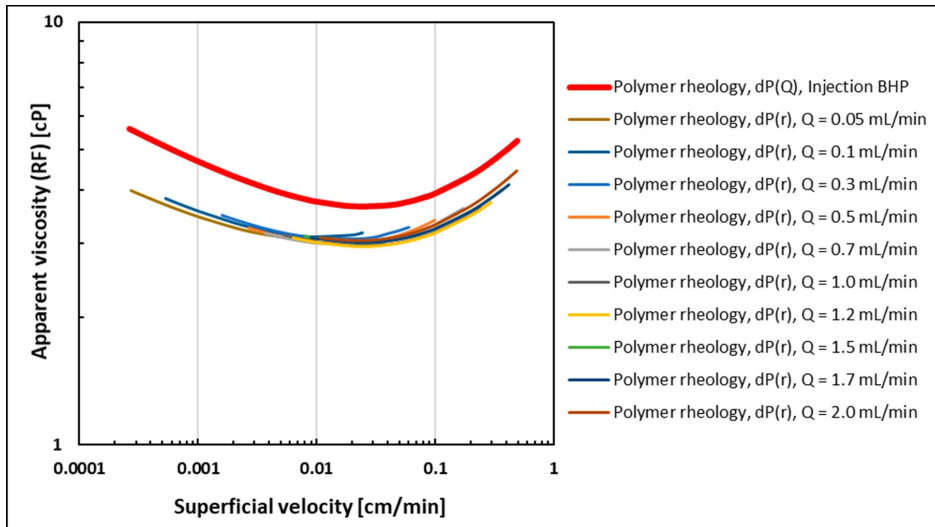
**Figure 7.** Polymer rheology curves obtained from history matching injection BHP as a function of the volumetric injection rate (red) and internal di*ff*erential pressures as a function of radial distance (remainder of curves).

The parallel shift between rheology curves obtained from injection BHP versus curves obtained from internal pressures is a consequence of performing history matches using the initial permeability (before the polymer is introduced). Since pressure measurements were conducted after retention was satisfied, permeability would be reduced both internally mainly due to adsorption, but also at a greater extent in the near wellbore region due to mechanical entrapment of polymer molecules. The greater local permeability reduction in the wellbore region versus the internal reduction would induce a higher pressure response for injection BHP and thus e*ff*ectively shift the apparent viscosity to higher values due to retention e*ff*ects. However, the consistency between the functional relationship obtained from injection BHP and internal pressures shows that injection BHP is a robust tool for estimating in-situ polymer rheology.

## 4. Field Scale Simulation Approach

A radial model was built using CMG STARS to simulate the field-scale polymer injection test at several injection rates for di*ff*erent in-situ rheology cases. The objective was to confirm the findings from the lab scale experimental and simulation studies in order to assess the design of polymer injectivity tests and define in-situ rheology signatures on BHP responses.

The model was used to test three di*ff*erent in-situ rheology behaviors: Shear thinning only, shear thickening only and shear thickening followed by shear thinning (combined). These three cases represent nearly all possible in-situ rheology behaviors expected in the near wellbore area of a polymer injector. The shear thinning case is representative for xanthan biopolymer, as well as types of synthetic polymers (such as HPAM) at certain low molecular weight and/or low concentrations, where shear flow dominates the in-situ behavior of polymer even at high shear [7]. In contrast, at certain high molecular weights or high concentrations, synthetic polymers might observe only shear thickening behavior in the near-wellbore region if they were dominated by extensional flow for the whole spectrum of encountered shear rates, shadowing the thinning behavior even at low shear rates. The third case (combined) represents the in-situ behavior observed in the lab for synthetic polymers where apparent shear thickening occurs at high shear rates followed by shear thinning away from the injection point.

Generic in-situ rheology curves were constructed using a modified version of the extended Carreau model introduced by Delshad et al. 2008 that relates apparent viscosity to Darcy velocity and includes both shear and extensional components [15]:

$$\mu_{app} = \mu_\infty + (\mu_0 - \mu_\infty) * \left[ 1 + (\lambda_1 u)^2 \right]^{\frac{n_1-1}{2}} + \mu_{max} * \left[ 1 - e^{-[\lambda_2 u]^{n_2-1}} \right]$$

where $\mu_{app}$ is polymer apparent viscosity, $\mu_\infty$ and $\mu_0$ are limiting Newtonian viscosities at high and low shear limits, respectively, $\lambda$ and n are empirical polymer constants, $u$ is the superficial velocity of the polymer in porous media and $\mu_{max}$ is the shear-thickening plateau viscosity.

Using this equation, apparent viscosity was calculated for the range of expected velocities in the near-wellbore region for all injection rates (Figure 8). The first part of the equation (shear flow component) was used for the shear thinning only case while the second part (extensional flow component) was used for the shear thickening only case. The sum of both parts was used for the combined rheology case. In order to ensure coverage of the entire expected velocity spectrum encountered in the reservoir, the model was first tested with the highest and lowest injection rates, then the velocity profiles were used as references for the rheology calculation. "$\mu_\infty$" was set at 1 cp since it represents pure solvent viscosity (water in our case). Other viscosity terms in the equation ($\mu_{max}$ and $\mu_0$) represent the endpoints of the rheology curve and can be obtained from lab measurements with reasonable accuracy. Both were assumed at 10 cp in our study. $\lambda$ and *n* parameters were tuned so that the curves are smooth and consistent for all rheology cases without compromising model stability. The sensitivity of shear thinning and shear thickening curves to $\lambda$ and n parameters is illustrated in Figures A1–A4. Table 1 below shows a summary of the extended Carreau model parameters used for rheology curves.
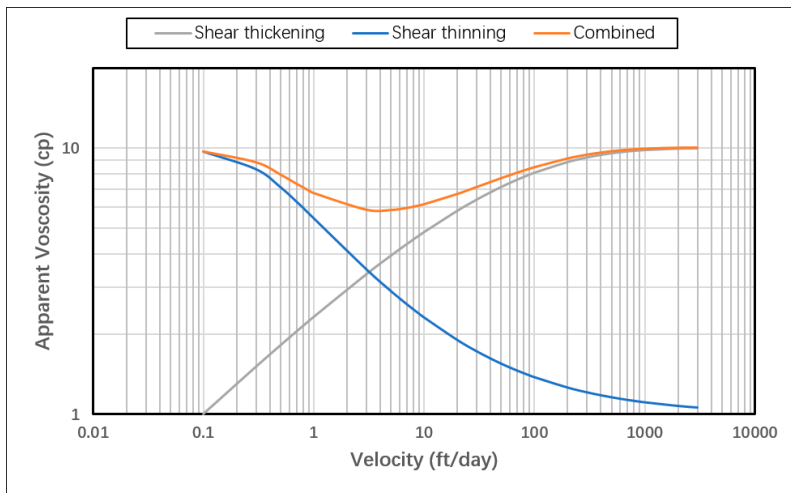


**Figure 8.** In-situ rheology curves obtained using extended Carreau model

**Table 1.** Extended Carreau model parameters used for rheology cases.

| $\mu_\infty$ | $\mu_0$ | $\lambda_1$ | $n_1$ | $\lambda_2$ | $n_2$ | $\mu_{Max}$ |
|---|---|---|---|---|---|---|
| 1 | 10 | $1.0 \times 10^6$ | 0.46 | $1.0 \times 10^4$ | 1.4 | 10 |

### 4.1. Model Description

The radial coordinates system was selected to minimize the error in the velocity calculation induced by the smear of the velocity front in the Cartesian gridding scheme. A grid system of exponentially increasing grid size was applied for the near-wellbore area around the injector up to a 100 ft. radius (Figure 9). This gridding scheme was selected in order to accurately capture the expected exponentially decreasing velocity profile, and to improve simulation e*ffi*ciency by avoiding unnecessary fine gridding further away from wellbore. The size of the innermost grid (injector grid) was set at 0.41 ft. while the size of the outermost grid was 5.58 ft. with a total of 60 grids in the radial direction.
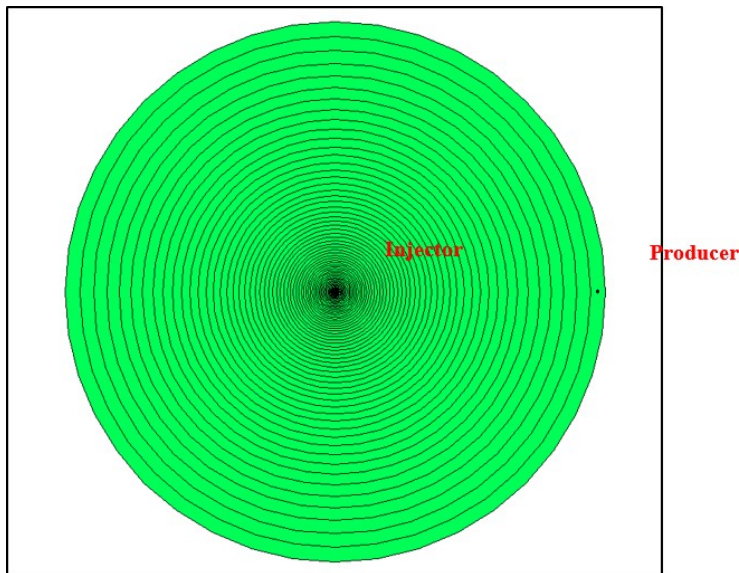


**Figure 9.** 2D aerial map showing the radial gridding scheme of the model.

This gridding system was generated automatically through the CMG Builder tool by defining a specific outer radius, the number of grids along the radius, and the size of the inner-most grid size (well grid). The arbitrarily selected grid sizing was based on the criterion of achieving su*ffi*ciently fine grids around the well-bore while maintaining model stability over all encountered viscosities at all injection rates. This is based on the fact that the finest-grid case represents the closest approximation to the realistic Darcy velocity at the wellbore sand-face and near-wellbore region, which is the only parameter that influences the predefined non-Newtonian viscosity functions that are inputted in the model as viscosity–velocity tables. Hence, grid sensitivity was not an issue of concern in this study.

Likewise, the model radius selection was subjective since it may not represent actual near-well bore area in many reservoirs as it varies widely based on reservoir properties. However, the radius was assumed at 100-ft to cover a wider spectrum of Darcy velocities/shear rates since the main objective is to inspect theoretical in-situ rheology impact on injection pressure rather than representing actual field cases. Therefore, the model was also assumed to be homogenous with no fractures or faults and saturated with water only.

Other factors that might impact BHP such as polymer adsorption and compressibility were not included as well. Polymer was injected at 800 ppm concentration represented by a $1.8 \times 10^{-6}$ mole fraction input. Polymer adsorption was neglected and linear mixing rule was assumed between

polymer and water viscosities. The range of tested rates is between 1000 and 10,000 bbl/day, which covers typical injection rates in field applications. The parameters of the model are summarized in Table 2 below.

**Table 2.** Basic parameters and assumptions of the field scale model.

| Parameter | Value |
|---|---|
| Well type | Vertical |
| Thickness | 50 ft |
| Injector grid size | 0.41 ft |
| Porosity | 15% |
| Permeability | 100 mD |
| Initial water saturation | 100% |
| Reservoir pressure | 2000 psi |

### 4.2. Producers Pattern Sensitivity

A simple sensitivity study was performed to assess the impact of the number of producers on the simulation output in order to optimize the model's pattern selection. The aim was to isolate the effect of polymer's non-Newtonian viscosity by increasing the number of producers placed at the model's outermost grids and thus eliminating a no-flow boundary impact on the injection pressure response. However, this may come at the price of increasing computation time by increasing the total number of grids in the model and hence lowering the simulation efficiency. The examined producer patterns were one producer only, two producers, four producers (five-spot), eight producers (nine-spot) and 12 producers. Figure A5 shows 2D maps of producer pattern sensitivity cases. Figure 10 shows the BHP response for each pattern under the conditions of an injecting polymer at 6000 bbl/day with a shear thickening in-situ rheology. The case with one producer shows a significant boundary effect after injecting 1 PV while the nine-spot and 12-producers patterns shows almost a no boundary effect. It takes 20 s to run the case with one producer compared to 120 s for the 12-producers case. It was decided that a nine-spot pattern was the most suitable for the purpose of this study, since the results were very close to the 12-produers case while simulation efficiency was not compromised significantly.
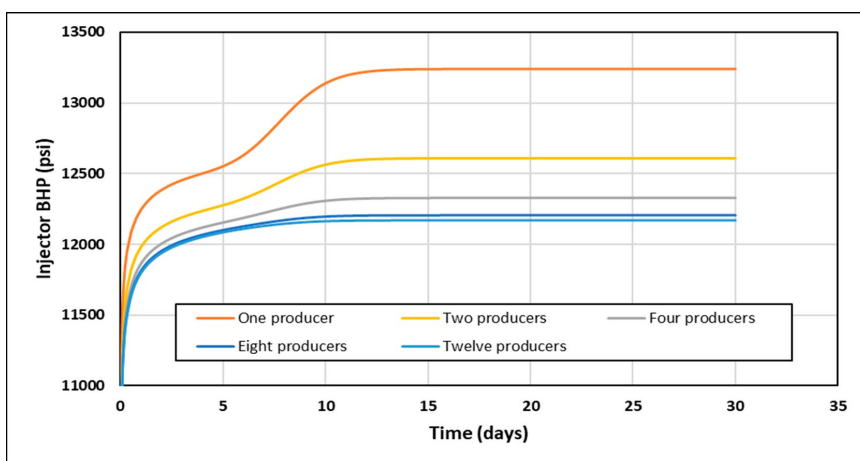


**Figure 10.** BHP response for each producer pattern at 6000 bbl/day with a shear thickeningin-situ rheology.

### 4.3. Viscosity Mixing in the Reservoir

One of the concerns when modeling polymer flooding is the mixing of polymer viscosity with other reservoir fluids viscosities, especially at the front of polymer slug. As the front is progressing, polymer viscosity behind it is following the predefined viscosity–velocity functions of the model. However, the viscosity ahead of the front will follow a viscosity mixing rule that creates a transition between polymer viscosity and reservoir fluid viscosity (Figure 11), and hence it would have an impact on the injector's BHP that does not follow input viscosity functions. To isolate the non-Newtonian behavior effect on injector's BHP, a minimum of 1 PV of polymer is required to be injected in order to achieve the intended viscosity profile within the near-wellbore region (Figure 12). In this study, STARS default linear mixing rule was applied between polymer and water viscosities.
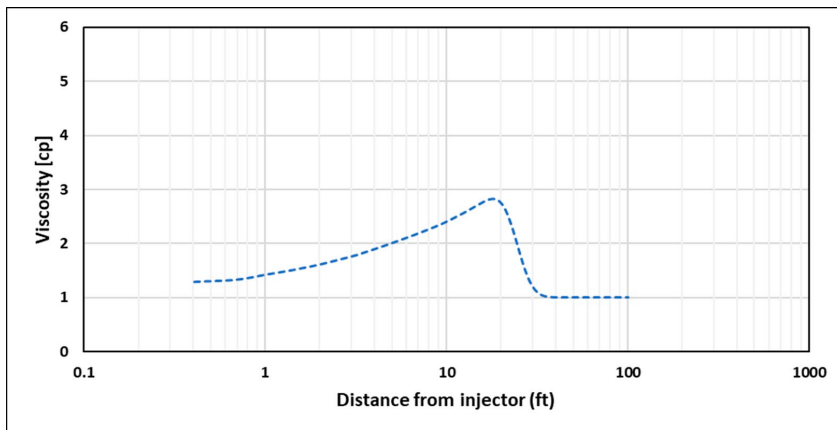


**Figure 11.** Viscosity profile after injecting 0.06 PV at 5000 bbl/day for shear thinning rheology.
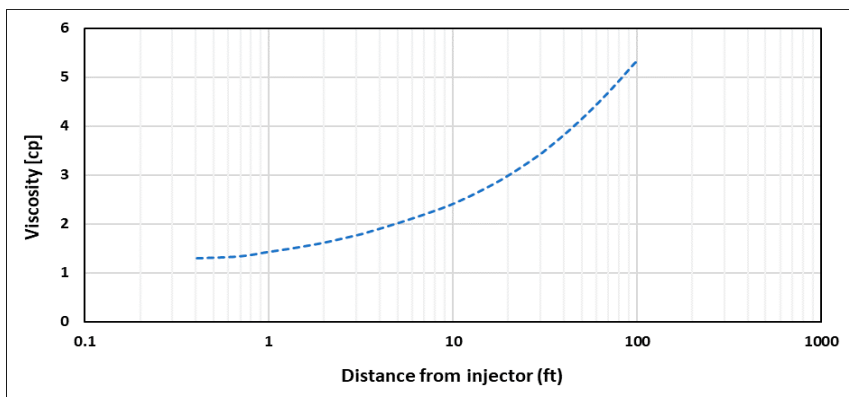


**Figure 12.** Viscosity profile after injecting 1 PV at 5000 bbl/day for shear thinning rheology.

### 4.4. Impact of High-Permeability Layers and Residual Resistance Factor

Heterogeneity of reservoirs adds more complexity to the challenges in determining in-situ rheology of a polymer from the injectivity test data. The presence of thief zones such as high permeability layers, open fractures, vuggy channels, etc., exposes the polymer to several different shear fields in the reservoir and creates the possibility of having several in-situ rheology behaviors occurring at the same

time in different locations. Besides, the skin effect induced by polymer adsorption and/or mechanical entrapment in low permeable zones is another factor to be considered when tackling heterogeneity. The skin effect is usually addressed through the residual resistance factor (RRF), which is a parameter measured in lab core-floods and defined as the ratio between differential pressure after and before polymer injection.

To test the impact of different polymer in-situ rheology on layered reservoirs, the base model was modified to have alternating high and low permeability layers. High permeable zones were assigned a permeability value of 1000 mD, while low permeability zones were at 100 mD (Figure 13). The same rheology curves used for homogenous cases were used to ensure consistency of comparison. To test the impact of polymer adsorption and retention on low permeability zones, an extra case was investigated where an RRF value of two was set to the 100-mD layers while maintaining no adsorption (RRF = 1) in the high permeability layers.
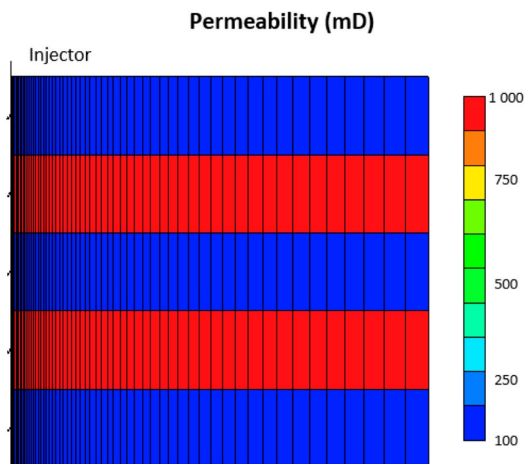


**Figure 13.** Cross section view showing the permeability distribution in the layered reservoir case.

## 5. Results and Discussion (Field Scale)

Results of simulations were used to plot stabilized BHP versus injection rate and time for homogeneous and layered cases at different in-situ rheology conditions.

### 5.1. Homogeneous Case

Figure 14 shows BHP versus injection rate for the homogeneous cases. The BHP was fitted to a second order polynomial. The coefficient of second order term is positive or negative dependent on the type of rheology. It was found that stabilized BHP trend has an increasing slope for shear thickening only and a decreasing slope for the shear thinning only cases. The combined rheology showed a combination of increasing and decreasing slopes along the trend. This is attributed to the effect of shear thickening behavior for high shear rate near-wellbore, and shear thinning behavior for lower shear rates further away.
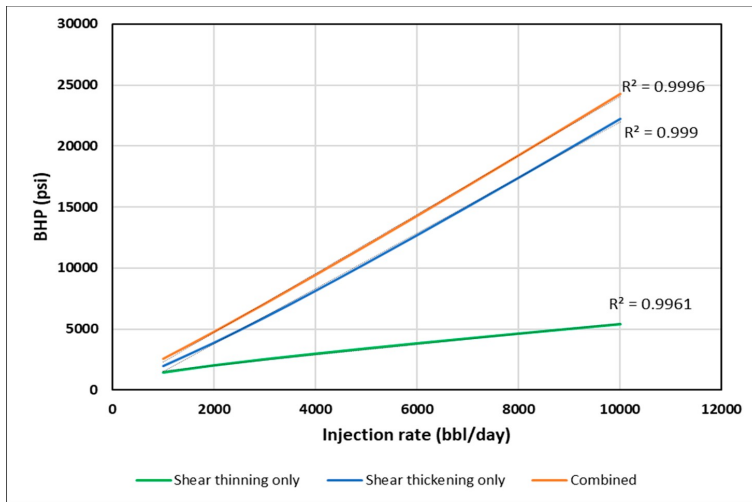
**Figure 14.** Stabilized BHP versus injection rate for different in-situ rheology in the homogeneous case.

As discussed earlier, stabilized pressure is not reached until at least 1 PV of the polymer is injected, as viscosity mixing at the front is eliminated and the steady-state condition is reached. This interval, however, is too long for polymer injectivity tests where rate steps are usually much shorter. Hence, BHP was plotted at 0.001 PV, 0.01 PV and 0.1 PV for each rate, to confirm if the same signal could be obtained at early times with transient condition and the presence of viscosity mixing. The slopes of BHP trends become less distinct with shorter injection times (Figures 15–17). The slope change, however, is detectable by using the coefficient of second order polynomial trendline function (Table 3).
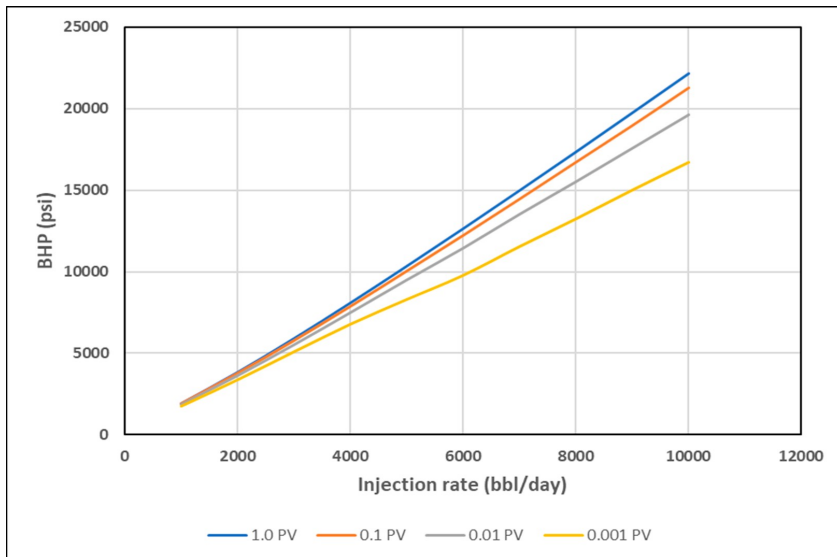


**Figure 15.** BHP vs. Q for shear thickening homogeneous case at different PVs.
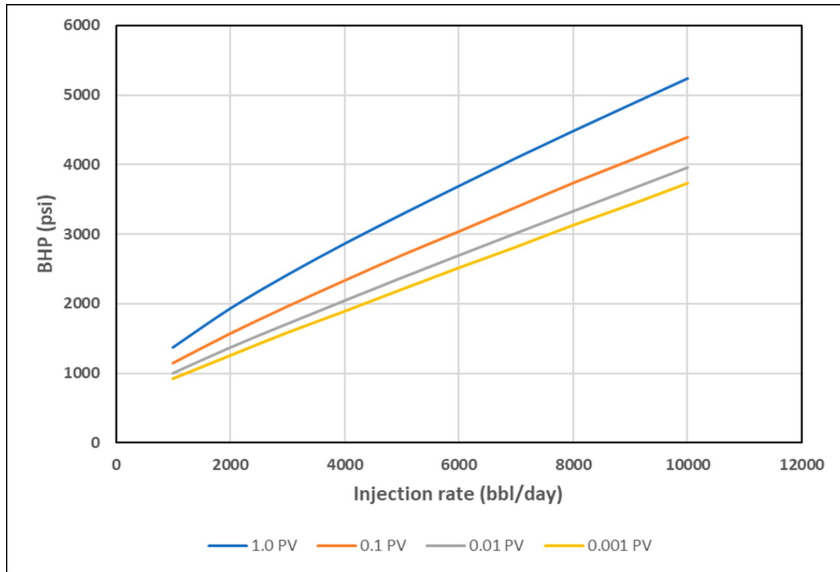
**Figure 16.** BHP vs. Q for shear thinning homogeneous case at di*ff*erent PVs.
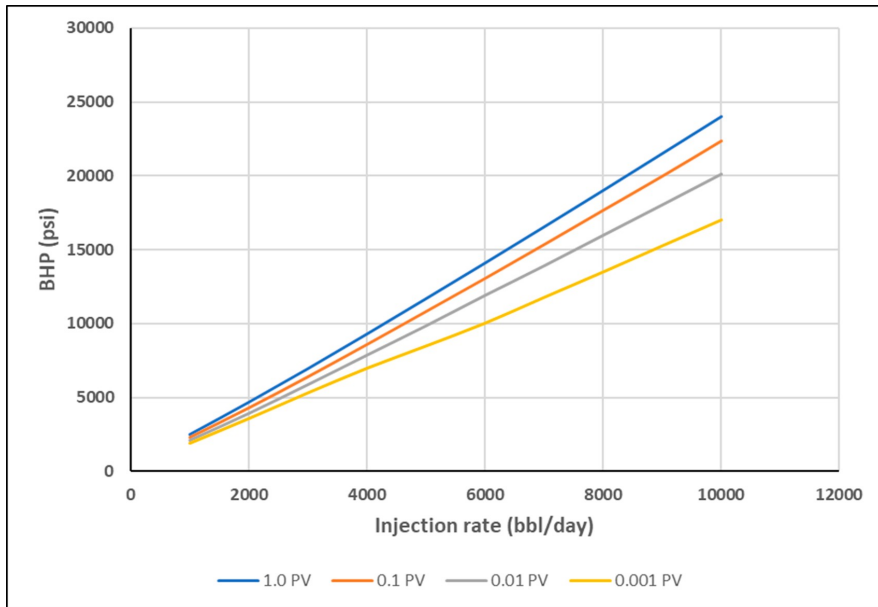


**Figure 17.** BHP vs. Q for combined rheology homogeneous case at di*ff*erent PVs.

**Table 3.** Coefficients of 2nd order polynomial trendline functions of BHP vs. injection rate at different injected PV's for different rheology cases.

| | Coefficient of 2nd Order Polynomial Trendline Function ($\times 10^{-5}$) | | | | | | | | | | | |
|---|---|---|---|---|---|---|---|---|---|---|---|---|
| | 0.001 PV | | | 0.01 PV | | | 0.1 PV | | | 1.0 PV | | |
| Rheology | High | Med | Low | High | Med | Low | High | Med | Low | High | Med | Low |
| Shear thinning | 0.8 | −0.4 | −0.2 | −0.03 | −0.3 | −1.0 | 0.3 | −0.4 | −2.0 | −0.2 | −0.5 | -4.0 |
| Shear thickening | −3.0 | 6.0 | 5.0 | −2.0 | 2.0 | 6.0 | 3.0 | 2.0 | 7.0 | 6.0 | 2.0 | 8.0 |
| Combined rheology | −1.0 | 6.0 | 3.0 | 0.9 | 0.5 | 6.0 | 4.0 | 1.0 | 5.0 | −0.05 | 1.0 | 4.0 |

Negative values indicate shear thinning while positive values indicate shear thickening. For more detailed analysis of the coefficients, injection rates were divided into three ranges: low range from 1000 to 3000 bbl/day, medium range from 4000 to 7000 bbl/day and high range from 8000 to 10,000 bbl/day. From the obtained coefficients one can see that shear thinning and shear thickening behaviors can be detected by negative and positive values, respectively, even if shorter injection rate steps were implied. However, the behavior is more detectable as the injection time increases. The combined rheology is generally showing shear thickening behavior (positive values) due to the fact that apparent viscosity gain is the first encountered behavior in the near well bore area. The outliers that show positive for shear thinning and negative for shear thickening are attributed to the viscosity mixing phenomena.

Although the signal is not significantly pronounced in the BHP vs. Q plots, the slope change verifies the significance of rate-stepping in polymer injectivity tests. A minimum of three rate steps is thought to be sufficient in order to be able to detect in-situ rheology near-wellbore since it would yield two slope points that can indicate an increase or decrease in viscosity. The rates selected have to be selected so that they cover high, medium and low ranges of expected in-situ velocity.

The second part of the analysis is focused on the BHP versus time plots. It was noticed that each in-situ rheology yields a distinctive signal during early times. Figure 18 shows, the BHP profile versus log time for each rheology at the injection rate of 5000 bbl/day. The shear thickening rheology reflects a sharp increase in BHP shortly after starting injection up to less than 0.005 PV. In contrast, shear thinning rheology is characterized by a gradual increase in BHP all the way to 1 PV. The combined rheology reflects a combination of the two behaviors of thickening and thinning. These signals are attributed to the viscosity that the injector "sees" first into the reservoir and then further away from it. These findings suggest that a minimum of 0.0001 PV of the near-well bore region may be sufficient to decide whether we encounter shear thickening or shear thinning rheology at the near wellbore area, however, the combined rheology would require longer periods of at least 1 PV to be detected through BHP versus time measurements. It is worth to note here that these findings are based on ideal case simulation results without considering other near well bore effects such as skin, fractures, filtrate cake, etc. Nevertheless, the suggested PV can be used as a base to analyze the BHP response near wellbore and to preassess in-situ rheology from early data obtained in the field.
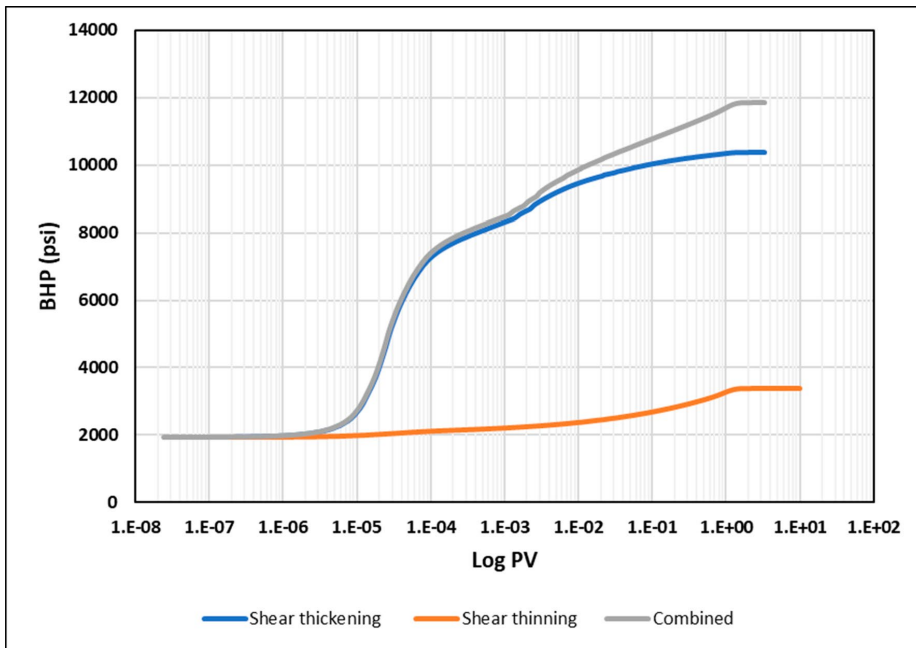
**Figure 18.** BHP versus log PV for different in-situ rheology at 5000 bbl/day in a homogeneous reservoir.

### 5.2. Layered Case

A basic heterogeneity case was investigated to observe the impact of high permeability streaks on the injection BHP compared to the homogeneous results. It is anticipated that high permeability layers can significantly enhance injectivity by lowering injection BHP. Nonetheless, we aim to find if heterogeneity can affect the distinctive signals of different in-situ rheology. The modified case is a layered reservoir with alternating high permeability (1000 mD) streaks (Figure 13). Figure 19 illustrates the BHP versus injection rate for the layered case. The trends of BHP responses are similar to the ones in homogeneous cases. This suggest that a similar method could be used for both homogenous and heterogeneous reservoirs. Besides, the signature on the BHP vs. log time is affected, and each rheology can be distinguished with the same characteristics observed in the homogenous case (Figure 20).
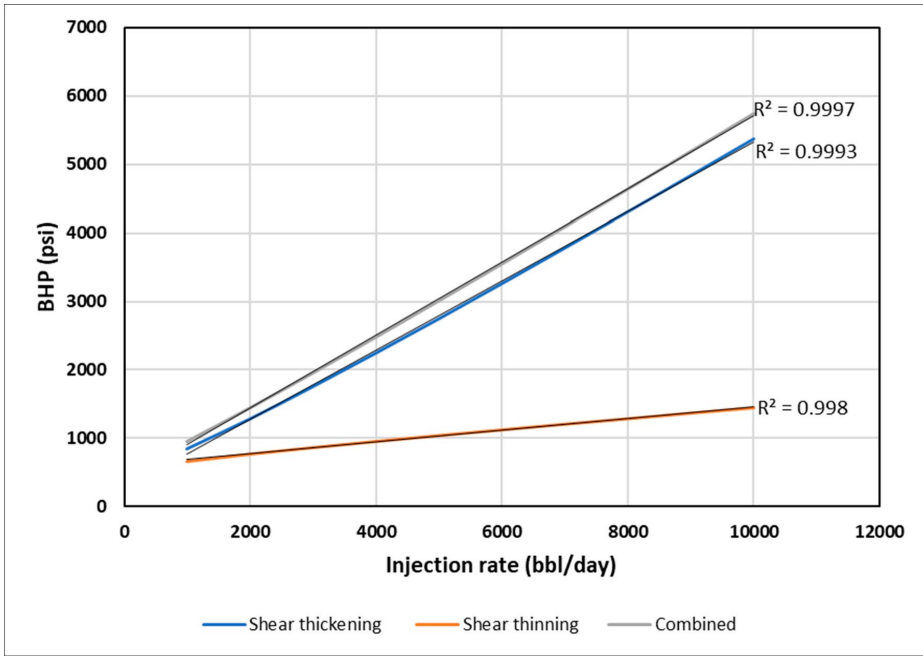
**Figure 19.** BHP versus injection rate for different in-situ rheology in the layered reservoir.
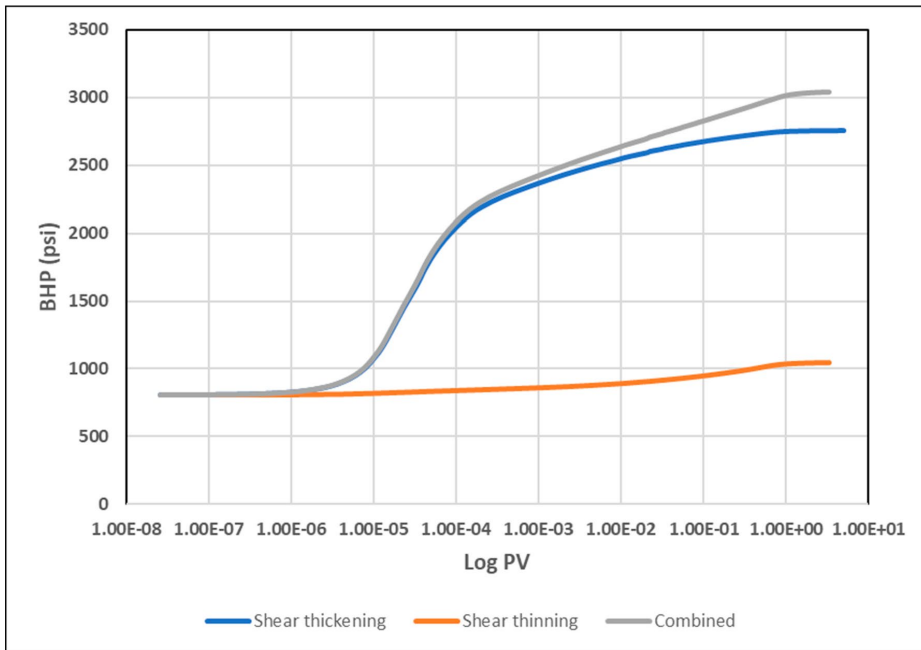


**Figure 20.** BHP versus log PV for different in-situ rheologies at 5000 bbl/day in the layered reservoir.

## 6. Conclusions

The findings presented in this study contribute to optimizing the design of polymer injectivity tests for enhanced oil recovery (EOR) polymer flooding projects. The main issue addressed was the impact of polymer in-situ rheology in porous media on the injector's BHP response, since BHP is the main—and sometimes the only—source of data available in field tests. We suggest from this study that adapting a rate-stepped scheme in polymer injectivity tests is of a significant benefit in optimizing our understanding of polymer in-situ rheology at reservoir conditions and hence optimizing the design of polymer injectivity tests based on each individual reservoir characteristics.

The main conclusions are based on two simulation approaches: (1) history matching the results of a radial water and polymer flood lab experiments, (2) using generic up-scaled field-size model to test the impact of different in-situ rheology on BHP.

The experiment results showed that it is possible to distinguish between water and polymer floods based on BHP pressure build-up time. Moreover, the experiment confirmed the ability to differentiate between different rheological regimes based on BHP pressure-build up time, where shear-thickening behavior stabilizes pressure quicker than shear thinning. Lab-scale simulation findings confirmed the injection BHP as a robust tool for estimating in-situ polymer rheology in radial flow in porous media.

The field-scale simulation approach confirmed that BHP could be used to obtain information about in-situ rheology if rate variation is included in the procedure of field polymer injectivity tests. The rate-variation should include a minimum of three rate steps covering the whole range of velocities from low to high. Respective BHP readings then are used to determine the polymer rheology behavior as it propagates into the reservoir.

Besides the rate variation, it is important to assess the time the pressure needs to stabilize so it can be representative of the rheology signal. The findings suggest that the time for pressure stabilization at a given injection rate, is slower for shear-thinning fluids, compared to Newtonian and shear-thickening fluids. In addition, combined rheology exhibits a combination of shear thickening and shear-thinning behaviors that can be detected from BHP vs. time. Although pressure stabilization is affected by viscosity mixing at the front and hence it is not achievable before at least 1 PV is injected, the results confirmed that a minimum of 0.0001 PV could still be used to detect rheology signal. That being said, one can obtain information from a stepped-rate injectivity test only when comparing equal injected PVs for each rate. This finding is highly subjective to the specific assumptions of the model, but it can be used as a rough estimate to decide minimum injection duration at each rate step.

Furthermore, for heterogonous-layered reservoirs, it was found that the method is still applicable, despite the fact the rheological signal is noticeably reduced.

For future studies, we recommend investigating the impact of other near well bore effects such as skin, fractures, filtrate cake, etc. In addition, the impact of viscosity mixing needs to be quantified and further assessed in order to have better understanding of its impact on BHP response.

**Author Contributions:** M.A.A. and J.G.J.: Simulation work, results analysis, and manuscript writing. A.S.: Results analysis and discussion. S.M., A.A.S. and Ø.P.: Reviewing the paper and following up. All authors have read and agreed to the published version of the manuscript.

**Conflicts of Interest:** The authors declare no conflict of interest.
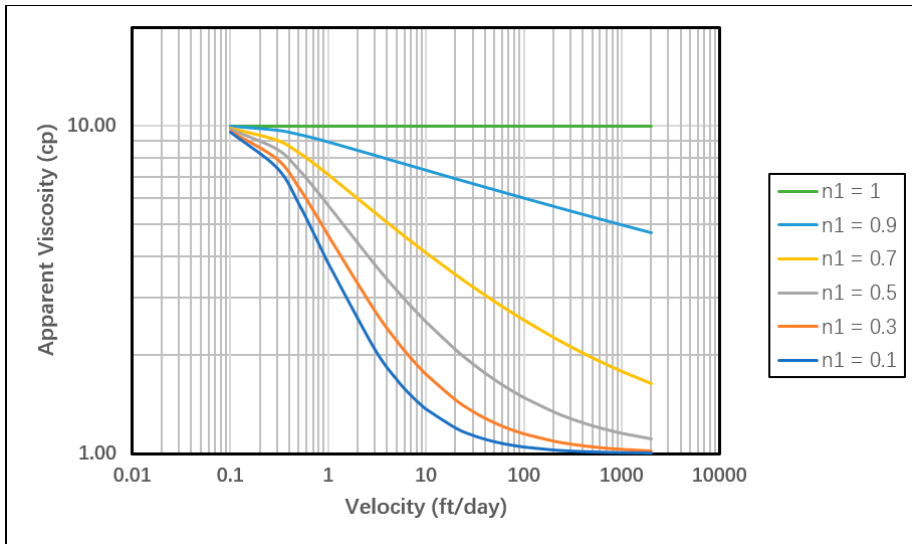
## Appendix A



**Figure A1.** Sensitivity of shear thinning curve to different n1 values.
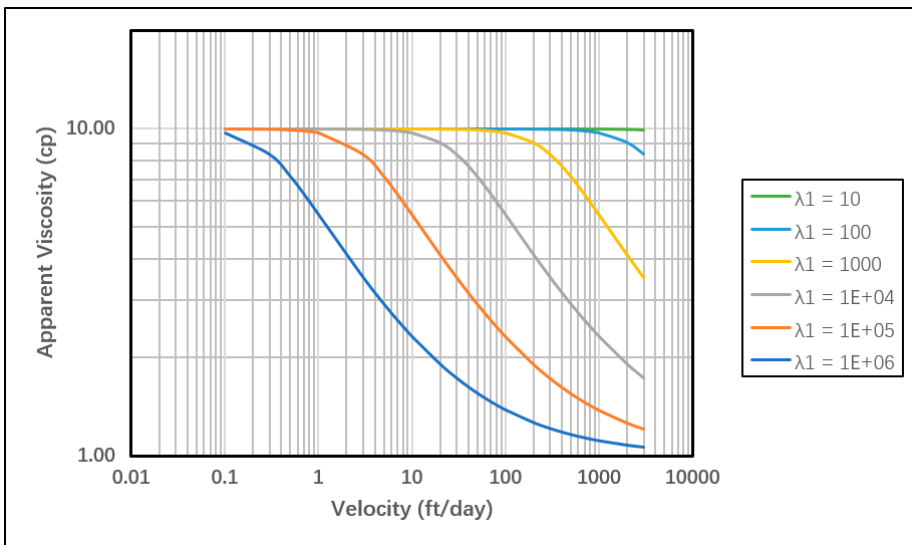


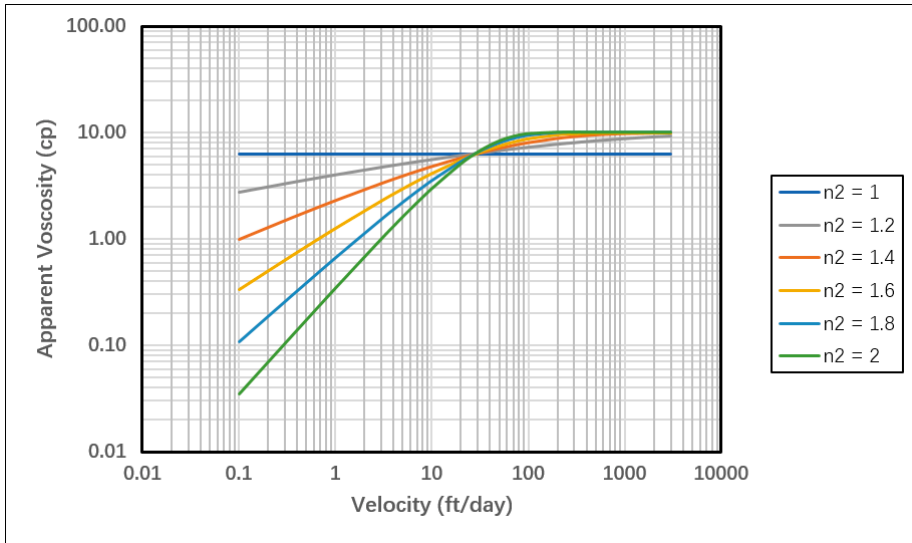**Figure A2.** Sensitivity of shear thinning curve to different λ1 values.

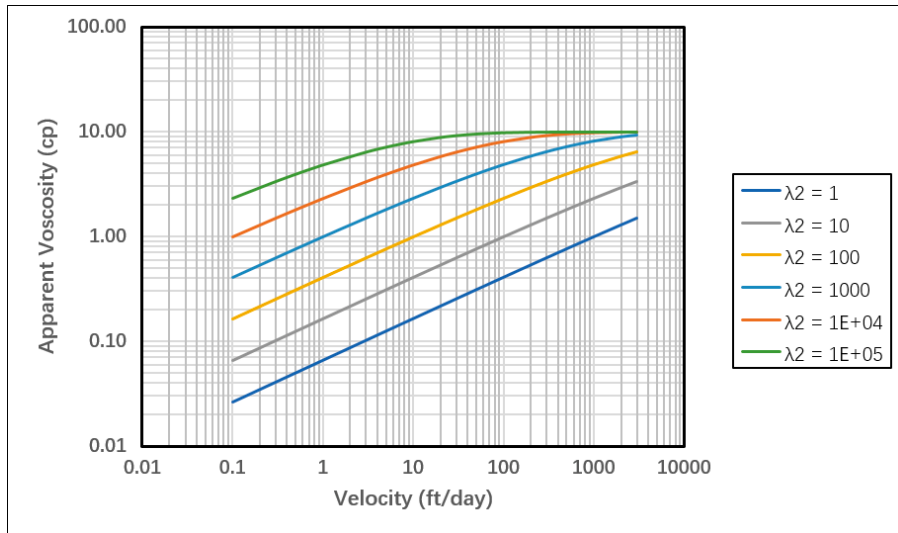**Figure A3.** Sensitivity of shear thickening curve to di*ff*erent n2 values.



**Figure A4.** Sensitivity of shear thickening curve to di*ff*erent λ2 values.
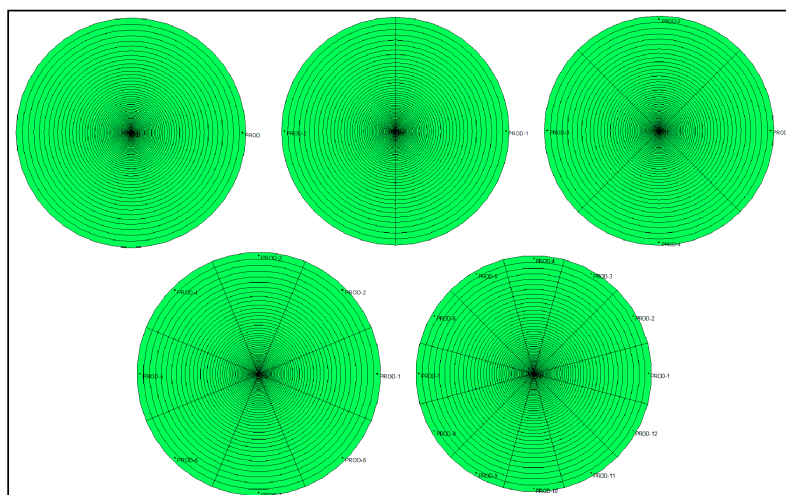
**Figure A5.** 2D maps of producer pattern sensitivity cases.

## References

1. Pope, G.A. The Application of Fractional Flow Theory to Enhanced Oil Recovery. *Soc. Pet. Eng. J.* **1980**, *20*. [CrossRef]
2. Masalmeh, S.; Hillgartner, H.; Al Mjeni, R.; Jing, X.D. Simultaneous Injection of Miscible Gas and Polymer (SIMGAP) to Improve Oil Recovery and Sweep Efficiency from Layered Carbonate Reservoirs. In Proceedings of the SPE EOR Conference at Oil & Gas West Asia, Muscat, Oman, 11–13 April 2010. [CrossRef]
3. Sheng, J.J.; Leonhardt, B.; Azri, N. Status of Polymer-Flooding Technology. *J. Can. Pet. Technol.* **2015**, *54*. [CrossRef]
4. Huh, C.; Pope, G.A. Residual Oil Saturation from Polymer Floods: Laboratory Measurements and Theoretical Interpretation. In Proceedings of the SPE Symposium on Improved Oil Recovery, Tulsa, OK, USA, 20–23 April 2008. [CrossRef]
5. Skauge, A.; Zamani, N.; Gausdal Jacobsen, J.; Shaker Shiran, B.; Al-Shakry, B.; Skauge, T. Polymer Flow in Porous Media—Relevance to Enhanced Oil Recovery. *Colloids Interfaces* **2018**, *2*, 27. [CrossRef]
6. Sorbie, K.S. *Polymer-Improved Oil Recovery*; Blackie and Son Ltd.: Glasgow, UK, 1991.
7. Skauge, T.; Skauge, A.; Salmo, I.C.; Ormehaug, P.A.; Al-Azri, N.; Wassing, L.M.; Glasbergen, G.; Van Wunnik, J.N.; Masalmeh, S.K. Radial and Linear Polymer Flow—Influence on Injectivity. In Proceedings of the SPE Improved Oil Recovery Conference, Tulsa, OK, USA, 11–13 April 2016. [CrossRef]
8. Al-Shakry, B.; Skauge, T.; Shaker Shiran, B.; Skauge, A. Polymer Injectivity: Investigation of Mechanical Degradation of Enhanced Oil Recovery Polymers Using In-Situ Rheology. *Energies* **2019**, *12*, 49. [CrossRef]
9. Zeito, G.A. Three Dimensional Numerical Simulation of Polymer Flooding in Homogeneous and Heterogeneous Systems. In Proceedings of the Fall Meeting of the Society of Petroleum Engineers of AIME, Houston, TX, USA, 29 September–2 October 1968. [CrossRef]
10. Bondor, P.L.; Hirasaki, G.J.; Tham, M.J. Mathematical Simulation of Polymer Flooding in Complex Reservoirs. *SPE J.* **1972**, *12*, 369–382. [CrossRef]
11. Seright, R.S. The Effectsof Mechanical Degradation and Viscoelastic Behavior on Injectivity of Polyacrylamide Solutions. *SPE J.* **1983**, *23*, 475–485. [CrossRef]
12. Lotfollahi, M.; Farajzadeh, R.; Delshad, M.; Al-Abri, A.-K.; Wassing, B.M.; Al-Mjeni, R.; Awan, K.; Bedrikovetsky, P. Mechanistic Simulation of Polymer Injectivity in Field Tests. *Soc. Pet. Eng. J.* **2016**, *21*. [CrossRef]

13. Goudarzi, A.; Delshad, M.; Sepehrnoori, K. A Critical Assessment of Several Reservoir Simulators for Modeling Chemical Enhanced Oil Recovery Processes. In Proceedings of the SPE Reservoir Simulation Symposium, The Woodlands, TX, USA, 18–20 February 2013. [CrossRef]

14. Gogarty, W.B. Mobility Control With Polymer Solutions. *Soc. Pet. Eng.* **1967**. [CrossRef]

15. Delshad, M.; Kim, D.H.; Magbagbeola, O.A.; Huh, C.; Pope, G.A.; Tarahhom, F. Mechanistic Interpretation and Utilization of Viscoelastic Behavior of Polymer Solutions for Improved Polymer-Flood E*ffi*ciency. In Proceedings of the SPE Symposium on Improved Oil Recovery, Tulsa, OK, USA, 20–23 April 2008. [CrossRef]

**Paper 3:**

**Analysis and Simulation of Polymer Injectivity Test in a High Temperature High Salinity Carbonate Reservoir**

*Article*

# Analysis and Simulation of Polymer Injectivity Test in a High Temperature High Salinity Carbonate Reservoir

**Mohamed Adel Alzaabi [1], Juan Leon Hinestrosa[2], Arne Skauge[1,3], Shehadeh Masalmeh[2]**

[1]   University of Bergen (UiB);
[2]   Abu Dhabi National Oil Company (ADNOC);
[3]   Energy Research Norway;

**Abstract:** Polymer flooding has gained much interest within oil industry in the past few decades as one of the most successful chemical enhanced oil recovery (CEOR) methods. The injectivity of polymer solutions in porous media is a major key factor in polymer flooding projects. The main challenge that faces prediction of polymer injectivity in field applications is the inherent non-Newtonian behavior of polymer solutions. Polymer in-situ rheology in porous media exhibits complex behavior that encompasses apparent shear thickening in addition to the typical shear thinning in bulk measurements. This shear-dependent behavior is usually measured in lab experiments with fair accuracy. However, data from field applications are usually limited to bottom-hole pressure (BHP) as the sole source of information. In this paper, we analyze BHP data from field polymer injectivity test conducted in a Middle Eastern heterogeneous carbonate reservoir characterized by extreme high-temperature and high-salinity (HTHS) conditions. The analysis involved incorporating available data to build a single-well model to simulate the injectivity test. Several generic sensitivities were tested to investigate the impact of rate stepping, concentration stepping, and residual resistance factor (RRF) dependence on permeability. Results demonstrated that non-Newtonian behavior can be distinguished from Newtonian one using BHP responses given the implementation of rate and/or concentration stepping. Non-Newtonian injection reflects a non-linear increase in pressure with injection rate as well as longer transient behavior toward steady state. In addition, results have shown the viability of using average RRF values over correlations. Besides, analysis of field BHP has proven the necessity of using complex in-situ rheology curves at several concentration levels to history match polymer injection.

**Keywords:** chemical EOR; polymer flooding; polymer injectivity; in-situ rheology; polymer simulation

## 1. Introduction

In polymer flooding CEOR technique, viscous polymer solutions are injected in oil reservoirs to improve sweep efficiency of water flooding by reducing mobility ratio between injected water and reservoir oil. This potential enhancement, however, comes in the expense of reducing well injectivity since higher viscosity results in higher injection pressure at a given injection rate. Generally, it is essential for any reservoir flooding process to estimate well injectivity under certain injection conditions based on reservoir properties with sufficient accuracy. Underestimating injectivity may result in injecting below required target rate and thus affecting project economics and objectives. On the other hand, overestimating injectivity can cause the well to operate under unfavorable fracturing conditions. Polymer injectivity can be more challenging to estimate due to polymers' complex non-Newtonian rheology in porous media. Unlike water, polymer solutions observe a shear-dependent

viscosity that generally follow a shear thinning pattern in bulk viscosity measurements, i.e. viscosity decreases with increasing shear rate. Nevertheless, numerous experiments and studies have shown that partially hydrolyzed polyacrylamide (HPAM), which is by far the most widely applied polymer in CEOR projects, exhibits a viscoelastic behavior characterized by apparent shear thickening above a critical shear rate in porous media. This behavior is referred to as extensional viscosity and it suggests that apparent viscosity of HPAM in near-wellbore region where shear rates are high, can be significantly larger than expected/measured lab viscosity. Many researchers have studied the factors that could increase, decrease, and/or delay apparent shear thickening in HPAM in lab-scale experiments. They concluded that this behavior is governed by both polymer and porous media properties. Skauge, A. et al (2018) [1] have summarized the effects of polymer concentration, polymer molecular weight, solution salinity, degree of hydrolysis, pressure, temperature, and porous media properties, on the onset and magnitude of apparent shear thickening in HPAM solutions. Beside in-situ rheology, inaccessible pore volume (IPV) and polymer retention due to adsorption and/or mechanical entrapment of polymer molecules may provide extra resistance to the flow and hence impair polymer injectivity. The impact of these factors is usually measured by RRF which is a measure of permeability reduction due to polymer retention in invaded reservoir zones.

Most lab experiments are conducted using nearly homogeneous samples under controlled conditions. The data obtained from these experiments are therefore abundant and can precisely describe polymer in-situ behavior. In contrast, data from field applications are rather limited and the only source of data is usually the injection BHP. Jacobsen, J. et al. (2020) [2] have demonstrated that it is viable to use pressure data to measure in-situ polymer rheology in radial flow systems. Their work was based on modeling and history matching radial polymer flow experiments conducted by Skauge et al. (2015) [3] on Bentheimer sandstone disc using HPAM. Moreover, Alzaabi, M. et al. (2020) [4] attempted to upscale these results to a generic field scale model in which various in-situ rheology curves were tested at different injection rates. They concluded that injection BHP can be utilized to evaluate polymer in-situ rheology given that rate variation was implemented in injectivity test procedure. They also investigated the impact of vertical heterogeneity and RRF and found that a BHP signal corresponding to a specific in-situ rheology could still be detected.

Injectivity tests on single wells are typically conducted prior to multi-well or full-field implementation of polymer flooding in order to establish the injectivity index of target reservoirs and assure that polymer can be pumped at targeted rates without issues. During injectivity tests, polymer solution is injected at multiple rates and/or concentrations to observe BHP response and gain information about reservoir effective permeability and skin zone radius. The majority of polymer flooding projects worldwide were conducted in sandstone reservoirs rather than carbonate reservoirs, mainly in low-temperature low-salinity formations. Sheng et al. (2015) [5] found that among 733 polymer flooding projects they surveyed, only 1/7th were implemented in carbonate reservoirs. Manrique et al. (2017) [6] stated that no polymer flooding projects in carbonate formations were documented after 1990. This is mainly due to the complex geology, heterogeneity, and relatively low permeability of carbonate formations compared to sandstones. Moreover, thermal stability and salinity tolerance of polymer solutions are among major limitations for applications in HTHS reservoirs [7]. Most of the proposed screening criteria for polymer flooding applications in the literature suggest a temperature below 100 °C and formation water salinity below 100,000 ppm for a successful implementation [5]. Recent studies have shown that stability of HPAM could be improved by introducing 2-Acrylamido-2-Methyl Propane Sulfonate (AMPS) as a copolymer [8 – 11]. They reported excellent thermal stability and salinity tolerance of SAV10, a high-AMPS-content acrylamide polymer manufactured by SNF, at temperatures between 120 and 140 °C and salinities up to 244,000 ppm.

This paper is aiming to demonstrate the robustness of using commercial reservoir simulator IMEX by Computer Modelling Group ltd (CMG) to predict SAV10 polymer in-situ rheology by history matching BHP data of a field injectivity test performed in a Middle Eastern heterogeneous carbonate reservoir. The test was the first of its kind to be performed ever in a HTHS carbonate formation.

**2. Field polymer injectivity test summary**

The single-well polymer injectivity test was performed as part of a larger project to implement full-field polymer flooding in a giant carbonate reservoir in the Middle East that is characterized by harsh temperature and salinity conditions up to 120 oC and 250,000 ppm, respectively [12]. The objective of the test was to evaluate polymer injectivity at target rates and concentrations in order to obtain information that would help optimizing the design of later stages in the project.

The reservoir is a Lower Cretaceous carbonate formation characterized by relatively high heterogeneity and stratigraphic cyclicity [13]. Reservoir's average thickness ranges from 150 to 300 ft. The major challenge that drove toward considering polymer flooding option in this reservoir is that it is divided into two main layers that have significant permeability contrast [14]. By implementing polymer injection in high permeability layer, vertical sweep efficiency can be improved by reducing crossflow between the two layers and thus preventing water channeling in high permeability layer and bypassing of oil in the low permeability layer.

According to Rachapudi et al. 2020 [12], a single water injection well was completed in the targeted high permeability zone with a perforation interval of 65 ft. Water injection baseline of 13 months was then established prior to polymer injection with rates ranging between 500 and 8000 bpd. During water injection, multi-rate production logging tool (PLT) logs were conducted to assess vertical injection distribution. Two acid stimulation jobs were also conducted to improve injectivity index. Subsequently, polymer injection phase started and spanned over 4.5 months period. Polymer injection was conducted on several sequences with variable polymer concentrations and injection rates. Moreover, injected polymer went through pre-shearing through dedicated shearing device prior to injection. Degree of pre-shearing ranged between 10% and 50%.

Two pressure fall off (PFO) tests were conducted during polymer injection phase to evaluate skin build-up and in-situ effective viscosity. PFOs interpretation through two-layer radial composite models showed increasing skin impairment with time and estimated in-situ effective polymer viscosity of 3 cp. Chase water injection continued after concluding polymer injection for about nine months.

**3. Simulation approach**

CMG IMEX commercial simulator was used to build a single-well radial model to simulate the injectivity test. The objective of the simulation approach in this study is to exclusively prove the concept of polymer in-situ rheology prediction through injection BHP data. Therefore, the workflow adopted for the objective of this study was exclusively as follows:

- Establish reliable model inputs by history matching water injection baseline BHP
- Test BHP sensitivity to rate and/or concentration stepping with generic in-situ rheology curves
- Investigate the impact of RRF dependence on permeability and sensitivity to different permeability-RRF correlations
- Use in-situ rheology and RRF as key parameters to history match polymer injection and chase water BHP
- Compare obtained polymer behavior to lab data

*3.1. Model description*

Choosing radial coordinates over Cartesian is recommended in polymer injectivity modeling as it prevents velocity smearing in the near-well bore region and hence allow more accurate recognition of in-situ rheology curves input. The model has 20 grids in the radial direction and 89 layers. A dummy producer was placed in the outermost grid for material balance purposes. Number of layers was based on provided up-scaled geological and petrophysical data. Fine gridding was applied in the near wellbore region to capture high Darcy velocities in wellbore vicinity. A summary of model parameters is shown in Table 1 below. Static inputs and assumptions for petrophysical, PVT, and rock-fluid data are shown in Table A1 and Figures A1 and A2.

Table1: Single-well model parameters

| Grid type | Radial |
|---|---|
| Well type | Vertical |
| Grid dimensions | 20 x 1 x 89 |
| Innermost grid size | 0.25 ft |
| Outermost grid size | 1125 ft |
| Total radius | 3000 ft |
| Layer thickness | 1.25 – 12 ft |
| Total thickness | 295 ft |
| Perforated section | Layers 23 to 55 (66 ft) |

*3.2. Water injection baseline history match approach*

Considering radial Darcy equation for flow in porous media:

$$\Delta P = \frac{Q\ \mu}{2\ \pi\ k\ h} \ln\left(\frac{r}{r_w}\right) + s$$

Where $\Delta P$ is the pressure drop between an injector with radius of $r_w$ and a point at $r$ distance in a reservoir with thickness of $h$, $Q$ is injection rate, $\mu$ is injected fluid viscosity, and $s$ is the skin factor; we could assume that that the main two parameters of concern to match water injection baseline are permeability and skin factor due to their relatively significant uncertainty. Data used for permeability distribution input were obtained from core data of off-set wells and corrected through indirect conversion of porosity and saturation logs. Due to this uncertainty and due to reservoir inherent heterogeneity, it is a common practice to apply permeability multipliers to the original input in order to match BHP response. PLT logs conducted during water injection baseline were utilized to justify proposed permeability multipliers. Six PLT sets were available for analysis of which three were conducted during water injection before acid stimulation jobs, one after acid stimulation, and two during polymer injection.

*3.3. Impact of rate and concentration stepping*

Several generic cases with different rate and concentration stepping scenarios were tested over the actual period of polymer injection phase. The objective was to investigate the sensitivity to different rate and concentration stepping at Newtonian and non-Newtonian conditions.

The following generic scenarios were considered:

- Constant rate and constant concentration
- Concentration steps at constant rate
- Rate steps with:
  - o Constant concentration
  - o Increasing concentration
  - o Decreasing concentration

Rate and concentrations assumed in the above scenarios are shown in Table 2 below.

Table 2: Rates and concentrations used for stepping generic scenarios.

| Scenario | Value(s) |
|---|---|
| Constant rate | 3000 bbl/day |
| Rate steps | 1000, 3000, and 5000 bbl/day |
| Constant concentration | 1600 ppm |
| Concentration steps | 600, 1600, and 2700 ppm |

For Newtonian rheology cases, water was injected at 0.43 cp viscosity, which is the viscosity of seawater used in the actual test. The rheology curves corresponding to non-Newtonian behavior were

created using an extended version of Carreau model that is used to fit complex elastic polymer rheology including shear-thinning and shear-thickening:

$$\mu_{app} = \mu_\infty + [(\mu_o - \mu_\infty) * [1 + (\lambda_1 u)^2]^{\frac{n_1-1}{2}}] + [\mu_{max} * (1 - e^{-[\lambda\ u]^{n_2-1}_{2}})]$$

where $\mu_{app}$ is polymer apparent viscosity, $\mu_o$ and $\mu_\infty$ are limiting Newtonian viscosities at high and low shear limits, respectively, $\lambda$ and $n$ are empirical polymer constants, u is the superficial velocity of the polymer in porous media and $\mu_{max}$ is the shear-thickening plateau viscosity.

Three curves were created to cover polymer concentrations applied in the test (Figure 1). The generated curves exhibit a combined shear effect that decreases with decreasing concentration toward a near-Newtonian behavior. Velocity range of the curves is between 0.1 and 1000 ft/day. The outcomes of simulations with rate and/or concentration steps will demonstrate the sensitivity of BHP when encountering various segments of complex rheology depending on calculated Darcy velocity values at each rate. Parameters of Carreau model equation used to generate the curves is in Table 3 below.
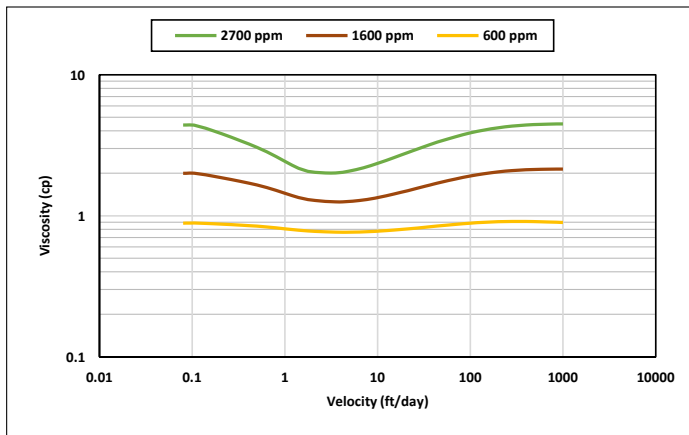


Figure1: In-situ rheology curves used in the rate and concentration stepping sensitivity

Table 3: Parameters used to generate in-situ rheology curves for sensitivity tests

|  | 2700 ppm | 1600 ppm | 600 ppm |
|---|---|---|---|
| **u** | 0.1 to 1000 ft/day | | |
| **μ_max** | 10 | 4.5 | 1.35 |
| **n2** | 1.5 | | |
| **λ2** | 1.00E+04 | | |
| **μ∞** | 0.43 | | |
| **μ0** | 10 | 4.5 | 2 |
| **n1** | 0.2 | 0.5 | 0.8 |
| **λ1** | 1.00E+06 | | |

*3.4. Impact of residual resistance factor (RRF)*

Permeability reduction due to polymer adsorption in porous media is measured by RRF, which is the ratio of water mobility before to after polymer flood.

$$RRF = \frac{\lambda_{w,init}}{\lambda_{w,p}} = \frac{k_{w,init}}{k_{w,p}}$$

In general, level of polymer adsorption increases in tighter formations due to increase in the fraction of pore-volume inaccessible to larger polymer molecules. The relationship governing RRF dependence on permeability is thus considered as a major tuning parameter for history matching polymer flooding. Several RRF-permeability correlations were tested based on lab-measured RRF data of SAV-10 polymer(Figure 2). Besides permeability-dependent RRF, average RRF values are often used in modelling polymer flooding to simplify history matching process. This method is usually more suitable for homogenous reservoirs; however, it may be applicable for heterogeneous reservoirs considering average formation capacity. Therefore, BHP response to weighted average RRF values of proposed correlations corresponding to the layers' permeability and thickness was also investigated.
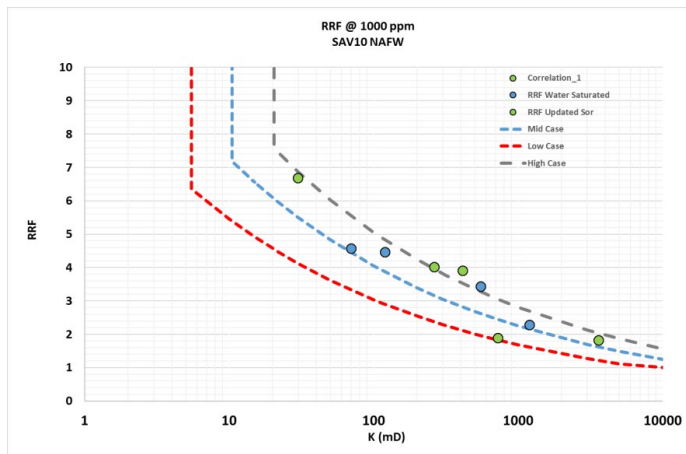


Figure 2: Proposed low, mid, and high RRF correlation based on lab data

### 3.5. Polymer injection history matching approach

The polymer injection phase was matched using information gained from generic sensitivity studies and integration of available lab and field data. Bulk viscosity and in-situ measurements that incorporate the impact of shear rate on SAV10 viscosity at different concentrations are shown in Figures 3a and 3b. Expirmental results show shear thinning only in bulk measurements and apparent shear thickening at high shear rates for flow in porous media, proving the inherent viscoelastic behavior of SAV10.  Besides, the effects of pre-shearing and oil presence were also investigated as shown in Figures 4a and 4b. It is evident from these results that both pre-shearing and presence of oil can reduce the degree of shear thickening and delay its onset to higher shear rates.

Field data used in this study include daily records of injection rates, injected concentrations, viscosity measurements across shearing device, degradation % from pre-shearing, and BHP. Four main injection rate steps were performed during the test at 800, 1500, 2000, and 1500 bpd as shown in Figure 5 below. Concentration stepping was implemented only during first sequence at 800 bpd. The second and third sequences had nearly constant concentrations, and the last sequence was dedicated for concentration tapering toward the end of the test. The test program also included pre-shearing the polymer solution prior to injection (Figure 6). Viscosity measurements were conducted upstream the shearing device choke for the whole test period. Downstream viscosity measurements were conducted when the well was operating at vacuum i.e. zero wellhead pressure. For periods when wellhead pressure is not zero, downstream viscosity was estimated from shearing device calibration correlation. Figure 7 shows both measured and estimated viscosity measurements upstream and downstream the shearing device. It is evident that measured downstream viscosities deviate slightly and are larger than the viscosities estimated from correlation. In addition, one can observe that the impact of pre-shearing is more pronounced at high concentrations. In order to

account for the impact of pre-shearing, the inputs for polymer concentrations in the model were reduced to mimic degradation % and therefore recognize viscosity reduction due to degradation.
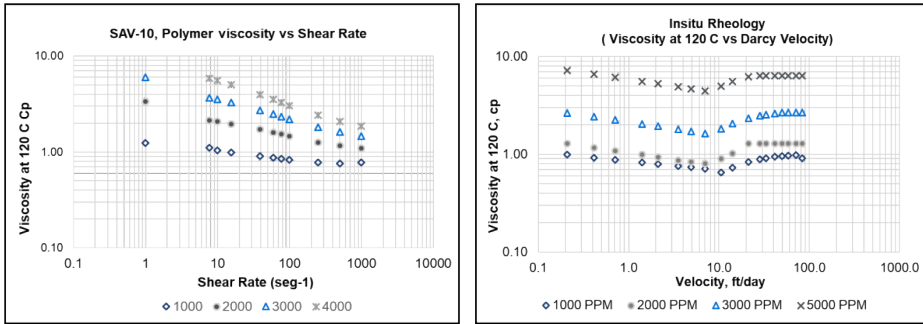


Figure 3: a) Bulk viscosity measurements of SAV-10 at different concentrations and b) In-situ viscosity measurements of SAV-10 at different concentration at 120°C
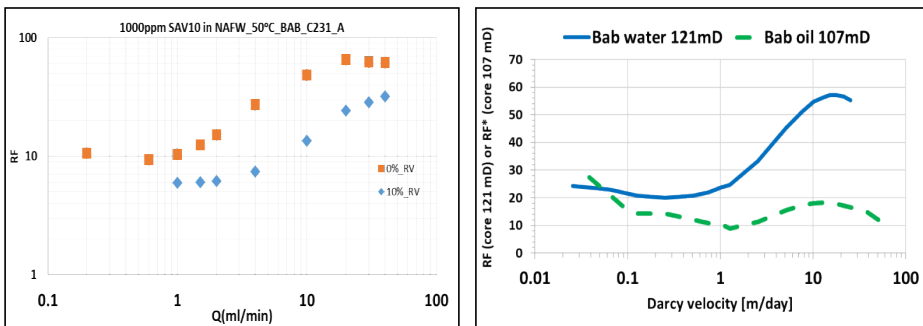


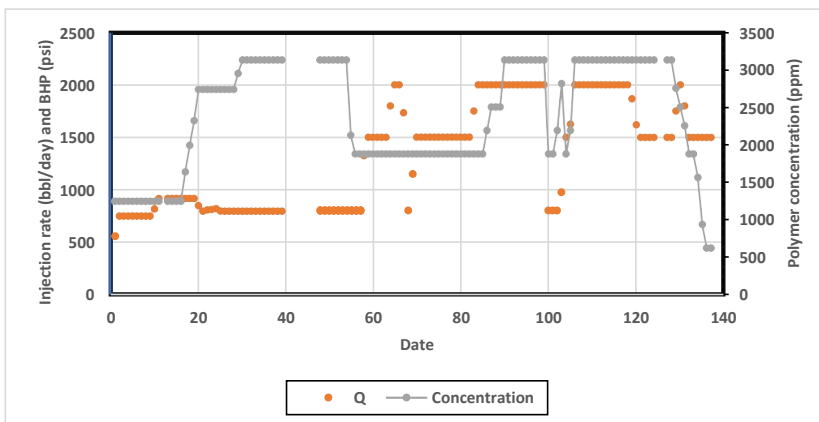Figure 4: a) Impact of degradation from pre-shearing and b) Oil presence, on the onset of SAV-10 apparent shear thickening in porous media



Figure 5: Data of injection rates and polymer concentrations used in the injectivity test
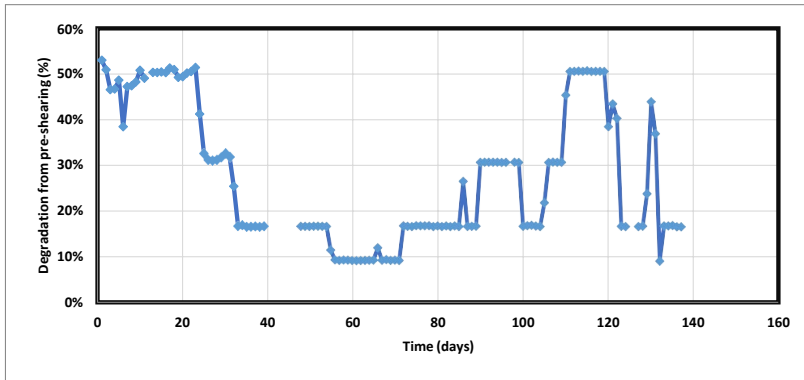
Figure 6: Percentage of degradation from pre-shearing applied on polymer solution prior to injection
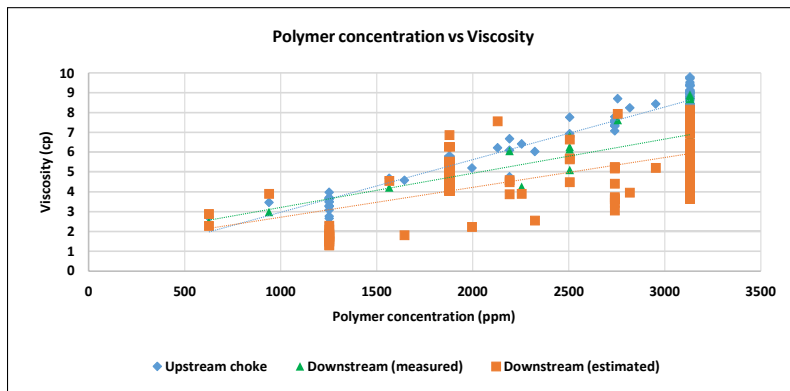


Figure 7: Polymer viscosity measurements across the shearing device choke and estimated downstream viscosities

## 4. Results and discussion

### 4.1. Water injection baseline history matching

It is evident from PLT results (Figure 8), that the uppermost sector of perforated section received significantly more injected fluid after acid stimulation jobs, this can indicate severe permeability alteration possibly as a result of an induced fracture or wormhole activation. Therefore, a dynamic permeability technique was applied to alter upper sector permeability multiplier by using simulation restart method. The objective was to match PLT logs of water injection baseline period in order to correct vertical permeability distribution. Figure 9 below shows the applied permeability multipliers and comparison to original data. Sectors within perforated zone were defined based on the results of PLT. For skin factor tuning, best matches were obtained with the following assumptions: 1) +3.5 skin before first acid stimulation, 2) +2.0 skin after first acid stimulation, and 3) -0.45 skin with permeability alteration in the upper sector after the second acid stimulation. The BHP history match for water injection baseline is shown in Figure 10.
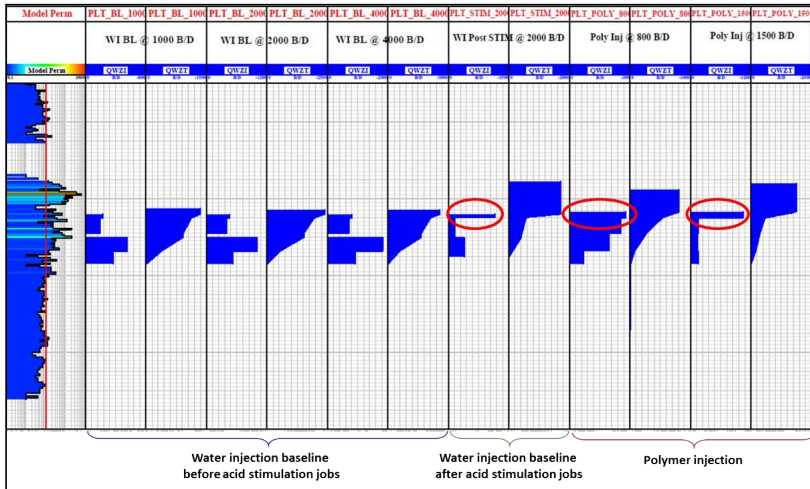
Figure 8: Production logging tool (PLT) logs conducted during injectivity test
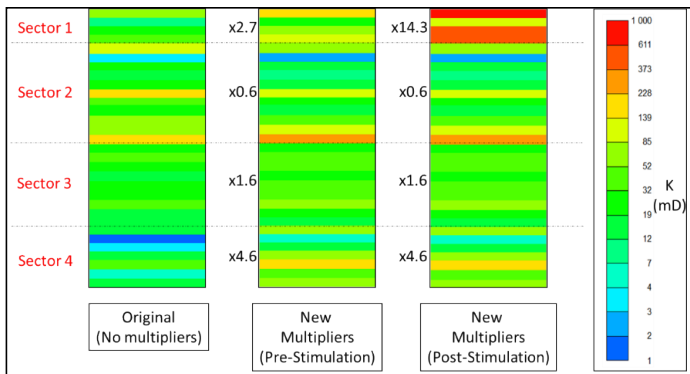


Figure 9: Permeability multipliers applied to match PLT logs pre- and post- acid stimulation jobs
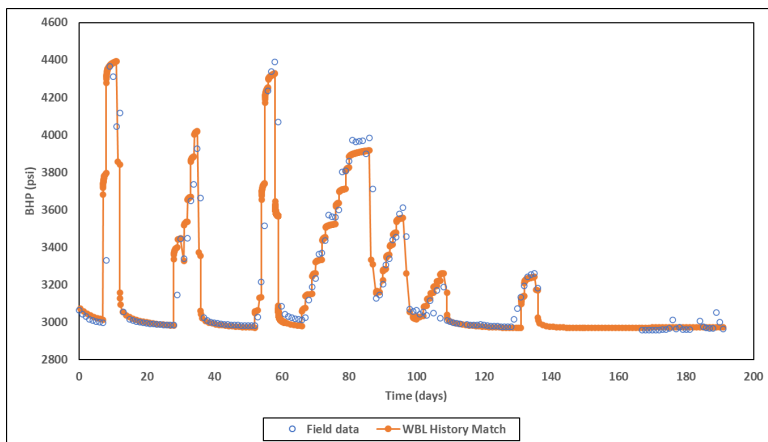


Figure 10: History match of water injection baseline BHP

### 4.2. Sensitivity to rate and concentration stepping

Results obtained from generic simulations of BHP sensitivity to rate (Q) and concentration (Cp) stepping are shown in Figures 11 and 12, respectively. Findings had confirmed that non-Newtonian injection takes significantly longer time to stabilize compared to Newtonian. This behavior is observed for both constant rate injection as well as in rates stepping case. Besides, shear thickening behavior in near-wellbore region is detectable through the gradual increase in BHP at every rate step indicating increase in viscosity with increasing Darcy velocity. The near-Newtonian behavior of BHP at the lowest rate step is reflecting the Newtonian plateau that exists between shear thickening and shear thinning segments in the rheology curve of applied concentrations. Concentration stepping has shown no impact of the concentration change direction whether it is increasing or decreasing as pressure increases and drops at the same magnitude. However, the transition of BHP response between concentration steps demonstrates more gradual trend when compared to the one between rate steps.
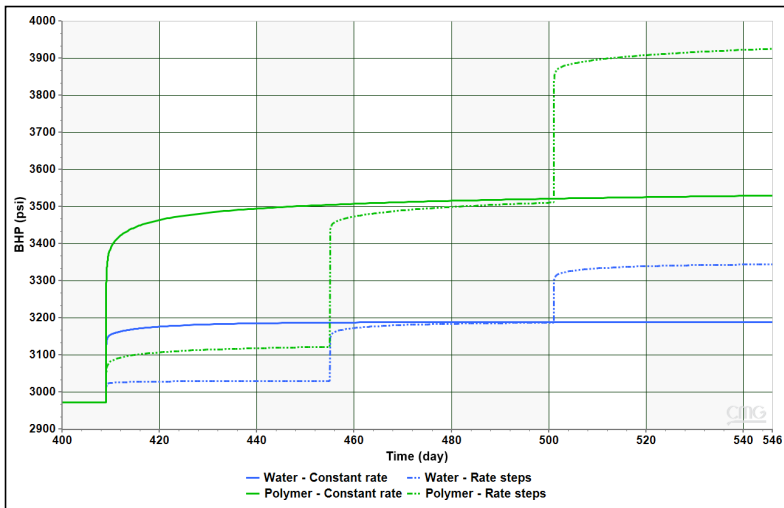


Figure 11: Impact of rate stepping on Newtonian and non-Newtonian injection
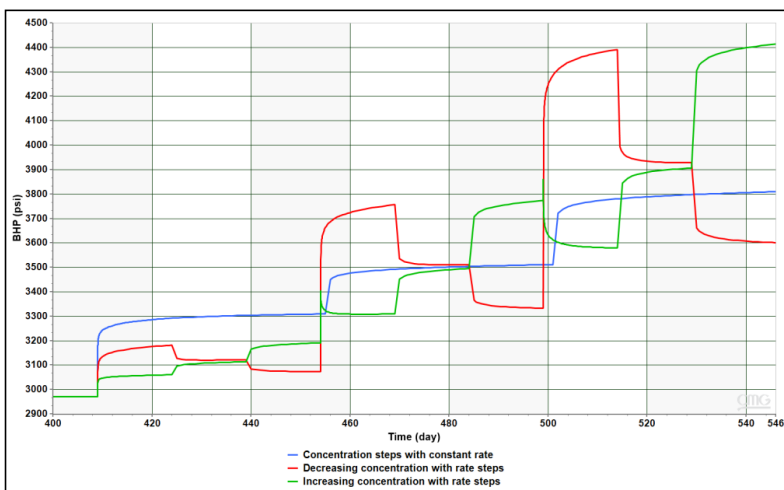


Figure 12: Impact of concentration stepping with different patterns on polymer injection

### 4.3. Sensitivity to residual resistance factor (RRF)

Several permeability dependent RRF correlations were proposed based on provided lab data. For each correlation, weighted average RRF was calculated using weighted formation capacity based on layer thickness and permeability. Table 4 below show the three correlations and their respective weighted average RRF. Results of BHP sensitivity to each case with concentration stepping and rate stepping are shown in Figures 13 and 14, respectively. Simulations have demonstrated that correlation and weighted average RRF's result in the similar pressure response. Besides, the observed effects of concentration stepping and rate stepping are not affected by applied RRF.

Table 4: Correlations proposed to fit RRF lab data with their respective weighted average

| Scenario | RRF correlation | $K_{min}$ | Weighted Average RRF |
|---|---|---|---|
| Low | $RRF = 9.6 \times (k)^{-0.251}$ | 5 | 4.171 |
| Mid | $RRF = 13.0 \times (k)^{-0.255}$ | 10 | 3.322 |
| High | $RRF = 16.4 \times (k)^{-0.255}$ | 20 | 2.506 |
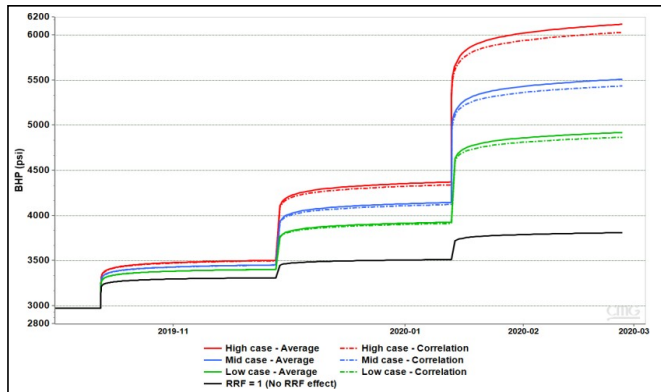


Figure 13: Impact of RRF correlations and averages on concentration stepping
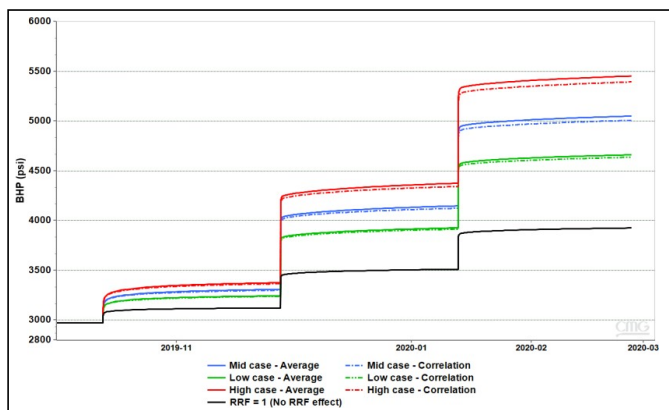


Figure 14: Impact of RRF correlation and averages on rate stepping

### 4.4. Analysis of field bottom-hole pressure data

It is evident from previous research findings [2,4], that non-Newtonian rheology behavior results in non-linear transient BHP response with longer stabilization time compared to Newtonian behavior. Injection of Newtonian fluid (like water) yields a linear response and significantly shorter buildup of BHP toward stabilization. One can detect these behaviors from plots of BHP versus injection rates and BHP versus time.

Field data of BHP during water injection baseline and polymer injection were analyzed to investigate BHP response to Newtonian and non-Newtonian flow. Although water injection took place over 13 months, pressure data is available only for the second half of that period (Figure 15). Besides that, the data see extreme rate fluctuations and very short interrupted injection periods. There is also the acid stimulation jobs impact which significantly affects pressure response. Therefore, the only analyzable pressure data found was in period after first acid stimulation where water injection took place for about 20 days with five 2000 bbl/day rate steps up to 10000 bbl/day (Figure 16). The plot of BHP versus injection rate shows a linear correlation which reflects Newtonian behavior (Figure 17).
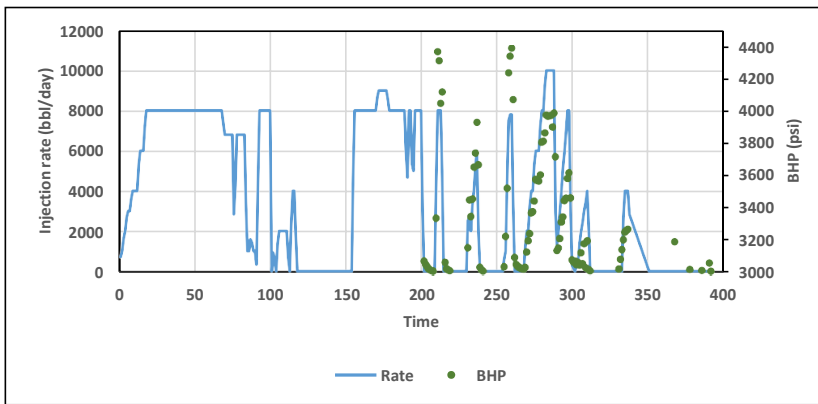


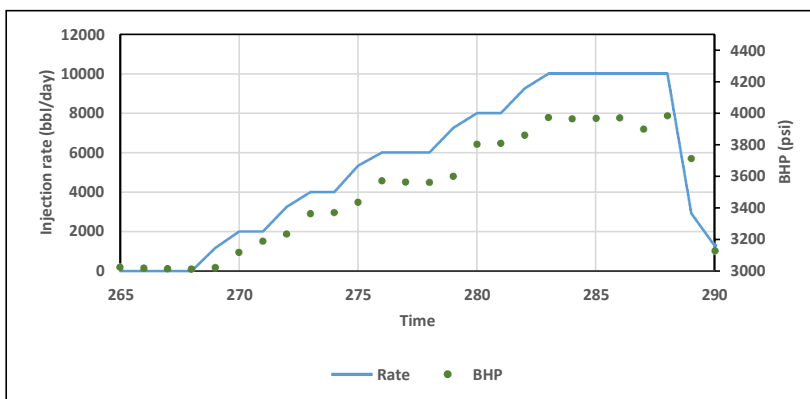Figure 15: Field data of injection rates and BHP during water injection baseline



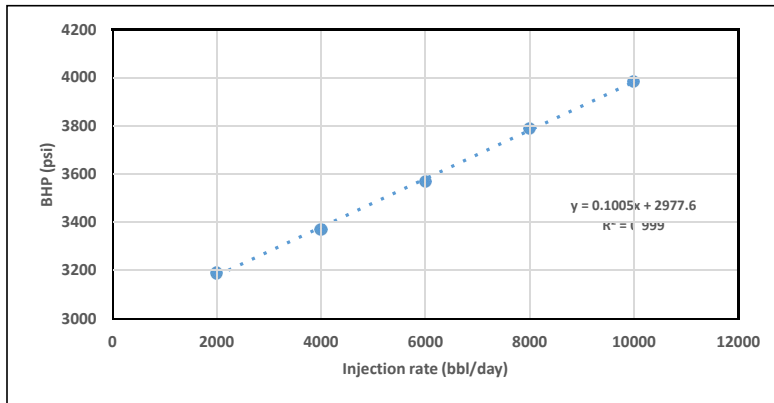Figure 16: Segment of water injection baseline used for BHP analysis with rate steps

Figure 17: Plot of BHP versus injection rate for part of water injection baseline

Oppositely, the analysis of BHP response during polymer injection shown a signal of active apparent shear-thickening behavior. This is demonstrated through plots of BHP vs. injection rate at several injected pore-volumes (PV's) (Figure 18). The increasing slope is a predicted signature of shear thickening as viscosity increases with Darcy velocity.

The BHP response versus time was also analyzed for each rate step as shown in Figure 19. The pressure profiles versus log PV exhibit sharp increases especially for higher rates (1500 and 2000 bpd) which is considered as a signal of shear thickening behavior in the near well bore region. At the rate of 800 bpd, one can notice that BHP increase in larger slope at higher concentrations. This evidence supports the assumption of the rheology leaning toward near-Newtonian behavior with decreasing concentration. In contrast to these observations, shear thinning would demonstrate decreasing slope in BHP vs. rate plots and gradual increase in BHP with time as demonstrated by Alzaabi et al. 2020 [4].
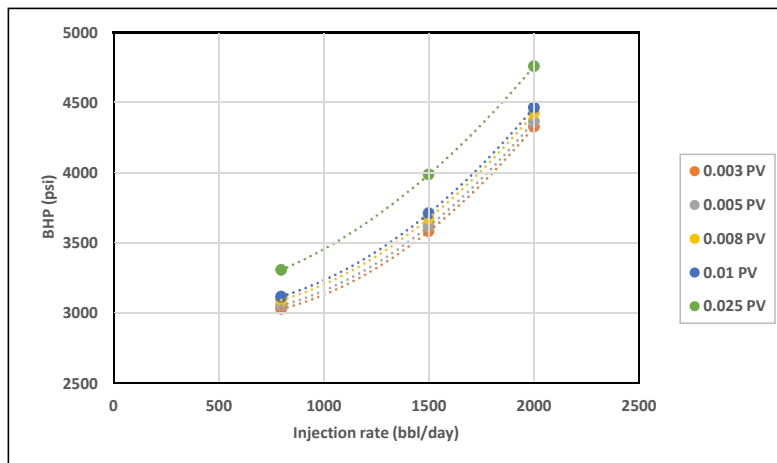


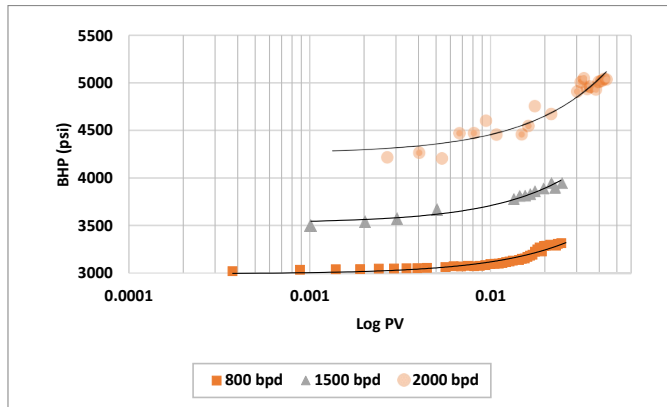Figure 18: BHP versus injection rate for polymer injection at several pore-volumes

Figure 19: BHP versus log pore-volume at different injection rates

*4.5. History matching polymer injection and chase water*

Following above results and findings, three scenarios that include only shear thickening behavior at high velocities were assumed for polymer injection history matching (Figure 20). The rheology curves were created using extended Carreau equation with the same average viscosity of 3 cp over the selected velocity range. These assumed scenarios are inclusive of all possible shear thickening behaviors in the near-well bore region. In CMG IMEX simulator, complex combined polymer rheology is defined through velocity tables. Each velocity table corresponds to a specific Darcy velocity value, under which user can input values for polymer concentration and corresponding viscosity. The simulator calculates water-polymer mixture velocity for each grid block and performs a two-dimensional interpolation to calculate relative polymer viscosity based on relative concentration. Therefore, the defined curves are all corresponding to a single concentration value, the maximum concentration in this case, and the simulator performs interpolations for lower concentrations. This implies that rheology curves for lower concentrations are essentially parallel shifted curves with the same slope as the defined curve.
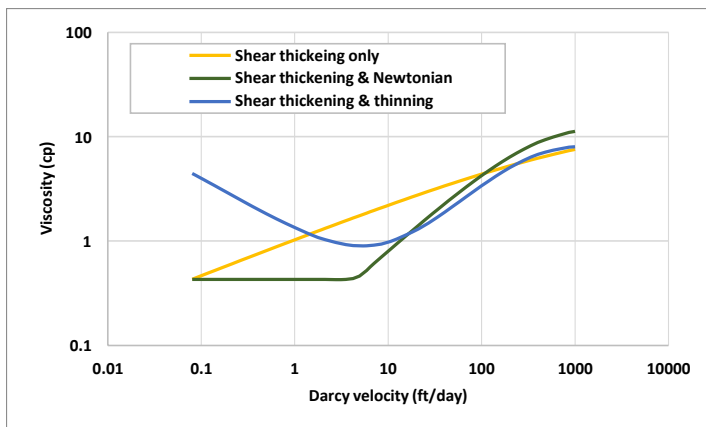


Figure 20: Shear thickening rheology scenarios tested for polymer injection history matching

The model was used to simulate actual polymer injection period with field injection rates and polymer concentrations using the three generic shear thickening cases. Results of simulated BHP are shown in Figure 21 along with injection rate and injected polymer mass rate. It is evident that the

shear thickening only scenario results in the highest pressure build up since it involves ever-increasing viscosity in near-wellbore region toward the injector. The combined effect scenario where shear thinning takes place at low velocities exhibits a slightly lower pressure response. This may indicate that the most acting velocity range is actually between 1 to 100 ft/day where the viscosity of shear thickening only case is larger. The pressure response is overall reflecting the trend of polymer concentration represented by polymer mass rate. However, due to different slopes of applied in-situ rheology curves, the pressure contrasts with concentration and/or rate variations are more pronounced for lower slopes. Moreover, the combined rheology with shear thinning at low velocities shows better representation for gradual changes in rate and concentration. It does however exhibit spiking pressure response at the points of injection resumption after shut-in periods which might be a simulator artefact.
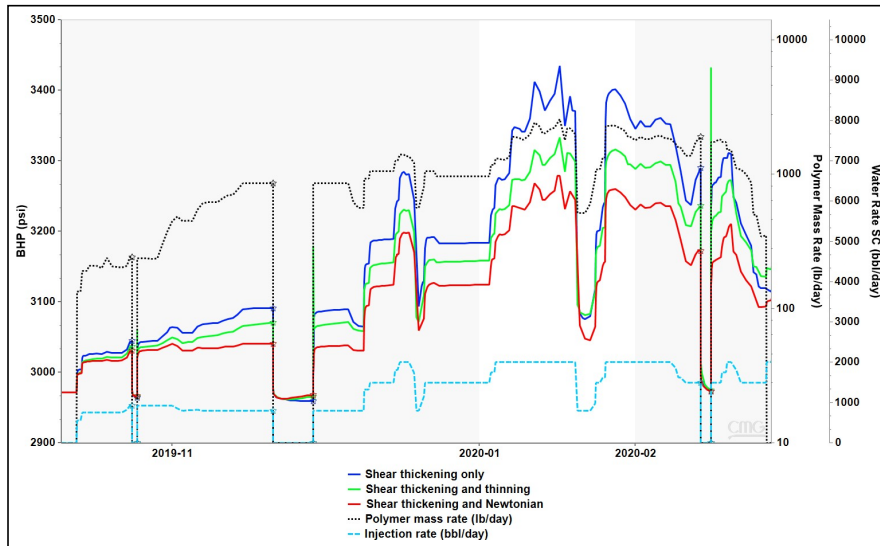


Figure 21: BHP response of the shear thickening cases using actual field rates and concentrations

Considering above analyses and findings, best match for polymer injection phase was obtained using a combined rheology effect with five-curve input representing five different concentration levels (Figure 22). The curves were generated using extended Carreau equation with the parameters shown in Table 6. The applied rheology exhibits a delay of shear thickening onset and larger slope as concentration decreases which reflects the impact of degradation from pre-shearing. Moreover, low concentrations have more pronounced Newtonian plateaus at high and low velocity endpoints. Maximum viscosities at highest velocities of the five curves ranged from 5 cp to 1 cp. A shear thinning component was also included and found essential for history matching with all curves having identical shear thinning parameters.

Both polymer injection and chase water matchings were achievable with an average RRF value of "4.1". which is the weighted average RRF value of the proposed high case correlation. A dynamic skin factor was essentially applied to mimic the skin impairment increase. Skin was thus updated monthly starting from -0.45 up to +7.5. The skin impairment was assumed as a temporary impact of polymer slug accumulation in the near-wellbore region, therefore better match to the chase water was obtained when skin was gradually reduced to its original prior to polymer injection (Figure 23). The history matched BHP of polymer injection and chase water is illustrated in Figure 24.
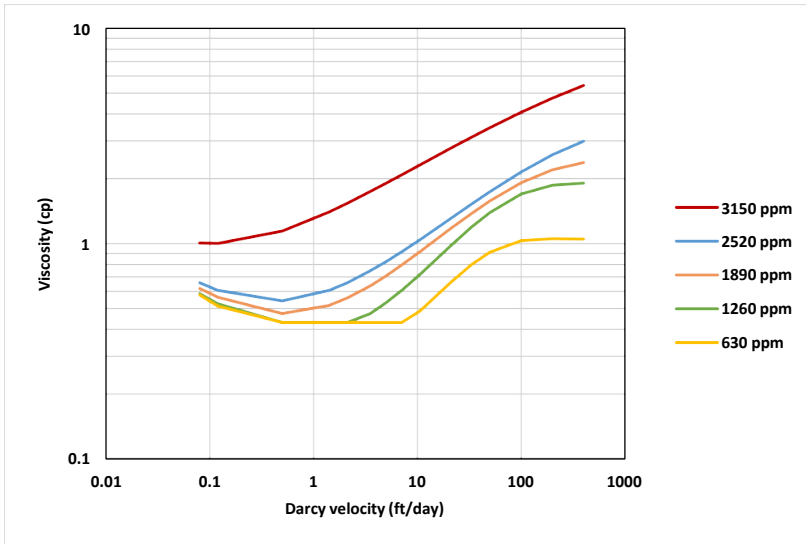
Figure 22: Rheology curves used in history matching polymer injection

Table 6: Extended Carreau equation parameters used to create matching rheology curves

|  | 3150 ppm | 2520 ppm | 1890 ppm | 1260 ppm | 630 ppm |
|---|---|---|---|---|---|
| u | 0.1 to 400 ft/day | | | | |
| $\mu\_max$ | 17 | 8 | 5.5 | 4 | 2 |
| n2 | 1.36 | 1.52 | 1.6 | 1.75 | 2.2 |
| λ2 | 1.2E+03 | 2.0E+03 | 4.0E+03 | 6.0E+03 | 1.0E+04 |
| $\mu\infty$ | 0.43 | | | | |
| μ0 | 2 | | | | |
| n1 | 0.5 | | | | |
| λ1 | 1.00E+07 | | | | |



Figure 23: Skin factor applied along polymer injection and chase water in history match
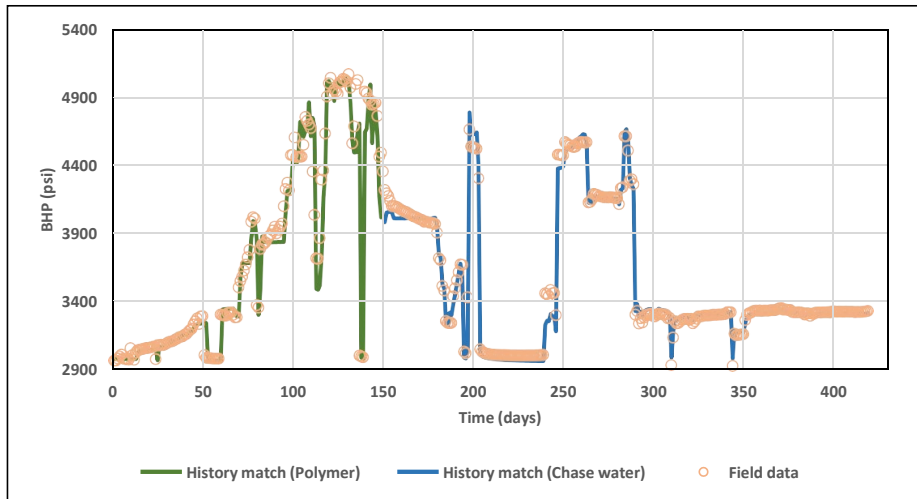
Figure 24: History matching BHP of polymer injection and chase water

## 5. Conclusions

In this paper, a polymer injectivity field test in a high temperature high salinity carbonate reservoir was analyzed through numerical simulation approach utilizing CMG IMEX simulator. The analysis involved investigating the sensitivity of rate and concentration stepping on BHP response as well as impact of permeability correlated RRF. The polymer injection BHP was successfully history matched with a set of in-situ rheology curves reflecting the impact of

The conclusions from this study can be summarized as follows:

- PLT logs of water baseline injection prior to polymer injection can be utilized to match vertical injection distribution across perforated zone. This practice can provide a more accurate permeability inputs especially for cases where significant uncertainty in permeability exists.
- The BHP response to non-Newtonian behavior in the near-wellbore region can be distinguished from the Newtonian behavior by the characteristics of longer transient pressure build up due to the velocity-dependent viscosity.
- Concentration stepping affects BHP signal differently than rate stepping in the used simulator. The response to rate changes is sharper and more abrupt compared to concentrations stepping. This is attributed to the time it takes to fulfill the required change in concentration in the near wellbore region.
- Average RRF values corrected to weighted average formation capacity are sufficient for BHP history matching purposes as they yield similar results as permeability-dependent RRF correlations.
- Plots of field downhole measurements of BHP versus injection rates can be utilized to detect in-situ fluid rheology. Newtonian water injection showed linear trend while polymer injection showed a non-linear trend with increasing slope reflecting shear thickening behavior.
- The sensitivity to different shear thickening scenarios revealed that BHP response varies significantly if shear thinning or Newtonian behavior were applied at low velocity range. This suggests that history matching polymer injection should include a representative in-situ rheology description to capture different signatures rather than applying average effective viscosity.

- Degradation percentage due to pre-shearing can be represented in the model by reducing injected concentration by the same percentage and applying multiple rheology realizations to account for degradation impact.
- The matching of polymer injection BHP was obtained with a set of five in-situ rheology curves bounded between maximum and minimum injected degradation-corrected concentrations. The anticipated impact of degradation on the onset and magnitude of shear thickening was verified and represented by modifying shear thickening slope and maximum apparent viscosity.

**Author Contributions:** M.A.A was responsible for simulations and writing the paper. J.H set up the simulation model and assisted in results analysis. A.S. and S.M contributed to planning of the study, discussion of results, and reviewing the paper. All authors have read and agreed to the published version of the manuscript.

## Appendix A

Table A1: PVT data used in the model

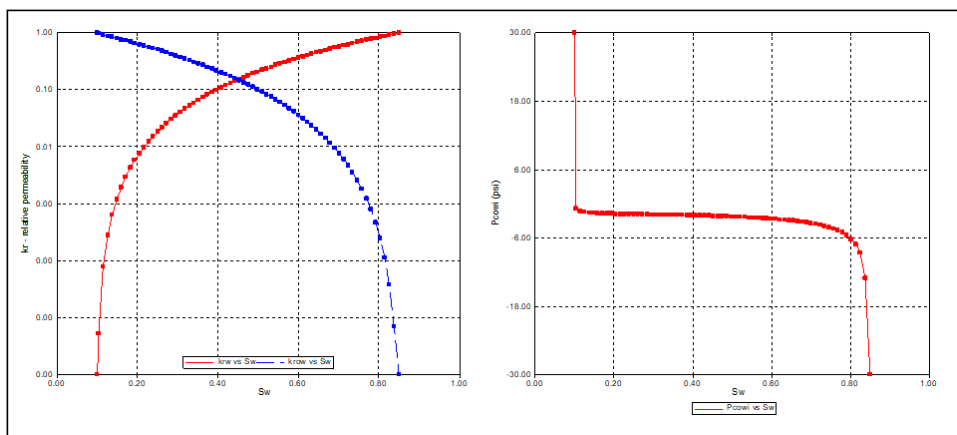| Parameter | Value |
|---|---|
| Reservoir temperature | 120 °C |
| Bubble point pressure | 2140 psi |
| Oil density | 815.18 Kg/m³ |
| Oil viscosity | 0.32 cp |
| Water density | 1174.79 Kg/m³ |



Figure A1: Oil-water relative permeability and capillary pressure curves for permeability above 100 mD
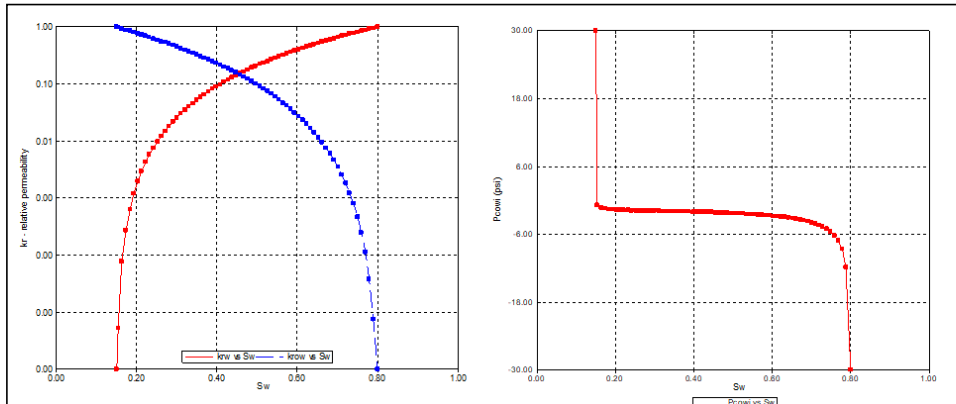
Figure A2: Oil-water relative permeability and capillary pressure curves for permeability below 100 mD

# References

1.  Skauge, A.; Zamani, N.; Jacobsen, J.G.; Shiran, B.S.; Al-Shakry, B.; Skauge, T. Polymer Flow in Porous Media: Relevance to Enhanced Oil Recovery. *Colloids Interfaces* **2018**, *2*, 1–28.

2.  Jacobsen, J. G.; Alzaabi, M.; Skauge, T.; Sorbie, K.; Skauge, A. Analysis and Simulation of Polymer Injectivity. Presented at the 20th European Symposium on Improved Oil Recovery, Pau, France, 8-11 April 2019.

3.  Skauge, T.; Kvilhaug, O.A.; Skauge, A. Influence of Polymer Structural Conformation and Phase Behavior on In-situ Viscosity. Presented at the 18th European Symposium on Improved Oil Recovery, Dresden, Germany, 14–16 April 2015.

4.  Alzaabi, M.A.; Jacobsen, J. G.; Sumaiti, A. A.; Masalmeh, S.; Pettersen, Ø.; & Skauge, A. Polymer Injectivity Test Design Using Numerical Simulation, *Polymers* **2020**, *12*, 1-23.

5.  Sheng, J.J.; Leonhardt, B.; & Azri, N. Status of Polymer-Flooding Technology. *J. Can. Pet. Technol.* **2015**, *54*.

6.  Manrique, E.; Ahmadi, M.; & Samani, S. Historical and Recent Observations in Polymer Floods: An Update Review. *CT&F, Tecnología y Futuro* **2015**, *6 (5)*: 17 – 48.

7.  Jouenne, S. Polymer Flooding In High Temperature, High Salinity Conditions: Selection of Polymer Type and Polymer Chemistry, Thermal Stability. *Journal of Petroleum Science and Engineering* **2020**, *195*, 107545.

8.  Dupuis, G.; Antignard, S.; Giovannetti, B.; Gaillard, N.; Jouenne, S.; Bourdarot G. et al. A New Thermally Stable Synthetic Polymer for Harsh Conditions of Middle East Reservoirs. Part I. Thermal Stability and Injection in Carbonate Cores. SPE 188479. Abu Dhabi International Petroleum Exhibition & Conference Held in Abu Dhabi. UAE 2017.

9.  Alfazazi, U.; AlAmeri, W.; Hashmet, M.R. Screening of New HPAM Base Polymers for Applications in High Temperature and High Salinity Carbonate Reservoirs. SPE 192805. Abu Dhabi International Petroleum Exhibition and Conference, Abu Dhabi, UAE 2018.

10. Masalmeh, S.; AlSumaiti, A.; Gaillard, N.; Daguerre, F.; Skauge, T.; Skuage, A. Extending Polymer Flooding Towards High-Temperature and High-Salinity Carbonate Reservoirs. Abu Dhabi International Petroleum Exhibition & Conference. Abu Dhabi, UAE November 2019.

11. Seright, R.S.; Wavrik, K.E.; Zhang, G.; AlSofi, A.M. Stability and Behavior in Carbonate Cores for New Enhanced-Oil-Recovery Polymers at Elevated Temperatures in Hard Saline Brines. *SPE Reservoir Eval. Eng.* **2020**, *24(01)*, 1-18.

12. Rachapudi, R. V.; Alshehhi, S. S.; BinAmro, Ahmed A.; Masalmeh, S. K.; Dey, A.; Al Nuimi, S. M.; Kenawy, M. M.; Fabbri, C.; Romero, C.; Xu, S.; Mabrook, M.; Garnier, O. F.; Wang, K.; Jouenne, S.; Cordelier, P.; Guillaume, D. World First Polymer Injectivity Test in High Salinity and High Temperature Carbonate Reservoir, Case Study from a Giant Reservoir in UAE. Paper presented at the Abu Dhabi International Petroleum Exhibition & Conference, Abu Dhabi, UAE, November 2020.

13. Masalmeh, S. K.; Wei, L.; Hillgartner, H.; Al-Mjeni, R.; Blom, C. Developing High Resolution Static and Dynamic Models for Waterflood History Matching and EOR Evaluation of a Middle Eastern Carbonate Reservoir. Paper presented at the Abu Dhabi International Petroleum Conference and Exhibition, Abu Dhabi, UAE, November 2012.

14. Masalmeh, S. K.; Wei, L.; Blom, C.; Jing, X.D. EOR Options for Heterogeneous Carbonate Reservoirs Currently Under Waterflooding." Paper presented at Abu Dhabi International Petroleum Exhibition & Conference. SPE-171900. Abu Dhabi, November 10-13 2014.

uib.no